

Axial Compressor Stability Enhancement

Timothy Oliver Houghton
Clare College

A dissertation submitted for the degree of
Doctor of Philosophy

February 2010



UNIVERSITY OF
CAMBRIDGE

Department of Engineering

Axial Compressor Stability Enhancement

Timothy Oliver Houghton

Summary

Aircraft jet engines must operate in a stable manner at all times. One source of instability is compressor stall. Stall problems can be reduced by machining cavities into the compressor casing adjacent to the rotor blades. This 'casing treatment' is the focus of the present work. Two treatment configurations are tested: circumferential grooves cut into the casing above the rotor blades, and axial slots cut into the casing adjacent to the rotor blade leading edges.

The performance of a single casing groove is measured at different axial locations over the blade tips. For the first time, it is shown that there are two locations where compressor stability is maximised; near the leading edge and near mid-chord. The interaction between the groove and the compressor flow field is then studied. It is found that when located near the leading edge, the groove has a strong interaction with the near-casing flow and tip leakage vortex, but when located near mid-chord, the interaction is more subtle and less damaging to efficiency. Since the groove works well in both locations, it is concluded that manipulating the tip leakage vortex is not critical for improving compressor stability.

Different groove numbers and cross-sections are then tested. For multiple grooves, the efficiency reduction is the sum of the constituent grooves, while the stall margin improvement is less than this sum. A simple square-section groove is found difficult to improve on, although in certain circumstances, a new 'intermittent groove' geometry is beneficial.

The performance of axial slots is then investigated. Different slot shapes are tested and the results added to previous work to suggest an optimum slot geometry. A computational flow study shows that large variations in blade loading occur as the blades pass the slots, which could cause noise and vibration. It is found that while the flow inside the slot is principally a quasi-steady recirculation, the interaction between the slots and blades is highly unsteady, and this unsteadiness should not be neglected in design. In general, it is found that casing treatments that generate large stability improvements cause large efficiency losses.

It is shown for the first time that the performance of casing grooves can be seriously reduced by changes in the stall inception mechanism. Maximum performance is achieved when the treated compressor stalls with a spike inception. Models from the literature are tested, but do not predict the stall inception mechanism well, which makes predicting the performance of casing grooves in a given compressor hard. Finally, it is shown that designing the blades and casing treatment as a unit may improve compressor performance.

Declaration

The research presented in this dissertation was conducted at the Whittle Laboratory in the Cambridge University Engineering Department between October 2005 and December 2009. This dissertation is the work of the author alone, and includes nothing which is the outcome of work done in collaboration, except where specifically indicated to the contrary. None of the work presented in this dissertation has been submitted to any other University or Institution for any other qualification. This dissertation contains approximately 58,000 words and 86 figures.

Timothy Oliver Houghton
February 2010

Publications

Houghton T O and Day I J (2012) Stability Enhancement by Casing Grooves: The Importance of Stall Inception Mechanism and Solidity. *ASME Journal of Turbomachinery*, **134**(2), doi:10.1115/1.4002986. Paper also presented at the 2010 ASME Turbo Expo, Glasgow.

Houghton T O and Day I J (2011) Enhancing the Stability of Subsonic Compressors Using Casing Grooves. *ASME Journal of Turbomachinery*, **133**(2), doi:10.1115/1.4000569. Paper also presented at the 2009 ASME Turbo Expo, Orlando.

Houghton T O and Day I J (2010) Compressor Casing. Patent GB1002250.7 filed at the United Kingdom Intellectual Property Office.

Acknowledgements

I am lucky to have been supported, helped and encouraged by many people during the course of my research. Unfortunately, I can only acknowledge some of them here.

The present work would not have been possible without the staff and students at the Whittle Laboratory. I would especially like to thank my supervisor, Ivor Day, for all his help and advice. He has been a great mentor and given his time generously; I have learned a great deal from him. I would also like to thank Chris Freeman for freely sharing his considerable 'real world' knowledge and experience, which has been invaluable. The technical support I have received for my experimental work from the technicians, especially from Dave Barlow, has been outstanding.

Writing the data logging and processing software used in my research would have been a far more daunting and time-consuming task without Tony Dickens' help, which I am grateful for. I would also like to thank Ed Naylor and Francesco Montomoli for getting me started on my computational work and providing continuing support, and Martin Goodhand for helpful technical discussions and the excursion.

I am fortunate to have been sponsored by Rolls-Royce. As well as providing funding, the technical input and help I have received from staff, particularly Mike Howard, John Bolger, Leigh Lapworth and Paolo Adami, has significantly improved the present work.

I would also like to thank John Adamczyk, Nick Cumpsty, Howard Hodson and Rob Miller for their contributions to various useful discussions, and express gratitude to the EPSRC for providing CASE funding and the administrators of the Darwin supercomputer for allowing me to use their excellent facilities at no cost.

On a more personal note, I would like to thank my parents for their support, in so many ways, throughout my life. Finally, I would like to thank Isobel for her love and encouragement, which has made all the difference.

Contents

1	Introduction	1
2	Background and Literature Review	4
2.1	The Unstable Operation of Axial Compressors	5
2.2	Tip Leakage Flow in Axial Compressors	7
2.3	Stall Inception	9
2.4	Stability Enhancement Methods	11
2.5	Discussion	17
3	Experimental Methods	22
3.1	The Compressors	23
3.2	Measurement Equipment	24
3.3	Experimental Techniques	26
3.4	Reynolds Number Independence of Stall	32
4	Computational Methods	38
4.1	Computational Tools	39
4.2	The Computational Model	40
4.3	Validation	44
4.4	Summary	46
5	Circumferential Groove Casing Treatments: Part 1	55
5.1	The Axial Location of a Single Casing Groove	56
5.2	Initial Experiments	57
5.3	Core Flow Effects	59
5.4	Near-Casing Flow Effects	61
5.5	Discussion	72
5.6	Grooved Casing Treatment Design using CFD	75
5.7	Conclusions	76

6	Circumferential Groove Casing Treatments: Part 2	95
6.1	Shallow Circumferential Grooves	96
6.2	Alternative Groove Geometries	98
6.3	Multiple Circumferential Grooves	102
6.4	The Impact of Tip Clearance on Multiple Groove Treatments	105
6.5	Discussion	106
6.6	Conclusions	108
7	Axial Slot Casing Treatments	117
7.1	Casing Slot Parametric Study	118
7.2	Initial Experiments	121
7.3	Core Flow Effects	122
7.4	Near-Casing Flow Effects: Unsteady Aerodynamics	126
7.5	Casing Slot Internal Flow	131
7.6	Entropy Generation by Casing Slots	133
7.7	The Effect of Increasing Tip Clearance	134
7.8	Discussion	135
7.9	Conclusions	139
8	Casing Grooves, Stall Inception and Solidity	161
8.1	The Impact of Grooved Casings on the Red Compressor	162
8.2	Casing Treatment and Stall Inception	164
8.3	Casing Treatment and Blade Solidity	173
8.4	Discussion	174
8.5	Conclusions	176
9	Conclusion	190
9.1	Circumferential Grooves	191
9.2	Axial Slots	192
9.3	A Comparison of Casing Grooves and Slots	193
9.4	Casing Treatment, Stall Inception and Solidity	194
9.5	Closure	195
9.6	Suggestions for Further Work	196

This dissertation was typeset using L^AT_EX and is hyperlinked for electronic readers.

Nomenclature

Latin Symbols

- a The Speed of Sound
- c Chord (c_x = Axial Chord, $c_{x,r}$ = Axial Chord of Rotor Blade Tip)
- C_{ma} Meridional Acceleration Coefficient $\left(\frac{V_{x,ri}}{V_{x,ro}}\right)$ This is defined at a given spanwise location and is not the axial velocity density ratio, or AVDR.
- C_p Pressure Coefficient $\left(\frac{P_s - P_{s1}}{P_{o1} - P_{s1}}\right)$
- $C_{p,rc}$ Greitzer *et al.* (1979) Rotor Casing Pressure Coefficient $\left(\frac{\Delta P_{s,rc}}{\frac{1}{2}\rho W_{ri}^2}\right)$
- DF_r Lieblein *et al.* (1953) Diffusion Factor for Rotors $\left(1 - \frac{W_{ro}}{W_{ri}} + \frac{\Delta V_\theta}{2\sigma_r W_{ri}}\right)$
- $DPFI$ Design Point Flow Rate Improvement $\left(100 \times \frac{\phi_{design,ct} - \phi_{design,sw}}{\phi_{design,sw}}\right)$ The percentage reduction in design point flow rate due to casing treatment.
- f Frequency
- h Specific Enthalpy
- \dot{m} Mass Flow Rate
- MEI Maximum Efficiency Improvement $(\eta_{max,ct} - \eta_{max,sw})$ The reduction in maximum efficiency due to casing treatment.
- P Pressure (P_s = Static Pressure, P_o = Total Pressure)
- PRI Pressure Rise Improvement $\left(100 \times \frac{\psi_{s,ct, stall} - \psi_{s,sw, stall}}{\psi_{sw, stall}}\right)$ The percentage reduction in pressure rise at stall due to casing treatment.
- s Pitch
- SMI Stall Margin Improvement $\left(100 \times \frac{\phi_{sw, stall} - \phi_{ct, stall}}{\phi_{sw, stall}}\right)$ The percentage reduction in flow coefficient at stall due to casing treatment.
- T Temperature (T_s = Static Temperature, T_o = Total Temperature)
- $\% tc$ Percentage of Tip Clearance Away From Casing Wall
- U Blade Speed (\bar{U} = Mid-Span Blade Speed)
- V Absolute Velocity (V_x = Axial, V_r = Radial, V_t = Tangential)
- W Relative Velocity (W_t = Tangential)

Greek Symbols

α	Absolute Flow Angles
β	Relative Flow Angles
η	Efficiency
λ	Wavelength
ρ	Density
σ	Solidity ($\frac{c}{s}$)
τ	Torque
ϕ	Flow Coefficient ($\frac{V_{x,in}}{U}$)
ψ	Total to Static Pressure Rise Coefficient ($\frac{\Delta P_{t-s}}{\frac{1}{2}\rho U^2}$)
ω	Rotational Speed

Subscripts

1	Inflow
2	Outflow
<i>sw</i>	Smooth Wall Case
<i>ct</i>	Casing Treatment Case
<i>o</i>	Stagnation Quantity
<i>s</i>	Static Quantity
<i>in</i>	Compressor Inlet
<i>r</i>	Rotor (<i>ri</i> = Rotor Inflow, <i>rc</i> = Rotor Casing, <i>ro</i> = Rotor Outflow)
<i>s</i>	Stage (<i>so</i> = Stage, and Stator, Outflow)
<i>t – s</i>	Total to Static (for characteristics)
<i>s – s</i>	Static to Static (for characteristics)
<i>stall</i>	At the Stall Point
<i>design</i>	At the Design Point

Superscripts

$\bar{\square}$	Average quantity
$\tilde{\square}$	Non-dimensional Quantity

Chapter 1

Introduction

Safety is critical in aviation. At best, accidents damage expensive equipment, alarm passengers and cause bad publicity. At worst, lives can be lost. It is therefore important that aircraft engines operate safely throughout a flight.

One potential engine failure mode is ‘surge’, which occurs when the flow through the engine’s compressor reduces, or even reverses. This reduces thrust and may severely damage the engine. Surge is an instability caused by the compressor stalling while operating at low flow rates, and thus becoming unable to maintain the pressure in the combustor. During surge, the combustor depressurises through the compressor and turbine, often causing flames to be ejected from the engine.

The present work studies a technology called ‘casing treatment’, which can be used to improve the stability of a compressor or fan at low flow rates. Casing treatment normally consists of cavities machined into the compressor casing in the vicinity of the rotor blades. There are many different casing treatment designs, but the most common are circumferential grooves and axial slots. These two treatments are explained schematically in Figure 1.1.

These two treatment designs are well known, but the optimal location, geometry and number of the grooves and slots is not. In the present work, experimental parametric studies are performed to investigate this.

The mechanisms by which casing treatments are able to delay stall in a compressor are also unknown, because the stall inception processes are not completely understood. The present work thus utilises experimental and computational flow studies to investigate the impact of the casing treatments on the compressor flow field in detail.

Casing treatment is often retrofitted to existing compressor designs as a ‘quick fix’ when a stalling problem has occurred. The present work investigates whether including casing treatment at the start of a design process could lead to a more efficient and stable compressor, and investigates circumstances in which casing treatments may not be as effective as hoped.

The structure used to present this work is as follows. In **Chapter 2**, the background to compressor stability problems is introduced, and relevant previously published work is reviewed. Then the experimental and computational methods used throughout the present work are presented in **Chapters 3** and **4**.

The analysis of casing treatment starts in **Chapter 5**, with the performance of a single groove being measured at different axial locations over the blade tips. A detailed experimental and computational study is then performed to link the observed performance of the casing groove to its impact on the compressor flow field at each location.

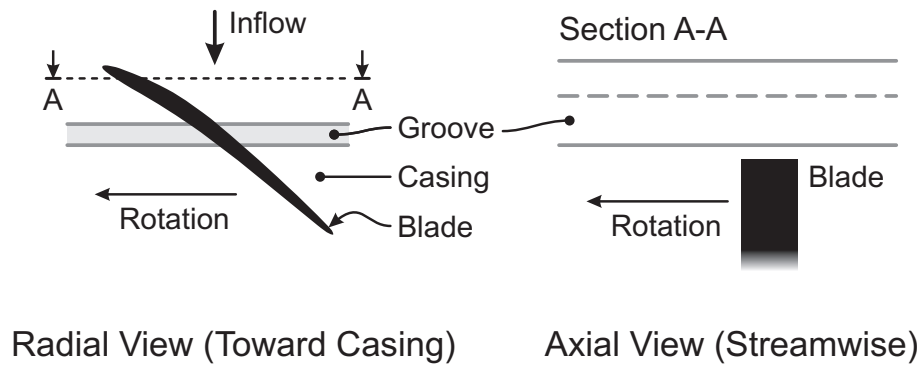
The geometry of the casing grooves is then investigated further in **Chapter 6**, where the impact of changing the shape and number of the grooves on the performance of the compressor is measured.

Casing slots are investigated in **Chapter 7**, starting with a parametric study to investigate the impact of changing the geometry of the slots on the performance of the compressor. The effect of the slots on the compressor flow field is then investigated, and the flow inside the slots themselves is also studied.

Finally, in **Chapter 8**, the impact of changes to the compressor’s stall inception pattern on the effectiveness of casing grooves is investigated, and published models are tested to ascertain whether they can predict the observed behaviour. The benefits of designing the compressor blades and casing treatment together, instead of retrofitting the treatment to an existing compressor design, are then investigated.

The main conclusions from the work are presented in **Chapter 9**.

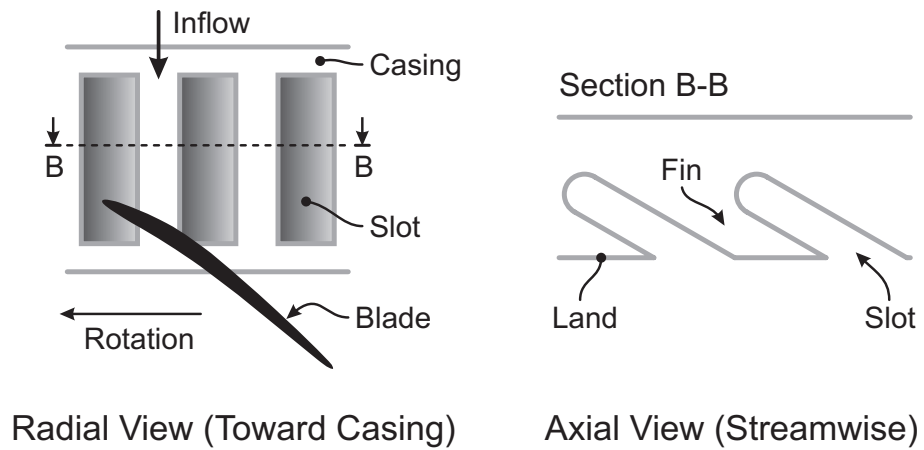
Circumferential Grooves



Radial View (Toward Casing)

Axial View (Streamwise)

Axial Slots



Radial View (Toward Casing)

Axial View (Streamwise)

Figure 1.1: Drawings of groove and slot based casing treatments installed in a compressor.

Chapter 2

Background and Literature Review

This chapter reviews the background to the present research. It focuses on concepts rather than detailed comparison of different results, which is saved for later chapters.

The review is divided into four parts. The first part introduces the stability problems encountered by aircraft engine compressors, and the consequences of unstable operation. The second part introduces the tip leakage flow, which has been linked to the process that leads to unstable operation. This process, called 'stall inception', is discussed in part three. In part four, techniques for delaying stall inception (thereby enhancing compressor stability) are reviewed alongside research into their operation. Finally, areas of the literature that require further study are identified and linked to the present work.

2.1 The Unstable Operation of Axial Compressors

Aircraft jet engines must reach maximum efficiency at cruise, to minimise fuel consumption. However, during take off, landing, changes in altitude or other manoeuvres, the engine must operate safely away from this maximum efficiency 'design point'. This requirement places a particular constraint on the design of the multi-stage axial compressor, which is prone to unstable operation at low flow rates. Unstable operation is unacceptable, so the stable operating range of the compressor should be as large as possible.

The stable operating range of a compressor at a given rotational speed is shown by a 'characteristic', which is a graph of pressure rise against flow rate. A typical characteristic is shown in Figure 2.1. At high flow rates, the characteristic becomes vertical as the blade rows choke. At low flow rates, the characteristic reaches the 'stability limit' and unstable operation occurs. The stable operating range is measured by the 'stall margin' between the design point and the stability limit. During design it is important to ensure an adequate stall margin between the maximum efficiency design point and the stability limit. Real multi-stage compressors operate over a range of speeds, so their operating range is shown by a 'performance map'. A typical performance map is shown in Figure 2.2.

Multi-stage compressors are also prone to unstable operation when operating away from their design speed, because the flow rates at either end of the compressor become mismatched (Cumpsty, 1989a). At rotational speeds lower than the design point value, each stage under-compresses the flow, so the density of the air at the high-pressure (rear) end of the compressor is too low. The Mach numbers of the flow thus increase, causing the rear stages to choke. This limits the mass flow through the compressor at a level lower than the design value, which overloads the blades at the low-pressure (front) end of the compressor due to positive incidence, making them stall. This low-speed stall generally occurs during starting and taxiing. At high shaft speeds, the reverse argument is true and stall is most likely at the rear of the compressor. High-speed stall generally occurs during take off or near the top of the ascent to cruising altitude. If the compressor does stall (at any speed) it becomes unstable and may exhibit 'rotating stall' or 'surge'.

Rotating stall is an instability of the compressor alone. It occurs when the flow becomes non-axisymmetric due to the appearance of one or more 'stall cells'. Stall cells are regions of reduced (or reversed) axial velocity that rotate around the annulus (Day and Cumpsty, 1978). They divert flow to the rest of the annulus, stabilising the blades away from the stall cell, and creating an annular flow pattern of stalled and unstalled flow. Rotating stall may take the form of part or full-span stall cells, which are shown in Figure 2.3. Part-span stall cells usually occur at the blade tips and there is normally more than one around the

annulus. They usually only cover a few blades circumferentially and one or two blade rows axially. These stall cells are normally seen on the high aspect-ratio blades in the front stages of compressors, so part-span stall normally occurs at low shaft speeds (see above). Full-span stall cells cover the whole blade span and there is normally only one cell circumferentially. They usually cover a large proportion of the annulus through the whole length of the compressor. These stall cells are normally seen on the low aspect-ratio blades in the middle and rear stages of the compressor, so full-span stall normally occurs at medium and high shaft speeds. Part-span stall cells will usually merge into full-span cells if the flow rate is reduced so that more than 30% of the annulus area is stalled (Day *et al.*, 1977). Both types of stall cell move around the annulus at between thirty and eighty percent of the rotor speed, but larger cells tend to rotate more slowly than small ones (Cumpsty and Greitzer, 1982; Camp and Day, 1998).

Surge is an instability of the whole compression system. It occurs when there is a pressurised volume (such as a combustion chamber) downstream of the compressor. A surge begins when the compressor stalls and becomes unable to maintain the pressure in the downstream volume (Moore and Greitzer, 1986; Day, 1994; Tryfonidis *et al.*, 1995). The downstream volume thus depressurises through the turbine and compressor. This causes the flow through the compressor to greatly reduce (called 'classic surge') or even reverse (called 'deep surge') depending on the compressor design (Greitzer, 1976). The reversed flow associated with a deep surge can reach near-sonic speeds in high-speed compressors (Cargill and Freeman, 1991; Day and Freeman, 1994). If the combustor flame is not blown out by the surge, the unloaded compressor may recover, over-pressurise the downstream volume and stall again, causing a 'surge cycle' (Day, 1994).

Rotating stall and surge are therefore two distinct modes of unstable operation that occur after a compressor stalls (crossing the stability limit is therefore often simply referred to as 'stall'). Rotating stall can reduce engine thrust and cause over-heating, vibration and wear. These problems are usually worse for full-span stall than part-span stall. Classic and deep surge cycles both cause a periodic loss of thrust. A deep surge can cause severe damage, which may take an engine out of service. Rotating stall or surge can be stopped by shutting down the engine, or reducing the back-pressure on the compressor by decreasing the fuel flow. If a pilot increases the fuel flow to correct for the loss of thrust caused by rotating stall or surge, the load on the compressor will increase. This will make the problem worse, and can turn a part-span stall into a full-span stall or a surge. Stall is therefore dangerous and must not be allowed to occur in aircraft engines.

If a compressor's tendency to stall cannot be controlled through normal aerodynamic design, stall prevention techniques must be used to move the stability limit to lower flow rates

and increase the stable operating range. These techniques are the focus of this thesis. Later sections will consider the processes that lead to stall and the technologies that can prevent it. However, the tip leakage flow is introduced first, because this is important for both.

2.2 Tip Leakage Flow in Axial Compressors

Compressors have a clearance gap between the rotating blade tips and the stationary casing. There is a pressure difference across the clearance gap caused by the blade's pressure loading, so the 'tip clearance flow' leaks through the gap. After the tip clearance flow emerges into the passage on the suction side of the blade, it rolls up to form the 'tip leakage vortex'. The tip clearance flow and the tip leakage vortex make up the 'tip leakage flow'. Tip leakage flows are generally detrimental to the stability and efficiency of compressors¹ (Peacock, 1982; Freeman, 1985; McDougall *et al.*, 1990; Storer and Cumpsty, 1994; Graf *et al.*, 1998). This work considers the tip leakage flow in low-speed compressors, but many of the concepts are also relevant to high-speed machines (Adamczyk *et al.*, 1993; Suder and Celestina, 1996; Chima, 1998; Gerolymos and Vallet, 1999). Storer and Cumpsty (1991) and Crook *et al.* (1993) used computational, experimental and theoretical methods to show that the tip clearance flow is primarily an inviscid phenomenon.

Figure 2.4 shows the tip leakage flow field pictured by Storer and Cumpsty (1991). The flow entering the tip clearance comes from three areas; the casing boundary layer (label '1'), the core flow ('2') and the boundary layer being centrifuged up the blade pressure surface ('3'). On reaching the pressure surface tip corner, the flow separates to form a vena contracta in the tip clearance ('4'). Compressor blades are normally too thin for the flow to re-attach, so the flow emerges from the clearance as a wall-bounded jet with separated flow near the blade. This emerging flow is not aligned with the core flow so there is a shear layer between the two ('5'), which generates large losses (Storer and Cumpsty, 1994). The tip leakage flow then meets the inflow and separates from the casing ('6'), before rolling up to form the tip leakage vortex ('7').

Chen *et al.* (1991) and Storer and Cumpsty (1991) present a useful model for considering the tip clearance flow. The model divides the flow into components directed along the blade camber-line (the through-flow component) and normal to the camber-line (the cross-flow component). The through-flow component is linked to the core flow rate, while the cross-flow component is linked to the blade loading. If the cross-flow component of the tip

¹ Cumpsty (1989a) and Gbadebo *et al.* (2007) report an optimal clearance, but this was smaller than is likely to be sustained in a real machine for mechanical reasons.

clearance flow increases relative to the through-flow component, the clearance flow emerges at a greater angle to the camber line, enlarging the tip leakage vortex and deflecting it further out into the blade passage.

The chord-wise variation in blade loading changes the cross-flow component of the tip clearance flow and the speed and direction at which this flow emerges from the tip clearance. Near the leading edge, the blade loading is small, so the cross-flow is also small. The flow emerging from the tip clearance is therefore slow and makes a small angle with the camber-line. This causes the tip leakage vortex to grow slowly (at label '8'). As the blade loading increases, the cross-flow increases and the tip leakage vortex grows more quickly ('9'). As the pressure difference across the tip clearance decreases to the trailing edge, the cross-flow velocities decrease, but the impact on the vortex is small as it is now fully formed ('10'). Figure 2.4 shows that the blade stagger angle, combined with the cross-flow, often causes the tip clearance flow to be axially reversed (McDougall *et al.*, 1990). This will be investigated further in Chapter 5.

As stall approaches, the blade loading increases, which strengthens the cross-flow. The tip leakage vortex therefore thickens and swings forward (Yoon *et al.*, 2006), increasing loss and blockage. Furukawa *et al.* (1999) and Wilke *et al.* (2005) also suggest that the vortex may 'burst' in highly-loaded blading, while Sirakov and Tan (2003) show that the vortex may impinge on the pressure surface of the adjacent blade, causing 'double leakage'. Both of these effects further increase the loss and blockage associated with the vortex as stall approaches. Storer and Cumpsty (1994), Khalid *et al.* (1999) and Suder (1998) found that tip leakage flow causes most of the loss and blockage in the tip region, and Howard *et al.* (1994) show that the tip leakage flow can also cause additional losses in downstream blade rows. Hoeger *et al.* (2000) show that the blockage caused by the tip leakage flow reduces through-flow velocities near the casing. Greitzer *et al.* (1979), McDougall *et al.* (1990), Shabbir and Adamczyk (2005) and others have linked this to stall. The blockage in the rotor and the blade loading will therefore be considered in the present work.

Although cascade studies of tip clearance flow can provide useful information (Cumpsty, 1989a) they must be interpreted carefully because cascades do not have centrifuged blade boundary layers or span-wise blade incidence changes caused by the inlet boundary layer. Casing flow visualisation on cascade endwalls by Kang and Hirsch (1994) and Saathoff *et al.* (2003) therefore appear different to those conducted on rotor casings by Saathoff *et al.* and Furukawa *et al.* (1999). For this reason, the present work uses rotating compressor rigs.

Having introduced the tip leakage flow, the next section discusses stall inception.

2.3 Stall Inception

Stall inception is the process of flow breakdown that occurs between stable axisymmetric flow and rotating stall. It can be divided into precursors and the inception itself. Stall inception occurs quickly (usually within a rotor revolution) and in a small area (often only a couple of blades in a whole compressor) so it is difficult to study experimentally. It is an inherently non-linear, stochastic process (Cumpsty, 1989b) and its occurrence is influenced by a range of external factors (e.g. tip clearance, stagger angle, blade erosion and inlet distortion) so it is also difficult to study computationally². Stall inception is therefore not yet fully understood.

Precursors Stall inception may or may not be preceded by modal precursors, which are circumferentially harmonic velocity variations that rotate around the annulus. Modes grow out of the axisymmetric flow field as the compressor is throttled toward stall and usually extend through the whole compressor (Greitzer and Moore, 1986; McDougall *et al.*, 1990). The harmonic velocity variation increases as stall is approached, so initial detection depends on the sensitivity of the measurement equipment (Camp and Day, 1998). When modal precursors are not present, stall inception suddenly occurs in an otherwise axisymmetric flow field (Day, 1993b). Experimental work by Camp and Day shows that the presence of precursors in a given compressor can be related to the gradient of the characteristic at stall. If the gradient is zero or positive, the compressor will tend to show modal precursors, but if the gradient is negative, the tendency is for no precursors to appear.

Inception Stall inception may be classified as ‘broad inception’ or ‘spike inception’. Broad inception affects several blade passages and directly creates a large stall cell that develops into stall. This inception normally occurs near the blade root, typically moves at the same speed as modal precursors (usually less than 50% of shaft speed) and is thought to be associated with growing three-dimensional separations (Camp and Day, 1998). By contrast, spike inception affects a small number of blades (one blade in Deppe *et al.*, 2005) and grows rapidly into a stall cell to cause stall. This inception normally occurs near the blade tip (Day, 1993b) and typically rotates faster (around 70% of shaft speed) than broad inceptions due to its smaller size. In both cases, the new stall cell slows down as it grows into a rotating stall cell (Camp and Day, 1998). The compressors used in the present work tend to stall with spike inception so this is considered further below.

² Simulations of stall inception are often compromised by stall inception being caused by numerical errors rather than flow physics.

Spike Inception The small size of spikes and the speed at which they move and grow makes them hard to study experimentally. There is therefore disagreement about what causes spikes and what they actually look like. Deppe *et al.* (2005) suggests that spikes are caused by tip leakage flow being suddenly pushed forward by axially reversed flow near the trailing edge. The computational results in Hoying *et al.* (1999) and Lu *et al.* (2006b) blame the tip leakage vortex spilling around the front of the neighbouring blade's leading edge and stalling it. Yoon *et al.* (2006) and Seitz (1999) explicitly disagree with Hoying's analysis, and Seitz blames the interaction of the tip leakage vortex with the core flow in the passage between the blades. Vo (2001), a co-author of Hoying, implicates both forward spillage of the tip leakage vortex and axially reversed flow occurring around the blade trailing edge. The underlying mechanisms of spike generation and their development into rotating stall cells are therefore not well understood. Numerical work by Gourdain *et al.* (2006) and Inoue *et al.* (2000) have predicted the flow field at the early stages of rotating stall, but these have yet to be verified experimentally. This subject will be revisited later in the present work.

A Compressor's Route into Stall Camp and Day (1998) show that the precursors can be related to the type of stall inception. If modal precursors are not present before stall, spike stall inception usually occurs. However, if modal precursors are present, they reduce the inflow velocity to a large number of blades simultaneously, which can lead to either broad or spike inception. Even in a given compressor the stall inception type is not necessarily constant and can be changed by altering the inflow (Simpson and Longley, 2007), shaft speed (Day *et al.*, 1999) or geometry (Dobrzynski *et al.*, 2007). The stall inception mechanism will therefore be checked for each new set of tests in the present work. Either or both inception types may occur in multi-stage compressors, but Day and Freeman (1994), Day (1994) and Wilson and Freeman (1994) report that the stall inception processes are similar in both high and low speed machines.

Predicting Stall The lack of understanding surrounding the mechanisms of stall inception (and their complexity) makes accurate prediction of the stall point difficult. Most methods involve some kind of diffuser analysis with corrections (Cumpsty, 1989a). Greitzer *et al.* (1979) compares loading on the rotor blades and the casing wall, and predicts stall when the loading on either reaches a critical level. However, this ignores the impact of the stator and the aspect ratio, which can both affect stability (Cumpsty, 1989a). Koch (1981) applies a straight diffuser approach to compressors using empirical correlations averaged over the whole stage at the mean radius. This simple approach gives a remarkably good indication of the stall point. Smith (2002) reviews some related methods. Camp and Day (1998) suggest

that there is a critical incidence (or tip loading) at which the compressor stalls. However, none of these methods give really good predictions. The stall point will also change during service because of external factors such as blade erosion due to foreign body ingestion or tip rubbing (CAA, 2004), the effects of rain or ice ingestion (NTSB, 1977; Day *et al.*, 2008) or enlarged tip clearances caused by differential expansion of the casing and blades, adding further complication. Predicting the stall inception type is equally difficult and will be discussed in more detail in Chapter 8.

2.4 Stability Enhancement Methods

To prevent stall in a compressor, stall inception must either be delayed or eradicated before it can grow into a rotating stall cell. The desired outcome is to improve the stall margin (stable operating range) without affecting the design point, as shown in Figure 2.5. This can be achieved using active or passive control techniques.

Active control methods use a feedback control system and actuators to modify the compressor flow. Problems with active control include mechanical and electrical complexity in the control and actuation systems and, in some cases, a need for thermodynamically expensive pressurised air. Passive control methods use localised changes to the compressor geometry to control stall with no external input of any kind. Problems with passive control include complex manufacture and reduced efficiency and mechanical integrity. While both types of system are potentially expensive, passive methods are simpler, lighter and safer due to the lack of a control system. The present work considers passive methods, but some relevant findings from flow studies considering active methods will be reviewed first.

2.4.1 Active Control Methods

Flow control techniques such as bleed valves and variable-stagger blade rows are commonly used to start multi-stage compressors and cater for off-design operation. Bleed valves remove air from the compressor to increase the flow through the front stages and prevent stall at low rotational speeds (see Section 2.1), while variable blade rows reduce the incidence changes associated with off-design operation (Paduano *et al.*, 1993). Both systems are heavy, bulky and expensive, so they cannot be applied throughout the whole compressor and do not cure all stall problems. Recent research has therefore focused on more precise active control methods that suppress stall by injecting or bleeding small quantities of air in or out of the compressor.

Injected air is normally aimed at the tip clearance to prevent spike stall. Suder *et al.* (2001) found that injectors should maximise the mass-averaged axial velocity close to the casing wall to re-invigorate the casing boundary layer and reduce the incidence (and loading) on the blade tip. Suder *et al.* use this technique to stop fully-developed rotating stall and even replace variable inlet guide vanes (albeit inefficiently). Cumpsty (1989b) agrees that casing boundary layers are important in stall inception. Deppe *et al.* (2005) varied the angle of injection about a radial axis and found that the best injection angles were between axial and -60° , against the rotor motion. Traverses showed that this increased the through-flow in the tip region. Therefore, both Suder *et al.* and Deppe *et al.* suggest that increasing the tip clearance through-flow and decreasing the cross-flow improve stability. Suder *et al.* (2001) also show that the compressor stalls with injection when the loading at the tip reaches the same level that caused stall without injection, which agrees with the critical incidence model of Camp and Day (1998).

Beheshti *et al.* (2006) injected air axially into the tip clearance via a wide circumferential groove (or trench) over the blade tips. The best results were gained when the flow was injected at high velocity along the camber line (in the relative frame). Bae *et al.* (2005) found that stream-wise air injection in the tip clearance was more effective than using oscillating jets to break up the flow. These papers agree with injector design work by Strazisar *et al.* (2004), which concludes that the optimum geometry provides high axial velocities into the tip clearance very close to the casing wall (using the Coanda effect). All these authors agree with Suder *et al.* (2001) that maximizing injected velocity is the key to stability enhancement. Other work on injection by Scheidler and Fottner (2003) shows that active control of air injection can cure stability problems associated with inlet distortion and significantly increase the pressure rise across a transonic compressor, although Scheidler and Fottner (2006) found that active stabilisation was less effective at low speeds.

This injection work shows that stability can be enhanced by injecting flow into the casing boundary layer just upstream of the blade row, or into the tip clearance itself. The key factor is that the flow must have a high velocity. The literature advises that the jet direction should be chosen to unload the tip (Suder *et al.*, 2001; Strazisar *et al.*, 2004) or follow the camber-line in the relative frame (Beheshti *et al.*, 2006). The effect of both of these viewpoints on the tip clearance flow as modelled by Chen *et al.* (1991) and Storer and Cumpsty (1991) is the same. The through-flow is augmented and the cross-flow is diminished. Reducing tip clearance cross-flow relative to tip clearance through-flow should therefore improve stability. This can be done by interrupting the cross-flow or augmenting the through-flow. This idea will be considered throughout the present work.

Constant air injection usually reduces efficiency (Dobrzynski *et al.*, 2008), so a controller

is needed to activate injection only when needed. This is complex because different approaches are required for different stall inception behaviours. Day (1993a) shows that precursor modes can be suppressed with a circumferentially-harmonic valve response, while spikes and small stall cells can be eradicated using a local valve response. Freeman *et al.* (1998) and Ffowcs Williams *et al.* (1993) extended this to engine compressors, and show that surge cycles can be stopped by preventing the stall that occurs prior to the surge. It would appear that modal precursors are much easier to target than spikes because they build up slowly and can be suppressed by a simple harmonic response. However, engine control systems must be able to handle a large range of stalling mechanisms because these can change during service (Day *et al.*, 1999). In some cases, complex signal analysis has been used to remove the need for *a priori* knowledge of the stall inception mechanism (Paduano *et al.*, 1993; Weigl *et al.*, 1998; Höss *et al.*, 2000; Leinhos *et al.*, 2002; Scheidler and Fottner, 2006; Christensen *et al.*, 2008) but despite this work, active control has not found widespread use.

2.4.2 Passive Control Methods

The most common passive method for stall control is some form of endwall treatment, either hub treatment (for cantilevered stators) or casing treatment (for rotors). Casing treatment is the most commonly used and has existed since the 1950s (Wilde, 1953). Hathaway (2007) reviews a variety of different casing treatments, but most are either groove or slot-based. Early forms of these treatments proposed by Osborn *et al.* (1971) and Moore *et al.* (1971) are shown in Figure 2.6. Groove-based treatments typically generate smaller stall margin improvements than the slot-based treatments, but usually cause smaller efficiency losses (Bailey, 1972; Fujita and Takata, 1984). Greitzer *et al.* (1979) suggested that casing treatment is only effective if stall inception occurs near the casing. This is investigated in Chapter 8.

Groove-Based Casing Treatments

Groove-based casing treatments usually consist of one or more circumferentially continuous grooves cut into the endwall above the rotor tips (see Figure 2.6). They provide better efficiency and mechanical integrity than casing slots, and although they generate a smaller stall margin, this may be all that a designer requires (e.g. to correct stage mis-matching).

Designing a grooved casing treatment is currently difficult because the interaction of the grooves with the flow field and stall inception processes are not fully understood. This leads to disagreement in the literature about how grooves work and where they should be located. Shabbir and Adamczyk (2005) used computational methods to show that near

the casing of a smooth-walled rotor, the net axial pressure force is balanced by the axial wall shear stress. They suggested that casing grooves can generate an additional axial force by transporting axial momentum radially, thereby increasing the net axial pressure force that the near-casing flow can tolerate, improving stability. The grooves near the leading edge generated this axial force more effectively, so it was concluded that these generate the greatest stability improvement. Computational work by Vo *et al.* (2008) suggested two criteria that must be met for stall to occur. The tip leakage flow must ‘spill’ around the leading edge of the adjacent blade and there must be axially reversed flow moving forward from the trailing edge. Lu *et al.* (2006b) and Müller *et al.* (2007) showed that grooves can deflect the tip leakage vortex downstream by manipulating the tip leakage flow. Grooves near the leading edge deflect the vortex most, so these authors suggest that such grooves stabilise the compressor most effectively by preventing forward spillage. Prince *et al.* (1974) suggested that casing grooves work by moving blade loading aft. By contrast, the experimental work by Bailey (1972) concluded that the optimum groove location is near mid-chord, not the leading edge. The literature does not fit together well, so the location of grooves and their interaction with the near-casing flow will be studied in detail in Chapter 5.

Fujita and Takata (1984) found that using multiple grooves increases stall margin but reduces efficiency, while Bailey (1972) found that deeper grooves were more effective than shallower grooves. Rounding off the grooves (Barnett *et al.*, 2003) or installing baffles within them (Prince *et al.*, 1974; Fujita and Takata, 1984) have also been investigated, but these studies did not consider the axial location of the grooves (and the rounding work was done on an inclined groove). Because these results are confusing, multiple grooves and different groove geometries will be tested in Chapter 6.

Slot-Based Casing Treatments

Slot-based casing treatments usually consist of a number of circumferentially discrete slots cut into the endwall above the rotor tips, which may extend axially upstream of the rotor. Although they reduce efficiency more than casing grooves, are less robust and do not work well with abradable casing linings, they can provide a large stall margin improvements.

The early NASA geometries (see Figure 2.6) had slots located entirely over the blade tips. This design generates large stability enhancements, but reduces the design point efficiency. Experimental flow studies by Prince *et al.* (1974), Smith and Cumpsty (1984) and Seitz (1999) show that there is significant recirculation through the slots caused by the rotor pressure rise. Smith and Cumpsty tentatively conclude that this recirculation stabilises the compressor by interrupting the tip leakage flow and removing blockage from near the casing. They

also suggest that unsteady effects within the slots can be disregarded. Unfortunately, the large recirculation through the slots (up to 10% of the mass inflow at stall according to Seitz, 1999) wastes pressurised air and leads to mixing losses, both of which cause unacceptable efficiency reductions of around 2%. However, Prince *et al.* (1974) found that adding circumferential baffles across the axial slots (to prevent recirculation) reduced the efficiency penalty with only a slight reduction in stability improvement. This suggests that steady recirculation is not the only mechanism and unsteady effects may also be important.

Waterman (1992) and Seitz (1999) developed the over-blade NASA geometry by moving it forward so that the greater part of the slots is upstream of the blades rather than over them. Seitz used a parametric study to set the extent of the slot from 75% $c_{x,r}$ upstream of the leading edge to 25% $c_{x,r}$ downstream, and also set the skew angle to 60°. This maintains the stability improvement, but reduces the efficiency penalty by a factor of four. Lu *et al.* (2009) made similar findings. The present work will expand these studies.

Seitz (1999) found that the reduction in efficiency loss with forward positioned slots is caused by the decrease in driving pressure force (caused by the decreased rotor overlap) reducing the recirculation through the slot to only 1% of the overall compressor mass flow at stall. Seitz also finds that the slots in the forward position have a smaller impact on the near-casing flow and blockage compared with the over-blade geometries (again suggesting that blockage and stall are not directly linked). However, the mesh resolution in the CFD used by Seitz was quite low and the blockage at very low flow-rates was not investigated. The present work will study the near-casing flow and outflow blockage further. This reduction in recirculated flow rate relative to the over-blade treatments adds weight to the results of Prince *et al.* (1974), who suggested that steady recirculation is not the only mechanism behind the performance of casing slots, but this is contradicted by Ning and Xu (2008) who successfully used a steady CFD analysis to model the impact of slots.

Wilke and Kau (2004) show that the flow inside forward slots applied to a high-speed machine is very similar to that observed by Seitz (1999) and Lu *et al.* (2009), despite the differences in casing static pressure field between transonic and subsonic compressors. Wilke and Kau also round off the rear of the slots to guide the recirculating flow smoothly through them (suggested for the over-blade treatment by Smith and Cumpsty, 1984). They conclude that the treatment works by weakening the tip clearance flow near the leading edge. The treatment works well, suggesting that recirculation is more important than unsteady effects in this case. However, Wilke *et al.* (2005) find that forward slots do not work so well with contoured endwalls, which could be a problem in transonic fans.

Lee and Greitzer (1990) and Seitz (1999) both used steady suction and blowing through slots to further understand the operation of both over-blade and forward slots. Suction from slots

extending from the leading edge to 25% chord, and blowing from the leading edge to 25% chord upstream, were both found to improve stability. Both authors found that constant suction and/or blowing improved stability less than the full casing treatment, although this may have been caused by the flows not correctly mimicking the treatment aerodynamics. However, both authors also found that the slots extending aft from the leading edge to 25% chord increased stability by 7% without blowing or bleeding (as found by Koch, 1970). This result leads Seitz to conclude that simple recirculation does not completely explain casing treatment behaviour, and unsteadiness should be considered. The role of unsteadiness is therefore unclear and will be investigated in Chapter 7.

Recirculating Casing Treatments

Recirculating treatments take air from one point in the compressor and return it at another, generally without any active control. The treatment studied by Azimian *et al.* (1990) bleeds flow from near the blade leading edge and feeds it back into the flow upstream after having been turned by vanes. The authors conclude that steady recirculation is the key to stability enhancement. Hathaway (2002) bleeds and then re-injects flow at many different axial locations and finds that in a transonic machine, the best place to bleed is just at the exit to the rotor, while the best place to inject is just in front of the point of greatest tip clearance flow. These locations are similar to the areas covered by the over-blade slots, but unlike the slots, the recirculating treatment did not reduce efficiency. Hathaway concludes that the good efficiency was caused by the removal of casing endwall blockage compensating for the losses in the treatment (made possible by careful injector design) and reduced mass flow through the treatment (made possible by using high injection velocities).

These results show that introducing high velocity flow into the tip clearance region is beneficial for stability, and that introducing loss in a casing treatment is acceptable if the treatment causes greater loss reductions in the blade row. The effectiveness of the Hathaway treatment also shows that simple rules of thumb are not sufficient for robust design. The effect of the treatment on the compressor flow field must be understood.

2.5 Discussion

The fundamentals of stall inception are not yet fully understood, so designing a casing treatment to precisely target inception phenomena is not currently possible. Understanding the stall inception process is an ongoing task. However, the literature provides many interesting observations which will be advanced in the present work.

The literature is divided on where circumferential grooves should be placed for best performance. The optimum location and number of casing grooves will therefore be investigated in detail. Different groove cross-sections and configurations will also be studied to find the best geometries. Past work on casing slots has defined the best choice for some of the slot dimensions. This work will extend this to cover all the dimensions of casing slots. The parametric results will be linked to detailed experimental and computational studies of the flow fields in order to improve design guidance and understanding.

Manipulating the tip clearance flow so as to enhance through-flow and reduce cross-flow in the tip clearance appears to increase stability. This decreases losses generated by the shear layer between the emerging tip clearance and core flows and deflects the tip leakage vortex back into the blade passage. This in turn reduces the size of (and therefore blockage caused by) the tip leakage vortex. These effects decrease the losses caused by the tip leakage flow and improve the passage through-flow in the tip region, which together improve efficiency and reduce the blade loading. The processes used to manipulate the tip clearance flow must target the flow very close to the casing to be effective. The present work will therefore investigate the impact of casing treatments on the outflow blockage, blade loading and near-casing flow fields.

The methods used to manipulate the tip clearance flow may themselves introduce additional losses. Therefore, to maintain efficiency at the design point, the casing treatment must either reduce losses in the blade row or handle such a small flow rate that the loss inside the treatment is negligible. The overall impact of casing treatments on efficiency will be analysed in this work.

Casing slots have been shown to contain both steady recirculation and unsteady effects. The literature is divided on the relative importance of these for providing increased stall margin. The importance of unsteady effects will therefore be investigated in the present work, using detailed experimental and computational methods to develop understanding and design guidance.

Greitzer *et al.* (1979) suggests that there is a limit to the effectiveness of casing treatment, caused when the location of stall inception changes. The present work will therefore check

for changes to the stall inception mechanism throughout. Later work in the 1990s introduced modal and spike stall inception and improved our understanding of the mechanisms of stall. This work will therefore investigate how changes to the stall inception mechanism may alter casing treatment performance.

The geometric complexity of casing treatments must to be traded off against performance. For example, the complex ducting in recirculating treatments greatly increases manufacturing costs and this must be justified. The present work therefore compares the performance of casing slots with less complex casing grooves to enable design choices to be made.

In summary, based on this literature review, the present work will investigate the optimum axial location and geometry for single and multiple casing grooves. The optimum geometry for casing slots will also be investigated by adding to existing work. The impact of casing grooves and slots on the near-casing flow, blade loading, blockage, stall inception mechanism and efficiency will be studied. The significance of unsteady effects inside casing slots will also be quantified. Finally, the impact of the stall inception mechanism on casing treatment performance and the advantages of combining blade and treatment design will be considered.

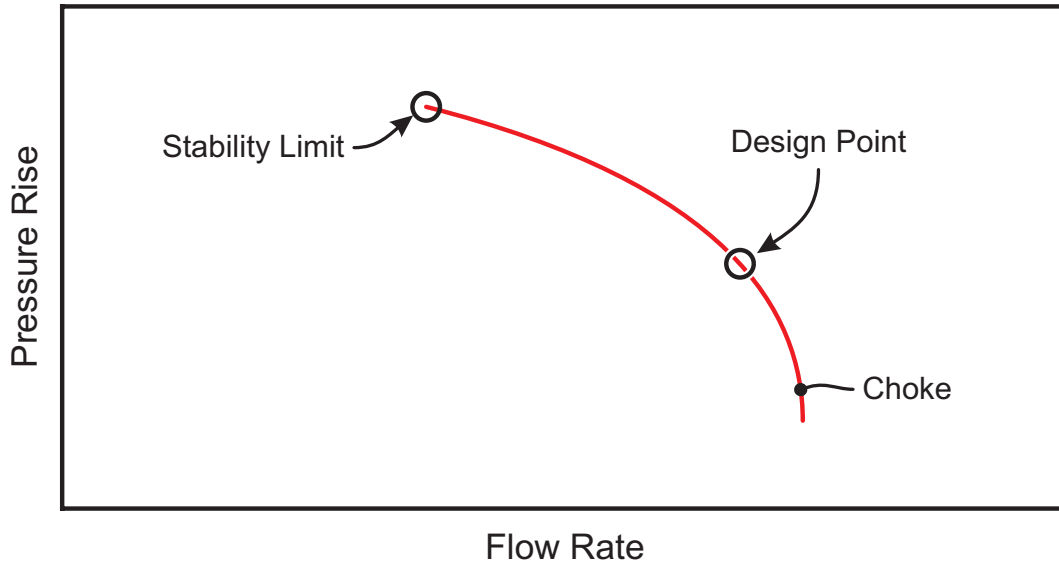


Figure 2.1: A schematic constant speed characteristic for a high-speed multi-stage axial compressor showing choke, the design point and the stability limit.

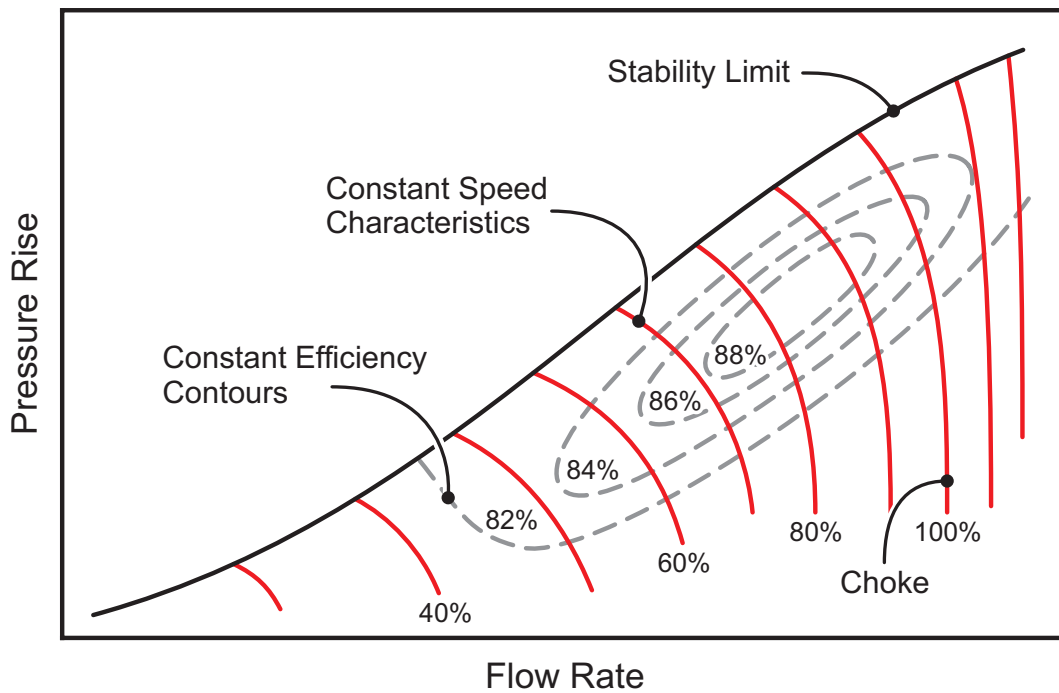


Figure 2.2: A schematic performance map for an axial compressor showing choke, the stability limit, characteristics at different rotational speeds and contours of efficiency.

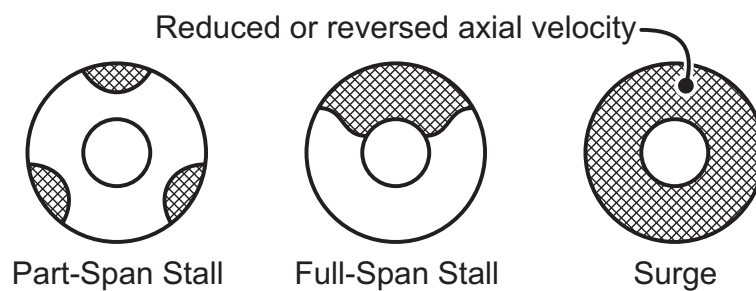


Figure 2.3: An axial cut showing the layout of part and full-span stall cells and surge.

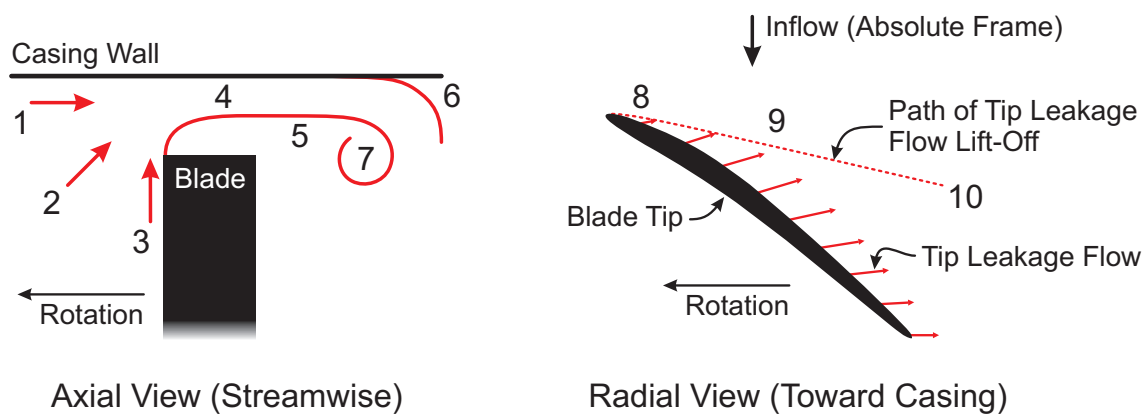


Figure 2.4: Two views of a typical tip leakage flow field in an axial compressor (shown in the relative frame of reference).

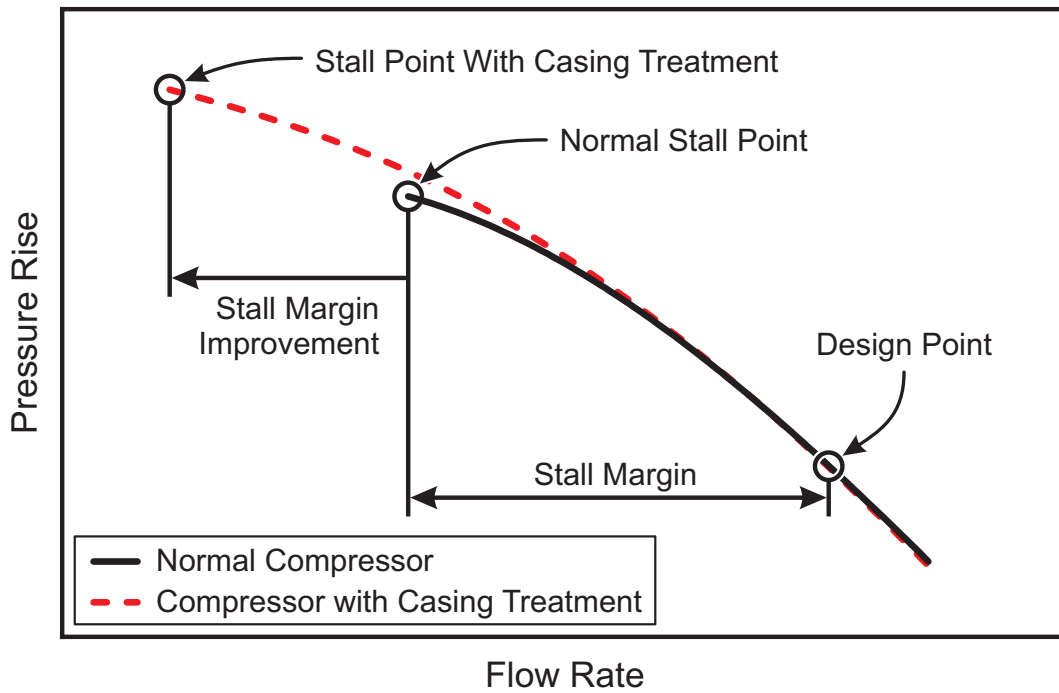


Figure 2.5: Constant speed characteristics showing a stability enhancement technique (casing treatment) moving the stall point to a lower flow rate without changing the design point. These characteristics are from the Natal compressor (see Chapter 3). Since this is a low speed compressor, the low speed definition of stall margin is shown.

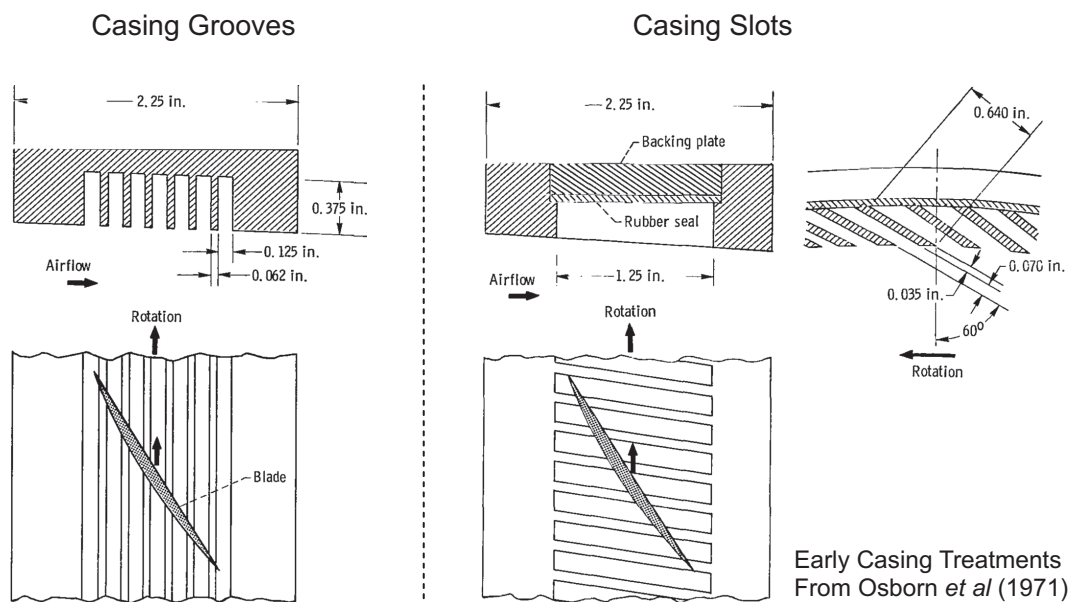


Figure 2.6: Early NASA grooved and slotted casing treatment designs (Osborn *et al.*, 1971).

Chapter 3

Experimental Methods

This chapter describes the experimental methods that were used to quantify the performance of different casing treatments, investigate the compressor flow field and calibrate computational fluid dynamics (CFD) models. The chapter is divided into four parts.

The first part introduces the compressors from which the data was gathered. The second part presents the measuring equipment that was used and its capabilities. The third part describes the different experimental and measuring techniques that were used. The fourth part contains the results of an initial study to check that the stalling behaviour of the compressors is unaffected by Reynolds number.

3.1 The Compressors

The two compressors used for the present experimental work were axial-flow, low-speed, single-stage, vertical-axis machines located at the Whittle Laboratory. The ‘Natal’ and ‘Red’ compressors are both models of subsonic stages in an aero-engine compressor. Figure 3.1 shows partial cross-sections of both compressors, with selected design parameters. Their design is discussed in more detail below.

Inlet and Flow Conditioning Air enters through an inlet at the top of the compressors. It then passes through a honeycomb flow straightener, a plenum and an inlet contraction to reduce large disturbances in the flow. The air then enters the parallel working section, where there is further flow conditioning. This consists of boundary layer trips to give realistic boundary layers and (in the Red compressor) a turbulence grid to generate the required turbulence levels. In the Red compressor, the turbulence grid generates a free-stream turbulence intensity of 2.5% at the rotor inflow. The Natal compressor is run in a closed room, so the rotor inflow turbulence level is 2.2% without a turbulence grid. These values of turbulence intensity are lower than the 4 to 6% found in embedded multi-stage rotor inflows (Camp and Shin, 1995; Cumpsty, 1989a), but Schlichting and Das (1969) show that they are sufficient to cause transition at the leading edge of the rotor blades outboard of mid-span. The blade roughness, noise and vibration will also encourage transition. Experiments were also performed to show that both compressors were operating at Reynolds numbers greater than those at which viscous effects such as laminar boundary layer separation affect the stalling behaviour and overall compressor performance (see Section 3.4).

Working Section The working section in the Red compressor contains rows of inlet guide vanes (IGVs), rotor blades and stator vanes. The IGV and rotor blade rows are axially spaced by $130\% c_{x,r}$ at the casing, and the rotor and stator rows are spaced by $140\% c_{x,r}$. The working section in the Natal compressor contains rows of rotor blades and stator vanes spaced by $125\% c_{x,r}$ (no IGVs). The large rotor-stator gaps reduce the coupling between the stator and rotor, reducing the complexity of the results. In both compressors, the stator vanes are cantilevered from the casing, so the hub adjacent to the vane tips rotates with the rotor. The tip clearances are shown in Figure 3.1. On both compressors, the casing is made of stacked rings that can be changed to install casing treatments (see Figure 3.1).

Both compressors have controlled diffusion blading designed by Rolls-Royce for the C106 compressor. The Red compressor has the same geometry as the C106 compressor, so the blades fit perfectly. The span and hub-to-tip ratio of the Natal and C106 compressors are similar, but the radius of the Natal compressor is smaller than the C106. The blades are thus

slightly under-twisted, but the incidence mis-match is small (less than 1°). To fit the Natal compressor, the C106 blades and vanes were shortened by 1.7 mm and re-staggered to give the correct mid-span incidence (using velocity triangles). Small gaps at the rotor and stator roots were then filled with silicone sealant to prevent leakage flow.

Exhaust Downstream of the working sections there is a settling length to decouple the working section from the throttle. The throttle in the Natal compressor is a flat plate, orthogonal to the compressor axis, which is moved up and down by a gear system to control the flow rate. The throttle in the Red compressor consists of two close-fitting annular sheets of metal containing three identical apertures, which are moved relative to each other (like shutters) to control the flow.

3.2 Measurement Equipment

This section describes the equipment used to measure, record and process data.

3.2.1 Pressure Measurements

In the present work, 'steady' pressures are those that vary with frequencies much lower than the shaft speed. Steady pressures were used to measure the compressor performance and the output from pneumatic traverse probes. By contrast, unsteady pressures vary with frequencies similar to the blade passing frequency. Unsteady pressures were used to measure stall inception and the blade-to-blade casing static pressure field.

Steady pressures were measured with Honeywell 1 psi pressure transducers (using plastic tubing for connections to tappings or probes). These were periodically re-calibrated using the same Furness Controls micromanometer with a range of 0-1.9 kPa. The transducer zero offset was recorded before every run and subtracted from the data before the calibration was applied (once the compressor and logging system was warmed up, zero-level drift was less than ± 2 Pa). The combined error in pressure measurement (including zero level drift, calibration and quantisation errors) was ± 3 Pa, or $\pm 0.4\%$ of a typical inflow dynamic head.

Unsteady pressures were measured with Kulite 5 psi high-frequency pressure transducers. The 1.5 mm diameter transducers were covered with a perforated screen and mounted flush with the casing wall. They were calibrated using the same Furness Controls micromanometer. The transducer zero offset was recorded before every run and subtracted from the data

before the calibration was applied. The output from the transducers was logged at 60 kHz and filtered at 30 kHz (well below the resonant frequency of 150 kHz) giving 20 and 30 data points per blade passage in the Red and Natal compressors respectively. The time-averaged pressures measured by the high-frequency transducers were subject to temperature drift, so when this data was required (e.g. for blade-to-blade measurements) the steady-state pressure was measured (as above) and combined with the unsteady pressure data.

3.2.2 Unsteady Velocity Measurements

Unsteady velocity measurements were used for recording turbulence parameters and blade-to-blade flow angle and velocity. A single element, normal, hotwire probe was used. This was yawed (rotated about the probe stem) to obtain measurements from which flow angles could be calculated (see Section 3.3). The hotwire was calibrated at the start and end of each day's testing using a steady-flow wind tunnel and the data was fitted to a fourth order polynomial (Jorgensen, 2005). The uncertainty in the velocity measurements due to the calibration drift was less than $\pm 3\%$ of typical free-stream values. The Bearman correction was always used to correct the hotwire output for changes in atmospheric temperature. The output from the hotwire was logged at 100 kHz and filtered at 30 kHz to avoid aliasing, giving 35 and 50 data points per blade passage in the Red and Natal compressors respectively.

3.2.3 Shaft Torque and Speed

These measurements were used for calculating the input power and blade speed. The motors driving both compressors were mounted in a freely-rotating gimbaled frame so that the torque reaction acted against a load cell. This was calibrated before each set of experiments using dead weights attached to a torque arm. The zero offset was recorded before every run and subtracted from the data before the calibration was applied. The zero-level drift, measured before and after each experiment, was never more than $\pm 0.5\%$ of the torque at full load. The torque calibration measurements never varied by more than $\pm 0.5\%$. Rotational speed was measured using a light-gate on the rotor and processed using a trigger box, which also provided the shaft angle trigger for data logging.

3.2.4 Atmospheric Conditions

The atmospheric temperature was measured using a mercury thermometer near the compressors. The atmospheric pressure was measured using a standard mercury barometer.

3.2.5 Data Acquisition and Analysis

Data was acquired using a National Instruments data acquisition card with a 16-bit resolution. This high resolution made the voltage quantisation levels small (0.15 mV for a typical 0-10 V measurement range). Sixteen sequential logging channels were available, sharing a maximum logging frequency of 1.2 MHz (i.e. one channel could be logged at 1.2 MHz, 10 channels could be logged at 120 kHz etc). The logging system was controlled by Lab-View. This controlled the data acquisition, wrote the raw data to files (for later processing), performed real-time data analysis (to monitor the experiments) and controlled the stepper motors (to move probes). The data was then processed using Matlab and Tecplot.

3.3 Experimental Techniques

This section describes the techniques used to record the experimental measurements.

3.3.1 Performance Characteristics

The flow coefficient (ϕ) is based on the average velocity of the inlet flow, which was found by calibrating the inlet. The stagnation pressure of the inlet flow was measured using pitot tubes. There were four pneumatically averaged pitot tubes in the Red compressor inlet and one in the Natal compressor. The stagnation pressure was corrected, using a loss coefficient, to give the average value downstream of the inlet. The loss coefficient was found using three-hole probe traverses downstream of the inlet, and was averaged over the compressor flow range. The static pressure was measured using casing tappings downstream of the contraction. There were eight pneumatically averaged tappings in the Red compressor inlet and four in the Natal compressor. The static pressure was corrected in the same manner as the stagnation pressure. The axial velocity and flow coefficient were calculated from the corrected pressures. The uncorrected axial velocity measurement error was $\pm 0.3\%$ at the design point, but the use of corrections reduced the absolute accuracy of these measurements to $\pm 1.5\%$ (due to inaccuracies from the traverse data). The repeatability between builds was better than $\pm 0.15\%$ (verified by repeated experiments).

The total-to-static pressure rise coefficient (ψ) is based on the stagnation pressure of the rotor inflow and the static pressure at the casing of the stator outflow. The rotor inflow stagnation pressure was gained from the stagnation pressure measured with the inlet pitot tubes by using corrections based on loss coefficients (as described above) to give the average

stagnation pressure at the rotor inflow (i.e. downstream of the turbulence grid and IGVs in the Red compressor). The outflow static pressure was measured downstream of the stator by eight pneumatically averaged casing tappings in the Red compressor and four in the Natal compressor. The measurement error was $\pm 0.8\%$ at the design point, reduced to $\pm 1.2\%$ by the correction inaccuracy. Repeatability between builds was $\pm 0.5\%$ (verified by repeated experiments).

To measure the characteristics, data was logged in sequential periods of 0.1 s at 100 kHz and each period was averaged to form a point on the characteristic. The compressor was throttled slowly (design point to stall taking two minutes) so that the operation of the compressor was quasi-steady. Compared to measuring discrete operating points, this continuous logging process is faster, allows more accurate measurement of the stall point and records any kinks or steps in the characteristics.

When the efficiency (η) was required, the shaft torque was also measured. The continuous logging process was still used, but the measurements were averaged over a longer period (0.4 and 0.5 s in the Red and Natal compressors respectively) to reduce the impact of drive system resonances. The compressor was thus throttled at a slower rate to ensure quasi-steady operation (design point to stall taking five minutes). The efficiency was calculated from the shaft torque and static pressure rise over the rotor and stator as shown in Equation 3.1. The static-to-static pressure rise can be used because both compressors have repeating, incompressible stages. Repeated experiments showed that the efficiency was repeatable within $\pm 0.1\%$ provided the compressor was warmed up properly, electrical interference was monitored, and the air was steady and at a roughly constant temperature.

$$\eta = \frac{\dot{m}\Delta P_o}{\rho(\omega\tau)} = \frac{\dot{m}\Delta P_s}{\rho(\omega\tau)} \quad (\text{for a repeating, incompressible stage}) \quad (3.1)$$

Total-to-static pressure rise and efficiency characteristics of the Red and Natal compressors are shown in Figure 3.2. Data is included for each compressor fitted with a smooth and treated casing wall for reference (see Chapters 7 and 8).

3.3.2 Parametric Tests

Parametric tests are used throughout this work to measure the relative performance of different casing treatments. In all these tests, two characteristics were measured with a smooth casing wall, then three with a treated casing wall, then another two with the smooth wall again. If the stalling flow coefficient or maximum efficiency of the four smooth wall,

or three treated wall, characteristics disagreed by more than the accuracies quoted below, the entire dataset was re-taken. This technique allowed the stall margin improvement (SMI) and pressure rise improvement (PRI) to be measured within 0.5% and the design point flow improvement (DPFI) and maximum efficiency improvement (MEI) to be measured within 0.1%. Once the compressor and logging system was properly warmed up, however, discarding a set of data was rarely necessary.

In Chapters 5, 6 and 8, various casing groove designs are tested at different axial locations. This was achieved, without changing the rotor-stator spacing, by placing circular shims (i.e. very thin casing rings) under the treated casings. This did not change compressor performance, but the differential testing outlined above was maintained for each shim configuration.

3.3.3 Pneumatic and Hotwire Probe Traverses

This section discusses the traverse gear, probes and techniques used to record traverse data.

The Traverse Gear

The same probes and traverse gear were used on both compressors. The traverse gear had three degrees of freedom that were all driven by computer-controlled stepper-motors. The probes were fixed in a yawing mount with a resolution of 0.3° per step. This was mounted on X and Y linear tables with resolutions of $6.5\ \mu\text{m}$ per step. The whole traverse gear could be moved axially (using sliding mountings) to allow access at any axial location.

The probe was inserted into the flow through a slot in the casing, which was lined with foam to prevent leakage. If the traverse slot was not in use, the foam lining was removed and the slot was blanked off. The probes themselves were located in the yawing mount by a key on the probe stem (see Figure 3.3). The probes were nulled to the accuracy of the yaw traverse gear before every set of experiments using a small calibration tube attached to an industrial vacuum cleaner. The radial probe location was set by lightly touching the hub with the probe and then withdrawing it so the closest measurement point was 0.8 mm (1.3% span) away from the hub wall. Home switches on the traverse gear were used to re-set the probe before each subsequent traverse.

During traverses, the probe was moved radially from the hub to the casing. When the probe yaw angle was changed (see below), the controlling software and stepper motors automatically corrected any corresponding changes to the lateral location of the probe head.

Pneumatic Probe Traverses

A three-hole cobra probe was used to measure the flow angle, stagnation pressure and static pressure at locations upstream, downstream and between the various blade rows. The probe was 3 mm in diameter and is shown in Figure 3.3.

Radial traverses were found to be sufficient for measuring the flow field downstream of the inlet and rotor blades. These traverses contained 45 radial points. Area traverses were required for measuring the flow downstream of the IGVs in the Red compressor. These measurements were used to obtain the loss coefficients used to correct the characteristic data (see above). For these traverses, 45 radial points and 17 tangential points were used. These numbers of points were sufficient to make the traverse data resolution-independent. For calculating the inflow angle in Chapter 8, this resolution was higher than necessary, so 15 radial points and 11 tangential points were used. Traverse points were equi-spaced tangentially and radially clustered toward the endwalls using a hyperbolic tangent function.

At each measurement point, the three-hole probe was first allowed to settle for 1 s. The logging system then checked that the overall compressor flow coefficient was correct to within 0.25% of the required value, checked that the probe was nulled properly (see below), waited for the rotor shaft trigger, and logged data for 2 s at 100 kHz. The mean of this data was then calculated and stored. The error in the results as a percentage of the mean was also monitored.

The three-hole probe was used in a nulled configuration throughout. This meant the probe was yawed so it pointed into the flow (to $\pm 0.3^\circ$) before the pressures were logged. The calibration (see below) was then applied to the data, and the probe setting angle was added to the measured flow angle. Therefore, only the most accurate part of the calibration curve (at small off-zero flow angles) was used. This is especially valuable behind the rotor, where the absolute flow angles are large. Use of a Newton-Raphson nulling method ensured that the time penalty associated with this procedure was reasonable.

The three-hole probe was calibrated using a steady-flow wind tunnel for angles of $\pm 45^\circ$ and at three Reynolds numbers. This process was automated and used the same yaw traverse gear that was used on the compressor. Reynolds number dependencies were small at moderate flow angles ($\pm 20^\circ$) and negligible at the small flow angles the probe encountered.

The error in flow angle was calculated to be $\pm 0.5^\circ$, the error in stagnation and static pressure was $\pm 0.6\%$ and $\pm 1\%$ of dynamic head respectively, and the error in velocity measurements was $\pm 2\%$. These errors are in agreement with experimental testing. Three-hole probe and hotwire traverses agreed well (see below), which gave confidence in both measurements.

Hotwire Traverses

The single-element hotwire (with the element normal to the probe stem) was used to measure the turbulence level of the rotor inflow and the blade-to-blade flow angle and velocity of the rotor outflow. The element was 1.5 mm long. The probe is shown in Figure 3.3. The hotwire calibration method is presented in Section 3.2. The inflow turbulence and rotor outflow traverses are dealt with separately below, due to the different approaches used in each case.

Rotor Inflow Turbulence Traverses In the Red compressor, area traverses were required for measuring the turbulence upstream of the rotor (i.e. downstream of the IGVs and turbulence grid). The traverses contained 29 radial points and 9 tangential points. In the Natal compressor, an area traverse was not necessary, so a radial traverse with 29 points was used. In both compressors, the probe element was held normal to the free-stream flow angle. At each point, the probe was allowed to settle for 0.5 s and it was checked that the overall compressor flow coefficient was within 0.5% of the required value. The shaft trigger then started the recording of 0.5 s of data. The data was then written to a binary file. Turbulence intensity and length-scale were calculated using the methods of Camp and Shin (1995).

Rotor Outflow Traverses Radial traverses were found to be sufficient for measuring the flow field downstream of the rotor. These traverses used 35 radial points (sufficient to give resolution-independent data), which were clustered radially in the same way as the three-hole probe traverses. To find the flow angle, the hotwire yaw angle was set to the flow angle measured by a three-hole probe, before the hotwire was yawed $\pm 30^\circ$ over 11 steps. At each step, the probe was allowed to settle for 0.5 s and it was checked that the compressor flow coefficient was within 0.5% of the required value. The shaft trigger then started the recording of 50 sets of 0.021 s of data (0.021 s is just over one rotor revolution), which were then ensemble averaged.

The phase-locked, ensemble-averaged data at each of the 11 yaw angle steps was then processed using the method of Dickens (2008) to give the unsteady flow velocity and angle at each traverse location (this method essentially finds the angle where the maximum velocity is recorded by the hotwire). The flow angle calculated using this method agreed with three-hole probe measurements by less than a degree. The velocity measurement uncertainty was $\pm 3\%$ of typical values due to the calibration drift during a set of experiments.

Traverse Data Averages

The area, mass, work and mixed-out averages (Cumpsty and Horlock, 2005) were always calculated to compare with each other. The results were remarkably similar (even downstream of the rotor) so for simplicity, area averaging was used for static pressure and mass averaging was used for velocities, angles and stagnation pressure.

3.3.4 Unsteady Pressure Measurements

The high-frequency pressure transducers mounted in the casing wall (introduced in Section 3.2) were used to measure the stall inception patterns and the blade-to-blade casing static pressure fields.

Stall Inception To measure the stall inception pattern, six transducers were equi-spaced around the circumference of the compressor $15\% c_{x,r}$ upstream of the rotor leading edge plane (see Figure 3.4). The output from the transducers was logged continuously using a buffered logging system that saved 0.9 s of data when a rise of inflow static pressure indicated that stall had occurred. The mean of the unstalled flow data was then subtracted, as this was not required for examining the stall inception pattern.

Blade-to-Blade Casing Static Pressure To measure the blade-to-blade casing static pressure field, thirteen transducers were installed in the casing over the rotor tips in a group, as shown in Figure 3.4 (the transducers were staggered to allow access). The logging method was similar to that used in hotwire traverses. For each set of data, it was checked that the overall compressor flow coefficient was within 0.5% of the required value. The shaft trigger then started the recording of 100 sets of 0.021 s of data (i.e. for just over one rotor revolution). The 100 sets of data were then ensemble averaged.

This phase-locked, ensemble-averaged data was then processed to correct for the tangential displacement of the probes and to remove the inter-channel multiplexing delay that occurs because the data acquisition card logs the channels sequentially. The mean was then removed because the steady-state level of the high-frequency pressure transducers was unreliable, and steady-state measurements were combined with the data (see Section 3.2).

3.3.5 Flow Visualisation

Flow visualisations were performed using powdered printer's ink suspended in diesel fuel to create a coloured visualisation oil. Red oil was used for the main visualisation, but to improve the contrast of the results, yellow oil was applied on top of the red base in key areas.

Once the visualisation oil was applied, the compressor was run for half an hour at the required operating condition while the diesel evaporated, leaving a pattern of ink deposited on the casing. This flow visualisation was then photographed under ultraviolet light to improve the clarity of the results.

3.3.6 Blade Setting

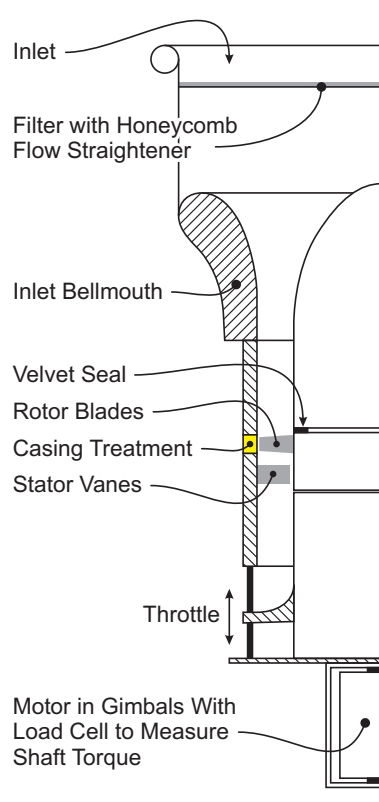
The blade stagger angle was set using an angle setting tool, which was set up with a vernier protractor. The stagger angle was correct when a bar on the angle setting tool just touched the leading and trailing edges of the blade. The use of bright illumination contrasting with a black background allowed the stagger angle to be set within 0.25° of the specified value.

3.4 Reynolds Number Independence of Stall

The Red and Natal compressors both have Reynolds numbers lower than that of a typical aircraft engine compressor. The inflow turbulence levels present in both compressors should be sufficient to cause transition at the leading edges of the blades, avoiding the effects of low Reynolds number (such as laminar boundary layer separations, see Section 3.1). However, to check this, tests were performed to ascertain whether the performance of the compressors was dependant on Reynolds number.

To this end, pressure-rise characteristics were measured at a variety of rotational speeds. The stalling flow coefficients for these characteristics are plotted in Figure 3.5. They show that the stalling flow coefficient of both compressors is unaffected by the Reynolds number, provided this is greater than 1×10^5 . The pressure rise at stall and overall characteristic shapes showed the same trend. Therefore, the impact of low Reynolds number effects on the results in the present work is small.

These observations agree with work on stall by Day *et al.* (1999), which was performed on both a high-speed aeroengine and a low-speed laboratory compressor.

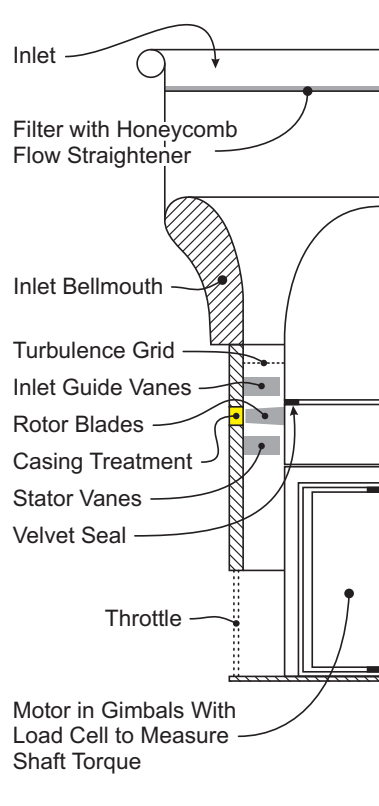


The Natal Compressor

	Rotor	Stator
No of Aerofoils:	38	37
Mid-Span Chord (mm):	35.6	36.2
Mid-Span Solidity:	1.25	1.23
Aspect Ratio:	1.74	1.71
Root Stagger Angle (°):	34.0	-23.0
Tip Clearance ¹ (% Span):	1.0	0.8
Reynolds Number ² :	1.5×10^5	1.0×10^5

Blade Design: C106 (Controlled Diffusion)
 Radially Stacked Sections
 Cantilevered Aerofoils
 No Inlet Guide Vanes

Design Flow Coefficient:	0.58
Stage Loading Coefficient:	0.41
Stage Reaction (%):	75
Rotational Speed (RPM):	2,940
Tip Radius (mm):	203.8
Hub to Tip Ratio:	0.70
Rotor Tip Mach No:	0.18
Rotor Tip Axial Chord (mm):	22.0



The Red Compressor

	Rotor	Stator
No of Aerofoils:	58	60
Mid-Span Chord (mm):	35.6	36.2
Mid-Span Solidity:	1.48	1.56
Aspect Ratio:	1.78	1.75
Root Stagger Angle (°):	30.7	-23.8
Tip Clearance ¹ (% Span):	0.9	0.6
Reynolds Number ² :	1.8×10^5	1.3×10^5

Blade Design: C106 (Controlled Diffusion)
 Radially Stacked Sections
 Cantilevered Aerofoils
 60 IGVs (13° Exit Swirl)

Design Flow Coefficient:	0.55
Stage Loading Coefficient:	0.38
Stage Reaction (%):	68
Rotational Speed (RPM):	3,000
Tip Radius (mm):	254.0
Hub to Tip Ratio:	0.75
Rotor Tip Mach No:	0.23
Rotor Tip Axial Chord (mm):	20.0

¹ running tip clearance

² based on true chord and relative inflow velocity

Figure 3.1: Partial cross-sections and aerodynamic data for the Natal and Red compressors.

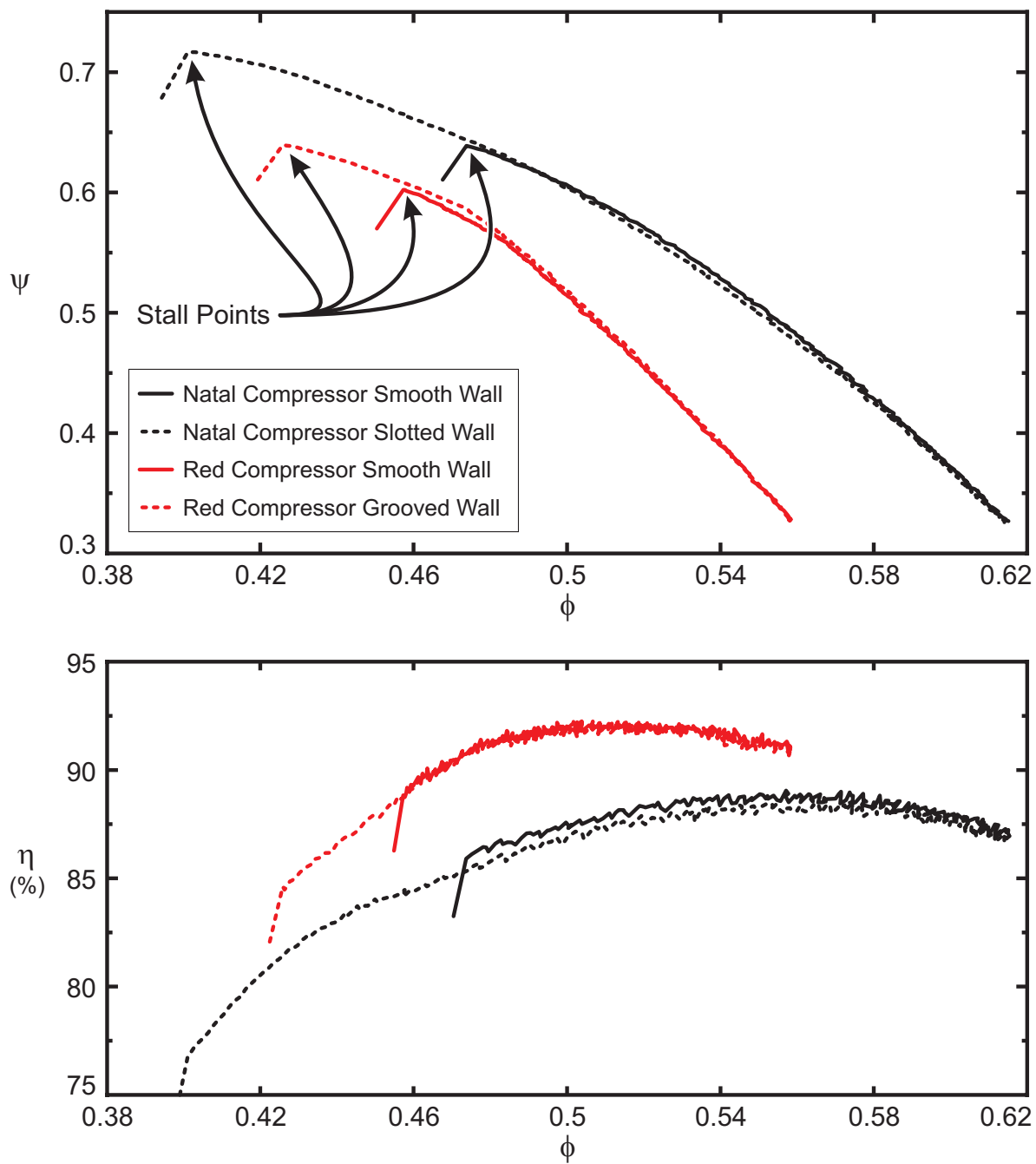


Figure 3.2: Total-to-static pressure rise and efficiency characteristics of the Red and Natal compressors with smooth and treated casing walls installed.

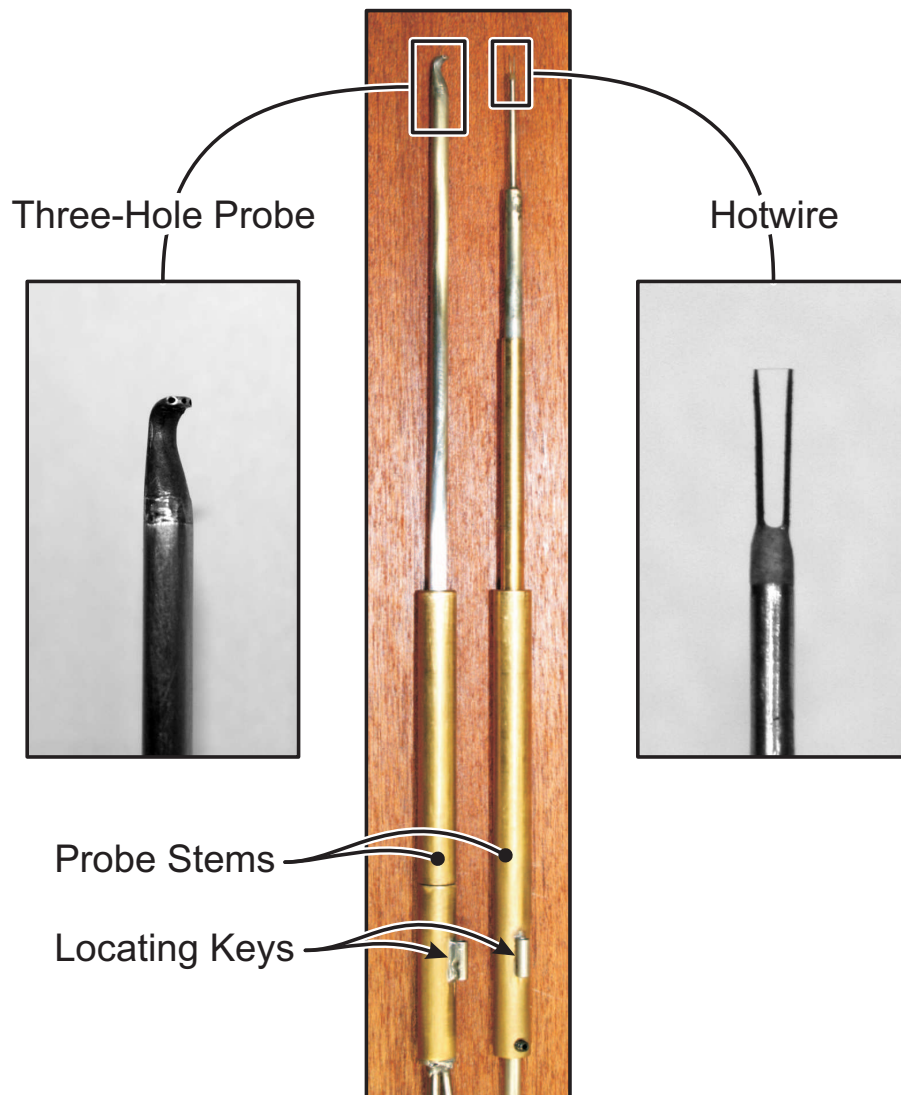
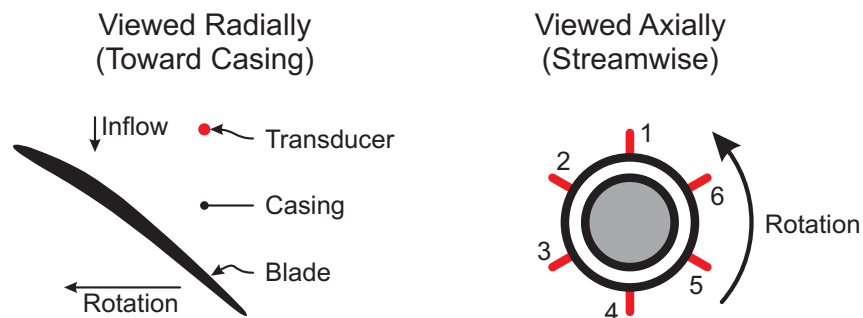


Figure 3.3: Photographs of the 3mm three-hole cobra probe and 3mm single-element normal hotwire used to measure traverse data.

Transducer Locations for Stall Inception Measurements



Transducer Locations for Blade to Blade Casing Static Pressure Measurements

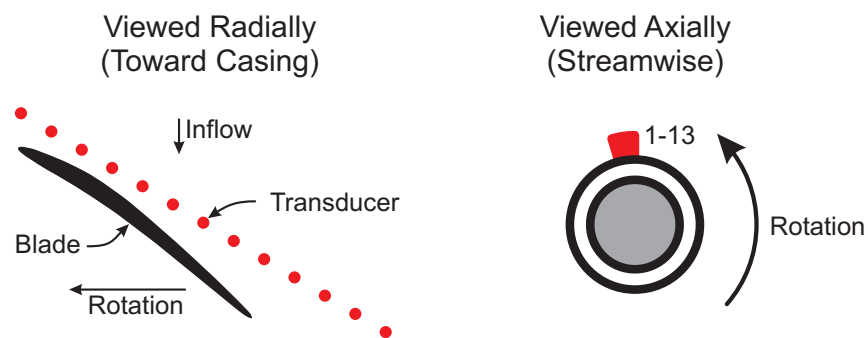


Figure 3.4: The locations of high-frequency pressure transducers used to measure the stall inception pattern and blade-to-blade casing static pressure.

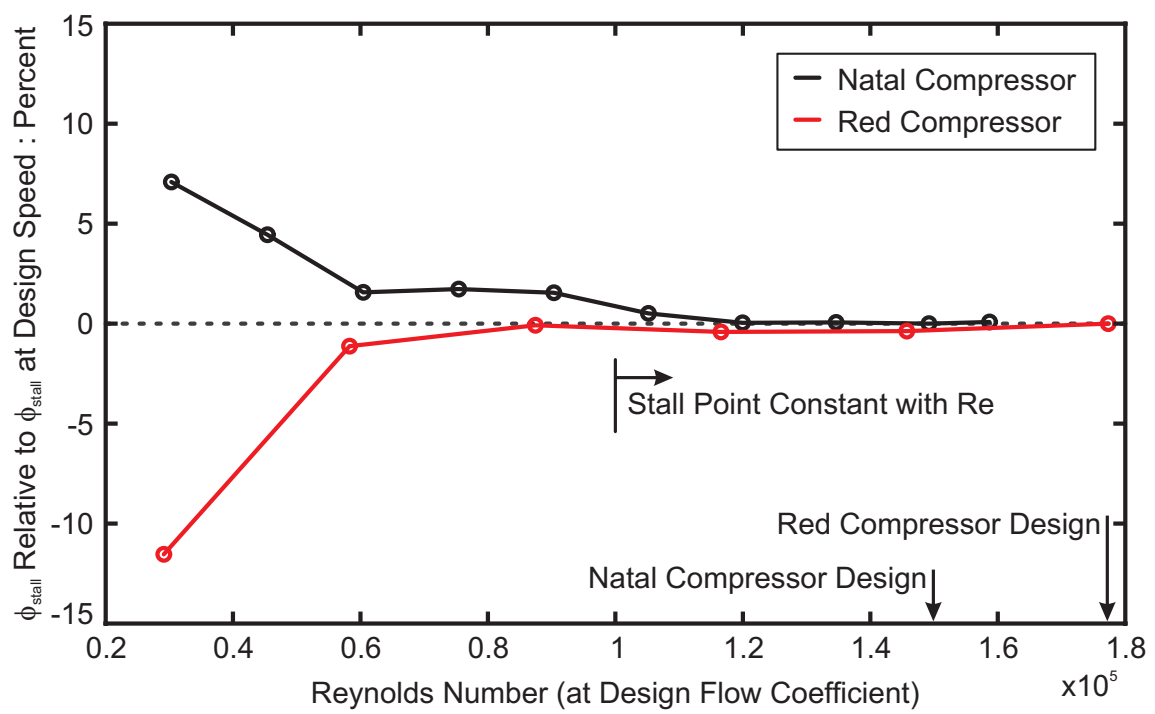


Figure 3.5: The effect of Reynolds number on the stalling flow coefficient of the Red and Natal compressors.

Chapter 4

Computational Methods

Computational fluid dynamics (CFD) is used to examine flow phenomena throughout the present work, in conjunction with experiments. CFD is useful because the whole flow domain can be interrogated without experimental constraints (i.e. access and probe size) and without disturbing the flow, which is especially important in the tip clearance. The experiments, in turn, are useful to improve the accuracy of the CFD.

This chapter introduces the computational models used in the present work. It is divided into three parts. The first part introduces the computer programs used to generate meshes, calculate the flow fields and process the results. The second part introduces the computational model and presents the meshes, boundary conditions, turbulence model and convergence criteria that are used in the calculations. The third part compares the computational results with experimental data, in order to validate the accuracy of the computational model.

4.1 Computational Tools

This section introduces the programs used to make meshes, solve flows and process results.

4.1.1 Mesh Generation

The meshes were generated using the Rolls-Royce PADRAM parametric mesh generator. PADRAM rapidly generates high-quality multi-block turbomachinery meshes from a simple input file. Shahpar and Lapworth (2003) provides background information on the program.

4.1.2 The Solver

The flow details were calculated using the Rolls-Royce HYDRA flow solver. The standard non-linear solver was used in the present work. This solves the Reynolds-Averaged Navier-Stokes equations using an unstructured, edge-based, finite-volume scheme. The Spalart-Allmaras, κ - ϵ and κ - ω turbulence models can be used. The flow field is iterated to a steady state using an explicit, five-stage Runge-Kutta scheme accelerated by a Jacobi preconditioner (described by Moinier and Giles, 1998). Unsteady calculations are performed using second-order implicit (backward Euler) dual time-stepping. Where sliding planes are used, the meshes on either side of the plane are overlapped to maintain second-order accuracy.

The solver is accelerated using low Mach number preconditioning and a four-level multi-grid, which is generated automatically using an edge-collapsing algorithm. The multi-grid was only used for steady calculations. The solver benefits from a parallel architecture that provides linear decreases in run time with processor count up to and beyond the 128 processor cores used for some calculations in the present work. The presence of sliding planes does not decrease this performance (Hills, 2007). The HYDRA system is discussed further in Madden and West (2005).

4.1.3 Post-processing Tools

Solutions were processed using Matlab, Tecplot and the Rolls-Royce JL09 post-processor. Cut planes were taken at the same locations as experimental traverses and the same averaging programs were used for both computational and experimental results to minimise the impact of the data processing methods on the results.

4.2 The Computational Model

This section presents the computational domain, meshes, turbulence model, boundary conditions and convergence criteria used for the HYDRA calculations.

4.2.1 The Computational Domain

The computational domain contains a single Natal compressor blade as shown in Figure 4.1. Limiting the computational domain to a single rotor blade allowed fine meshes to be used to provide high resolution of the flow in critical regions (e.g. near the casing and in the tip clearance) while maintaining reasonable computational cost. Multi-blade calculations did not improve the accuracy of flow modelling or stall point prediction (see below). The stator was not modelled, because the rotor and stator are widely spaced in the Natal compressor ($125\% c_{x,r}$) and the computational rotor outflow agreed well with experimental traverse data without including the stator in the model.

The computational domain extends from one and a half blade chords upstream of the leading edge to one chord downstream of the trailing edge. This was considered sufficient to separate the inflow and outflow boundary conditions from the flow around the blade.

4.2.2 Mesh Designs

The Basic Blade Mesh

Although Hydra is an unstructured solver, structured meshes were used for two reasons. First, node locations can be easily specified in structured meshes, so the mesh design is easier to control. Second, to model the flow in the slotted casing treatment, a sliding plane parallel to the casing is required; this can only be applied to structured mesh in HYDRA. All blade row meshes have an H-O-H topology (see Figure 4.2). The tip clearance is filled with H-mesh, and O-mesh is then wrapped around both the blade surfaces and the tip clearance H-mesh. The blade passages on either side of the blade and the up and downstream meshes are then filled with H-mesh. This topology gives good control over the mesh in the regions that are important to this work, i.e. near the blade and casing walls and inside the tip clearance.

To test for mesh independency, meshes with 0.7, 1.5, 2.6 and 6.9 million nodes were created by multiplying the dimensions of the 2.6 million node mesh by suitable factors. The effect

of each mesh on fishtailing¹, y^+ levels and agreement with the experimentally measured characteristics, outflow field and casing static pressure was studied. It was found that the 0.7 and 1.5 million node mesh results were inaccurate, and the 10 and 15 points across the tip clearance in these meshes were not sufficient to capture the flow in this crucial region. The 2.6 million node mesh gave accurate results at a much lower computational cost than the 6.9 million node mesh, and the 20 points across the tip clearance gave sufficient flow resolution. The 2.6 million node mesh is shown in Figure 4.3. The correct rotating extent of the hub, hub-to-blade fillet and protuberance corresponding to the boss used to hold the blade in place are applied. Figure 4.2 is a close up of this mesh with the different mesh blocks labelled.

The meshes used throughout the present work are almost identical, in order to allow fair comparison between results. There are two small exceptions. Firstly, the blade meshes used for casing grooves in Chapters 5 and 6 have 200 radial (spanwise) nodes, while the meshes used for casing slots in Chapter 7 have 180 radial nodes. This is to reduce the considerable computational expense of the unsteady calculations required to model casing slots. Secondly, the groove meshes have 40 streamwise nodes in the upstream H-mesh, but the slot meshes have 50 nodes. This is to better resolve the flows associated with the casing slots. These small differences do not affect the flow field.

The Casing Treatment Meshes

The casing grooves and slots were added to the basic blade mesh using different methods.

Casing grooves are circumferentially continuous, so they were added by modifying the mesh to include a groove in the casing. This was done by subdividing (or refining) the mesh, in order to create two tangential parallel lines corresponding to the leading and trailing edges of the groove (Lapworth, 2007). The mesh refinement was performed for 34 nodes radially downward into the blade row mesh, to prevent the transition between refined and unrefined mesh regions affecting the tip clearance flow field. The mesh between the two parallel lines was then extruded radially outward by the required groove depth. The resulting mesh is shown in Figure 4.4 for a groove located near the leading edge (the hardest region to refine due to the sheared blade mesh). A mesh independency study was performed by doubling the number of radial nodes within the groove. This did not affect the flow, so the number of nodes used is adequate. Two groove depths were required, so care was taken to ensure that the mesh expansion into the groove from the tip clearance was

¹Fishtailing is fictitious negative blade loading at the trailing edge (thought to be caused by the RANS method failing to model turbulent flow structures in this region), which can cause inaccurate exit flow angles.

the same in both cases (to allow fair comparison between them). While the refined areas of mesh did not affect the flow field, grooved cases are always compared to smooth wall cases containing identical mesh refinement as a precaution.

Casing slots are circumferentially discrete, so the slots must be meshed separately, and the slot mesh moved relative to the blade mesh with a sliding plane. The sliding plane was placed in the middle of the tip clearance, so that half of the tip clearance was in the original blade mesh and the other half was in the new slot mesh. The slot mesh was constrained by the slot geometry, which is very different to the blade row mesh. To minimise interpolation errors across the sliding plane, nodes in the slot mesh were placed so that the mesh densities on either side of the sliding plane were as similar as possible at key locations, such as near the most vigorous tip leakage flow and where flow enters and leaves the slot. Wall distances were interpolated across the sliding plane for the turbulence model. The mesh is shown in Figure 4.5, and the effect of the sliding plane on the results is considered in Section 4.3.

4.2.3 Turbulence Modelling

The Spalart and Allmaras (1992) turbulence model was used throughout this work. In back-to-back tests, this model generated a very similar flow field to the κ - ω model and was much more computationally robust. Transition modelling was tested (by setting the intermittency to zero from the leading edge to peak suction) but this did not change the flow field and was therefore not used. This is supported by the work of Schlichting and Das (1969) whose results suggest that the turbulence intensity of the Natal compressor's inflow is sufficient to make the boundary layers turbulent outboard of mid-span (the region of interest for this work). The blade roughness, vibration and noise will also aid transition.

4.2.4 Boundary Conditions

The inflow boundary conditions were specified using radial profiles of stagnation pressure and temperature, radial and tangential flow angle and Spalart-Allmaras variable. The stagnation pressure and tangential flow angle were measured experimentally using three-hole probe traverses at each operating point. The stagnation temperature was assumed constant and set to the atmospheric temperature measured during the three-hole probe traverses. The radial flow angle was assumed to be zero, because the inflow duct is parallel for more than five annulus heights upstream of the rotor. The Spalart-Allmaras variable was derived from experimental hotwire traverse measurements of turbulence intensity and length scale. The same values of tangential inflow angle and Spalart-Allmaras variable were used for all

operating points because these quantities were invariant with operating point. Experimental traverses showed that the addition of casing slots and grooves did not change the inflow, so the same boundary conditions were used for all configurations.

Outflow boundary conditions were defined using casing static pressure and the radial equilibrium equation. The casing static pressure was set so that the mass-averaged flow coefficient at inflow matched the operating point required to within 0.2%. Experimental three-hole probe traverses downstream of the rotor confirmed that the radial profile of static pressure in this region was correct.

Wall boundary conditions were defined using experimentally measured rotational speed and the walls were defined as adiabatic and smooth.

4.2.5 Convergence Criteria

Steady calculations away from the stall point were deemed to have converged when the residuals had decreased by more than three orders of magnitude. The mass flow rate and minimum pressure were also monitored to ensure that they reached a constant level.

The method used to find the ‘stall point’ of the model, or the lowest flow rate for which a stable solution exists, was as follows (steady calculations were used because unsteady calculations are currently too expensive for practical design). First, a fully converged solution was obtained near the experimentally measured smooth-wall stall point (this operating condition was used as a starting point for both treated and smooth-wall cases so the initial guess couldn’t affect the result). Second, the outflow back-pressure was increased in 1Pa steps until it became unstable. Each step was re-started from the first solution so the initial guess couldn’t affect the result. These calculations were run for five times longer than normal to clearly differentiate between unstable and stable cases. Once the stable calculation with the greatest backpressure had been obtained, stall margin improvements were calculated using the same method that was used in the experiments.

The convergence of unsteady calculations was determined in the same way as the steady calculations. The periodicity of the calculated flows was also monitored using twenty probes at key locations in the computational domain.

4.3 Validation

This section presents a number of comparisons between experimental and computational data in order to validate the computational model.

4.3.1 Performance Characteristics

To check the overall accuracy of the computational model, the total-to-static characteristics from the compressor and the model were compared. Since there are no stators in the model, the total-to-static pressure rise was measured over the rotor. The experimental data was gathered using the methods detailed in Chapter 3.3. The computational data was extracted using cuts through the model at axial locations corresponding to the experimental measurement locations, at various operating points up the characteristic and at the 'stall point' (see previous section). The tests were performed for the smooth, grooved and slotted walls, and the results are shown in Figure 4.6.

The characteristics of the smooth, grooved and slotted-wall cases are well captured by the computational model. The pressure rise predicted by the model is around 5% too high and the kink in the slotted wall characteristics at low flow rates is under-predicted, but these effects are small. The predicted stalling flow rates are also too low, but since the physics of stall are not captured by the calculations, this error is unsurprising. The computational model thus predicts the overall performance of the Natal compressor well.

4.3.2 Outflow Measurements

To check that the core flow structures are modelled correctly, the rotor outflow predicted by the computational model was compared with experimental data. Results in Chapters 5 and 7 show that the core flow is largely unaffected by casing treatments in the present work, so only the smooth results are presented. The normalised relative velocity of the rotor outflow from the model and experiments, with the compressor operating near the design point and stall, is shown in Figure 4.7.

Near the design point flow rate (upper plots in the figure) there is good agreement between the model and experiments. The flow distribution and blade wakes are well modelled, with only small differences in the mixing out of the tip leakage vortex. Near the stall point, the core flow and wakes are again well modelled, but the model does not capture the growth of the hub separation or the mixing out of the tip leakage vortex as well.

To give a more qualitative result, the experimental and computational results were circumferentially averaged to give radial profiles of normalised axial velocity and flow angle. This data is shown in Figure 4.8. Both sets of profiles show good agreement from 60% span to the casing (100% span). From 60% span to the hub (0% span) the agreement is less good due to the CFD under-predicting the corner separation, especially near stall.

These results show that although there are differences in the secondary flows, the core flow through the compressor is well modelled. Further tests to improve the agreement between experimental and computational secondary flows (as described in Section 4.2.3), made no further improvements.

4.3.3 Casing Static Pressure

In the previous section, the mixing out of the tip leakage vortex was different in the experimental and computational traverse results. In the present work, the near-casing flow will be studied in detail, in order to assess the impact of casing treatments on the flow. To check that the computational model correctly predicts the near-casing and tip leakage flow structures over the blade itself, the casing static pressure was studied. To this end, the casing static pressure was extracted from the computational model and measured using high-frequency pressure transducers as described in Chapter 3.3.

The results are shown in Figure 4.9. They show very good agreement between the experiments and the CFD. The overall layout of the data and the trajectory of the low pressure core of the tip leakage vortex (labelled in the diagram) is the same in both plots.

These results show that the near-casing and tip leakage flows are well captured by the computational model. Since the tip leakage flow is primarily inviscid (see Chapter 2), the accuracy of the results is not reduced by the simple turbulence model and the problems caused by the mixing out of secondary flows.

4.3.4 Sliding Plane Accuracy

When modelling the rotor with casing slots, a constant-radius sliding plane was required between the blade and slot meshes, near the casing. Sliding planes can cause interpolation errors, which would be unacceptable near the casing in the present work. To check that the sliding plane did not cause errors, identical smooth wall cases (i.e. no casing slots) were created with and without the sliding plane. The near-casing and outflows were then compared. The sliding plane had no impact on the near-casing flow or the rotor outflow.

The sliding plane did not cause problems when casing slots were installed, either. This can be seen in Figure 7.19, where the left-hand plots contain axial cuts through the computational model of the casing slots showing contours of entropy. There are no jumps or discontinuities in the entropy contours as they cross the sliding plane.

The sliding plane, therefore, did not reduce the accuracy of the present computational model. It is thought that this was a result of the fine meshes and the care taken to match the mesh densities on either side of the sliding plane (see Section 4.2).

4.3.5 Validation with Casing Treatment

Throughout the present work, the impact of casing slots and grooves on the compressor flow field was studied. Where possible, experimental and computational data were compared to provide additional validation. These results are contained within the body of the thesis, and summarised below.

The tangentially averaged near-casing flow field was compared with casing flow visualisation for the smooth wall (Figure 5.9), grooved wall (Figure 5.16) and slotted wall (Figure 7.14) cases. The agreement was very good, again indicating that the computational model models the near-casing flow accurately.

The effect of a single casing groove in different axial locations on the casing static pressure is shown in Figure 5.13. The changes in static pressure caused by the various treatments are well captured by the computational model.

The unsteady pressure and velocity of the flow inside the casing slots is compared in Figures 7.15 and 7.18, which gives an unsteady validation for the computational model. The agreement in the static pressure results is very good, and acceptable in the velocity results.

4.4 Summary

This chapter has shown that the computational model can be used to give reliable predictions of the steady and unsteady flows in the Natal compressor when a smooth, grooved, or slotted wall is installed. The prediction of the overall performance and core flow is acceptable, while the prediction of the near-casing flow (the area of interest for the present work) is very good. Comparison between the model and experimental data throughout the present work also shows that the model predicts the impact of casing treatments well.

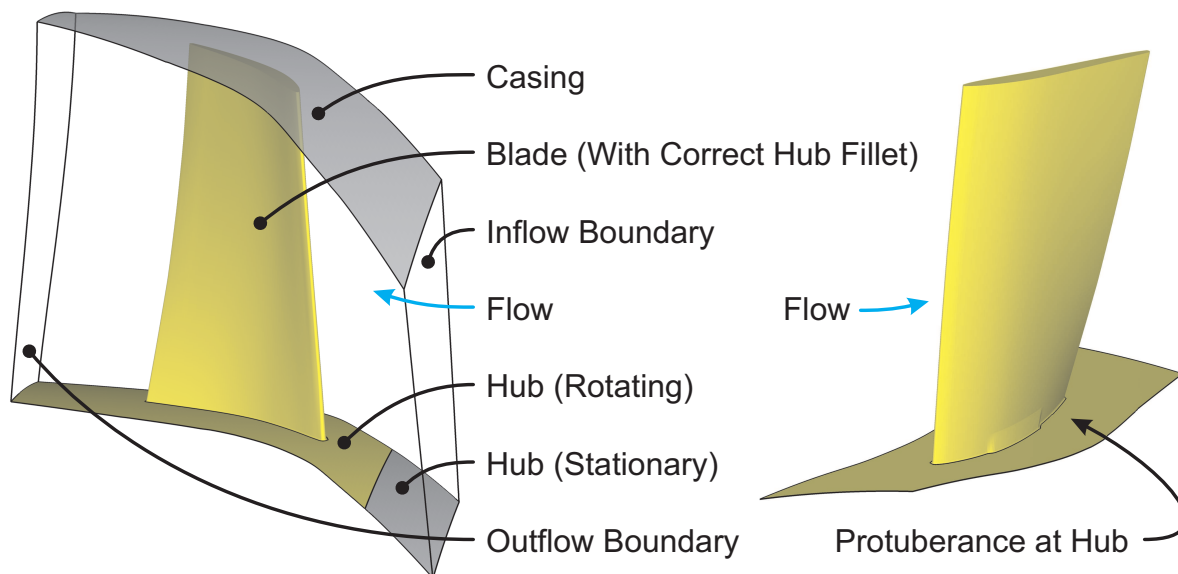


Figure 4.1: The Natal compressor computational domain. Rotating components are shown in yellow. Rotation is anti-clockwise looking downstream.

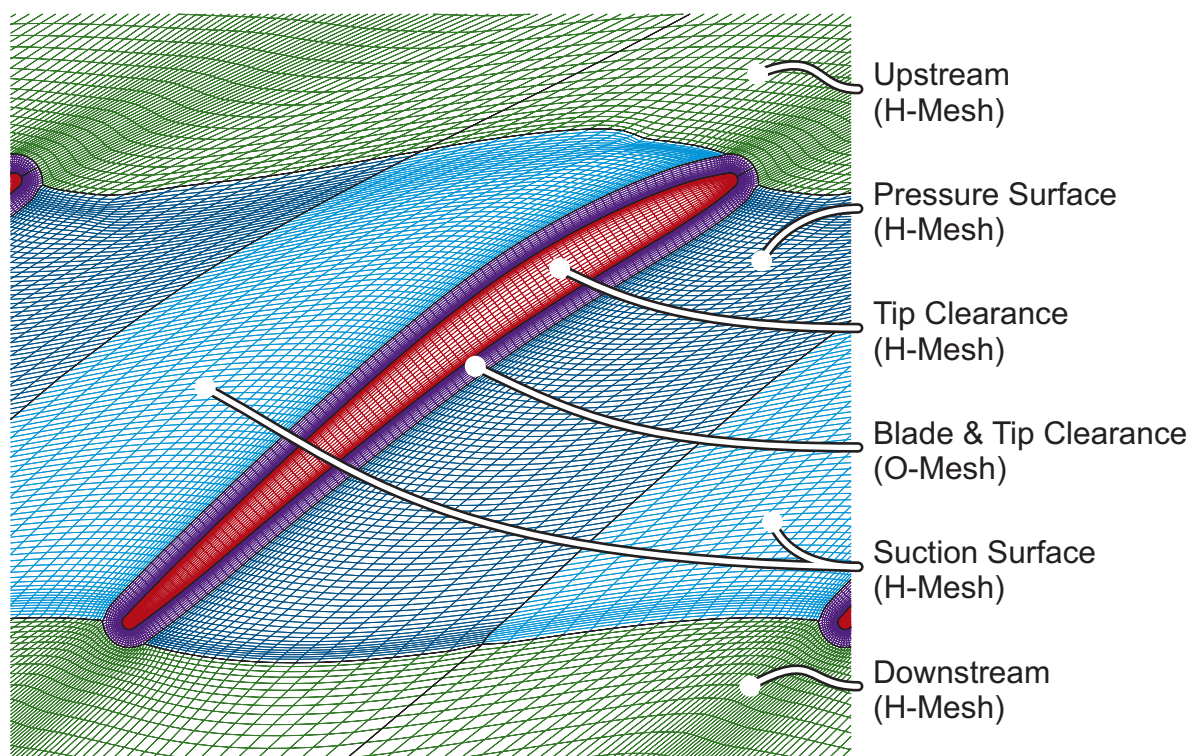


Figure 4.2: Picture of the standard blade mesh on a constant radius cut near the casing wall, showing the multiple block mesh topology. Since the cut is taken near the casing (and thus in the tip clearance) the blade is not visible.

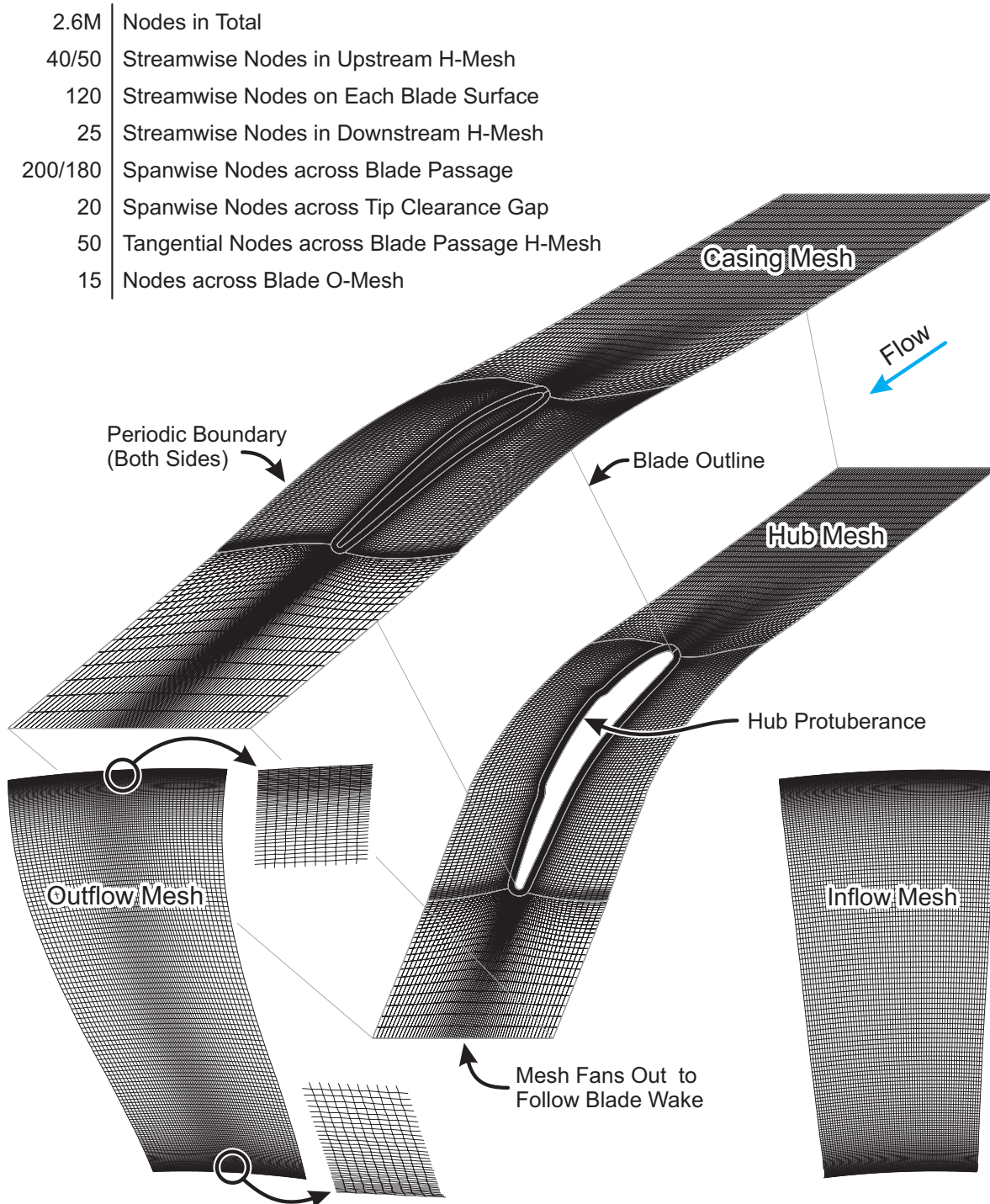
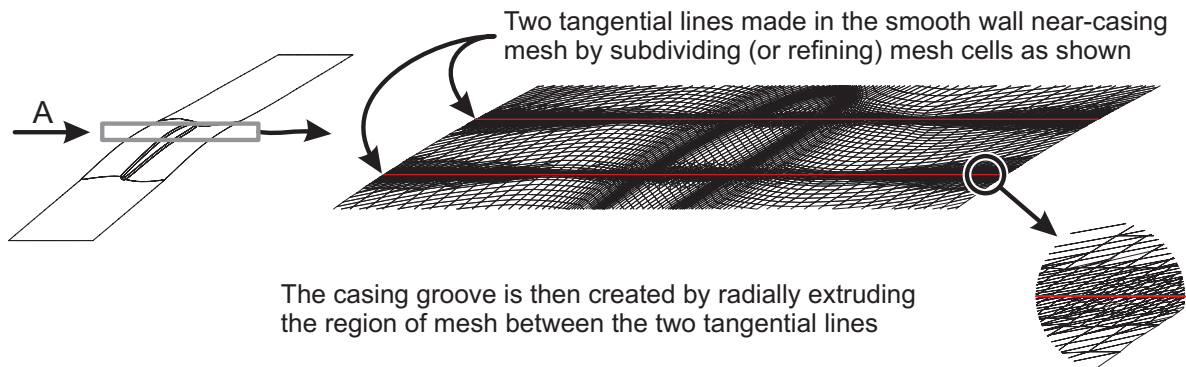
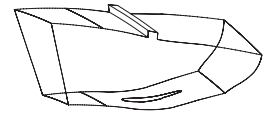


Figure 4.3: The basic smooth-wall rotor mesh, shown using cuts taken from the inflow, out-flow, casing and hub boundaries. All the cuts are shown as plan views to avoid distortion. Figure 4.2 shows a close-up of the mesh around the blade itself.

50/40	Radial Nodes in Deep/Shallow Grooves
34	Radial Nodes Affected by Mesh Refinement (Away From Casing)
25	Streamwise Nodes Across Both Grooves (Approximate)



Two Meridional Views on Arrow 'A' Showing Deep and Shallow Groove Meshes on the Periodic Boundary

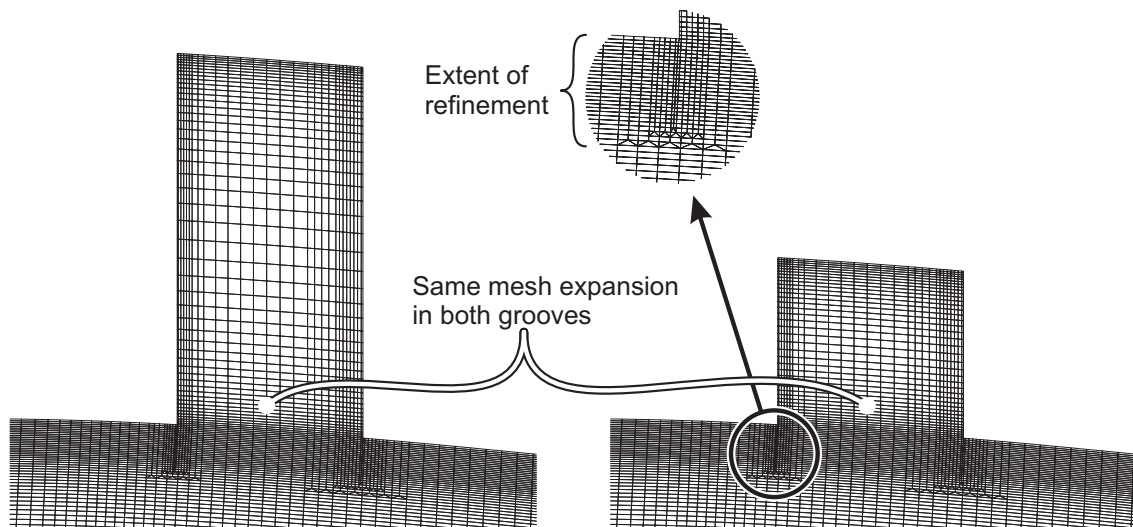
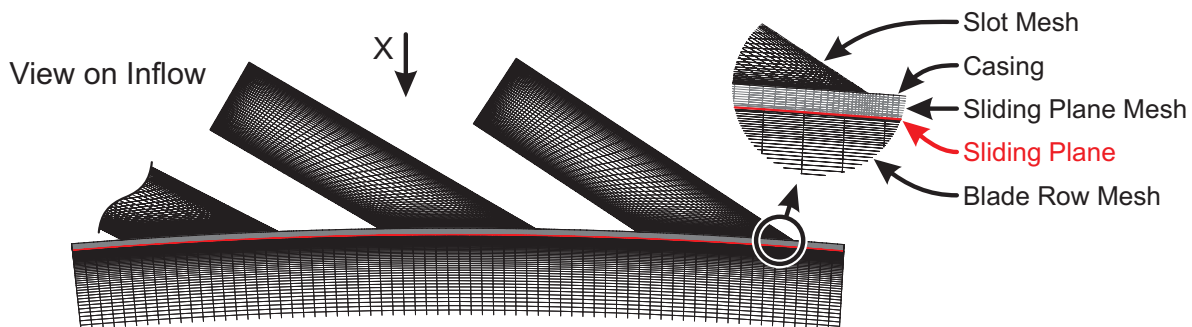
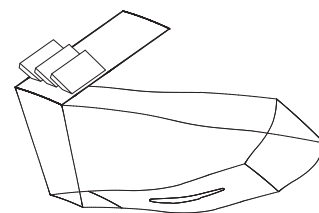


Figure 4.4: Adding casing grooves of two different depths to the basic blade row mesh. The top part of the figure shows how the basic smooth wall mesh is altered to include two tangential lines. The mesh between these lines is then extruded radially outward to form the meshes shown in the bottom part of the figure.

100	Streamwise Nodes in Each Slot
52	Pitchwise Nodes in Each Slot
75	Spanwise Nodes in Each Slot
275	Streamwise Nodes in New Casing Mesh
35	Streamwise Nodes in New Casing Mesh Upstream of Slots
270	Pitchwise Nodes in New Casing Mesh



Two Views on Arrow 'X' Showing (a) the Casing and (b) Sliding Plane Meshes

(The casing meshes are symmetrical so half of each is shown for clarity)

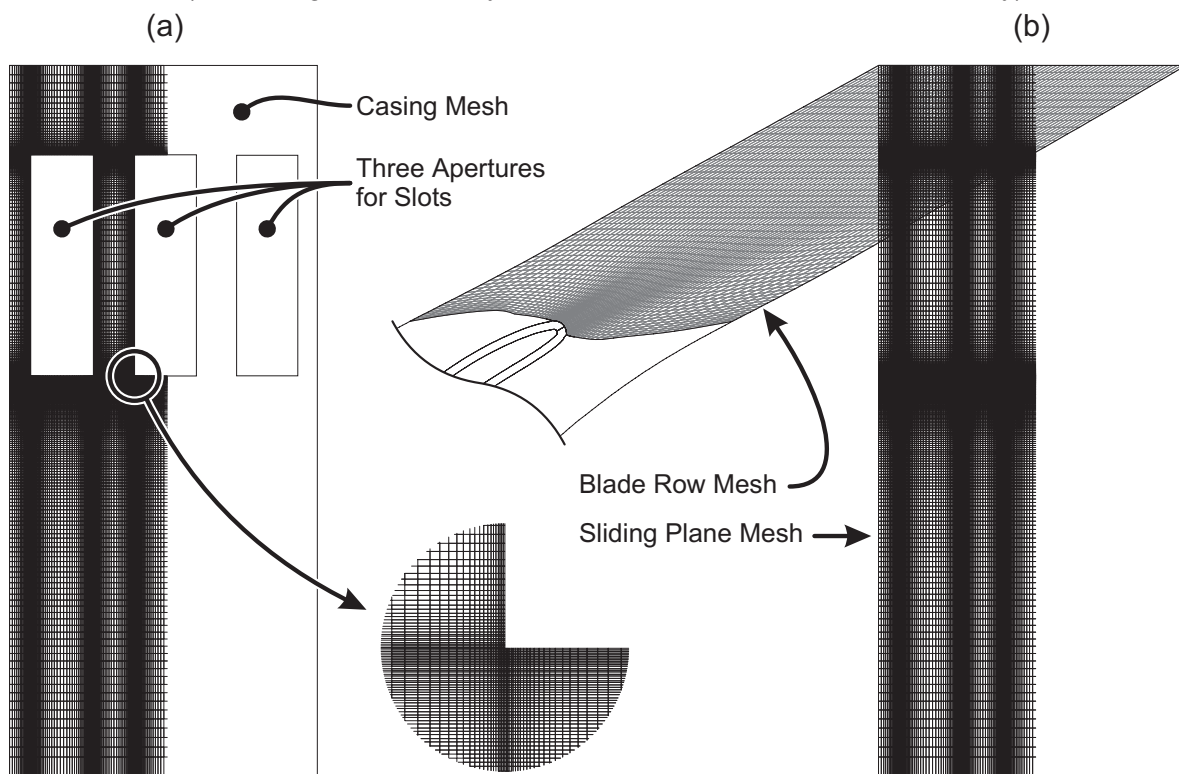


Figure 4.5: Adding casing slots to the basic blade row mesh using a sliding plane. The top part of the figure shows a view looking axially onto the domain inflow. The bottom part of the figure shows two views looking radially inward toward the casing mesh and the two meshes either side of the sliding plane.

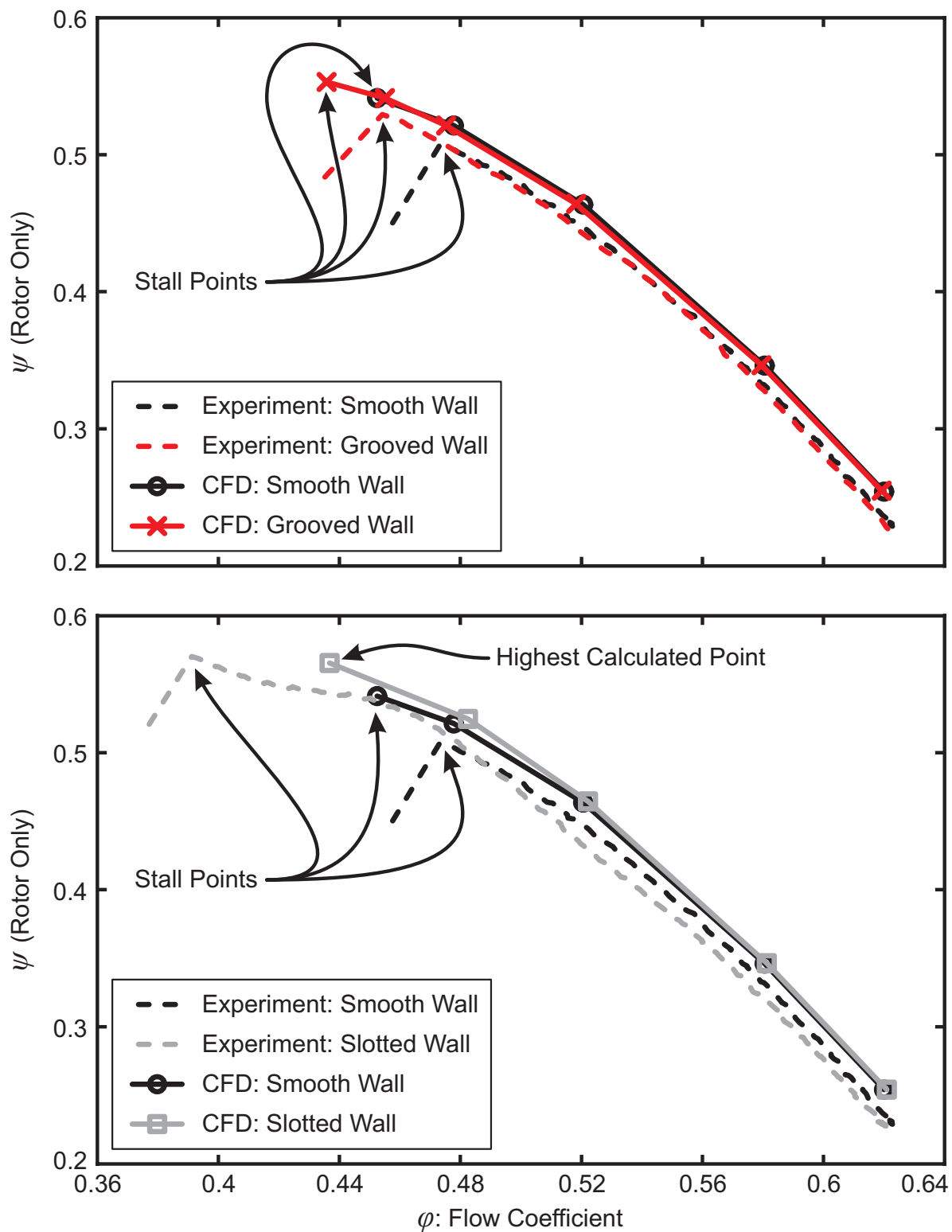


Figure 4.6: Rotor-only total-to-static characteristics for the Natal compressor from both experiments and CFD. The upper graph shows the grooved and smooth-wall cases, and the lower graph shows the slotted and smooth-wall cases.

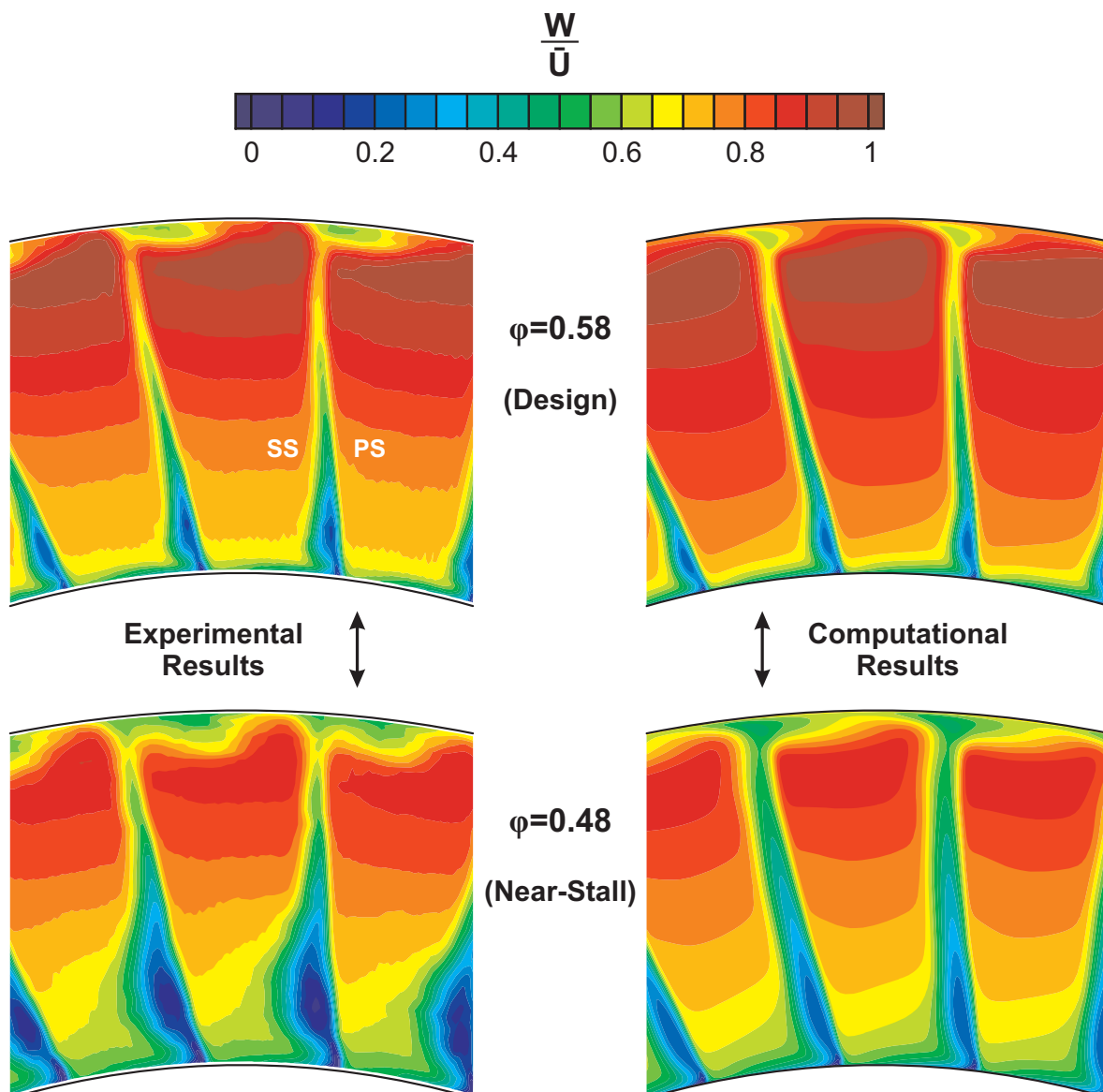


Figure 4.7: The relative velocity of the smooth-walled Natal compressor rotor outflow from experiments and CFD. The upper plots show the results near the design point ($\phi=0.58$) and the lower plots show the results near the stall point ($\phi=0.48$). All plots show the view looking upstream toward the rotor blades.

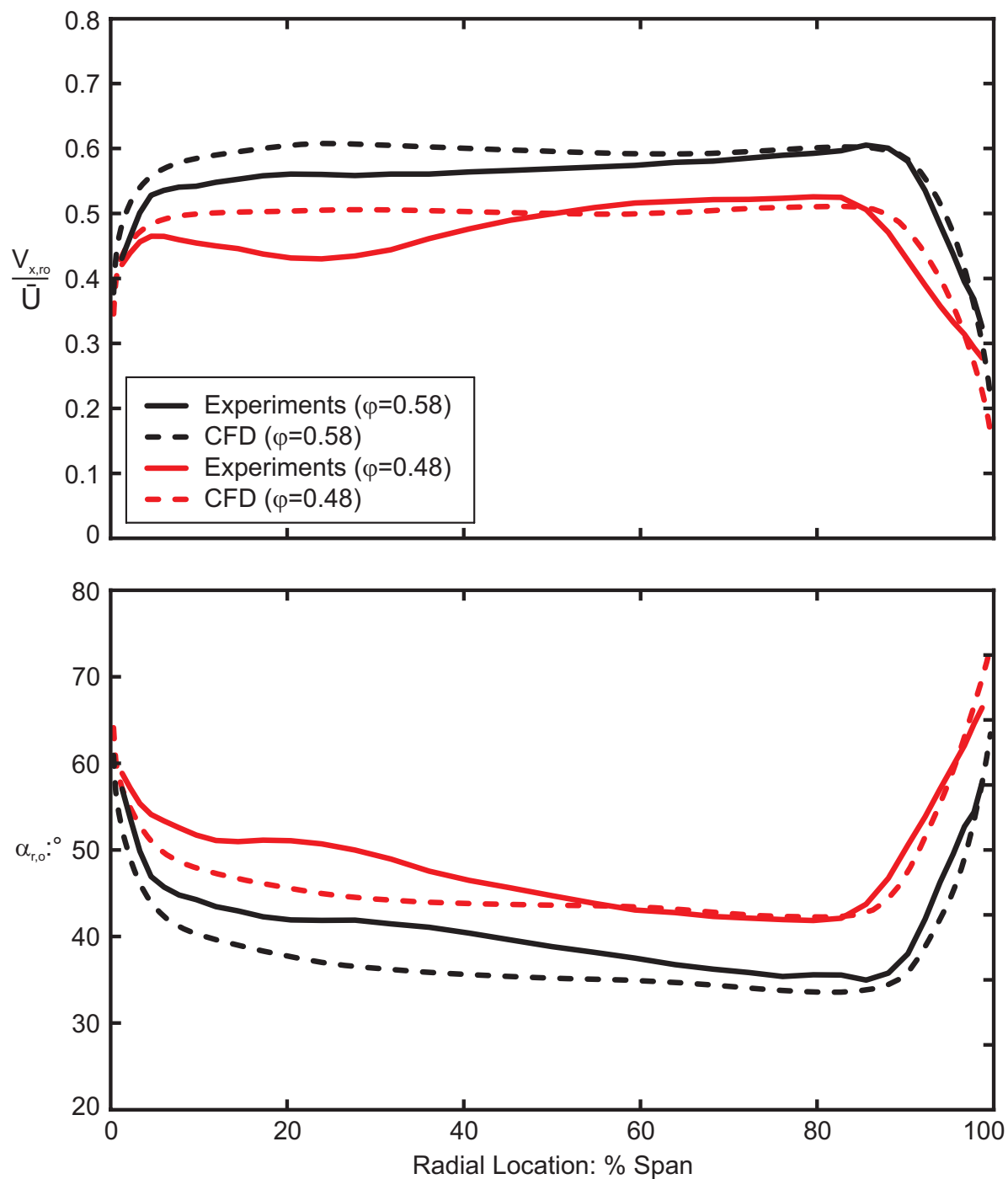


Figure 4.8: Natal rotor outflow profiles from experiments and CFD near the design point ($\phi=0.58$) and near stall ($\phi=0.48$) for the smooth-wall case. The upper graph shows the normalised axial velocity and the lower plots show the absolute flow angle.

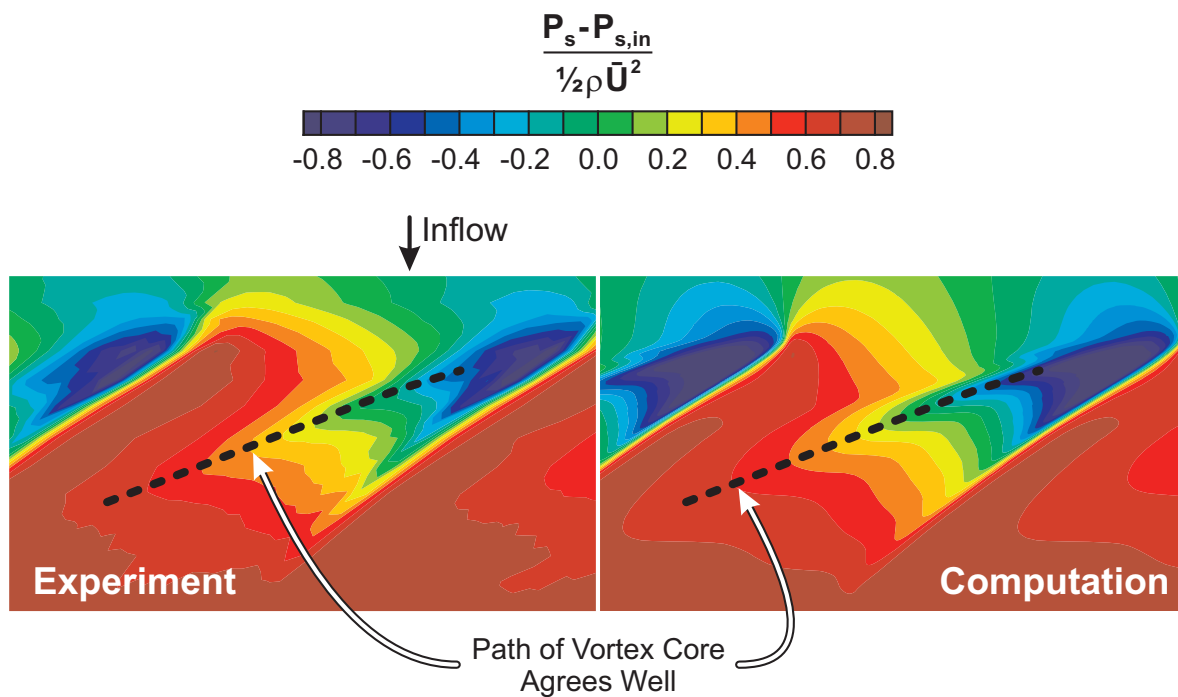


Figure 4.9: The casing static pressure over the smooth-walled Natal compressor rotor blades from experiments and CFD, halfway between the design point and stall ($\phi=0.52$). View is radially inward, from the casing to the hub.

Chapter 5

Circumferential Groove Casing Treatments: Part 1

This chapter investigates the application of a casing treatment consisting of a single circumferential groove to an axial compressor rotor. The groove is cut into the casing above the rotor blade tips as shown in Figure 5.1. Dimensions used to define the groove geometry are shown in the same figure. The groove tested in this chapter has a width (w_g) of 3 mm (14% $c_{x,r}$) and a depth (d) of 6 mm (27% $c_{x,r}$) giving an aspect ratio of 2.0. The groove's 'leading edge' is the groove corner on the casing wall closest to the blade leading edge.

The work is divided into three parts. The first part is an experimental parametric study that finds the best axial location to apply the circumferential groove. The second part is a detailed flow study that uses computational and experimental methods to explain the results of the parametric study. The third part considers the implications of the results for casing treatment design, with reference to existing published work. All the work in this chapter uses the Natal compressor, which is introduced in Chapter 3.

5.1 The Axial Location of a Single Casing Groove

These experiments investigate the impact of the casing groove's axial location on its performance. In a series of tests, the groove was moved axially from the rotor blade leading edge to the trailing edge as described in Chapter 3. Four performance parameters, which are defined in the nomenclature, were then evaluated; improvements in stall margin (SMI), pressure rise at stall (PRI), maximum efficiency (MEI) and design point flow rate (DPFI). The results are presented in Figure 5.2.

The results show an interesting relationship between the axial location of the groove and the stall margin improvement it generates. The stall margin graph has two maxima that occur when the groove leading edge is $8\% c_{x,r}$ and $50\% c_{x,r}$ aft of the blade leading edge. The upstream maximum is a narrow peak with a stall margin improvement of 4%. The downstream maximum is much broader and has a stall margin improvement of 4.5%. The groove gives the least stall margin improvement when its leading edge is located 0, 18 or $85\% c_{x,r}$ aft of the blade leading edge. The pressure rise improvement trend is similar to that of the stall margin, with a maximum pressure rise improvement of 3.5%.

The maximum efficiency improvement results show that the groove reduces efficiency when its leading edge is between 0 and $55\% c_{x,r}$. Aft of $55\% c_{x,r}$, the efficiency loss becomes negligible. The design point flow rate results show similar trends to the maximum efficiency improvement results.

These experiments show that the best location for a single groove is near mid-chord, where there is a broad, safe peak in stall margin improvement and the efficiency loss is small. The groove works well in this location, generating a useful stall margin improvement with a negligible efficiency penalty. The double maximum stall margin improvement, the minimal efficiency loss near mid-chord and the marked changes in performance that occur when the groove moves small distances are unexpected results. The present results also show that the differing optimum groove locations found in the literature in Chapter 2 (some authors recommended placing the groove near the leading edge, while others recommended mid-chord) may not be mutually exclusive.

Subsequent sections of this chapter will study the interaction of the groove with the flow field in order to explain these results. Four key groove locations will be used throughout. Location 'A' corresponds to the first SMI peak at $8\% c_{x,r}$ and 'B' corresponds to the minima at $18\% c_{x,r}$. Locations 'C' and 'D' are the two places on the second SMI peak where the SMI magnitude is equal to that of A; locations C and D are thus at $39\% c_{x,r}$ and $58\% c_{x,r}$ respectively.

5.2 Initial Experiments

Before studying the detailed flow dynamics, it is necessary to check that three possible complications do not affect the results. The first of these is changes to the stall inception mechanism, the second is the impact of interactions between the treated rotor and the stator, and the third is the dependence of the results on the compressor used.

5.2.1 Changes to the Stall Inception Mechanism

To ascertain whether casing grooves alter stall inception in the Natal compressor, the stall inception pattern was measured with the smooth wall and a casing treatment containing four grooves installed. The four-groove treatment was used because it generates a greater stall margin (5%) than the single groove treatments tested in Section 5.1 and thus provides a robust test. The leading edges of the four grooves were at 12, 39, 66 and 93% $c_{x,r}$, and each groove had the same geometry as that used in Section 5.1. The stall inception pattern was measured using six high-frequency pressure transducers as described in Chapter 3. The data is presented in Figure 5.3, with schematics showing the groove and pressure transducer layouts.

The results show that the smooth and grooved wall cases have the same stall inception pattern, with the stall cell emerging from a spike inception without modal precursors. Further, the spike is first detected at the same point on the casing when the rotor is at a similar angular displacement in both cases (within a couple of blades). This agrees with the observation by Day (1993b) that stall occurs when “a particular part of the rotor is adjacent to a particular part of the casing”. The results also show that the developing stall cell moves at the same speed whether or not casing grooves are present. Therefore, the addition of casing grooves does not change the stall inception mechanism, the location on the casing and rotor at which the inception first occurs, or the speed of the cell once it has formed.

The shape of the pressure oscillations caused by the spikes agrees with the results of Deppe *et al.* (2005), who used high-frequency pressure probes up and downstream of the rotor to study spike behaviour. In this work, the probe near the leading edge faced downstream toward the blades, and showed that the flow decelerated, over accelerated and then returned to normal levels as the spike passed. Figure 5.3 agrees with these observations, as do the hotwire measurements of Day (1993b) and the static pressure measurements of Camp and Day (1998). These results all suggest that spikes contain vorticity with the axis pointing radially outward (in right handed coordinates). The probes in Deppe *et al.* (2005) also detected axially reversed flow up and downstream of the rotor blades when the spike

formed. If spikes extend through the rotor, a groove at mid-chord could interfere with them, which may explain the effectiveness of the groove in this region.

5.2.2 Interactions with the Stator

The region of flow directly affected by the groove moves axially as the groove's location changes. The Natal compressor's rotor and stator are well spaced ($125\% c_{x,r}$ apart), but stators can affect stall in compressors generally (e.g. reducing rotor-stator spacing can improve stability). It is therefore necessary to check that the results in Figure 5.2 are not affected by interactions with the stator. In order to test this, all the stator vanes were removed. The 'rotor only' characteristics and stall margin improvement were then measured with the groove at locations A, B and C (see Section 5.1). The results are shown in Figure 5.4.

The characteristics show that removing the stator only has a small effect on the rotor. The greatest difference (at the stall point) is only 1.2% of flow coefficient, and there is little impact at high flow rates. The lower graph shows that the stall margin improvement generated by the groove as it is moved axially is not changed by removing the stator. The effect of the stator on the results in this work is therefore small.

5.2.3 Compressor Dependence

To check that the results do not only apply to the Natal compressor, the performance of the single groove treatment was measured at different axial locations in the Red compressor (introduced in Chapter 3). These results are reported in Chapter 8. The Red and Natal compressor results show similar trends in stall margin improvement and efficiency loss as the groove is moved. The results presented in Section 5.1 are therefore not an artefact of the Natal compressor.

The results in this section show that the trend in stall margin improvement seen in Figure 5.2 is not caused by changes to the stall inception mechanism or the changing distance between the groove and the stator, and is not unique to the Natal compressor. The next section investigates the impact of the groove on the compressor flow field in order to explain the results of the parametric study in Section 5.1.

5.3 Core Flow Effects

This section ascertains whether groove performance is linked to two important core flow parameters: the outflow blockage and the blade loading.

5.3.1 The Effect of Grooves on the Rotor Outflow Blockage

Takata and Tsukuda (1977), Greitzer *et al.* (1979) and Shabbir and Adamczyk (2005) linked stall margin improvement to reductions in the rotor outflow blockage (see Chapter 2). This section studies the rotor outflow to see whether there is a link between the blockage and the stall margin improvement generated by the groove.

To this end, the single groove was moved to locations A, B and C from Section 5.1. The groove generates the same stall margin improvement at locations A and C, so if there is a simple link between blockage and stall margin these cases should reflect this. The axial velocity of the rotor outflow was then measured by traversing a hotwire close to the rotor trailing edge (as described in Chapter 3). The outflow of the equivalent smooth wall case was also measured, to ensure that the different shim layout in each case did not affect the results. The flow coefficient was set close to the smooth wall stall point, at $\phi=0.48$. The overall blockage level was quantified for each blade passage using the method of Khalid *et al.* (1999) and averaged over 34 blade passages. Figure 5.5 shows the contours of normalised (non-dimensional) axial velocity for the smooth and grooved wall cases, along with the calculated overall blockage level.

The results show that the changes in overall blockage level caused by the groove are insignificantly small (never more than 0.2%). The flow away from the casing is also unaffected by the groove. There are some changes in the distribution of blockage near the casing, however. First, the groove slightly increases the blockage near the casing in all cases. Second, the tip leakage flow blockage moves toward the suction surface in cases A and B. Third, the radial extent of the tip leakage blockage reduces in cases B and C.

These small changes in blockage do not match the stall margin improvement trend observed in the parametric study (see Figure 5.1). The blockage in case B is little different to that of case A or C. In case B, the overall blockage reduces, the tip leakage blockage is moved to the suction surface and its radial extent is reduced. Takata and Tsukuda (1977) and Vo *et al.* (2008) suggest that these effects should both improve stall margin, yet case B generates the lowest stall margin. These results, therefore, show no *clear* link between the changes in outflow blockage and the stall margin improvement generated by the casing groove.

The present results can be compared to Shabbir and Adamczyk (2005), where a five-groove treatment in a low speed compressor was modelled computationally. In this work, small changes to the near-casing blockage caused by the grooves were dwarfed by the removal of a large region of blockage that exists in the untreated compressor near stall. This effect enabled the five-groove treatment, which generates a stall margin improvement of 14%, to reduce the outflow blockage by 2.7%. The smooth walled Natal compressor does not have an equivalent region of blockage for the grooves to remove. Adding casing grooves thus removes much less blockage relative to the stall margin improvement than was possible in Shabbir's compressor.

Blockage near the blade tip reduces the through-flow, increasing the tip loading and reducing the stall margin. Shabbir and Adamczyk showed that casing treatment may reduce blockage and this may improve stall margin indirectly. However, comparison of results shows that this effect is machine dependant, so the link between outflow blockage reduction and stall margin improvement is weak.

The effect of the casing groove on the outflow blockage does not explain the stall margin improvement that it can generate. The next section considers the effect of the groove on another important core flow parameter: the blade loading.

5.3.2 The Effect of Grooves on the Blade Loading

The blade loading (the pressure difference between the blade surfaces) increases as a compressor approaches stall, which increases the pressure difference across the blade tip. This strengthens the pressure-driven tip clearance flow, which intensifies the shear layer between the tip leakage and core flows, pushes the tip leakage flow further away from the blade, and increases the size of the tip leakage vortex (see Section 2). Storer and Cumpsty (1991) and Khalsa (1996) showed that these effects increase blockage, so loading and blockage are linked near the casing, but Vo *et al.* (2008), Suder *et al.* (2001) and Camp and Day (1998) suggested that stall may occur when the blade tip loading (rather than blockage) is too large. This section therefore adds to the blockage results by studying the link between the effect the groove has on blade loading and the stall margin improvement it generates.

To this end, the computational model validated in Chapter 4 was used to calculate the flow in the smooth and grooved wall cases A, B and C. The flow coefficient was set at $\phi=0.48$ (near the smooth-wall stall point). The blade loading distributions with smooth and grooved casings were then compared near the blade tip (at 98% span). The blade loading plots are shown in Figure 5.6. The blade loading near the hub and mid-span was also studied, but was unaffected by the presence of casing grooves and is therefore not presented.

In case A, the results show that the blade loading is reduced near the groove and increased immediately downstream, so the groove moves the blade loading away from the leading edge. The results for case B show a similar trend, but the blade loading changes are smaller than in case A. The groove does not affect the blade loading in case C. Therefore, the effect the groove has on blade loading does not explain the trend in stall margin improvement observed in Section 5.1. These findings also apply if the blade loadings with smooth and grooved walls are compared at their respective stall points.

When stall occurs via spike inception (as in this case), blade rows are more likely to stall when the blade tips are heavily loaded (Camp and Day, 1998), so blade loading can affect stall. These results, however, show that there is no clear link between the impact the groove has on the blade loading and the stall margin. The effect of the groove on outflow blockage and blade loading is therefore similar. The groove does not affect these parameters away from the tip region and causes the greatest changes in the tip region when located near the leading edge. This behaviour does not explain the stall margin improvement trend in Figure 5.2, but it does show that the near-casing region is the most important area to consider. The next section analyses the flow in this near-casing region.

5.4 Near-Casing Flow Effects

This section analyses the impact of casing grooves on the near-casing flow, in order to explain the results presented thus far. The near-casing flow field in an untreated rotor must be understood before the impact of casing grooves upon it can be considered, so the first step is to study this near-casing flow.

5.4.1 Casing Flow Visualisation in an Untreated Rotor

This section introduces experimental casing flow visualisations and then compares them with computational results. The experimental flow visualisations were created using oil applied to the casing wall as described in Chapter 3, which essentially creates a map of the tangentially-averaged shear stress on the casing. Experimental visualisations usually have three different regions in both high and low-speed compressors (Bennington *et al.*, 2007; Deppe *et al.*, 2004).

The three regions are labelled on a typical Natal compressor flow visualisation in Figure 5.8. Region '1' (see figure) is formed by the inflow boundary layer. The flow is initially axial (following the inflow), but is deflected slightly against the blade motion as it approaches

the rotor. Downstream of the rotor leading-edge plane, the visualisation becomes lightly scoured, indicating increased shear forces and hence increased flow speed. Region '2' is formed by near-casing flow features associated with the rotor blades (which is studied later). The visualisation shows axially reversed flow and is well scoured, indicating high-speed flow close to the casing. Region '3' shows the flow moving away down the compressor. Between regions 1 and 2 there is a line of deposition above a line of scouring (enlarged in Figure 5.8). This is called the 'black line', because the removal of visualisation oil makes it appear black under the ultra-violet light used to illuminate the results.

In order to investigate the cause of the black line and further validate the computational model, experimental flow visualisations were created on the smooth wall at three flow coefficients: $\phi=0.58$ (near the design point), $\phi=0.52$ and $\phi=0.48$ (near stall). Constant-radius cuts were then taken from the computational model at $5\% tc$ (5% of the tip clearance away from the casing) and the time-averaged flow field in the absolute frame was found. This was done by copying the cuts 24 times, rotating them to equispaced angles across a blade pitch and then averaging them.

The results are presented in Figure 5.9. The left-hand plots show the experimental flow visualisations. As observed by Deppe *et al.* (2004) and others, the black line moves forward as the flow coefficient reduces, approaching the leading edge near stall. The central plots show the experimental visualisation overlaid with arrows indicating the absolute velocity direction (time-averaged in the absolute frame) from the CFD. In each case, the flow directions in the three regions introduced above agree well. In the vicinity of the black line the agreement is also good, with the axial location of the black line in the experimental results matching that of a 'convergence line' in the CFD, and the tangential movement of flow as it enters the convergence line from downstream being captured. The right-hand plots show the absolute velocity magnitude alongside the direction arrows from the central plots. The increased near-casing flow velocity that causes the scouring in region 2 is clearly visible.

The computational results suggest that the location of the black line is set by an axial momentum balance. The good agreement between experimental and computational results is also reassuring from a validation perspective. However, in the black line area, the experimental results show lines of deposition and scouring, while the time-mean CFD appears to show two flows meeting at the convergence line and separating from the casing wall. A separation should not cause scouring; the oil should collect under the separation where there is low shear-stress. The convergence line in the CFD does not, therefore, explain the pattern of flow visualisation at the black line. To further investigate the black line, the near-casing flow structures must be examined without averaging (which hides a lot of detail). The next two sections consider this.

5.4.2 The Near-Casing Flow in an Untreated Rotor: Introduction

This section introduces the detailed structure of the near-casing flow field. To study the flow, computationally derived flow maps were created near the smooth-wall stall point ($\phi=0.48$) using constant radius cuts at $5\%tc$. Cuts at this radius were used because this region is most affected by casing treatment, and changes here affect the whole tip leakage flow. Radial velocities are insignificant this close to the casing wall. The flow field is shown in Figure 5.10 schematically, and in Figure 5.11 with contours of static pressure and axial, tangential and overall velocity. The absolute, rather than the relative, flow field is used because this avoids detail being obscured by large tangential velocity components (which are caused by the large blade speed). Since the absolute flow field is unsteady, the flow direction is indicated with arrows. These only show flow direction (not magnitude) for clarity. There are four regions of flow containing five key flow features.

Region 'a' is the inflow, which is axial far upstream of the rotor because there are no IGVs. This circumferentially uniform boundary layer flow is drawn down the casing wall to the saddle point in front of each blade at label '1'. The flow is pushed between the saddle points of adjacent blades, with the greatest velocity occurring at '2'. This is shown by the orange areas in the axial velocity plot in Figure 5.11. These effects cause the patterns seen in region 1 of the experimental flow visualisation described in the previous section.

Region 'b' is the tip leakage flow, which is bounded by an attachment line at '3' and a separation line at '4'. The attachment line divides the flow being instantaneously forced into the tip clearance (by the cross-blade pressure gradient) from the flow being forced across the blade passage at '5' (by the cross-passage pressure gradient). The separation line divides the tip leakage flow and the inflow, and is shown as a line of low-speed flow in the axial and absolute velocity plots in Figure 5.11. The tip leakage flow itself has a large absolute velocity, which reduces the static pressure of the near-casing flow. This large velocity is axially reversed (shown by the blue areas on the axial velocity plot in Figure 5.11) due to the blade loading distribution and stagger angle. Once the flow has separated from the wall at 4, it moves into the blade passage and rolls up into the tip leakage vortex (the path of the vortex core is labelled 'TLV' in Figure 5.10). The vortex itself is not visible on the casing wall, but its effect on the casing static pressure is shown by the trough of low pressure adjacent to the separation line. The vortex has a narrow, intense core near the leading edge, which fills and enlarges as it moves down the blade passage. Near the leading edge, the flow in region 'b' is vigorous, with large velocities and a clearly defined separation line. Away from the leading edge, near '5', the velocities are lower, the separation line widens out and the flow moves tangentially in the direction of the rotor.

Region 'c' is the blade passage boundary layer. This exists between the saddle point at 1 and the separation line at 4. The flow in region 'c' is being driven slowly across the passage by the influence of the blade passage pressure-gradient. Region '2' of the experimental flow visualisation is formed by an average of the wall bounded shear layer caused by the tip leakage flow (region 'b' above) and the blade passage boundary layer (region 'c'). The shear stress on the wall is much greater in region 'b' than 'c' (because the flow in region 'b' moves faster) so the experimental flow visualisation averages these to show axially reversed flow.

In Region 'd', at rotor exit, the rotor outflow starts to drag the near-casing flow away from the tangential direction and downstream, away from the rotor. This causes region 3 of the experimental visualisation.

This section has introduced the near-casing flow and linked it to experimental flow visualisations. The next section considers the most important features in more detail and relates these to the black line.

5.4.3 The Near Casing Flow in an Untreated Rotor: Detail

This section continues the investigation of near-casing flow, starting with the flow around the separation line (introduced in the previous section).

The two-dimensional separation line is caused by the opposing normal velocities on either side of it, associated with the inflow and tip leakage flow. However, the flows moving towards the separation line also have velocity components directed along the line. This is shown by the flow schematic in Diagram 5.1. Near the leading edge, these components cause the flow *at the separation line itself* to be instantaneously pushed away from the leading edge along the separation line. Away from the leading edge, the flow at the line is pushed toward the leading edge (the flow does not move along the separation line continuously because the absolute velocity field is unsteady). This creates a point on the separation line where flow is instantaneously pushed inwards from all directions. This instantaneous 'three-dimensional separation point' is marked with a yellow circle in Diagram 5.1.

To investigate the behaviour of the three-dimensional separation point, the experimental flow visualisation results from Section 5.4.1 were compared with constant radius cuts at $5\%tc$ taken from the smooth-wall computational model at three flow coefficients: $\phi=0.58$ (near the design point), $\phi=0.52$ and $\phi=0.48$ (near stall). These cuts were then processed to show the absolute and relative flow fields. The results are presented in Figure 5.12. The absolute velocity field is shown using arrows (for direction) and contours (for magnitude) in the plots at the centre of the figure. The relative velocity field is shown using streamlines

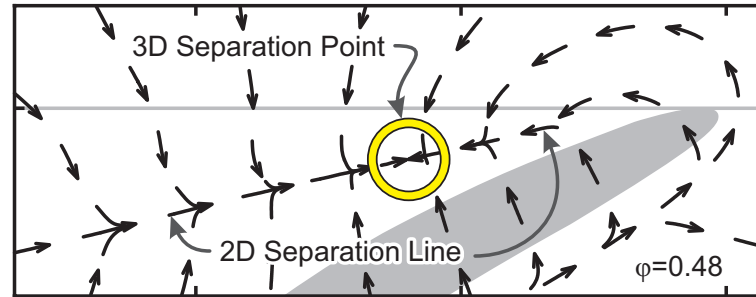


Diagram 5.1: Flow schematic showing the separation line and separation point.

and contours at the right of the figure. The computational results have not been time-averaged as they were previously.

The absolute velocity plots in the centre of Figure 5.12 show that the separation line moves forward as the flow coefficient reduces. This occurs because the inflow momentum decreases (due to the decreasing flow coefficient) and the leakage flow momentum increases (due to the increasing blade loading). The three-dimensional separation point also moves forward as the flow reduces for two reasons; firstly, it is on the separation line, which is itself moving forward, and secondly, it moves up the separation line toward the leading edge of the blade. At all three operating points, the axial location of the three-dimensional separation point matches the location of the black line (and thus the location of the convergence line from Section 5.4.1). The black line therefore appears to be caused by the separation point as it moves around the compressor wall with the rotor blades. This indicates that the axial location of the separation point, the black line and the convergence line are all set by a balance of axial momentum between the inflow and the tip leakage flow. The separation point is located on the separation line at the axial location where this balance occurs.

The agreement between the axial location of the black line and the separation point is compelling. However, as observed in Section 5.4.1, flow separating from a wall should not remove visualisation oil, yet the black line is caused by oil removal. An explanation for this contradiction can be found by considering the visualisation patterns near the black line.

Figure 5.8 shows that there is a region of increased oil deposition just upstream of the black line. This is consistent with flow moving against the rotor motion, thereby reducing the absolute velocity of the near-casing flow and encouraging the build-up of oil. At the black line itself, the oil is scoured away. This is consistent with flow moving with the rotor motion, thereby increasing the absolute velocity of the near-casing flow and scouring oil away. The black line also has very well-defined edges. These observations are consistent with the flow near the separation point having vorticity, with the rotational axis pointing radially outward in right-handed coordinates (as indicated by the dotted lines in Figure 5.8). The CFD model

shows that the vorticity of the flow in the vicinity of the separation point has this sense. It is therefore possible that this vorticity causes the three-dimensional separation to 'hoover' the visualisation oil off the casing, forming the black line.

The presence of vorticity does not mean a vortex actually forms and the computational model does not predict one forming here. It is, however, possible that this apparent vorticity could be linked to observations of vortices shedding from the separation line (near the separation point seen in this work) by März *et al.* (2002) and Inoue *et al.* (2004). It is also interesting to note that the pre-stall spikes measured in Section 5.2 appear to contain vorticity with this sense as well. Work by S. Popp on the link between the black line, tip leakage vortex instability and stall inception is presently underway at the Whittle Lab.

The relative flow field is also shown in Figure 5.12 (with the yellow circle from the central plots superimposed). The large tangential velocity components obscure a lot of detail, but pseudo streamlines can be drawn because the flow field is steady and radial velocities are small (see above). Two particular streamlines have been highlighted in blue. These go around the whole annulus in a continuous loop, dividing the inflow, reversed flow (over the rotor) and outflow. Although the upstream dividing streamline approaches the separation point at stall, their locations are different, so the black line does not indicate a physical dividing line between inflow and axially reversed flow as suggested by Deppe *et al.* (2005).

The effect that grooves have on these near-casing flow structures is explored later. First, the impact of grooves on near-casing flow variables is analysed, starting with static pressure.

5.4.4 The Effect of Grooves on Casing Static Pressure

The casing static pressure field is caused by the blade-to-blade and tip leakage flow static pressure fields. These two pressure fields are linked to the blade tip loading, so the effect of the groove on the casing static pressure field should be linked to its effect on blade loading. In Section 5.3 it was found that the effect of the groove on blade tip loading decreased as the groove moved from location A to C. The effect of the groove on the casing static pressure should therefore also decrease as the groove is moved from location A to C. To confirm this and explain the changes in blade loading, the effect of the groove on the casing static pressure was investigated using both experimental and computational methods.

The casing static pressure was extracted from the near-stall CFD solutions for cases A, B and C. The smooth-wall data were then subtracted from the equivalent grooved-wall data. This generates a 'difference plot' showing the effect that the addition of the groove has on the casing static pressure (see Figure 5.7 for a pictorial explanation). In the experiments,

four fast-response pressure transducers were installed flush with the casing downstream of the groove. No more than four transducers could be installed due to spatial constraints. The static pressure was then measured as described in Chapter 3 and a difference plot was made in the same manner as the CFD results. The static pressure difference plots are shown in Figure 5.13. While the CFD results cover the whole flow (right), the four pressure transducers provide a band of data (left).

In case A, the groove causes large changes in the casing static pressure field. Near the groove entrance, the pressure near the blade pressure surface is reduced at '1', while near the suction surface it is increased at '2'. This causes the reduction in blade loading seen in Figure 5.6. The red stripe leading away from the blade leading edge near '2' indicates that the low-pressure core of the tip leakage vortex (shown in Figure 5.11) has been removed from this area. The blue region at '3' suggests that the tip leakage vortex grows rapidly near the downstream corner of the groove, reducing the pressure near the blade suction surface and increasing blade loading. The early growth of the tip leakage vortex therefore appears to be limited by the groove, so when the vortex does grow it is closer to the suction surface (as seen in the hotwire traverses in Section 5.3). The same effects are seen at location B, but the changes are all smaller (again agreeing with the hotwire results). At location C, the groove has almost no effect. Experimental and computational results agree in all cases.

The results in this section agree with the blade loading study. They show that as the groove is moved aft from location A, the impact it has on the static pressure of the near-casing flow reduces. By location C, the groove has almost no effect. The stall margin trend in Figure 5.2 is therefore not explained by the effect the groove has on the casing static pressure field. The good agreement between experimental and computational results is reassuring from a validation perspective.

5.4.5 The Effect of Grooves on Near-Casing Flow Total Pressure

The impact of the groove on the blade and casing static pressure fields does not explain the stall margin trend in Figure 5.2. This section includes dynamic pressure (or momentum) in the analysis by investigating the relative total pressure. The relative total pressure is difficult to measure accurately on a compressor with a sub-millimetre tip clearance and a treated casing, so data was extracted from the near-stall CFD solutions. Constant radius cuts were taken at two locations; near the casing at $5\% tc$ and near mid-clearance at $50\% tc$. Difference plots were then made using the method described in the previous section. The cuts were taken at these locations because the cut at $50\% tc$ is near the lower edge of the vena contracta and the cut at $5\% tc$ is near the casing wall-bounded shear layer. The effect

of the groove on the two main flow features in the tip clearance can thus be revealed in two sets of plots. The plots are shown in Figure 5.14 for cases A, B and C.

At 50% tc (at right), the impact of the groove on the relative total pressure follows a similar trend to that seen in previous sections. As the groove is moved from location A to C, the effect of the groove diminishes so that by location C it has little effect. At 5% tc (at left) however, the impact of the groove decreases from location A to B and then *increases* from B to C. The effect of the groove on the relative total pressure is therefore quite different at mid-clearance (50% tc) and near the casing (5% tc). The groove at location A also affects the flow much further away from the casing it does at location C. More importantly, this is the first sign of the groove at location C altering the flow field at all.

These results show that the velocity of the near-casing flow at 5% tc is most important for explaining the performance of casing grooves. The next step is to study the impact of the groove on the near-casing flow velocity in order to investigate the phenomena behind these interesting results.

5.4.6 Effect of Grooves on Near-Casing Flow Velocity

A review of previous work (see Section 2) suggested that stability could be improved by decreasing the cross-flow and increasing the through-flow components of the tip clearance flow. This implies that positive increases in the axial and tangential components of the near-casing flow velocity should improve stability. To investigate this, data was taken from the near stall computational model for cases A, B and C (because measuring the near-casing flow velocity experimentally is difficult). Constant radius cuts were taken at 5% tc and difference plots of axial, radial and tangential velocity were made as before. They are shown in Figure 5.15.

In case A, the axial velocity plot (at left) shows that the groove increases the axial velocity of the near-casing flow at '1', where the tip leakage flow meets the inflow in the smooth walled rotor. This implies that the groove interferes with the axially reversed tip leakage flow, moving the separation line and tip leakage vortex toward the suction surface (which agrees with the casing static pressure results). The radial velocity plot (at centre) shows the flow moving into the groove near the blade pressure surface at '2', before emerging near the suction surface at '3'. Comparing this with the static pressure plot (Figure 5.13) shows that the flow entering the groove reduces the pressure on the pressure surface, while the flow moving out of the groove increases the pressure on the suction surface. The changes in blade loading are thus partly caused by flow moving in and out of the groove. These

changes in axial and radial velocities continually diminish as the groove is moved aft from location A to C. The groove has little effect on the axial and radial velocities at C.

The trend in tangential velocity (at right) is different. The effect of the groove decreases from case A to B, before increasing again to case C (red areas in the figure mean flow pushed left to right). The greatest changes occur right next to the blade. By comparing Figure 5.14 and Figure 5.15, it is clear that the tangential velocity changes are principally responsible for the changes in relative total pressure at 5% tc . This increase in tangential velocity very close to the casing is caused by the fact that there is no casing where the groove is located, so the shear forces normally caused by the casing wall are absent. These forces normally retard the flow being forced across the blade passage by the cross-passage pressure gradient (in the absolute frame), so their absence increases the tangential velocity near the groove. This is the principal effect that the groove at location C (and at all locations aft to the trailing edge) has on the near casing flow field near stall.

In summary, the groove at location A alters the pressure and all velocity components of the near-casing flow. The magnitude of these changes decrease as the groove moves to location B. From location B to C, the impact of the groove on the static pressure and axial and radial velocities continues to decrease, but the impact on tangential velocity increases toward C and is sustained to the trailing edge. The link between this behaviour and stall inception is not yet understood. As found in the literature, these results suggest that decreasing the cross-flow and increasing the through-flow components of the tip clearance flow improves stability.

The effect of the groove on the properties of the near-casing flow has been linked to the stall margin improvement generated by the groove. The next section will consider the impact of this behaviour on the structure of the near-casing flow.

5.4.7 Changes to Near-Casing Flow Structures Caused by Grooves

The difference plots showed that the most important region to consider when explaining the performance of casing grooves is the region close to the casing wall. This section considers the effect of the groove on the detailed structure of the near-casing flow (introduced earlier). As previously, experimental oil-flow visualisation and cuts through the computational model at 5% tc are used. Data was gathered near the smooth-wall stall point with the groove installed at locations A, B and C. The results are shown in Figure 5.16. The left-hand plots show the experimental visualisation overlaid with time-mean absolute velocity direction arrows from the CFD. The central and right-hand plots show the absolute and relative

flow fields using the techniques explained in Section 5.4.3. The yellow circle shows the location of the separation point in the smooth wall case, and the colour bars match Figure 5.12 with added range for clarity.

In case A, the leading edge of the groove is at the same location as the black line in the smooth-wall case. The black line is not visible in the experimental visualisation and the computational results do not show a separation point forming on the casing wall. The absolute velocity plot shows that the groove stops the separation line from forming upstream of $25\% c_{x,r}$ by preventing the near-casing tip leakage flow from moving out into the blade passage. When the separation line appears and tip leakage vortex starts to grow (at '1'), they remain closer to the suction surface, as seen in the hotwire traverses in Section 5.3. The absolute velocity plot also shows flow being pushed along the separation line into a swirling flow structure near the groove. This appears to be the three-dimensional separation, which has been swallowed by the groove and moved closer to the blade suction surface by the increased tangential velocity. The relative velocity plot shows that the groove traps the upstream dividing streamline, and thus divides the inflow and the axially reversed flow over the rotor.

In case B, the groove is too far away from the leading edge of the blade to affect the separation line (and tip leakage vortex) formation, which occurs near the leading edge as normal (at '2'). The separation point forms on the separation line, and its location again matches the black line on the experimental visualisation, which is a little downstream of its smooth wall position. The groove only interferes with the separation line and tip leakage vortex while they are in its vicinity, so both features move slightly closer to the suction surface. The effect is much smaller than seen in case A, which agrees with the hotwire traverses and difference plots. In the relative velocity plots, the groove traps the upstream dividing streamline as it did in case A, moving it downstream.

In case C, the groove has no effect on the flow structures upstream of $30\% c_{x,r}$, so the separation line, separation point and tip leakage vortex are all largely unaffected by it. The separation point is again aligned with the black line on the experimental visualisation, which is in the same location as it was in the smooth wall case. By the time the tip leakage vortex reaches the groove, it is a large structure that extends some distance away from the casing, so although the groove increases the tangential velocity of the near-casing flow, this does not alter the tip leakage vortex. This agrees with the hotwire traverse results. In the relative velocity plots, the upstream dividing streamline is also unaffected by the groove. The effect of the groove on the flow is therefore small.

These results show that the different interactions between the groove and the near-casing flow occur because the flow near the groove is very different in each case. In case A,

the groove inhibits the formation of the tip leakage vortex both upstream of the groove and in its immediate vicinity. As a result, the tip leakage vortex is moved downstream and remains closer to the blade suction surface. The groove also swallows the three-dimensional separation point, removing the black line as a result, and traps the upstream dividing streamline. In case B, the groove does not affect the tip leakage vortex formation or the black line, but it does move the vortex toward the blade suction surface and traps the dividing streamline. In case C, the groove has little effect on the formation and growth of the tip leakage vortex upstream of $30\% c_{x,r}$. It merely increases the tangential velocity of the near-casing flow in its immediate vicinity.

Having investigated the impact of the groove on the near-casing flow field with respect to stall margin improvement, the next section considers entropy in order to explain the trend in efficiency as the groove is moved.

5.4.8 Entropy Generation by Casing Grooves

This section considers the effect of the groove on efficiency. Figure 5.2 shows that the efficiency reduction caused by the groove reduces as it is moved aft. According to Denton (1993), the only rational measure of loss in an adiabatic machine is entropy creation, so this section investigates the entropy generated by the groove. The smooth-wall case is compared with grooved cases A and D (defined in Section 5.1), which span the trend in efficiency improvement in Figure 5.2. Eight meridional cuts are taken through the blade row to show the increase in entropy relative to the inflow at mid-span. The cuts also provide a flow visualisation, since entropy moves with the flow in a similar manner to smoke (Denton, 1993). The cuts are shown in Figure 5.17.

In case A, the groove is positioned over the most vigorous region of the tip clearance flow. The near-casing flow velocity is high and it is not directed along the groove. Entropy is therefore generated by corner separations and radial mixing as the axially reversed tip leakage flow is forced deep into the groove by the vigorous tip clearance flow (cuts 2 to 5). This vigorous interaction causes the flow to penetrate 80% of the groove's depth, but because flow enters the groove instead of flowing over the tip clearance, the loss associated with the tip clearance vortex decreases slightly. As the blade moves away (cuts 5 to 8), high-entropy flow is drawn back out of the groove into the blade passage, where it rolls up with the tip leakage vortex. This increases the entropy contained in the tip leakage vortex compared to the smooth-wall case. Therefore, the groove increases entropy appreciably.

The groove at location D generates little additional entropy compared with the smooth wall case. The tip leakage flow and associated vortex develop similarly in the smooth

and grooved wall cases because the groove is downstream of the areas where the vortex forms and grows most (see previous section). Therefore, the main regions of loss associated with the vortex are fully developed before the groove is reached. Since the groove only affects the near-casing flow, it has little effect on the preformed tip leakage vortex and its associated loss. The groove at location D does not create much additional entropy through corner separations because the near-casing flow is well aligned with the groove and moving relatively slowly. Radial mixing losses are also low because radial velocities are low and the flow only penetrates 50% of the depth of the groove.

These results show that the principle sources of loss caused by the groove are radial mixing and corner separations. As the groove moves toward the trailing edge, the tip leakage flow becomes less vigorous and more aligned with the groove (reducing corner separations), the penetration of flow into the groove decreases (reducing mixing loss) and the groove becomes less able to interfere with the tip leakage vortex (and cannot change the main source of loss). Therefore, entropy gains (and efficiency losses) reduce when the groove is moved from the leading edge to mid-chord.

5.5 Discussion

Casing grooves interact differently with the compressor flow field over the fore and aft regions of the rotor blades. These different interactions cause two locations where the groove generates a maximum stall margin improvement: when its leading edge is near $8\% c_{x,r}$ and $50\% c_{x,r}$.

At $8\% c_{x,r}$, the groove interacts strongly with the flow field because it is located adjacent to the most vigorous part of the tip leakage flow. Radial flow in and out of the groove reduces the blade loading near the groove. The axial and tangential velocities of the near-casing flow are changed so as to prevent tip leakage flow near the casing from moving into the blade passage either upstream of, or adjacent to, the groove. This limits the development of the separation line and tip clearance vortex. The three-dimensional separation point is swallowed by the groove and the black line does not form in the experimental visualisation. The separation line and tip leakage vortex only grow downstream of the groove, and the latter's low-pressure core increases the blade loading in this region. In this way, the blade loading and the tip leakage vortex are both moved aft by the groove. Since the vortex is moved aft, it remains closer to the blade suction surface with a groove installed. This strong interaction between the groove and the rotor flow field means that the groove affects the flow away from the casing and the flow penetrates the groove deeply. The entropy rises associated with this strong interaction cause efficiency to reduce.

At 50% $c_{x,r}$, the groove interacts more subtly with the flow field, increasing the tangential velocity of the near-casing flow in the direction of the blade motion. This occurs by shear transport (due to the lack of radial mixing) and only affects the flow very close to the casing. This weak interaction means that flow does not penetrate the groove deeply and the entropy rises (and thus efficiency losses) are small. The formation, growth and trajectory of the tip leakage vortex upstream of 30% $c_{x,r}$ are not affected by the groove, so manipulation of the tip leakage vortex is *not* a panacea for stability improvement.

These results show that the importance of the groove location relative to near-casing flow structures cannot be ignored during design. Analytical methods that do are likely to be over-simplified and lead to poor designs. If careful attention is paid to the location of the groove with respect to the near casing flow structures, it is possible to design grooved treatments that generate a useful stall margin improvement without reducing efficiency (even in where there is no large region of blockage that the grooves can remove).

The study of the near-casing flow field suggests that the black line on an experimental flow visualisation is caused by a three-dimensional separation point that occurs at the boundary between the inflow and the tip leakage flow. The location of this separation point is set by an axial momentum balance. The black line does not appear to be a simple dividing line between the inflow and axially reversed flow, nor does it directly indicate the trajectory of the tip leakage vortex. The fact that the black line is close to the leading edge at stall does not (of itself) indicate that the tip leakage vortex is near the blade leading edge plane at stall as suggested by Saathoff *et al.* (2003). Indeed, the present results show that the tip leakage vortex is *not* close to the leading edge at stall, agreeing with Yoon *et al.* (2006).

It is useful to compare these results with the literature that was reviewed in Chapter 2. Shabbir and Adamczyk (2005) concluded that stall margin improvement by grooves is due to the radial transport of axial momentum, which augments the wall shear stress and allows the rotor to operate stably with a greater static pressure rise over the tip clearance. This mechanism makes sense for the groove at 8% $c_{x,r}$, which facilitates radial transport of axial momentum and increases the axial momentum of the near-casing flow. However, this mechanism cannot apply to the groove at 50% $c_{x,r}$ because here only the tangential velocity is altered by the groove, and this cannot generate a pressure rise in the axial direction. In order to investigate why it is possible for stability to be improved by increasing the tangential velocity of the near-casing flow in this region, the static-to-static rotor only characteristics with a smooth wall and a groove at 50% $c_{x,r}$ were measured using static pressure tappings up and downstream of the rotor blades. The results are plotted in Figure 5.18. For the near-casing flow, the static-to-static characteristic is the same as the total-to-static because the inflow velocity is small.

The figure shows that the rotor static pressure rise does not increase near stall but actually 'rolls over'. Since the characteristics overlie, this roll over causes the static pressure rise over the rotor tip clearance to be lower in the grooved wall than the smooth wall case. It is thus not necessary to increase the static pressure rise over the rotor tip clearance to increase stall margin. This observation could affect casing groove design. If the rotor-only static-to-static characteristic of the rotor in question has a zero or positive gradient at stall (as in this case), the best location for the groove is around $50\% c_{x,r}$, where the stall margin and efficiency improvement are optimal. However, if the static-to-static characteristic of the rotor has a negative gradient near stall, a groove at $50\% c_{x,r}$ may not work because it cannot generate additional pressure rise. In this case, grooves would have to be located near $8\% c_{x,r}$, where they can increase the pressure rise through Shabbir's mechanism. In this way, Shabbir's conclusion that the best groove location is near the leading edge could be explained.

In other published work, Bailey (1972) found that the best location for a casing treatment with three grooves is near mid-chord. Three grooves would fit on the broad maximum stall margin at mid-chord found in the present work. The present results show that casing grooves only have a small effect on the flow field near mid-chord, so it is probable that the effect of the grooves would add together in this region, leading to good performance. A three-groove treatment would not fit on the narrow maximum stall margin near the leading edge found in this work however. This could explain why multiple grooves were not effective in this region. Prince *et al.* (1974) found that casing grooves moved blade loading aft, and all the designs tested by Prince *et al.* had grooves located near the leading edge. The present results show that grooves located near the leading edge do indeed move blade loading aft, while grooves further aft do not affect blade loading.

These comparisons show that the small stall margin improvement relative to efficiency reduction often caused by multiple-groove treatments may be due to some grooves being poorly located. The present results suggest that each groove in a multiple-groove treatment should be individually placed, not simply equi-spaced over the rotor tip. This will be investigated further in Chapter 6.

High and low-speed subsonic rotors have similar tip clearance flow structures and stall inception mechanisms, so these results are expected to be applicable to high-speed subsonic rotors. Further work is needed to assess their applicability to transonic rotors.

5.6 Grooved Casing Treatment Design using CFD

Until the fundamental stall inception processes are fully understood, it will not be easy to explain how casing treatments work. This chapter has therefore focussed on understanding the effect that casing treatments have on the rotor flow field to help designers apply the parametric study results to different compressors. However, this detailed analysis is difficult. It would be much easier if the stall margin improvement generated by the casing treatment could be directly predicted by CFD. This section investigates one method of attempting to do this.

To this end, CFD calculations were used to find the stable solution with the highest back-pressure for a number of cases from the experimental study. The method used to achieve this is discussed in Chapter 4. Once stable solutions with the greatest back-pressure had been obtained, the stall margin improvement was calculated. The experimental and computational results are plotted in Figure 5.19.

Although the CFD predicts two local stall margin maxima, the positional accuracy is poor. Worse, the CFD predicts a maximum stall margin improvement at a groove location where the experimental results show a minimum. Using CFD-derived stall margin results to design a casing treatment would, therefore, result in the groove being placed in the worst possible location. The values of stall margin improvement are also inaccurate. Using multi-passage calculations did not improve these results.

The CFD model used in this work is of a higher standard than would currently be used for design (in terms of mesh density, boundary condition accuracy and validation against experimental results). The CFD accurately predicts the flow field near the casing, where stall inception occurs. However, these results show that the CFD cannot predict the stall point accurately, as found by Hah *et al.* (1999). The non-linear, stochastic physics of stall inception are not captured by steady RANS calculations and these should not be trusted to predict the stall margin generated by grooved casing treatments accurately.

5.7 Conclusions

It is concluded that:

1. Experiments show there are two locations over the rotor tips where a single circumferential groove generates a maximum stall margin improvement. The first location is near the leading edge (at 8% chord) and the second is at 50% chord. By contrast, stall margin improvement is minimised at three locations: at the blade leading and trailing edges and at 18% chord.
2. When the groove is near the first stall margin maximum (8% chord) it interacts strongly with the highly energetic near-casing flow field, changing the tip leakage flow, tip leakage vortex development and blade loading. These complex interactions cause considerable losses due to separations and radial mixing, and this reduces the efficiency of the compressor. The leading edge of the groove at 8% chord is aligned with the near-stall location of the 'black line' in a smooth walled experimental flow visualisation (see below).
3. When the groove is near the second stall margin maximum (50% chord) it interacts weakly with the near-casing flow field, merely increasing the tangential velocity of the flow adjacent to the groove. This interaction occurs through viscous shear, causes minimal loss, and therefore does not reduce the efficiency of the compressor. The groove near 50% chord therefore generates a good stability improvement with minimal efficiency loss.
4. Some apparent contradictions in the literature regarding optimum groove location can now be explained as a result of finding two locations where stall margin is maximized.
5. Grooves installed near 8% and 50% chord generate similar stall margin improvements, but only the groove at 8% chord changes the early growth and trajectory of the tip leakage vortex. The fact that the stall margin is improved by the groove at 50% chord shows that altering the tip leakage vortex is not a necessary requirement for stall margin improvement.
6. There is no clear link between outflow blockage or blade loading and stall margin improvement.
7. The 'black line' that forms in a flow visualisation on the casing of the Natal compressor is caused by a three-dimensional separation point that occurs on the separation line between the incoming and tip leakage flows. The black line is not caused by some average of the dividing line between the inflow and the axially reversed flow over the rotor blade.

8. Steady-state RANS computational models should not be trusted to accurately predict the stall margin improvement generated by casing grooves. When designing a compressor with casing grooves, it is more informative to analyze the impact of grooves on the near-casing flow field.
9. The impact that casing grooves have on compressor stability is due to effects local to the rotor tip region and is not affected by the presence of stator vanes. In the Natal compressor, the stator vanes have little effect on the rotor only total-to-static characteristic.
10. The stall inception pattern in the Natal compressor (spike-type) is not affected by the presence of casing grooves, even when the groove alters the development of the tip leakage vortex.

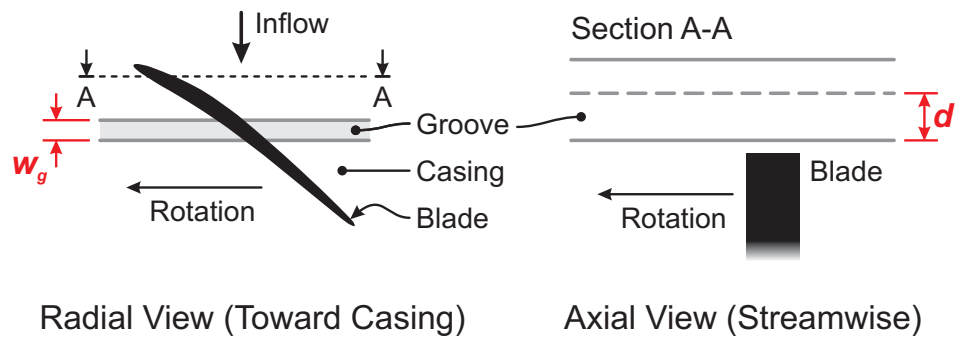


Figure 5.1: A schematic showing the geometry of the circumferentially continuous groove-based casing treatment, with dimensions.

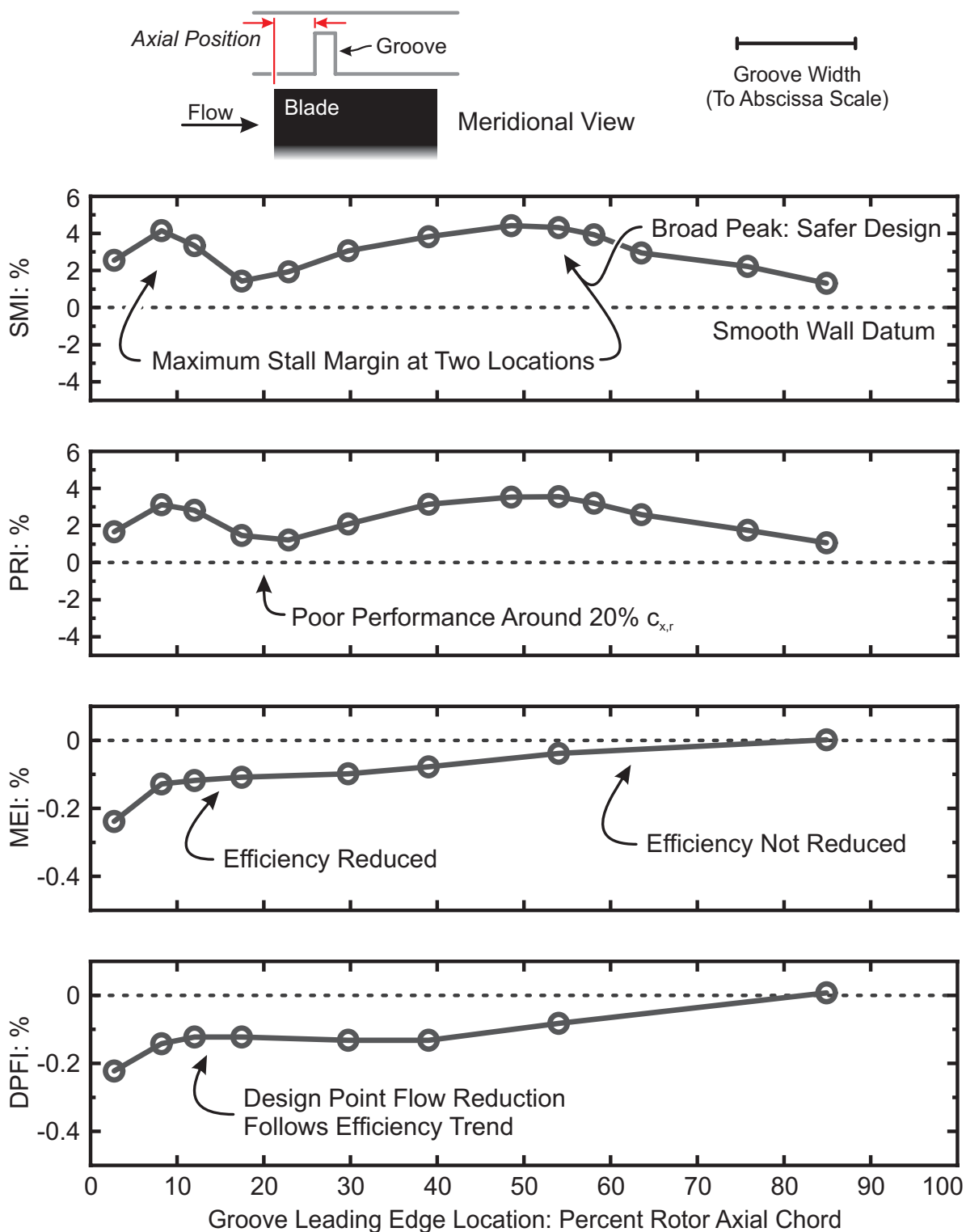


Figure 5.2: The effect of altering the axial location of a single circumferentially continuous casing groove on stall margin improvement (SMI), pressure rise improvement (PRI), maximum efficiency improvement (MEI) and design point flow increase (DPFI).

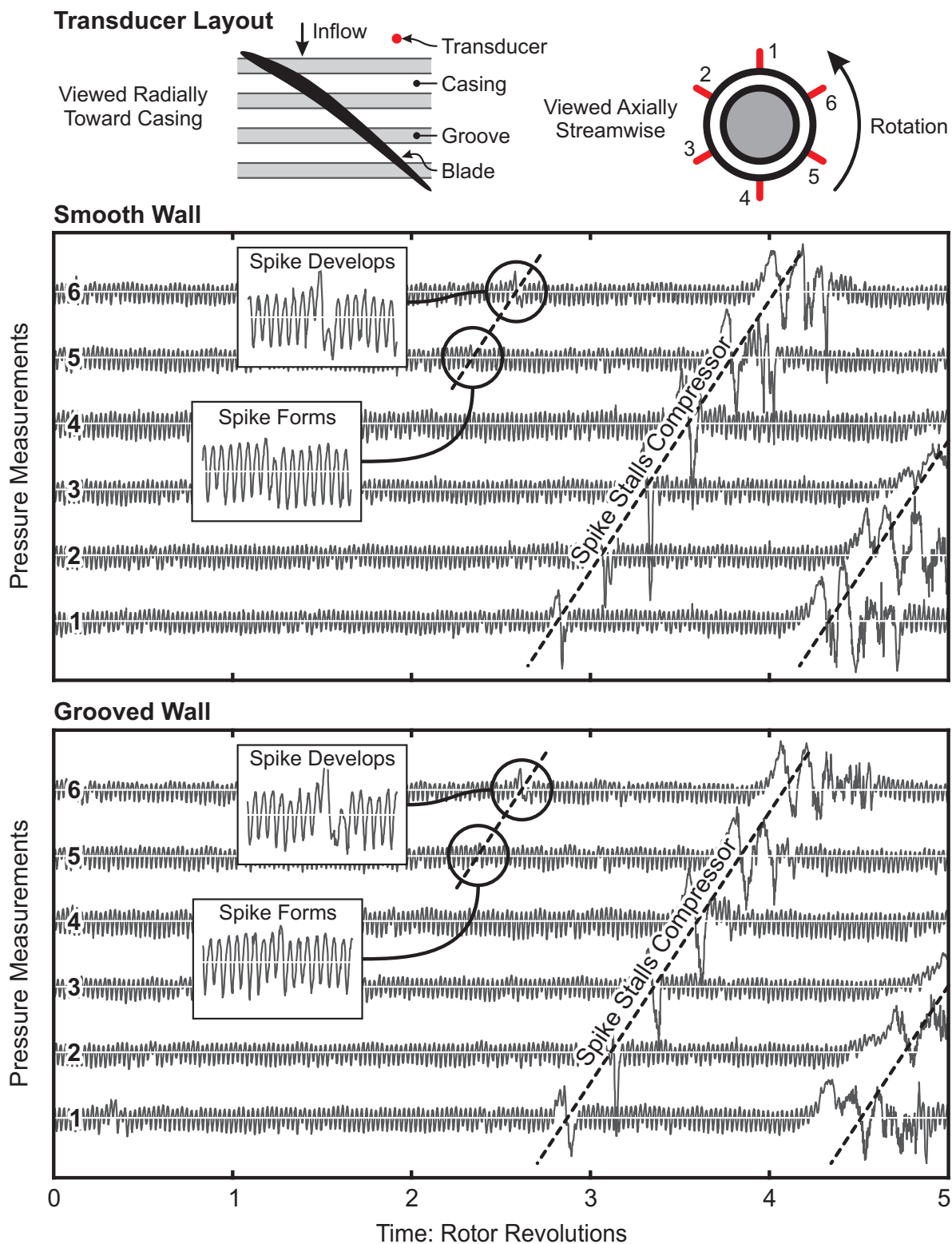


Figure 5.3: The effect of adding casing grooves on the stall inception behaviour of the Natal compressor, showing Kulite pressure measurements at six circumferential locations just upstream of the rotor blade tips during stall inception.

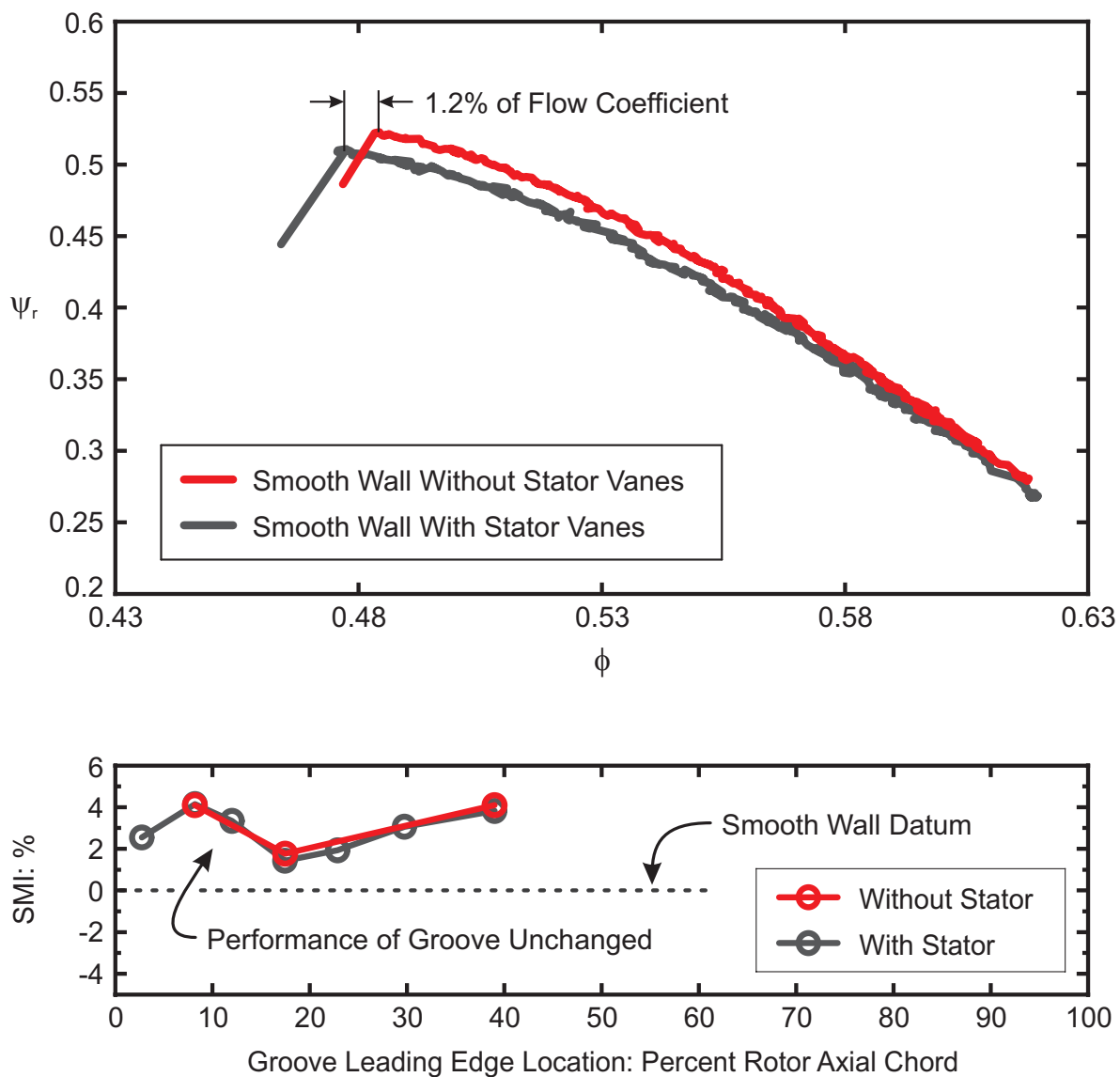


Figure 5.4: The effect of removing the stator vanes. The upper graph shows the rotor-only characteristics with and without stator vanes installed. The lower graph shows the stall margin improvement generated by the groove with and without stator vanes.

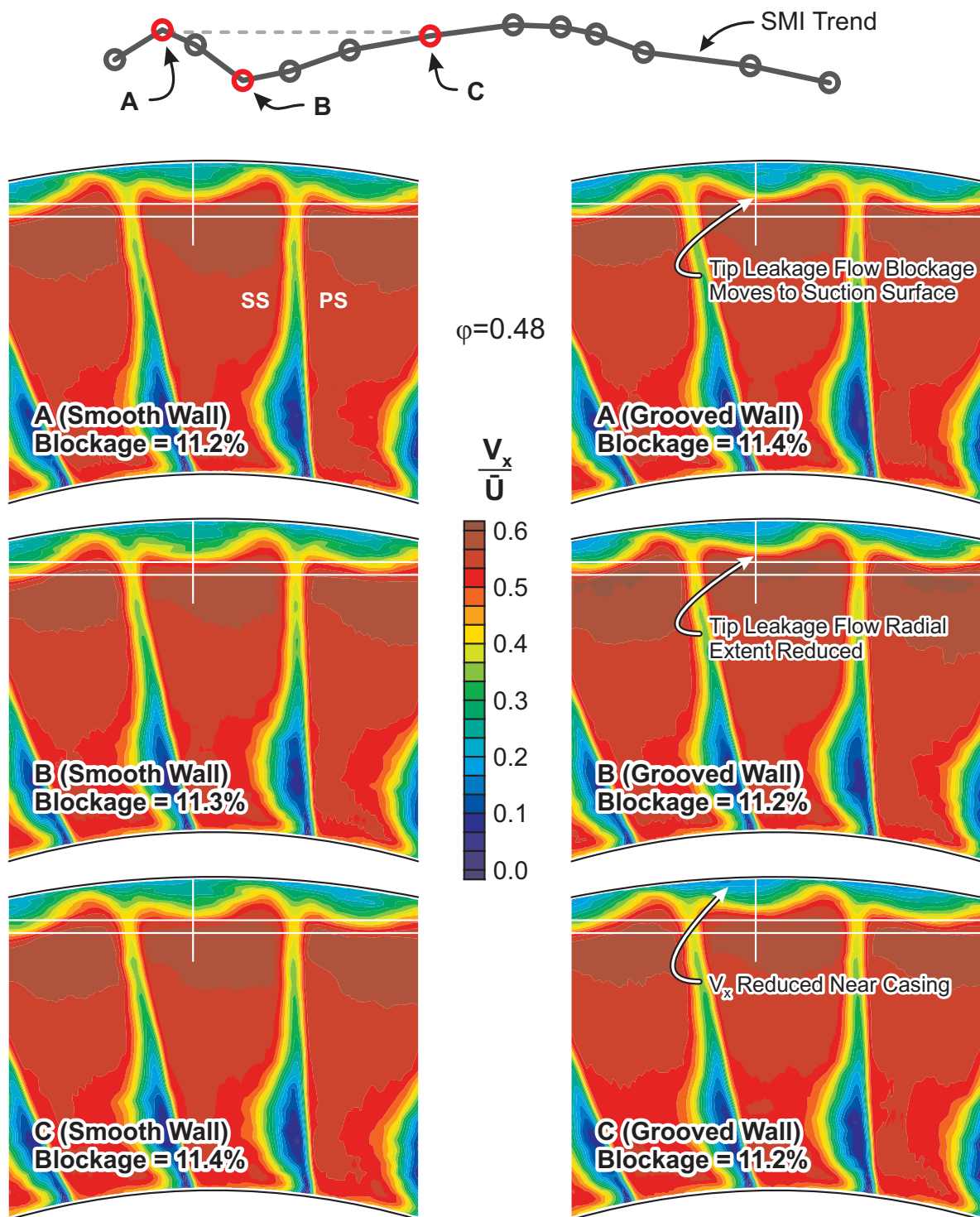


Figure 5.5: The effect of adding the casing groove on the rotor outflow blockage with the groove in three different locations (A, B and C). The plots show contours of axial velocity measured using hotwire traverses immediately downstream of the rotor trailing edge (regions of low axial velocity are considered blockage).

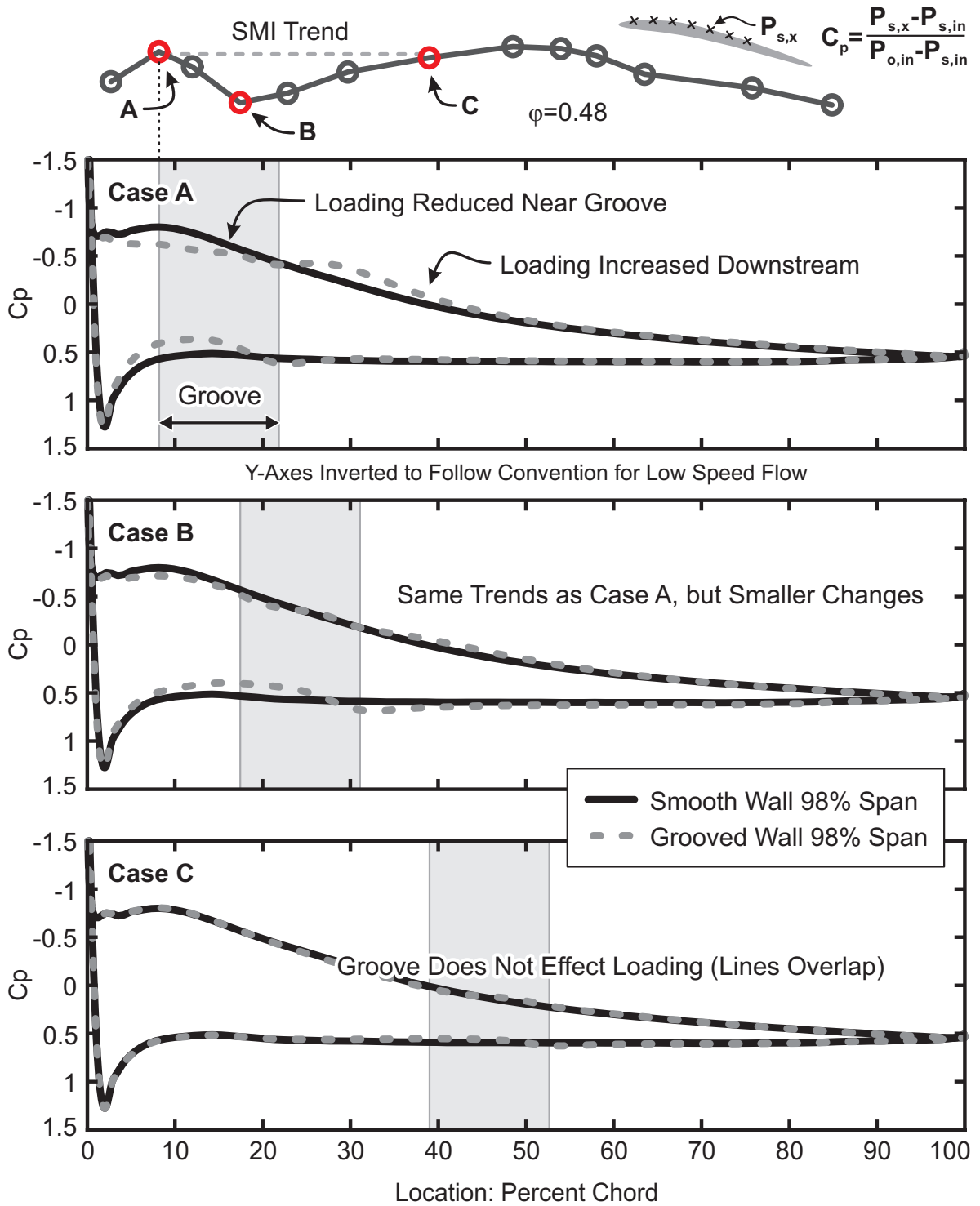


Figure 5.6: The effect of adding the groove on the blade tip loading with the groove in three different locations (A, B and C). The plots show normalised surface pressure distributions from CFD solutions of the smooth and grooved walls at 98% span. The y-axes are inverted to follow convention for low speed flows.

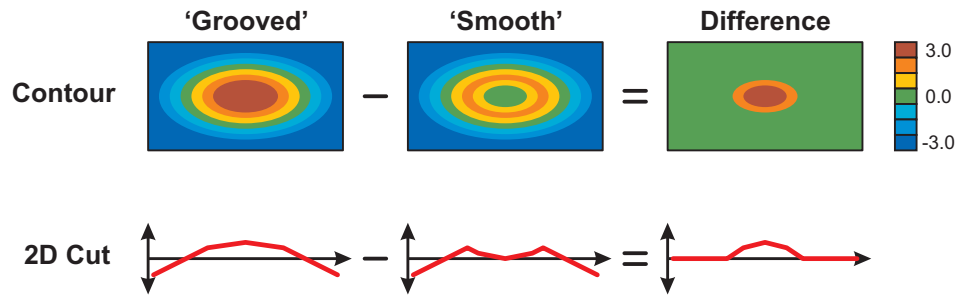


Figure 5.7: An example of creating a difference plot, using two arbitrary contour maps representing the grooved and smooth wall cases. A 2D cut through the contour data is also shown, to aid interpretation.

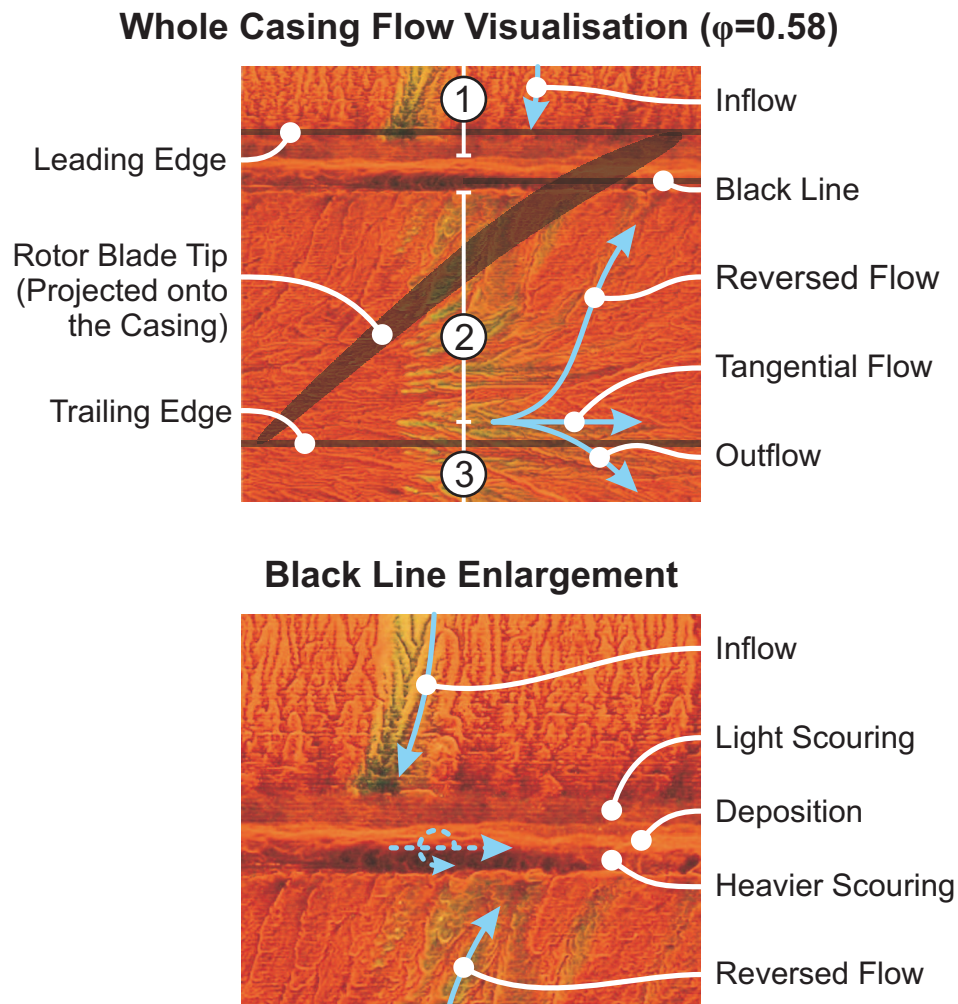


Figure 5.8: Two labelled views of an oil-flow visualisation performed on the casing wall of the Natal compressor when operating near the design point. The view shown is radially inwards through the casing.

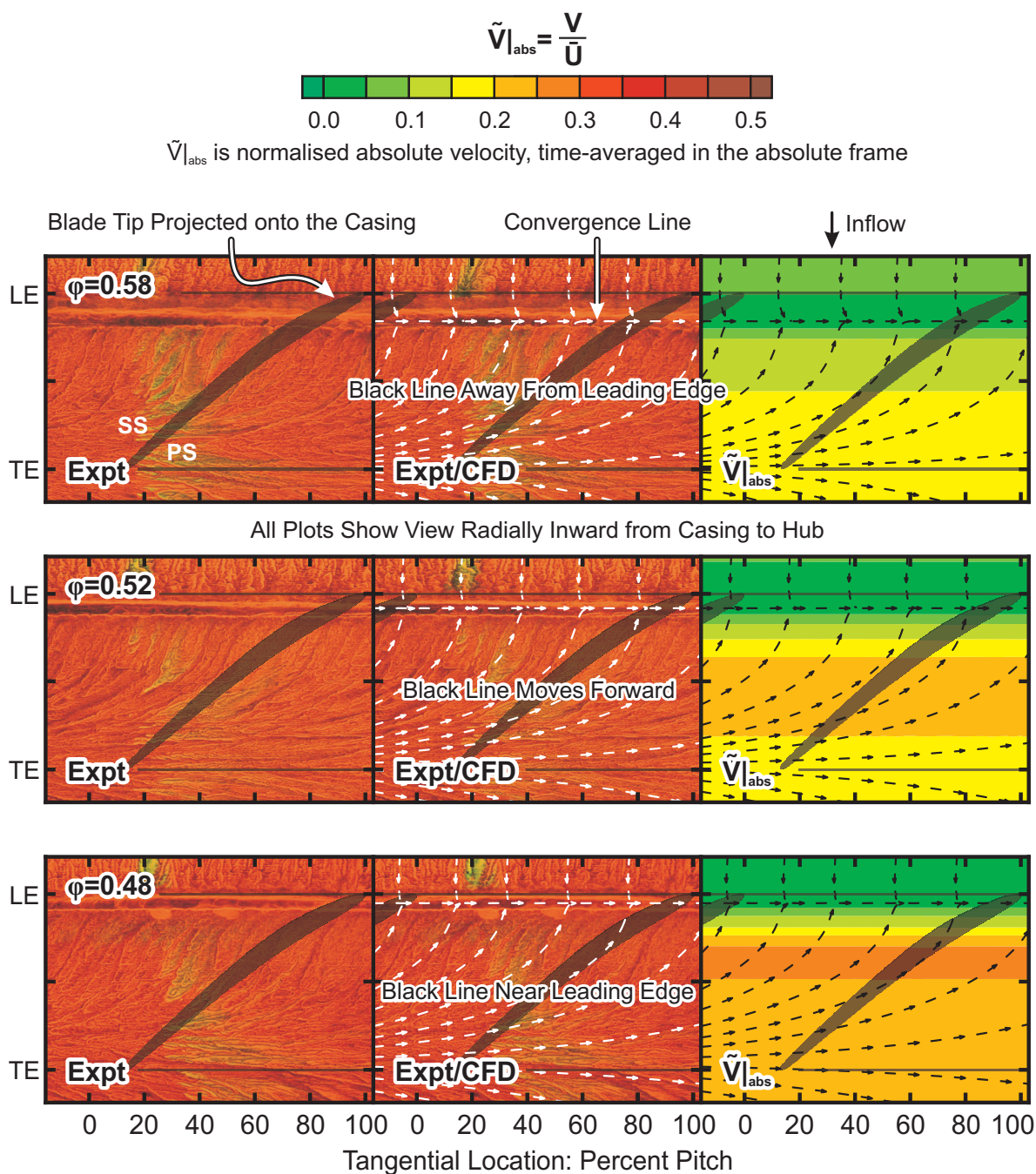


Figure 5.9: The black line (shown using experimental flow visualisation) and the convergence line (shown using constant radius cuts taken from the CFD model at $5\%tc$). The left-hand plots show the experimental flow visualisation. The right-hand plots show the normalised absolute velocity field from the CFD model (which has been time-averaged in the absolute frame) using arrows (for direction) and contours (for magnitude). The plots in the centre show the arrows from the CFD model overlaid on the experimental flow visualisation to aid comparison between CFD and experiment. Data is shown for three flow coefficients from the design point ($\phi=0.58$) to stall ($\phi=0.48$).

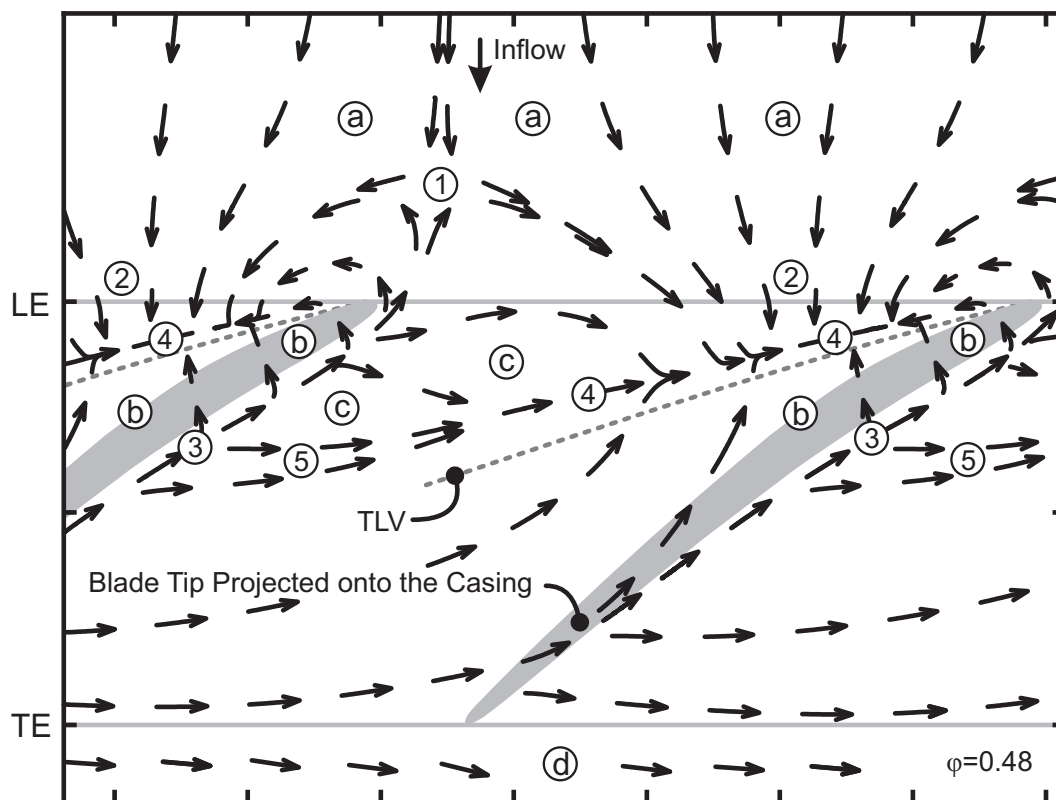


Figure 5.10: The pattern of near-casing flow shown in the absolute frame, shown using a cut taken at $5\% tc$ from the computational model, of the flow near the smooth wall stall point. Arrows (showing flow direction) are used because the absolute flow field is unsteady. The dotted line marked 'TLV' shows the path of the core of the tip clearance vortex. The view is radially inward, from casing to hub.

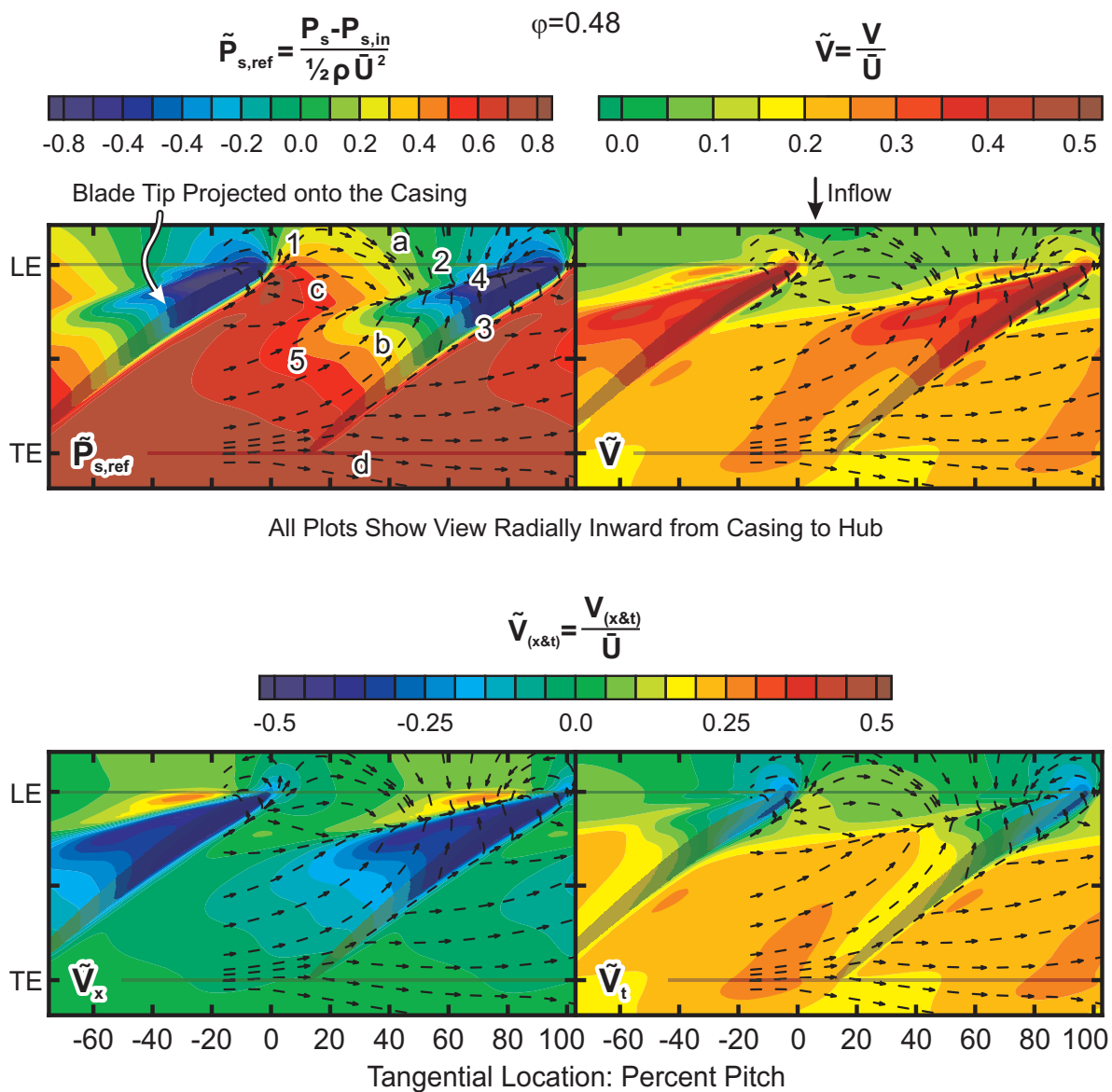


Figure 5.11: Near-casing flow in the Natal compressor rotor with a smooth wall installed. Contours of referenced static pressure and normalised absolute flow velocity, axial velocity and absolute tangential velocity at 5% tc are shown near stall ($\phi=0.48$). The right-hand blade in each plot is overlaid with arrows showing the instantaneous direction of the absolute velocity.

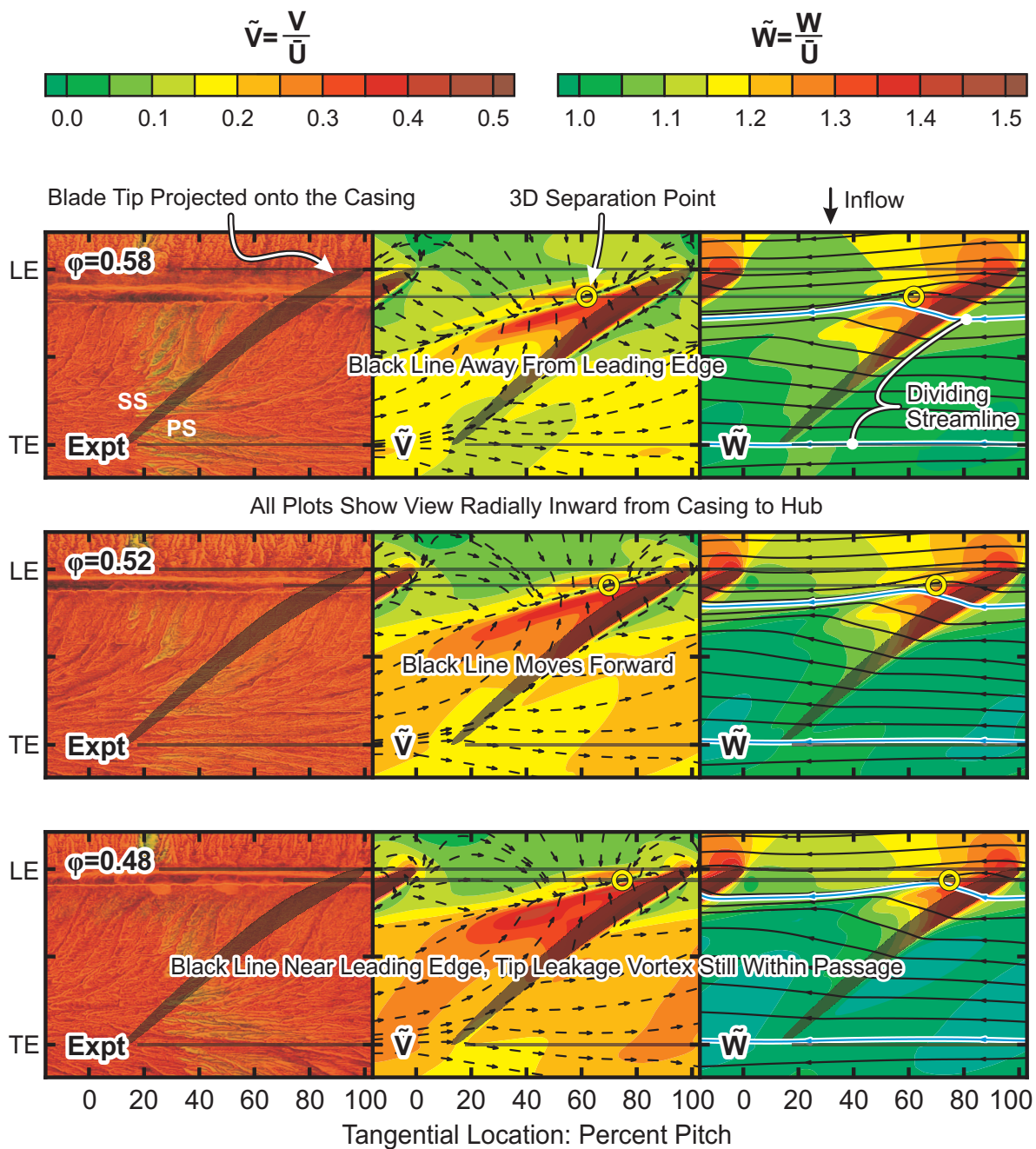


Figure 5.12: The cause of the black line. The left-hand plots show the experimental flow visualisation. The central plots show normalised absolute velocity using arrows (for direction) and contours (for magnitude) extracted from the CFD model using constant radius cuts at 5% tc . The right-hand plots show relative velocity overlaid with streamlines (also extracted from the computational model at 5% tc). Results for three flow coefficients from the design point ($\phi=0.58$) to stall ($\phi=0.48$) are shown. The location of the three-dimensional separation point at each flow coefficient is shown by a yellow circle.

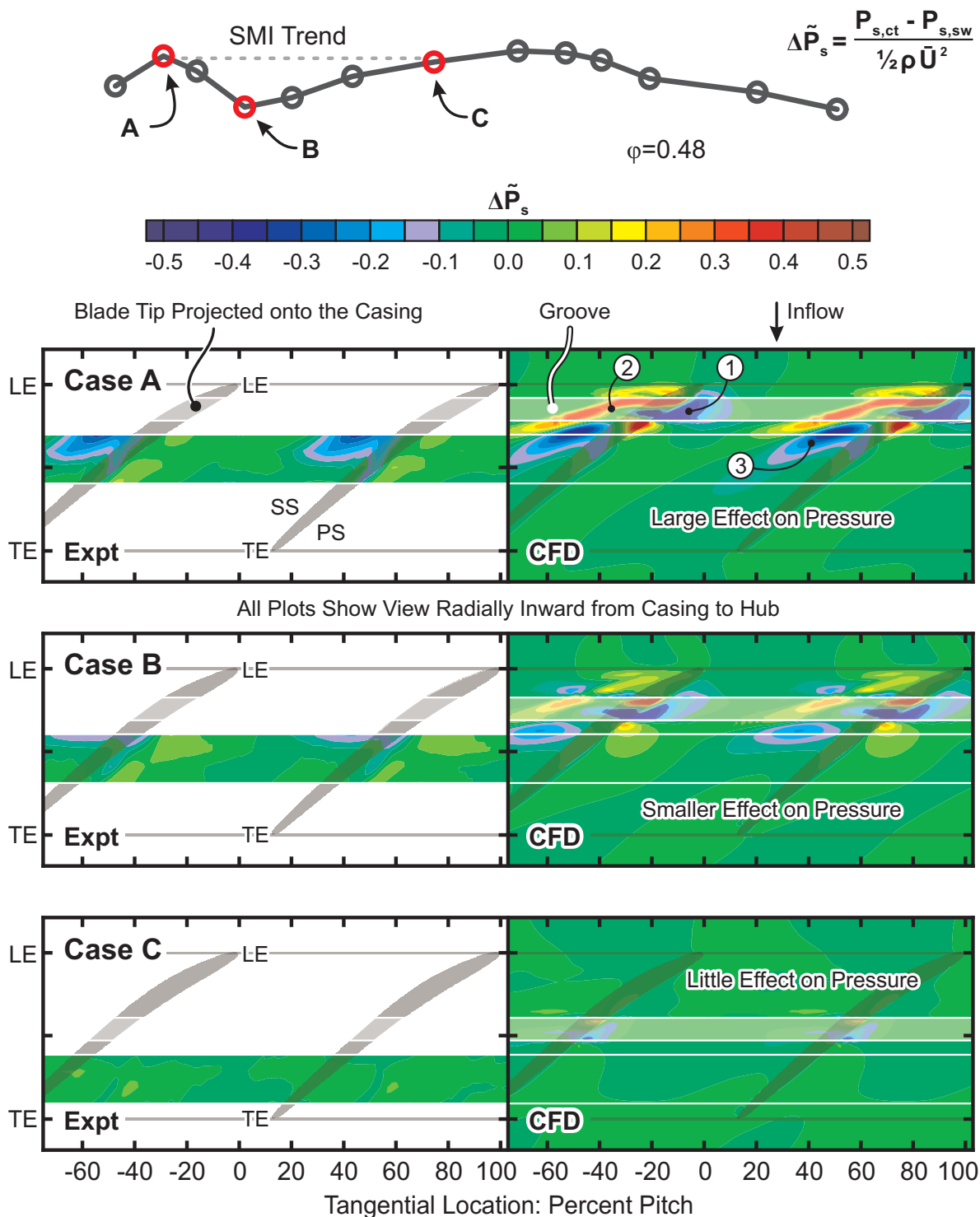


Figure 5.13: The effect of adding a single groove at locations A, B and C on the casing static pressure near the smooth-wall stall point ($\phi=0.48$). Contours show normalised changes to the casing static pressure ($\Delta \tilde{P}_s$) created by subtracting the smooth-wall case from the equivalent grooved case (as shown in Figure 5.7).

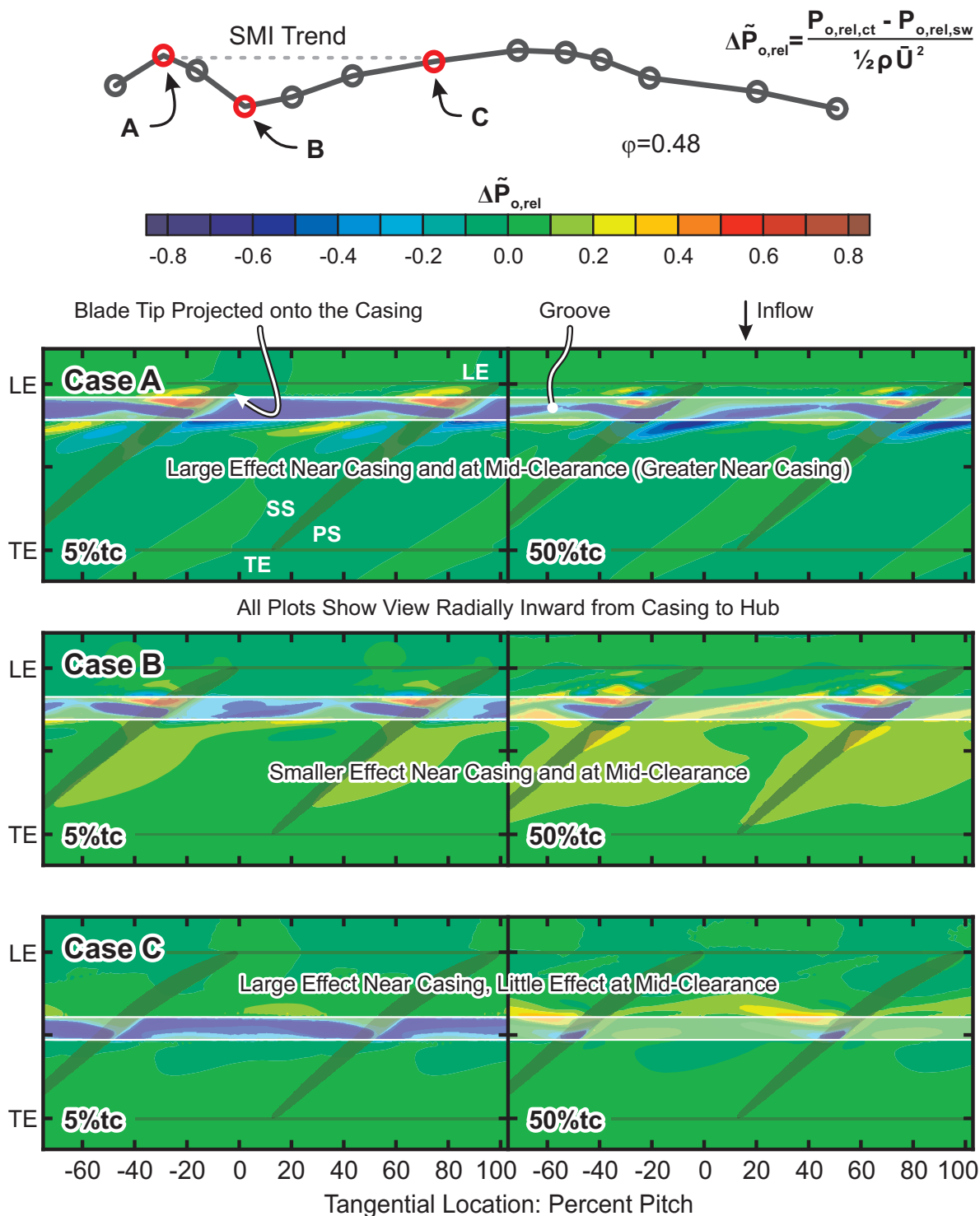


Figure 5.14: The effect of adding a single groove at locations A, B and C on the relative total pressure of the near-casing flow near the smooth-wall stall point ($\phi=0.48$). The data was extracted from the CFD model using constant radius cuts at 5% tc (left-hand side plots) and 50% tc (right-hand side plots). The contours show normalised changes to the relative total pressure ($\Delta \tilde{P}_{o,rel}$) created by subtracting the smooth wall case from the equivalent grooved case (as shown in Figure 5.7).

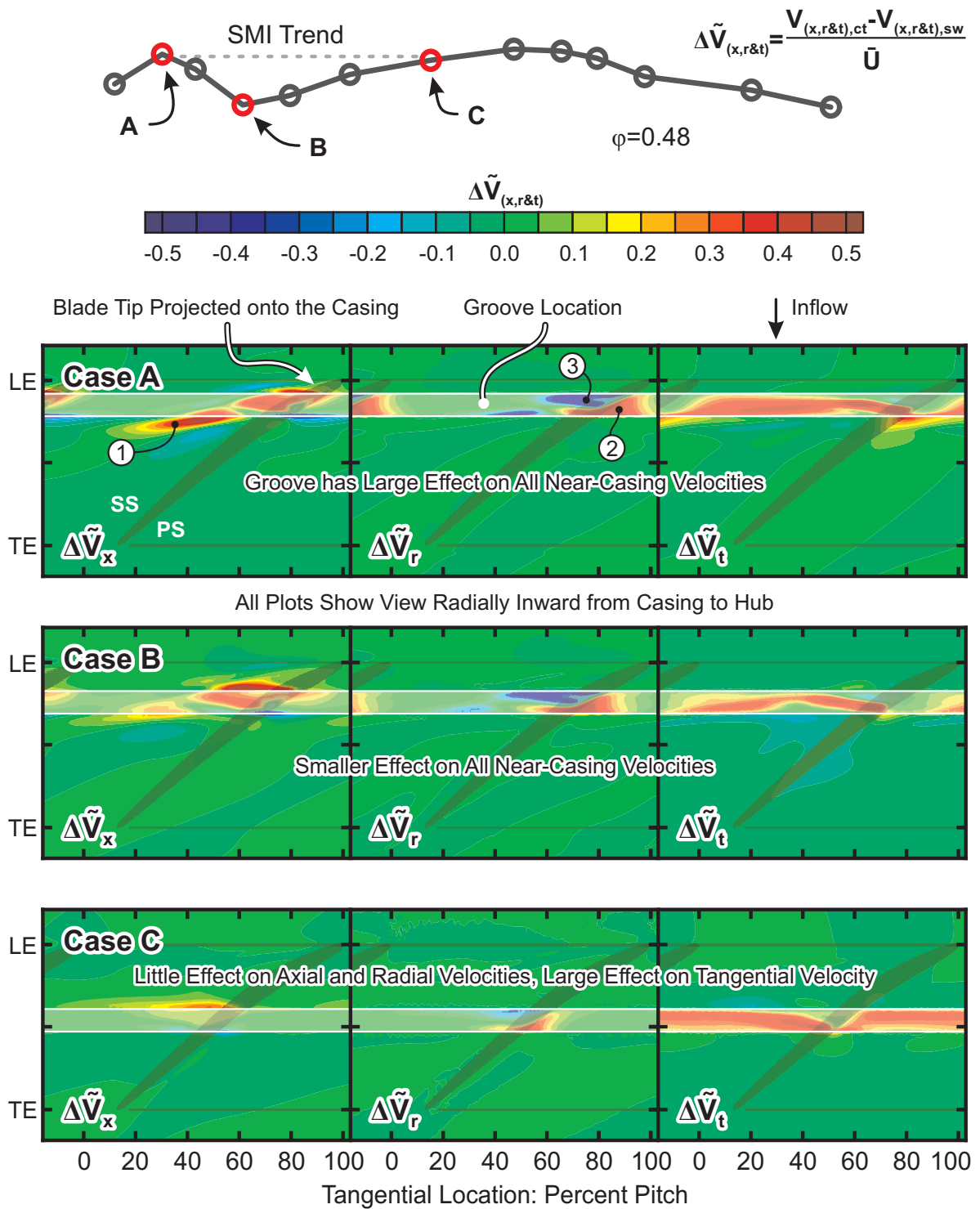


Figure 5.15: The effect of adding a single groove at locations A, B and C on the velocity of the near-casing flow near the smooth-wall stall point ($\phi=0.48$). The data was extracted from the CFD model using constant radius cuts at 5% t_c . The contours show normalised changes to the velocity components ($\Delta \tilde{V}_x$, $\Delta \tilde{V}_r$ and $\Delta \tilde{V}_t$) created by subtracting the smooth-wall case from the equivalent grooved case.

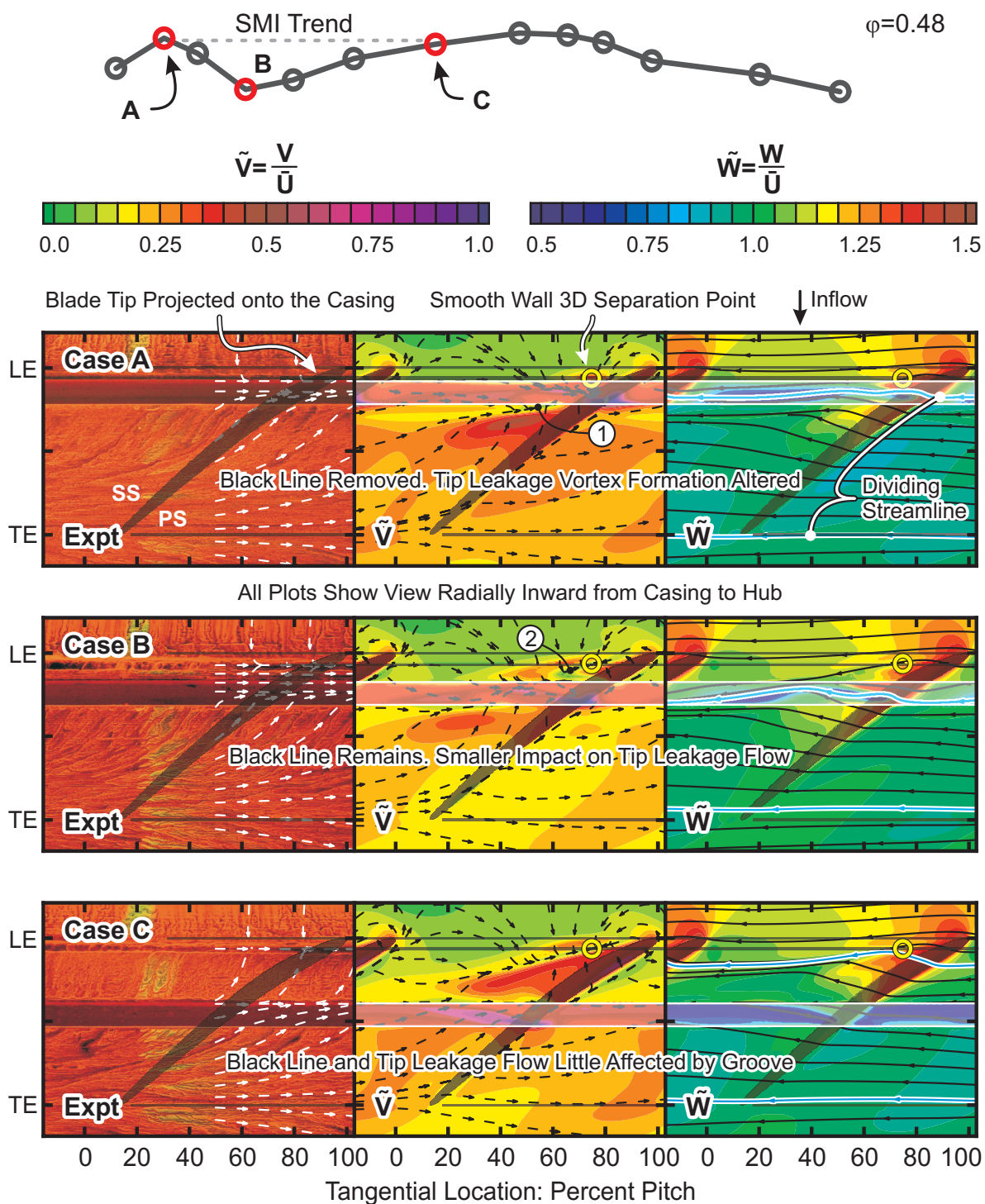


Figure 5.16: The effect of a single groove at locations A, B and C on the near-casing flow patterns near the smooth-wall stall point ($\phi=0.48$). The left-hand plots show the experimental flow visualisation with the time-averaged absolute flow field from the CFD model overlaid for comparison. The central plots show the normalised absolute velocity (extracted from the CFD model at $5\% tc$) using arrows (for direction) and contours (for magnitude). The right-hand plots show the relative velocity from the CFD model overlaid with streamlines.

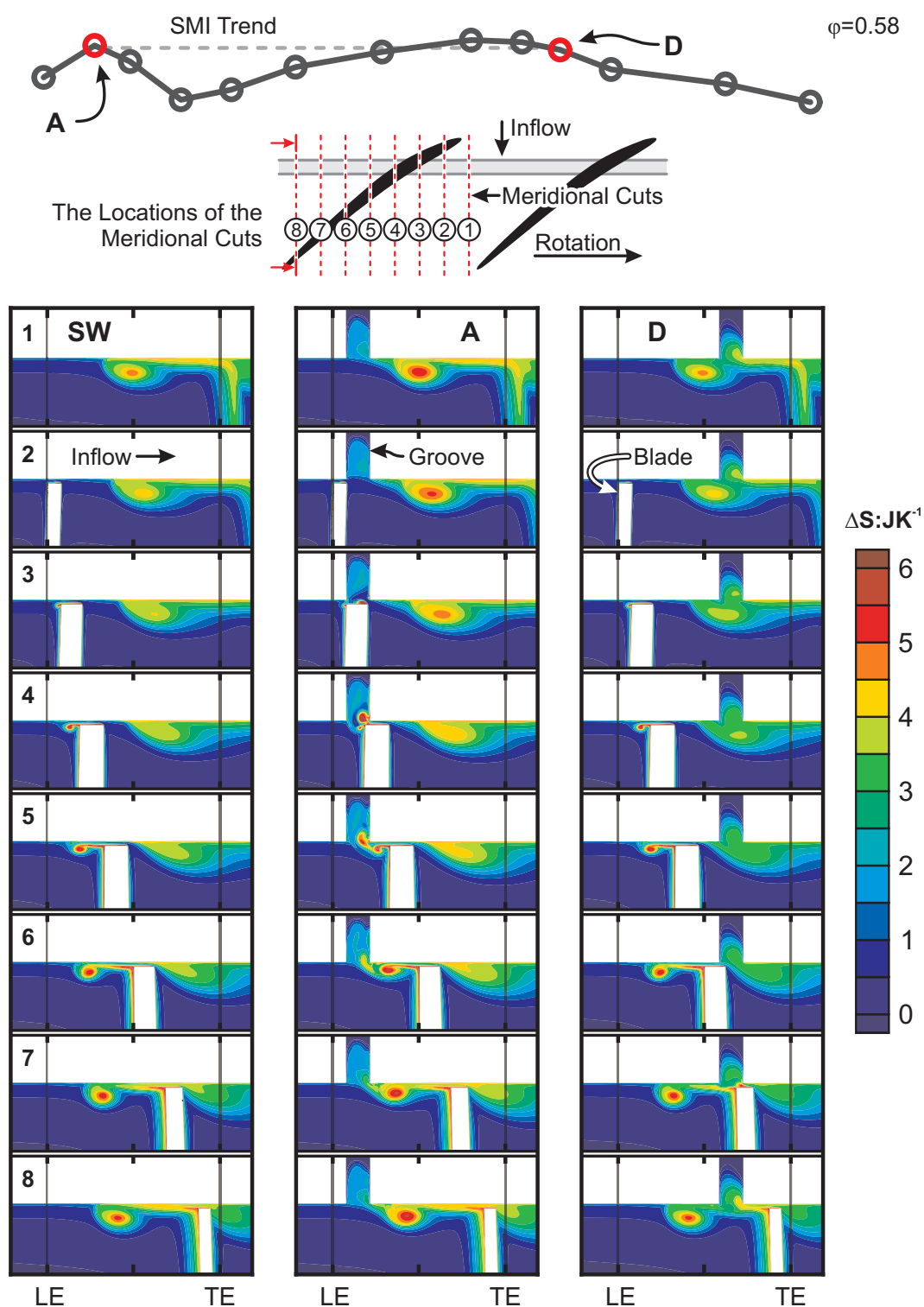


Figure 5.17: Eight meridional cuts showing changes in entropy relative to the mid-span inlet flow near the design point ($\phi=0.58$). The left-hand plots show the smooth-wall results, the central plots show the results for the groove in location A, and the right-hand plots show the results for location D. The core flow moves from left to right in all cuts. Only the flow near the casing is shown in each cut.

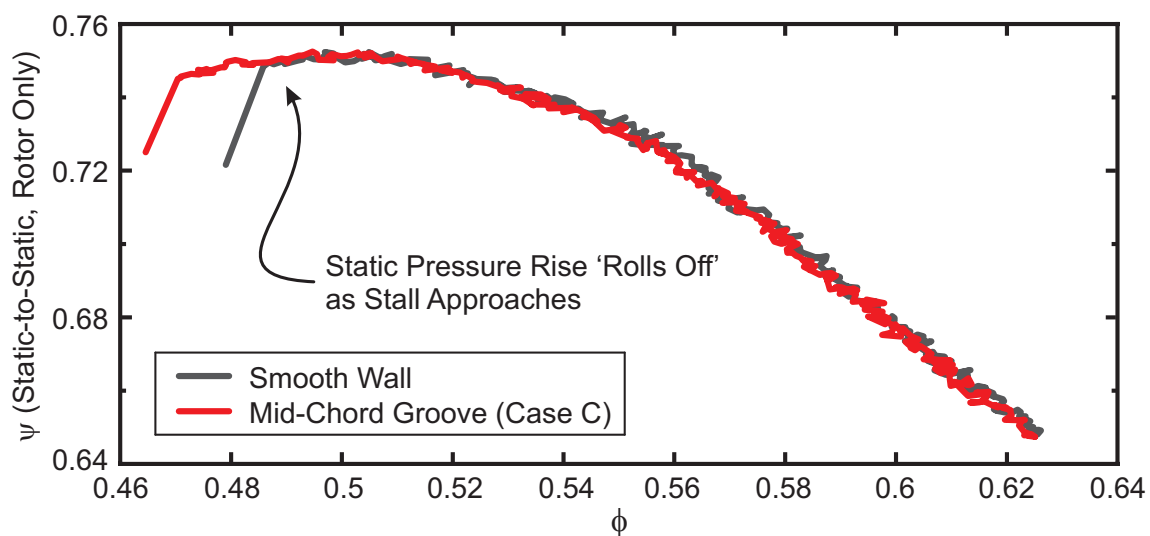


Figure 5.18: The Natal compressor rotor static-to-static characteristic, showing the ‘roll off’ as stall approaches in both smooth wall and grooved cases. An increase in the static pressure rise across the rotor tip clearance is therefore not needed to improve stability.

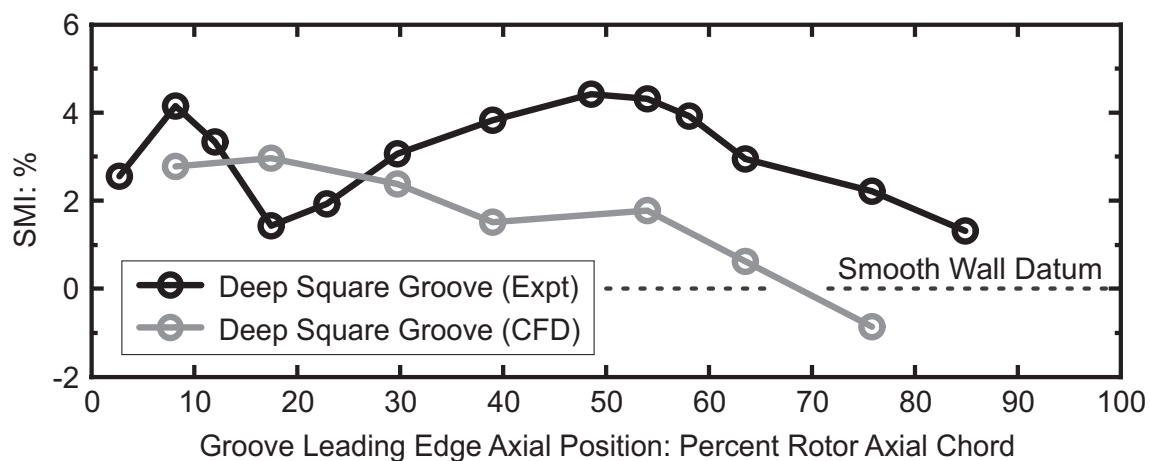


Figure 5.19: The changes in stall margin generated by a single circumferential groove as it is moved axially over the rotor tip, from experimental and computational data.

Chapter 6

Circumferential Groove Casing Treatments: Part 2

In Chapter 5, a casing treatment consisting of a single circumferential groove was investigated in detail. The simplicity of this treatment enabled its performance at different axial locations to be linked to its impact on the compressor flow field. This chapter extends these results to more complex geometries.

The work is divided into four parts. The first part investigates the impact of the depth of a groove on its performance. The second part considers whether the performance of a single circumferential groove can be improved by altering its cross-sectional shape. The third part assesses the impact of combining multiple grooves on the performance of the casing treatment. The fourth part considers the effect of changing tip clearance on casing treatment performance. All the work in this chapter was performed on the Natal compressor, which is presented in Chapter 3.

6.1 Shallow Circumferential Grooves

In Chapter 5, it was shown that the performance of a single circumferential casing groove changes as the groove is moved axially over the rotor tip, because of changes in the interaction between the groove and the near-casing flow field. The interaction was strongest when the groove was near the leading edge (due to the vigorous near-casing flow in this region) and weakened as the groove is moved aft. As a result, the flow penetrated further into the groove when it was located near the leading edge compared to when it was located aft of mid-chord. The optimum depth of the groove may therefore change as it is moved axially, and this is investigated here.

6.1.1 Parametric Study

The performance of two single circumferential casing grooves of different depths was evaluated. The first groove was that tested in Chapter 5. This groove (the 'deep groove' hereafter) has a width of 3mm ($14\% c_{x,r}$) and a depth of 6mm ($27\% c_{x,r}$) giving it an aspect ratio of 2.0. The second groove is a new shallow design with the width and depth both equal to 3mm ($14\% c_{x,r}$) giving it unity aspect ratio. In two series of tests, both grooves were moved axially from the leading to the trailing edge of the rotor blade using the same methods as Chapter 5. The effects of moving both grooves on improvements in stall margin (SMI), pressure rise at stall (PRI), maximum efficiency (MEI) and design point flow rate (DPFI) are shown in Figure 6.1.

The variation in stall margin improvement as the shallow groove is moved aft from the leading edge is similar to that of the deep groove, with maxima when the upstream edges of the grooves are $8\% c_{x,r}$ and $55\% c_{x,r}$ aft of the blade leading edge, and minima at 0, 18 and $85\% c_{x,r}$. From 0 to $55\% c_{x,r}$, however, the deep groove generates a 1% greater stall margin compared with the shallow groove. Aft of $55\% c_{x,r}$, the stall margin improvement generated by both grooves become the same. As seen in Chapter 5, the stall margin and pressure rise improvement trends are similar.

The maximum efficiency improvement results show that the shallow groove causes negligible efficiency reduction provided its leading edge is more than $10\% c_{x,r}$ aft of the blade leading edge. The deep groove only causes a negligible efficiency reduction when its leading edge is aft of $55\% c_{x,r}$. The shallow groove is therefore more efficient than the deep groove forward of mid-chord. The measurements of design-point flow rate show the same trends as the efficiency.

These experiments show that upstream of mid-chord the deeper groove generates a greater stall margin but also a greater efficiency loss than the shallow groove. Both grooves provide the same performance if they are located downstream of mid-chord. As found in Chapter 5, the best location for both grooves is near mid-chord, where there is a broad peak in stall margin improvement and efficiency losses are small.

Following sections will use experimental and computational methods to study the interaction of the grooves with the rotor flow field. The four key groove locations from Section 5.1 will be used. Location 'A' corresponds to the first SMI peak at $8\% c_{x,r}$ and 'B' corresponds to the minima at $18\% c_{x,r}$. Locations 'C' and 'D' are the two points on the second SMI peak where the SMI magnitude is equal to that of A. Therefore, C and D are at $39\% c_{x,r}$ and $58\% c_{x,r}$ respectively.

6.1.2 Flow Study

This section investigates the interaction of the grooves with the near-casing flow in order to explain the results in the previous section. The near-casing flow velocity is used because this was found to be the most useful quantity to consider in Chapter 5. The differences between the near-casing flows with deep and shallow grooves are much smaller than between the grooved and smooth walls, so the grooved cases are compared directly. To this end, constant radius cuts were taken near the casing at $5\% tc$ (5% of the tip clearance away from the casing) and difference plots of axial, radial and tangential velocity were made by subtracting the *shallow groove* case from the *deep groove* case. Red areas therefore show an increased effect that the deep groove has on the flow field compared to the shallow groove. Figure 6.2 shows these velocity difference plots for groove locations A (near blade leading edge) and D (aft of mid-chord). It is useful to compare this figure with Figure 5.15 to aid orientation.

In case A, the two grooves interact with the near-casing flow differently. In the axial velocity plot (left of figure), the red area extending across the blade passage at '1' indicates that the deep groove moves the separation line and its associated tip leakage vortex closer to the suction surface than the shallow groove (see Chapter 5 for definitions of these terms). The radial velocity plot (middle) shows that the flows in and out of the deep groove near the pressure and suction surfaces (at '2') are greater than with the shallow groove. The tangential velocity plot (right) shows that the deep groove pushes the tip leakage flow (at '3') in the direction of blade motion more than the shallow groove. Interestingly, the tangential velocity on the pressure side of the blade passage is reduced with the deep groove, which implies that this region is not important for stability enhancement.

In case D, the interaction of both grooves with the flow field is exactly the same. The deep

and shallow grooves have the same effect on the axial, radial and tangential velocity of the near-casing flow.

These results are in agreement with those presented in Chapter 5. In case A, the deep groove interacts more strongly with the vigorous near-casing flow than the shallow groove (the results in Section 5.4.8 show that flow penetrates 80% of its depth as a result). The shallow groove is half as deep as the deep groove, so the flow cannot penetrate the shallow groove as far as it does the deep groove. Therefore, the shallow groove does not interact with the flow field as strongly as the deep groove, and radial mixing is reduced. The deep groove therefore generates increased stall margin but reduced efficiency relative to the shallow groove in case A. In case D, the flow only penetrates the deep groove to the depth of the shallow groove and so the interaction of both grooves with the rotor flow-field is the same. This results in both grooves generating the same stall margin and efficiency.

This section has shown that the weakening interaction between the near-casing flow and the groove as it is moved aft results in the optimum groove depth changing. Upstream of mid-chord, the deep groove generates a greater stall margin improvement because it interacts more strongly with the flow field, but this stronger interaction reduces efficiency. A trade-off must therefore be made between stall margin improvement and efficiency reduction. Downstream of mid-chord, the shallow groove has the same affect on the flow field (and therefore stability and efficiency) as the deep groove and is therefore favoured for its increased ease of manufacture.

6.2 Alternative Groove Geometries

In the previous section, rectangular grooves of two different depths were tested. This section evaluates two alternative types of groove geometry to see whether they offer superior performance to the simple rectangular designs.

6.2.1 Rounded Circumferential Grooves

This section investigates the performance of single grooves with the aft (or downstream) corner of the groove entrance rounded off.

Design

In Chapter 5 it was found that the sharp aft corner of the rectangular grooves causes flow separations that generate entropy. These separations also block part of the groove entrance, reducing the interaction of the groove with the near-casing flow field, which Chapter 5 found was needed for stall margin improvement. Two new groove geometries of different depths were therefore designed with the same rounded entrance geometry (see Diagram 6.1). The entrances of both grooves have the same throat width (minimum width of entrance) as the rectangular grooves tested in the previous section. Since the downstream corner is rounded, the axial width of casing actually affected by the rounded grooves is slightly larger than in the rectangular groove designs (as shown in Diagram 6.1).

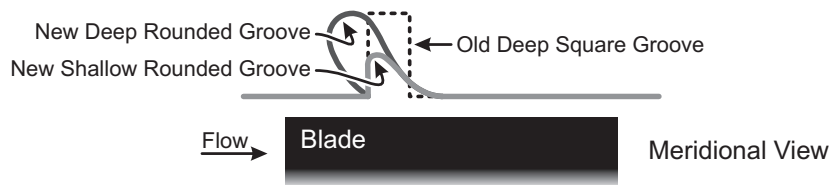


Diagram 6.1: The rounded circumferential groove geometries.

The shallow rounded groove is the same depth as the shallow rectangular groove (3mm, 14% $c_{x,r}$). The forward face of this groove is at right angles to the casing wall as in the case of the rectangular grooves (see Diagram 6.1). The deep rounded groove is the same depth as the deep rectangular groove (6mm, 27% $c_{x,r}$), but its forward face cannot be normal to the casing because the rounded aft face of the groove would close off the groove before it reached full depth. Therefore, the forward face of this groove is cut away to form an upstream recess inside the casing wall (as shown in the diagram).

Parametric Study

The two rounded groove designs were tested using the same methods as Section 6.1. The effects of moving the rounded grooves axially over the rotor on improvements in stall margin (SMI), pressure rise at stall (PRI), maximum efficiency (MEI) and design point flow rate (DPFI) are shown in Figure 6.3. These four performance parameters are defined in Chapter 3. The deep rectangular groove results from the initial parametric study in Chapter 5 are included in the figure for comparison.

The variation in stall margin improvement generated by the deep rounded groove as it is moved aft from the leading edge is similar to the deep rectangular groove. When located

forward of 45% $c_{x,r}$, the deep rounded groove generates a greater stall margin improvement than the deep rectangular groove, while aft of this point the stall margin improvement is smaller. The shallow rounded groove actually *reduces* the stall margin of the compressor when located forward of 30% $c_{x,r}$. Aft of 30% $c_{x,r}$, the stall margin generated by the shallow rounded groove increases to a maximum of 3% at 55% $c_{x,r}$. Aft of this point, its performance matches that of the deep rounded groove. The pressure rise trend matches that of the stall margin.

The deep rounded groove is less efficient than the rectangular groove when located forward of 30% $c_{x,r}$, but aft of this point, the efficiency of the deep rectangular and deep rounded grooves are similar. The shallow rounded groove reduces efficiency relative to the deep rectangular groove when located forward of 55% $c_{x,r}$. Aft of 55% $c_{x,r}$ the shallow rounded groove has the same impact on efficiency as both the deep grooves. The trend in design-point flow rate follows the trend in efficiency.

Overall, the rounded grooves perform little better than the rectangular grooves. Upstream of mid-chord, the deep rounded groove generates slightly larger stall margin improvements, especially near the minimum at 18% $c_{x,r}$, but this is negated by reductions in efficiency. The shallow rounded groove gives the worst performance of any tested geometry upstream of mid-chord. Aft of mid-chord, both rounded grooves generate smaller stall margin improvements at similar efficiencies to the deep rectangular grooves. These results show that rounding off the downstream corner of a groove gives little performance benefit. From a practical perspective, the extra complexity and machining cost of the rounded grooves over the rectangular grooves is unlikely to be justifiable.

6.2.2 Baffled and Intermittent Circumferential Grooves

This section investigates the possibility of improving the performance of a deep rectangular casing groove by interrupting the groove to eliminate continuous circumferential flow.

Design

The flow study in Chapter 5 shows that the interaction between the rectangular grooves and the near-casing flow changes as the groove is moved aft from the blade leading edge. Near the leading edge, the rectangular grooves alter all the velocity components of the near-casing flow, while aft of mid-chord only the tangential velocity is altered. The flow study also shows that when the forward edge of the groove is 18% $c_{x,r}$ aft of the blade leading

edge, the stall margin improvement is minimised while the interaction changes between these two different regimes.

Blocking the grooves with baffles (thin strips of metal), or making the groove intermittent, will increase the radial momentum exchange between the groove and the near-casing flow by repeatedly developing tangential flow over a short length of groove before throwing it out into the near-casing flow. This should increase stall margin improvement because of the increased interaction of the groove with the near-casing flow, and may also reduce the minimum stall margin improvement at $18\% c_{x,r}$ because the interaction between the groove and the near-casing flow should not change as much as the groove is moved aft from the leading edge. To test this, two new groove geometries were designed using the deep rectangular groove of Section 6.1 as a baseline. The geometries are shown in Diagram 6.2 (the baffles completely block the groove, being flush with the casing wall and all the internal groove faces).

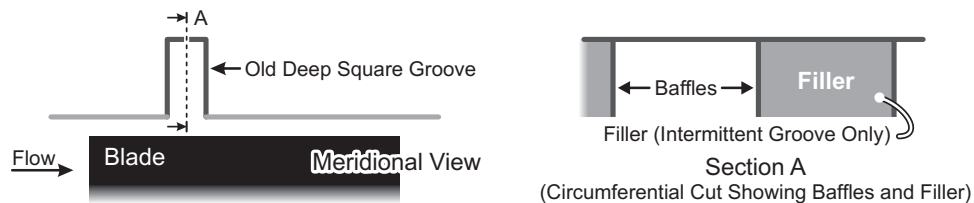


Diagram 6.2: The baffled and intermittent circumferential groove geometries.

The 'baffled groove' design has one thin baffle corresponding to each rotor blade pitch (38 equi-spaced thin baffles in total). However, work in previous sections has found that radial mixing is an important source of loss, so the radial mixing caused by the large number of baffles could well reduce efficiency. Another treatment was therefore designed with equal lengths of groove and smooth wall around the annulus (see Diagram 6.2) to provide a different trade-off between stall margin and efficiency. This 'intermittent groove' design should offer excellent mechanical integrity in an engine, because it does not require the abradable lining to be cut around the whole annulus.

Parametric Study

The baffled and intermittent grooves were tested in a series of experiments using the same methods as Section 6.1. The impact of both designs on improvements in stall margin (SMI), pressure rise at stall (PRI), maximum efficiency (MEI) and design point flow rate (DPFI) are shown in Figure 6.4. The continuous deep rectangular groove results from the initial parametric study in Chapter 5 are included for comparison.

The results show that the baffled groove generates the greatest stall margin improvement of all the single groove geometries tested so far (particularly near the leading edge), with maximum values of 6 and 5% at 20 and 45% $c_{x,r}$ respectively. The minimum stall margin improvement near 18% $c_{x,r}$ is also smoothed out with a least value of 4% (a great improvement over the un-baffled deep rectangular groove in this region). Aft of mid-chord, the stall margin improvement generated by the baffled case tends to that of the un-baffled case. The stall margin improvements generated by the intermittent groove are similar to the un-baffled deep rectangular groove. The maximum stall margin improvement values are slightly lower, but the minimum near 18% $c_{x,r}$ is greater at 2% (so the trend is smoother). As the intermittent groove is moved aft from mid-chord, the stall margin tends to that of the full baffled case. The trend in pressure rise at stall matches that of the stall margin.

The baffled groove reduces efficiency compared to the un-baffled groove over the whole chord, although near the trailing edge the efficiency loss is small. The efficiency of the intermittent groove could only be measured at one point, but the efficiency reduction is half that of the baffled groove, which is sensible (in this case, the efficiency reduction is equal to the un-baffled groove). The design-point flow trend follows that of the efficiency (for the baffled groove).

The results show that the baffled groove generates a greater stall margin improvement than the un-baffled groove over the whole blade, but at a reduced efficiency due to increased radial mixing. The intermittent groove has a similar maximum stall margin and efficiency to the un-baffled groove. Baffled and intermittent grooves both have smoother stall margin trends than the rectangular grooves, which makes positional accuracy less important. They are therefore much safer near the blade leading edge because the reduction in performance near 18% $c_{x,r}$ is much less pronounced.

These results show that while single casing grooves can be effective, they do not generate stall margin improvements greater than 6% in the Natal compressor. The next section investigates combining grooves to increase the stall margin improvement further.

6.3 Multiple Circumferential Grooves

The results in the previous sections show that the conventional rectangular circumferential groove is hard to improve on, particularly when the manufacturing complexity of alternative geometries is considered. This section therefore investigates combining multiple rectangular grooves to increase casing treatment performance. Three multiple-groove treatments are assessed and a flow study is used to interpret the results.

6.3.1 Parametric Study

Three multiple-groove treatments were tested, two of which contained two grooves and one of which contained three grooves. The first two-groove treatment has grooves at locations C and D from Section 6.1 (39% $c_{x,r}$ and 58% $c_{x,r}$). These grooves were chosen because they are both situated on the broad stall margin improvement maximum near mid-chord discovered in Chapter 5. This treatment should therefore generate a good stall margin improvement with little efficiency loss. The second two-groove treatment has grooves at locations A and C (8% $c_{x,r}$ and 39% $c_{x,r}$). The grooves are therefore located near the stall margin improvement maxima that occur near the leading edge and near mid-chord. The three-groove treatment consists of grooves at locations A, C and D. Since it has grooves at all the best locations for stall margin improvement identified in Chapter 5, this three-groove treatment should generate the greatest improvement of any grooved treatment yet tested.

The performance of the three treatments is shown in Figure 6.5 with the single groove results from Chapter 5.1 also shown for reference. The first two-groove treatment generates a stall margin improvement of 6%, which is 2% greater than the best single groove. However, the efficiency losses are also greater than the single groove treatments located around mid-chord. While the efficiency losses could be predicted by adding together the performance of the treatment's constituent grooves, the stall margin improvement is less than expected. The second two-groove treatment generates a lower stall margin improvement than the first at 5.5%. The three-groove treatment generates an SMI of 6.5%. This is only 2.5% greater than the best single groove and much less than would be predicted by adding the performance of the grooves together. The efficiency losses, however, are again similar to the sum of all the efficiency losses of the component grooves. As observed previously, the trend in pressure rise at stall matches that of stall margin improvement and the trend in the design point flow increase matches that of efficiency.

These results show that where grooves are combined, simply 'adding up' the stall margin improvements of the constituent grooves over-predicts the stall margin improvement achieved by the multiple-groove treatment. However, adding up the efficiency losses of the constituent grooves does lead to a reasonable estimate of the efficiency loss of the multiple groove treatment. For this reason, these results show it is best to locate the grooves in a multiple-groove treatment near mid-chord, because this minimises efficiency loss and maximises stall margin improvement.

The next section considers the impact of the multiple groove configurations on the near-casing flow in order to explain these results.

6.3.2 Flow Study

In Chapter 5 it was found that the near-casing flow velocity was the most useful quantity to consider when assessing the impact of casing grooves on the compressor. Since difference plots are the clearest way of highlighting the impact of grooves, constant radius cuts were taken near the casing ($5\%tc$) and difference plots of axial, radial and tangential velocity were made by subtracting the smooth wall case from the multiple groove cases. Figure 6.6 shows these velocity difference plots for two of the multiple-groove treatments tested in the previous section; the three-groove treatment and the best two-groove treatment, with grooves at locations C and D. These results may be compared with the single-groove data in Figure 5.15 to aid orientation.

The interaction of the two-groove treatment with the near-casing flow is the sum of the component grooves in isolation. Both grooves only affect the flow in their immediate vicinity and do not change their interaction with the near-casing flow when combined. The impact of the two-groove treatment on the near-casing flow is therefore a superposition of the impact of each component groove taken in isolation. The result for the three-groove treatment is similar. The interaction of the middle groove (at location C) in the multiple-groove configuration is slightly different to its interaction when isolated because the groove near the leading edge alters the flow near the middle groove, but the difference is small.

The impact of the grooves in a multiple-groove treatment on the near casing flow is therefore a superposition of the impact of each isolated constituent groove. There is little interaction between the grooves. This explains why the efficiency losses are a superposition of those associated with the constituent grooves; the entropy gains associated with the groove's interaction with the near-casing flow are added together. It does not, however, explain why increases in stall margin improvement get progressively smaller as more grooves that perform well in isolation are added to a casing treatment. The results show that as the stall margin improvement generated by a grooved casing treatment increases, it becomes progressively harder to generate further improvements by adding more grooves. The results also show that grooves near the leading edge are best avoided in multiple-groove treatments if possible. This has not previously been appreciated.

Having considered the impact of grooves at different axial locations and in different combinations, the next step is to evaluate the performance of casing grooves when the tip clearance gap is increased.

6.4 The Impact of Tip Clearance on Multiple Groove Treatments

All the work done on grooves thus far has been performed using the standard tip clearances quoted in Chapter 3. The tip clearances on a real engine are, however, rarely constant throughout its life. Tip clearances can increase with time as the blades rub against the abradable casings, which can also lead to the casings becoming trenched. Differential heating of the casings can lead to eccentric tip clearances (Graf *et al.*, 1998). This section therefore studies the impact of changing the tip clearance, eccentricity and trenching on the performance of grooved casing treatments. These three variables would need a great number of different casings and blades to study in detail. The present study is therefore an initial test designed to ascertain whether the performance of casing grooves is changed with varying tip clearances, rather than quantifying any such changes in detail. Since this is an initial test, efficiency is not considered.

The four-groove casing treatment from Chapter 5.2 was used for all the experiments. The grooves are the same shape as the deep rectangular groove tested in Section 6.1. The leading edges of grooves 1, 2, 3 and 4 are at 12, 39, 66, and 93% $c_{x,r}$ respectively (grooves 1, 2 and 3 are thus close to locations A, C and D introduced in Section 6.1). The stall point of the compressor was measured using the method described in Chapter 3 with the smooth wall, groove 1 only exposed, and then all four grooves exposed at each tip clearance. Seven tip clearances were investigated, consisting of three un-trenched concentric cases, two eccentric cases at two different mean clearances (with a constant eccentricity, or shaft offset, of 0.7% span) and two trenched cases (concentric and eccentric at an average clearance of 1.4%). The values of ϕ_{stall} and $\psi_{s,stall}$ were used to compare cases instead of the stall margin and pressure rise improvements because altering the tip clearance changes the performance of the smooth wall case and these performance metrics conceal this information.

The results for the un-trenched concentric and eccentric cases are shown in Figure 6.7. To reduce complexity, the concentric and eccentric results are considered on separate graphs. The concentric results show that as the tip clearance increases, ϕ_{stall} and $\psi_{s,stall}$ increase and decrease respectively. In the grooved cases, the linear changes in ϕ_{stall} are parallel to the smooth wall case, so the treatments generate a constant stall margin improvement of 2 and 5% respectively. In the eccentric results, as the mean tip clearance is increased in the grooved cases, ϕ_{stall} and $\psi_{s,stall}$ increase and reduce linearly and the lines have similar gradients. However, the gradient of the smooth wall case is smaller, indicating that the increasing tip clearance (with eccentricity) has a larger negative impact on the grooved wall cases than the smooth wall cases. This causes the least effective single groove case to generate no stall margin improvement at the larger eccentric clearance.

As expected, the eccentric cases stall at higher flow coefficients than the concentric cases for a given mean clearance, but the offset decreases as the mean tip clearance increases. The impact of eccentricity on stall is normally modelled by considering the maximum clearance (Graf *et al.*, 1998), but if this were true, the concentric and eccentric lines should be parallel. These results therefore suggest that considering eccentricity as a proportion of the mean clearance is a better method (the eccentricities are 60 and 40% as a percentage of mean clearance in the smaller and larger mean clearance eccentric cases respectively).

The trenched cases are plotted in Figure 6.8. Because the trenched casing experiments were performed at a different tip clearance to the other cases (due to mechanical constraints), these cases are included with the other concentric and eccentric results to allow comparison. The results show that trenching reduces the stability of both the smooth and grooved wall cases, but the grooved wall cases are less affected than the smooth walls.

These results show that casing grooves continue to improve stability when the tip clearance increases concentrically, or is trenched, but eccentricity can decrease their performance. The impact of eccentricity on stability does not appear to scale with the maximum clearance. More work is justified in investigating the detailed impacts of changing tip clearance on the performance of grooved casing treatments.

6.5 Discussion

When located forward of mid-chord, a deeper groove with an aspect ratio of two generates a greater stall margin improvement, but causes a greater efficiency loss, than a shallow groove with an aspect ratio of one. This is because deeper grooves have a more vigorous interaction with the near-casing flow. Grooves must be positioned to avoid the stall margin trough near $18\% c_{x,r}$ regardless of their depth. Aft of mid-chord, the performance of both grooves (and their interaction with the near-casing flow) becomes the same, so the extra depth of the deep groove is not required. Since deeper grooves may be more difficult to manufacture, the optimum groove depth reduces as the groove is moved aft.

These results can be compared with Bailey (1972), who used multiple-groove casing treatments to show that a groove aspect ratio of 3.0 was better than 1.0. All the groove configurations tested in Bailey had grooves located upstream of mid-chord, so these findings agree with the present work. The grooves upstream of mid-chord generate a greater stall margin if they are deeper, while the performance of the grooves downstream of mid-chord is unaffected by their extra depth.

The alternative groove geometry tests suggest it is difficult to improve on rectangular casing grooves. The baffled (and to a lesser extent deep rounded) grooves generate the greatest stall margins, but also the lowest efficiencies. The shallow rounded groove offers poor performance, so it is sensible to check that the downstream corner of shallow rectangular grooves would not be rounded off during service. The intermittent groove does not provide superior performance to the optimally placed deep rectangular groove, but is a more robust design near the leading edge, where the stall margin improvement that it generates does not reduce as much near $18\% c_{x,r}$. Therefore, if accurate positioning is not possible due to rotor movement in service, the intermittent groove should be considered in this region. The intermittent groove design also offers better mechanical integrity than a continuous casing groove, and allows for non-uniform circumferential or axial distribution of the groove sections, which may be useful in mitigating the effects of inlet distortion, non-uniform tip clearance or clashes with other components. Downstream of mid-chord, the performance of all the different groove geometries is remarkably similar, suggesting that the shape of casing grooves is not very important in this region.

These baffled groove results can be compared with Prince *et al.* (1974) and Fujita and Takata (1984), who also recorded an increased stall margin with reduced efficiency when twelve baffles were added to a five-groove treatment. Prince suggests that “high circumferential velocities are helpful for efficiency” while “low circumferential velocities are helpful for stability”. The present work, however, shows that all the velocity components of the near-casing flow must be considered, and it cannot be assumed that each groove interacts with the near-casing flow in the same way. Circumferential velocities are helpful for stability, but so are radial and axial velocities, while efficiency is mainly influenced by losses due to radial mixing and corner separations.

It is also difficult to improve the performance of grooved casing treatments by combining multiple grooves. When grooves are combined, the interaction of each constituent groove with the near casing flow field is similar to that of the isolated groove. As a result, the losses associated with each groove add together and the efficiency reduction caused by the multiple groove treatment is the sum of the efficiency reductions caused by each constituent groove. However, the stall margin improvement is smaller than the sum of the stall margin improvements due to each of the constituent grooves. As a result, the best multiple-groove treatments are those with grooves near mid-chord, where the efficiency reduction for the constituent grooves is low.

6.6 Conclusions

It is concluded that:

1. When located forward of mid-chord, a rectangular groove with an aspect ratio of 2.0 (deep groove) generates a greater stall margin improvement but reduced efficiency compared to a groove with an aspect ratio of 1.0 (shallow groove). This is because the deeper grooves interact more strongly with the near-casing flow. When positioned downstream of mid-chord, the deep and shallow grooves have the same impact on the near-casing flow and give the same performance.
2. A deep rounded groove generates a slightly larger stall margin improvement and efficiency loss than a deep rectangular groove, when placed forward of mid-chord. A shallow rounded groove generates a poor stability improvement and large efficiency reduction in this region. Aft of mid-chord, both rounded grooves generate a slightly lower stall margin improvement than rectangular grooves. Rounding off the aft corner of circumferential grooves does not, therefore, improve performance.
3. Installing one baffle per rotor blade in a deep rectangular groove increased stall margin improvement relative to the un-baffled groove, but with a reduced efficiency. An intermittent groove, with equal circumferential lengths of smooth wall and groove, generated a similar performance to the un-baffled groove. The baffled and intermittent grooves generated a smoother stall margin improvement trend than the un-baffled groove, which makes them useful forward of mid-chord because their performance does not suddenly reduce near $18\% c_{x,r}$.
4. When multiple grooves are combined in a casing treatment, the interaction they have on the near-casing flow is the same as when the constituent grooves are applied separately. The efficiency loss caused by multiple grooves is thus the sum of the losses generated by the component grooves, but the stall margin improvement is less than the sum of the improvement due to the component grooves. It is better to combine grooves around mid-chord because this reduces efficiency reductions.
5. Initial testing shows that the performance of casing grooves is maintained if tip clearance increases concentrically, but may decrease if the casing becomes eccentric.
6. It is difficult to design a grooved casing treatment that offers a better trade-off between stall margin improvement and efficiency reduction than a single rectangular groove placed at mid-chord. The performance of different groove geometries downstream of mid-chord is remarkably similar.

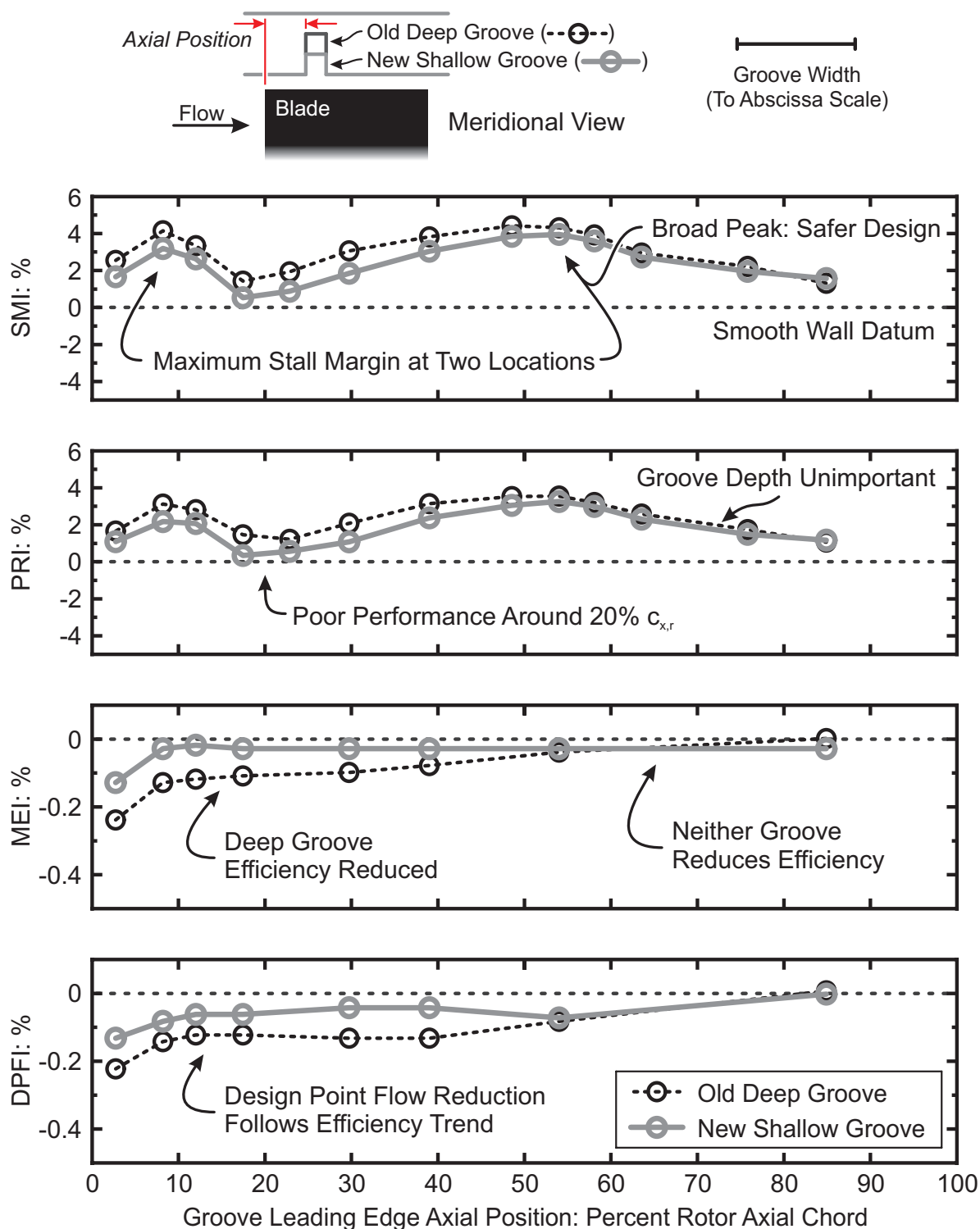


Figure 6.1: The effect of altering the axial position of two rectangular casing grooves of different depths on stall margin improvement (SMI), pressure rise improvement (PRI), maximum efficiency improvement (MEI) and design point flow increase (DPFI).

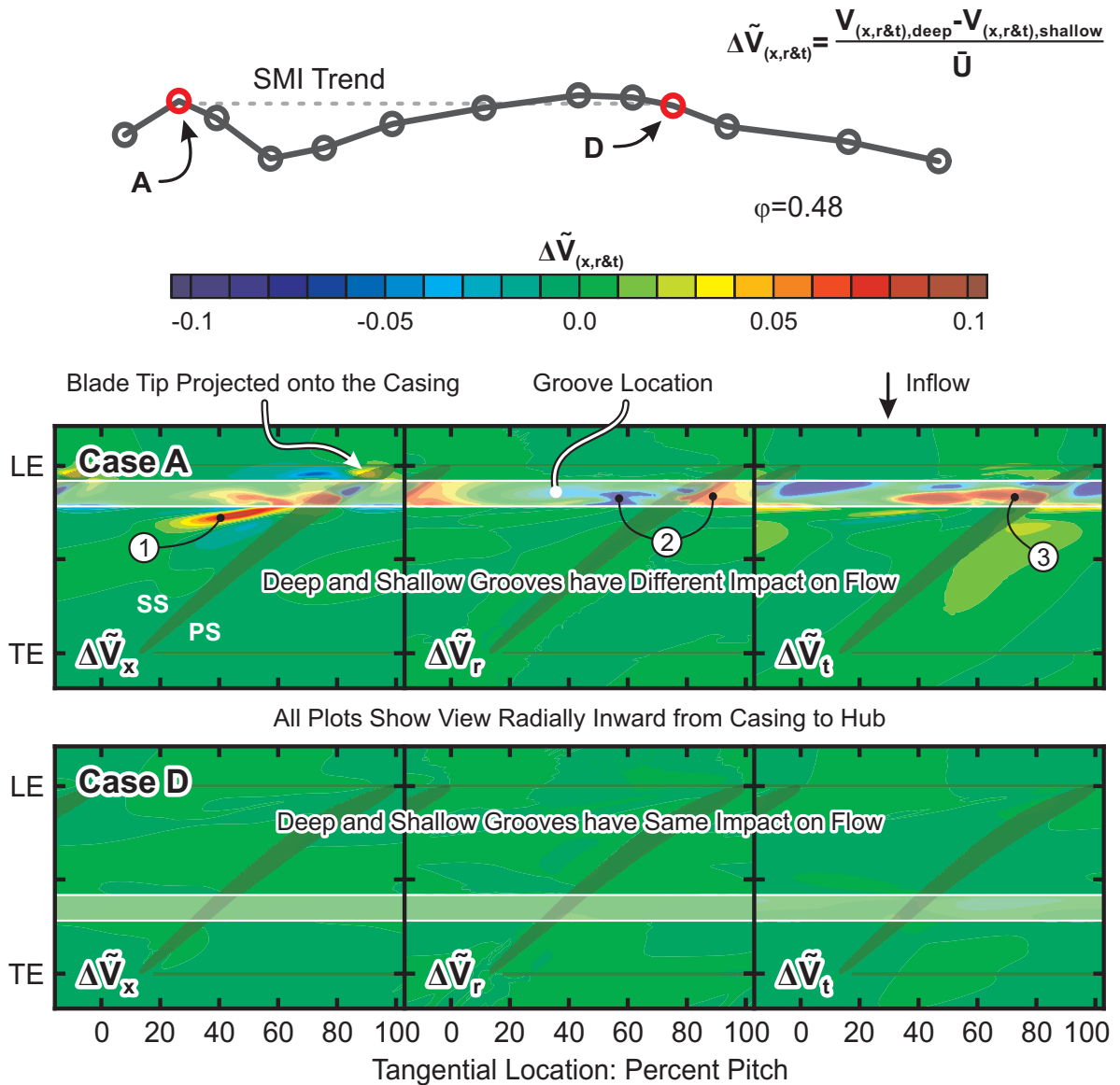


Figure 6.2: The impact of deepening a casing groove near the leading edge or mid-chord on the near-casing flow. Contours of normalised changes to the velocity components ($\Delta \tilde{V}_x$, $\Delta \tilde{V}_r$ and $\Delta \tilde{V}_t$) of the near-casing flow caused by the groove in locations A and D are shown near the smooth-wall stall point ($\phi=0.48$). Constant radius cuts were taken from the deep grooved wall CFD model at 5% tc and the plots were created by subtracting the equivalent shallow groove case.

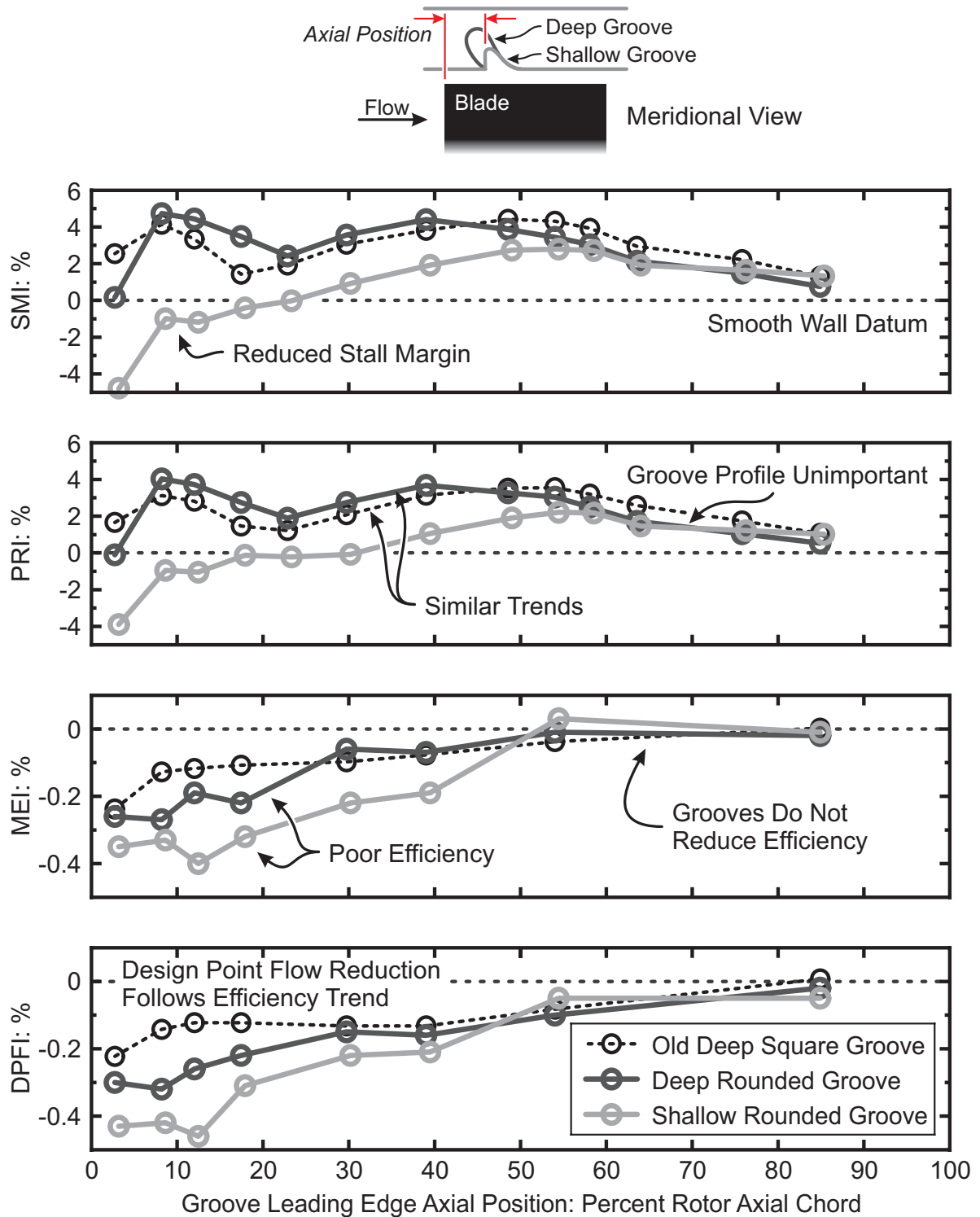


Figure 6.3: The effect of altering the axial location of two rounded casing grooves on stall margin improvement (SMI), pressure rise improvement (PRI), maximum efficiency improvement (MEI) and design point flow increase (DPFI). The single groove results from Chapter 5.1 are also shown.

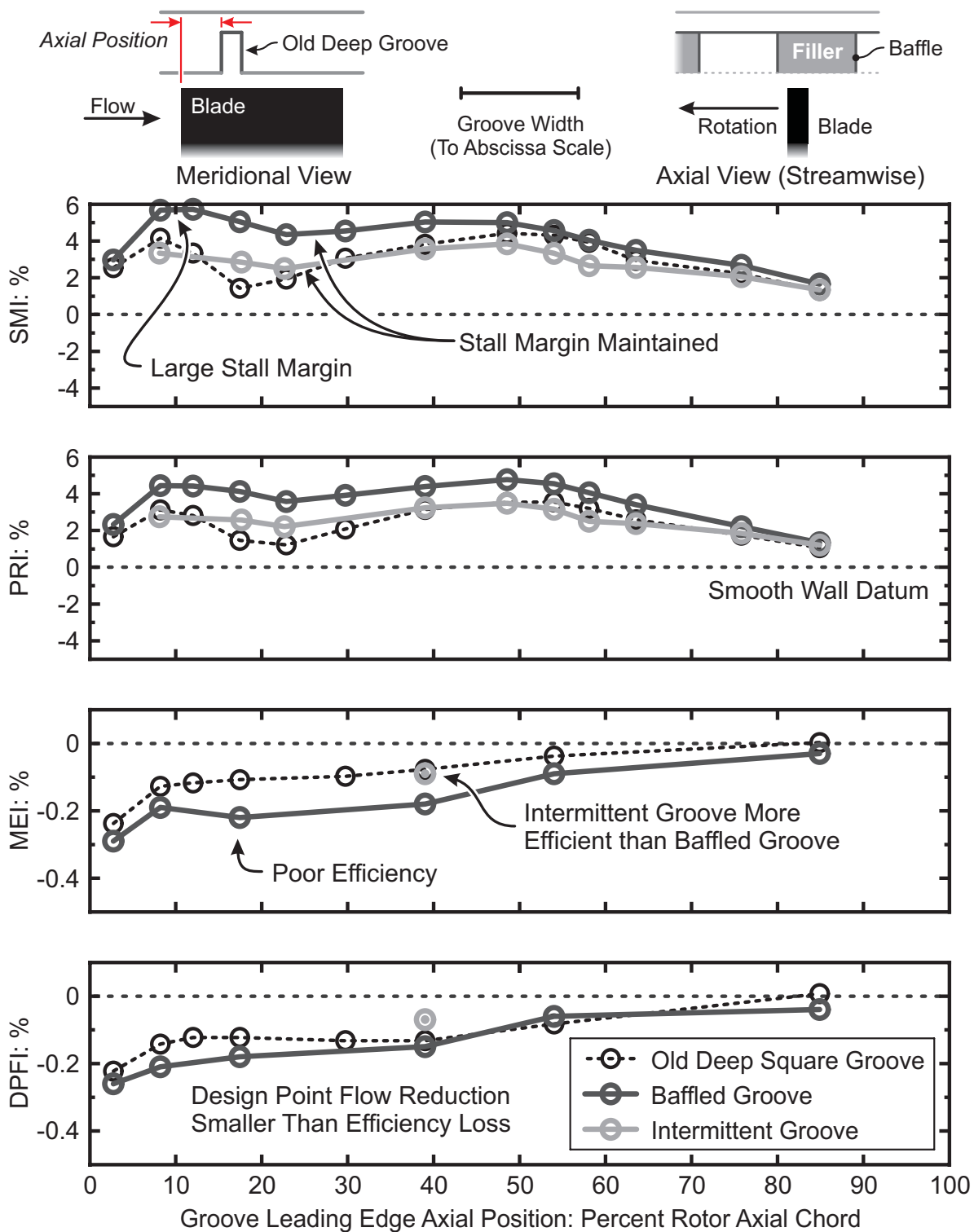


Figure 6.4: The effect of altering the axial location of baffled and intermittent casing grooves on stall margin improvement (SMI), pressure rise improvement (PRI), maximum efficiency improvement (MEI) and design point flow increase (DPFI). The single groove results from Chapter 5.1 are also shown.

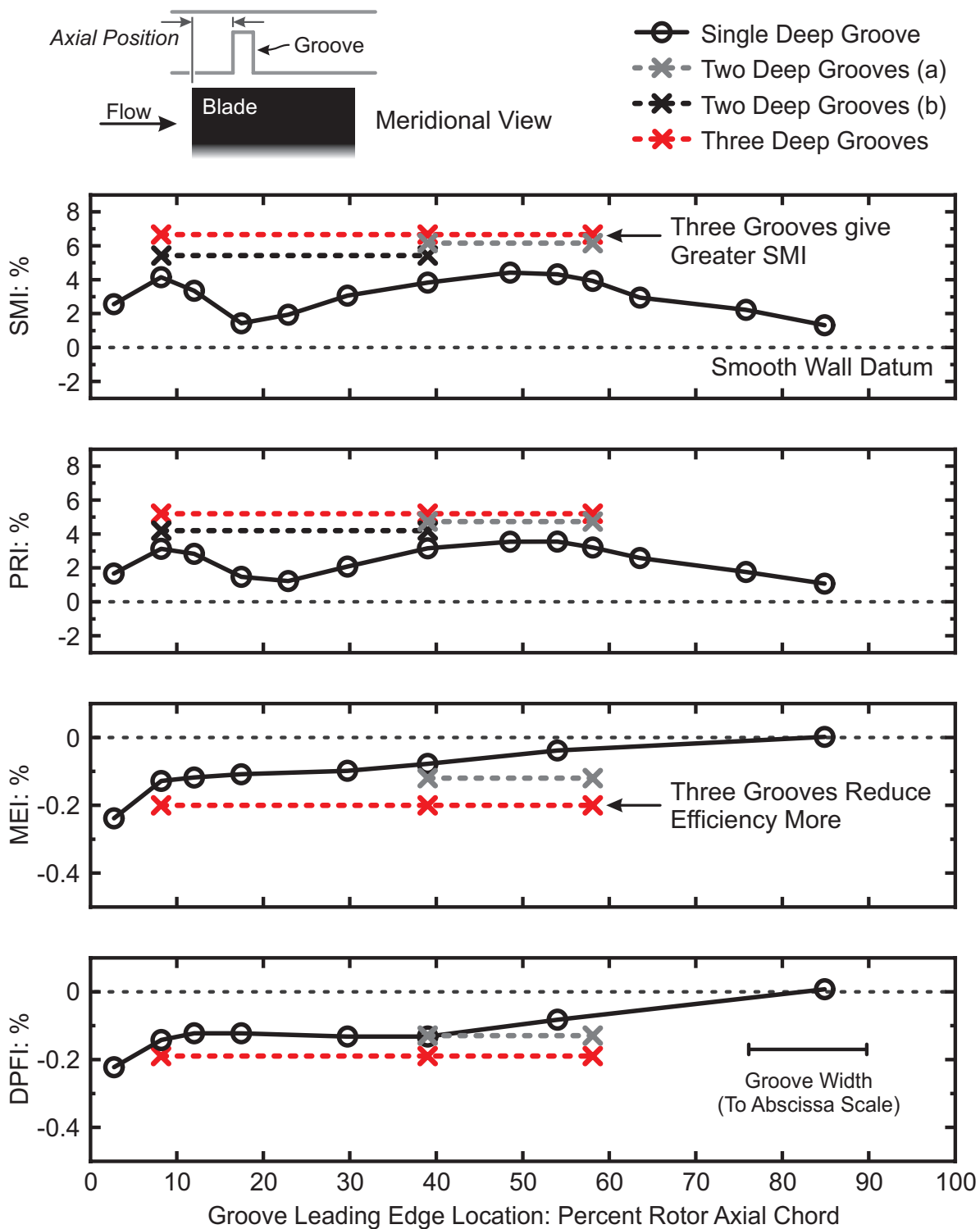


Figure 6.5: The effect of installing casing treatments containing two or three circumferential grooves on stall margin improvement (SMI), pressure rise improvement (PRI), maximum efficiency improvement (MEI) and design point flow increase (DPFI). The single groove results from Chapter 5.1 are also shown.

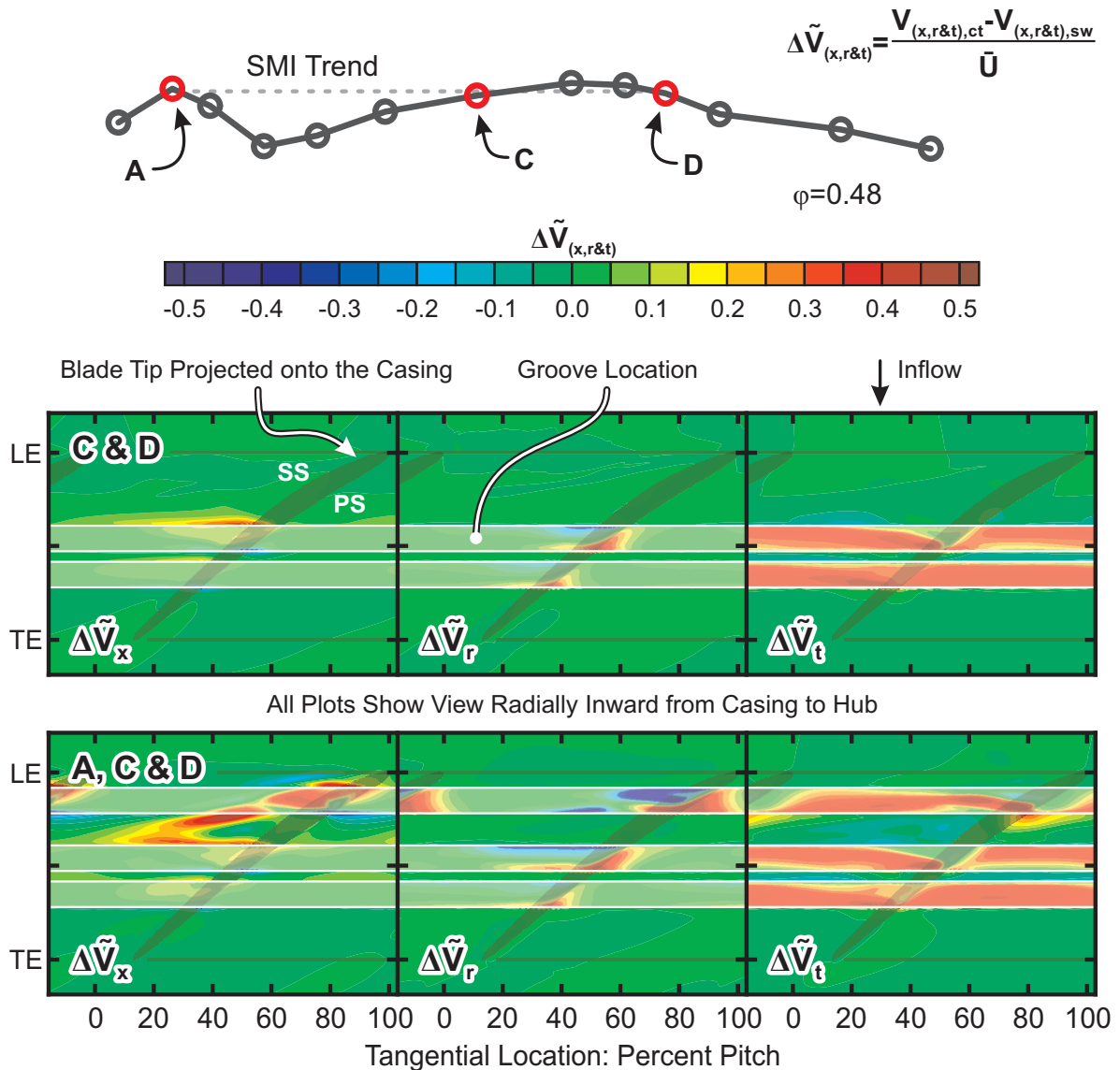


Figure 6.6: The impact of multi-groove casing treatments on the near-casing flow. Contours of normalised changes to the velocity components ($\Delta \tilde{V}_x$, $\Delta \tilde{V}_r$ and $\Delta \tilde{V}_t$) of the near-casing flow caused by a two-groove treatment (consisting of grooves at locations C and D) and a three-groove treatment (consisting of grooves at locations A, C and D) are shown. Constant radius cuts were taken from the grooved wall CFD model at $5\% tc$ and the plots were created by subtracting the equivalent smooth-wall case, with the compressor operating near the smooth-wall stall point ($\phi=0.48$).

Figure 6.7: Four graphs showing the variation in stalling flow and pressure rise coefficients with mean tip clearance of the smooth wall and grooved cases with one and four grooves. Concentric and eccentric cases are shown on separate plots for clarity. Stall margin and pressure rise improvement values are shown as percentages in colour-coded boxes close to the marker they are calculated for.

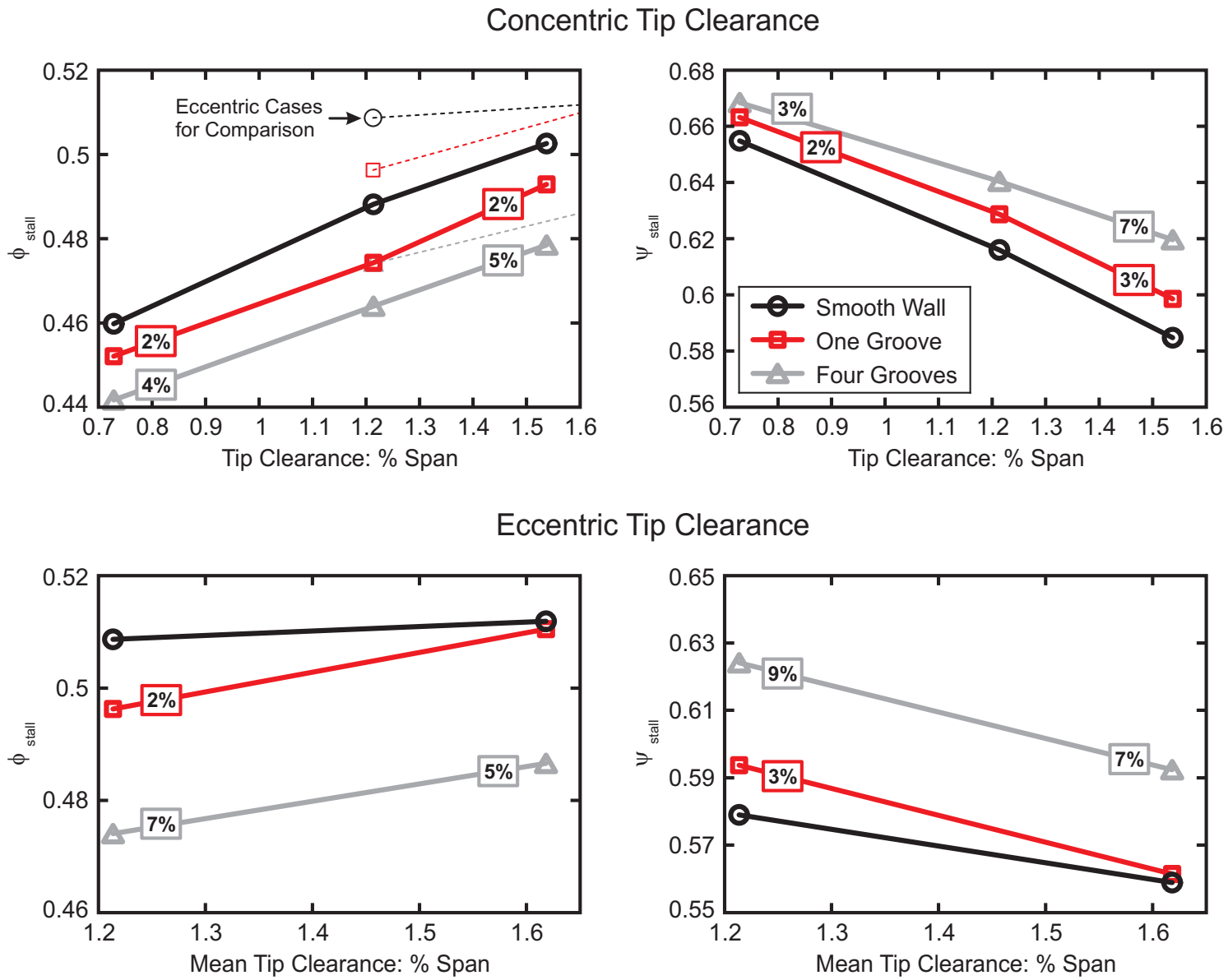
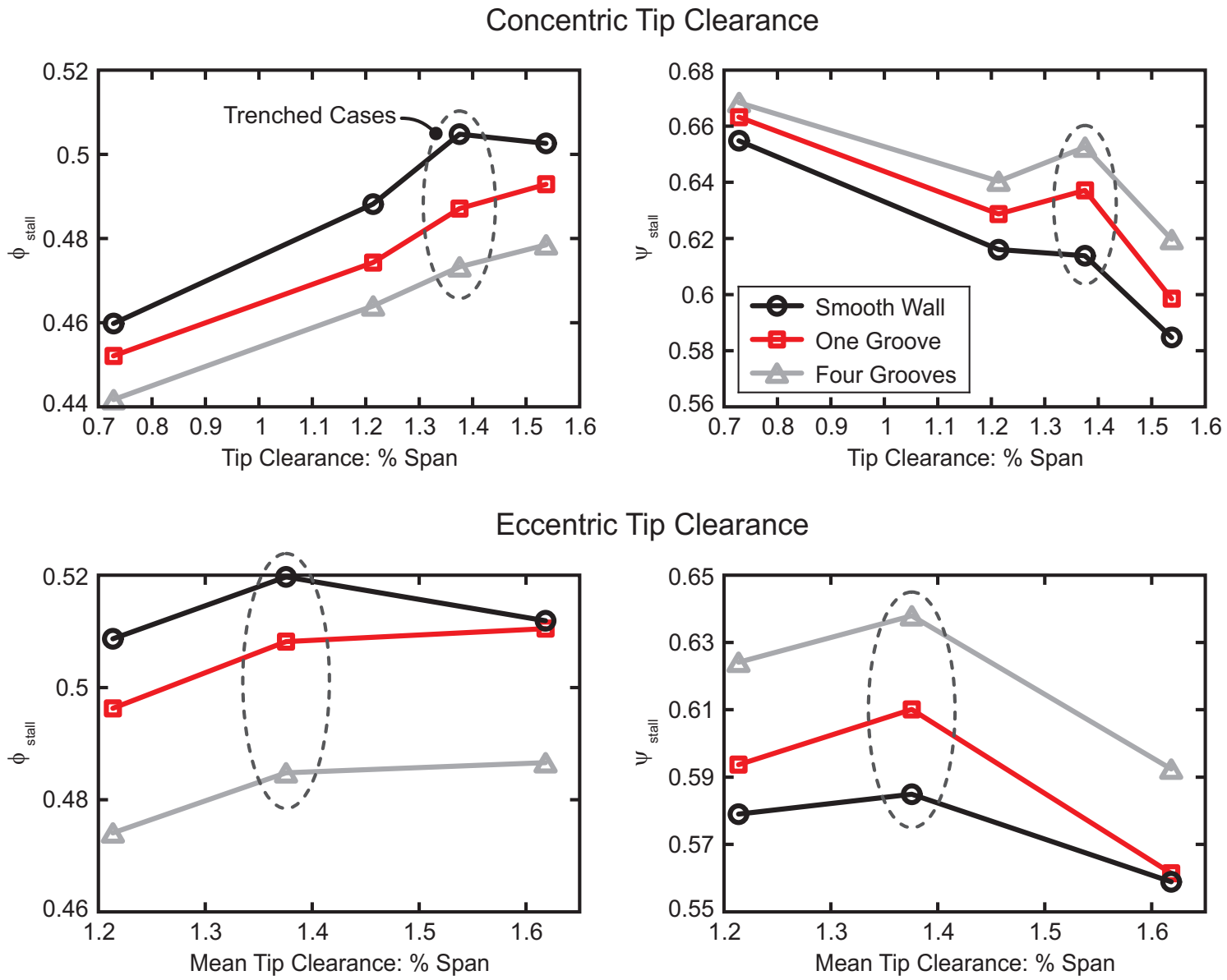


Figure 6.8: Four graphs showing the variation in stalling flow and pressure rise coefficients with mean tip clearance of the smooth wall and grooved cases with one and four grooves. Concentric and eccentric cases are shown on separate plots for clarity and the trenced results are also shown, highlighted with dashed lines.



Chapter 7

Axial Slot Casing Treatments

Chapters 5 and 6 considered the impact of circumferential casing grooves on the overall performance and detailed flow field of an axial compressor. This chapter extends the study to axial casing slots. The slots are cut into the casing adjacent to the rotor leading edge plane and are skewed from radial as shown in Figure 7.1. This figure also shows the dimensions used to describe the slot geometry.

The chapter is divided into three parts. The first part is a parametric study of the impact of the slot geometry on compressor performance. The second part is a flow study, which considers the affect of casing slots on the core and near-casing flows and investigates the flow inside the slots themselves. The third part considers the application of these results to casing treatment design, with reference to published work. All the work in this chapter is based on the Natal compressor, which is introduced in Chapter 3.

7.1 Casing Slot Parametric Study

These experiments investigate the impact of varying the slot depth (dimension d), slot width (w_s) and the width of the land between the slots (w_l) on compressor performance (see Figure 7.1 for definitions of these dimensions). The usefulness of porosity as a design parameter is then discussed. The present work adds to that of Seitz (1999) discussed in Chapter 2. Following Seitz' recommendations, the upstream slot length (l_u) is 77% $c_{x,r}$, the downstream length (l_d) is 24% $c_{x,r}$ and the skew angle (α) is 60° throughout this chapter.

7.1.1 The Optimum Slot Depth

This section investigates the impact of varying the slot depth (d). Eight depths of 15, 32, 41, 50, 54, 64, 73 and 83% $c_{x,r}$ were tested. The slot width (w_s) and land width (w_l) were 31 and 27% $c_{x,r}$ respectively. The performance of each treatment was measured using the method described in Chapter 3. Four performance parameters are used to present the results; improvements in stall margin (SMI), pressure rise at stall (PRI), maximum efficiency (MEI) and design point flow rate (DPFI). The smooth wall is included a slot with zero depth.

The results are presented in Figure 7.2. When the slots are shallower than 25% $c_{x,r}$, the casing treatment is entirely deleterious to compressor performance (all parameters are negative). When the slot depths are between 25 and 65% $c_{x,r}$, deeper slots offer better performance, with the stall margin and pressure rise improvements reaching 15 and 12% respectively at 65% $c_{x,r}$. When the slots are deeper than 65% $c_{x,r}$, the stall margin and pressure rise improvements are maintained, but the efficiency and flow rate both reduce. The smallest reductions in design point flow rate and efficiency improvement (-0.3%) occur with slots between 50 to 65% $c_{x,r}$ deep.

The results show an optimum slot depth of about 60% $c_{x,r}$. At this depth, the stall margin and pressure rise improvements are maximised, while the efficiency and flow rate reductions are minimised. The trends in pressure rise at stall and stall margin improvement match each other, and so do the trends in flow rate and efficiency (as seen in the casing groove studies). The next section considers the width of the treatment slots.

7.1.2 The Optimum Slot Width

These experiments investigate the effect of changing the slot width (dimension w_s) on the four performance parameters considered in the previous section (SMI, PRI, MEI and DPFI).

Three slot widths of 18, 31 and 57% $c_{x,r}$ were tested. The land width (w_l) was 27% $c_{x,r}$ and the slot depth (d) was 52% $c_{x,r}$ (as close to the optimum 60% $c_{x,r}$ as possible). Since the land width was constant, increasing the slot width reduced the total number of slots. The results are shown in Figure 7.3. The smooth wall is included as a slot with zero width.

As the slot width increases from 0 to 31% $c_{x,r}$, the stall margin improvement increases linearly. Once the slots are wider than 31% $c_{x,r}$, the stall margin remains constant. The maximum stall margin improvement generated is 16%. The trend in pressure rise at stall matches that of the stall margin improvement; the maximum pressure rise improvement is 12%. The trends in efficiency and flow rate are again similar. Both these parameters are optimised when the width of the slots is 30% $c_{x,r}$. At this optimum, the efficiency improvement is -0.4% and the flow rate improvement is -0.3%.

The results suggest there is an optimum slot width of 30% $c_{x,r}$. All performance parameters are lower with narrower slots, while wider slots reduce efficiency and flow rate without gaining stall margin or pressure rise at stall. As previously, the trends in stall margin and pressure rise, and efficiency and flow rate, show the same trends. The next section considers the land width.

7.1.3 The Effect of Varying the Land Width

This section investigates the impact of varying the width of the land between the casing slots (dimension w_l) on the four performance parameters (SMI, PRI, MEI and DPFI). Five land widths were tested: 8, 20, 27, 47 and 85% $c_{x,r}$. The slot width (w_s) and slot depth (d) were 31 and 52% $c_{x,r}$ respectively (both are as close as possible to the optimum values). Increasing the land width with constant slot width thus reduced the total number of slots. The results are shown in Figure 7.4.

In general, the treatments with the narrowest lands generate the greatest stall margin improvements. The narrowest land case generates a stall margin improvement of 30%, which reduces progressively to 10% for lands wider than 50% $c_{x,r}$. The trend in pressure rise at stall matches the trend in stall margin; the treatment with the smallest land gives the greatest pressure rise improvement (of 20%). The widest land case generates the smallest stall margin and pressure rise improvements (both around 6%).

The efficiency trend opposes that of stall margin; narrower lands cause greater efficiency reductions. The case with the widest land generates the best efficiency improvement (least efficiency loss) of -0.2%. The efficiency of the treated cases becomes especially low when

the land is narrower than 20% $c_{x,r}$, with the efficiency improvement reducing to -0.8%. As previously, the trend in flow rate matches that of efficiency.

There is a trade off between the efficiency and stall margin generated by the casing treatment as the land width changes. Narrow lands cause large stall margin improvements but low efficiencies and *vice versa*. This allows the performance of slotted treatments to be tuned, although lands narrower than 20% $c_{x,r}$ should be avoided because they cause large efficiency reductions. The next section uses the data from these land and slot width tests to ascertain the importance of porosity as a design parameter.

7.1.4 Porosity as a Design Parameter

The porosity of a slot-based treatment is the percentage of the casing wall circumference that is cut away to form the slots. It is sometimes used as a design parameter and is defined in Equation 7.1 below. This section evaluates the usefulness of porosity as a casing treatment design parameter, by re-plotting the data from the land and slot width tests above. The effect of changing porosity on the four performance parameters (SMI, PRI, MEI and DPFI) is shown in Figure 7.5. The smooth wall is included as a case with zero porosity.

$$\text{Porosity} = 100 \times \left(\frac{w_s}{w_s + w_l} \right) \quad (7.1)$$

In general, the higher porosity treatments generate a greater stall margin and a lower efficiency. The trends are approximately linear, with a 10% increase in porosity giving a 3% increase in stall margin and a 0.1% decrease in efficiency.

If the performance of casing slots varied completely linearly with porosity, this would suggest that steady effects are more important to the functioning of the slots than unsteady effects and the circumferential length-scales that would create them (i.e. the precise land and slot widths, or the number of slots). However, there are two significant outliers to the linear trends. The first is the narrowest slot width case (labelled in the figure), which has a lower efficiency than the linear trend predicts. The second is the widest slot width case, which has a lower stall margin than the linear trend predicts. These outliers occur because porosity combines land and slot width, hiding the different impacts of these two parameters on treatment performance. The outliers indicate that unsteady effects may be important to the functioning of casing slots. The relative importance of unsteady and steady flow effects will therefore be considered in later sections.

7.2 Initial Experiments

Before studying the detailed flow dynamics, it is necessary to check that two possible complications do not affect the results. The first of these is changes to the stall inception mechanism, and the second is the circumferential phase angle of the slotted casing.

7.2.1 Changes to the Stall Inception Mechanism

Installing casing grooves did not change the stall inception mechanism of the Natal compressor (Chapter 5). However, casing slots can enable operation at much lower flow rates than grooves, so this section investigates whether slots can alter the stall inception pattern. The most effective slotted wall (29% SMI) could not be tested because the land width was too small to mount transducers on, so another effective treatment (16% SMI) was used to provide the best possible test. For this treatment (slotted wall 'A' hereafter), the land width (w_l), slot width (w_s) and slot depth (d) were 27, 31 and 52 % $c_{x,r}$ respectively, giving 100 slots in total. The stall inception mechanism was measured using six high-frequency pressure transducers mounted flush with the casing wall as described in Chapter 3. The results are shown in Figure 7.6 alongside schematics of the slot and transducer layouts.

The plots show that the compressor stalls with a spike-type inception when both smooth and slotted walls are installed. In both cases, the pressure of the near-casing flow rises and then falls as the spike passes (before returning to normal as the spike moves away), which agrees with the groove results. However, in the slotted wall case, the blade-passing pressure signals *before stall* are much more unsteady than they are in the smooth and grooved wall cases, and spikes also appear regularly before stall, only to disappear before traversing the annulus (in the smooth and grooved wall cases the first spike to form usually causes stall). These pre-stall spikes in the slotted case are strongest at transducer one (labelled in Figure 7.6) and occur once per revolution, indicating that they occur when "a particular part of the rotor is adjacent to a particular part of the casing", as observed by Day (1993b) for spike-initiated stall. Unlike the smooth and grooved wall cases, the slotted wall also slightly reduces the propagation speed of the spikes (indicated by the gradient of the black dashed lines in the figure reducing).

These results show that casing slots do not fundamentally change the stall inception mechanism of the Natal compressor, but do change the pre-stall behaviour and reduce the propagation speed of spikes. Casing slots can prevent spike formation (like grooves) *and* destroy and retard the progress of emerging spikes (unlike grooves).

7.2.2 Casing Treatment Phase Angle

It is possible that the performance of casing slots, being discrete in the circumferential sense, could be affected by their position relative to other stationary components, such as the stators. To check that this is not the case, slotted wall 'A' was rotated through six equispaced steps across one stator pitch. At each step, the stall inception mechanism and stall point was measured. In all cases, the compressor stalled at the same flow coefficient via a spike inception originating at the same location. The performance of the casing slots is therefore independent of phase angle relative to the stator blades.

The parametric study results are therefore not affected by changes to the stall inception mechanism or the phase of the casing slots. The following sections investigate the impact of casing slots on the compressor flow field to try and explain the parametric study results and allow comparison with casing grooves.

7.3 Core Flow Effects

The work on casing grooves in Chapter 5.3 found no direct link between stall margin improvement and outflow blockage or blade loading. This section extends this work to slots.

7.3.1 The Outflow Blockage

Seitz (1999) found that while casing slots located entirely above the rotor blades reduced the outflow blockage, forward positioned slots (located over the leading edge, as here) did not. However, Lu *et al.* (2009) suggested that slots over the leading edge do reduce blockage. This section determines the impact of casing slots on rotor outflow blockage and also considers the blockage at low flow rates, when the slots are stabilising the compressor.

The Impact of Casing Slots on Blockage The outflow blockage was measured near the smooth wall stall point ($\phi=0.48$) for the smooth wall and the second most effective treatment (19% SMI). This treatment (slotted wall 'B' hereafter) has the same depth (d) and slot width (w_s) as slotted wall 'A', but a land width (w_l) of 20% $c_{x,r}$ instead of 27% $c_{x,r}$, giving 114 slots in total. The axial velocity of the rotor outflow was measured by traversing a hotwire close to the rotor trailing edge as described in Chapter 3. The overall level of blockage was then quantified for each blade passage using the method of Khalid *et al.* (1999) and averaged over 34 blade passages. Contours of normalised axial velocity for the smooth and slotted

wall cases are shown in the upper part of Figure 7.7. The velocity is normalised by mean blade speed to allow comparison with the grooved wall cases in Figure 5.5. The calculated overall blockage level is also shown.

The flow away from the casing is unaffected by the presence of the casing slots. Near the casing, the blockage associated with the tip leakage flow (arrowed in the figure) moves slightly closer to the suction surface and its radial extent reduces slightly. These changes are similar to those caused by casing grooves in locations A and B, when the grooves are close to the area covered by the slots (see Figure 5.5). As a result of these slight differences, the overall blockage level reduces by only 0.2% when the slotted wall is applied. The impact of the slotted wall on blockage is therefore small, so there is no *clear* link between blockage reduction and stall margin improvement at the smooth wall flow coefficient.

Blockage at Low Flow Rates Effective casing grooves generate stall margin improvements of 5 to 7%, while casing slots can generate a 30% stall margin improvement. Therefore, while the blockage does not greatly increase between the smooth and grooved wall stall points, it may increase between the smooth and slotted wall stall points.

To investigate this, the outflow blockage was measured in three cases with the compressor operating close to the stall point of *each case*. The first case was the smooth wall, the second was slotted wall 'B' (19% SMI) and the third was the most effective slotted wall (29% SMI). This treatment (slotted wall 'C' hereafter) has the same depth (d) and slot width (w_s) as slotted wall 'B', but a land width (w_l) of $8\% c_{x,r}$ instead of $20\% c_{x,r}$, giving 150 slots in total. The blockage was measured and quantified as previously, but the axial velocity was normalised by the mass-averaged axial velocity at the inlet (instead of the mean blade speed) to remove the effect of the different flow coefficients in each case.

The data is plotted in the lower part of Figure 7.7. The smooth wall plot presents the same data as the smooth wall plot in the upper part of the figure to allow comparison (so the blockage patterns are the same). The blockage level with slotted wall B installed is 13.3% and with slotted wall C installed is 13.8%. At these extremely low flow rates the blockage can vary considerably between blade passages. Most of the increased blockage occurs near the casing, particularly for wall C, where large separations increase blockage levels to 15.6% in some blade passages.

These results show that there is no simple 'critical blockage level' at which the compressor stalls; indeed, the blockage increases as the stall margin is extended. This agrees with previous conclusions: there is no clear link between blockage reduction and compressor stability. These large areas of near-casing blockage would also decrease the through-flow near the

tips of any downstream rotors, potentially reducing the stability of subsequent blade rows (Simpson, 2005). Therefore, casing treatments that generate large stability improvements in single-stage environments may not be as effective in a multi-stage environment.

7.3.2 The Blade Loading

This section studies the effect of casing slots on the blade loading. Since the slots are circumferentially discrete, time-mean and unsteady effects are both considered.

Blade Loading Distributions The loading distributions were extracted from the computational model (as in the work on casing grooves) with the smooth wall and slotted wall 'B' installed. The flow coefficient was set near the smooth wall stall-point ($\phi=0.48$) and the loading distributions were compared at 98% span (near the blade tip). This location was chosen because the impact of casing slots is clearest near the blade tips. The results are shown in Figure 7.8.

The time-mean impact of the slots on the blade loading distribution is shown in the upper plot of Figure 7.8. The main effect of the slots is to move the loading slightly aft relative to the smooth wall case. Comparing these results with grooved wall 'A' (a single groove near the leading edge) in Figure 5.6 shows that while both slots and grooves located near the leading edge move the time-mean blade loading aft, the slotted wall has a *smaller* impact than the grooved wall. The stall margin improvement generated by the slotted wall is four times larger than the grooved wall, so there is no *clear* link between the impact of casing slots on the time-mean blade loading and the stall margin improvement they generate (as found in the work on grooves).

The unsteady impact of the slots on the blade loading distribution is presented in the lower plot. This shows loading distributions at twelve equispaced instants during a slot-passing, with a schematic showing the location of the blade leading edge at each instant. The results show that large and complex changes in blade loading occur as the blade passes a slot. The instantaneous blade loading distributions deviate much more from the smooth wall case than the time-mean results. As seen in the grooved wall cases, these unsteady changes in blade loading are confined to the tip region of the blade. The next section investigates the unsteady blade loading in more detail. The plots also show that the overall pressure rise is slightly greater when the blade leading edge is adjacent to a slot; this is investigated in Section 7.4.

Unsteady Blade Loading It is difficult to analyse the unsteady blade tip loading using the plots in Figure 7.8, so the changes in blade loading with time *at a number of chord-wise locations* were considered. The blade loading at six chord-wise locations was found by calculating the normalised pressure difference across the blade (normal to the camber-line) for the slotted and smooth-wall cases. The smooth-wall value was then subtracted from the unsteady slotted wall data to form a 'difference plot' of blade loading at each chord-wise location. To aid interpretation of the results, this process was performed for two slot-based treatments; slotted wall 'B' (three slots per blade) and a similar treatment with only one slot per blade row. The blade loading differences are plotted against time in Figure 7.9.

The upper graph in Figure 7.9 shows the impact of the one slot-per-blade treatment on the blade loading at each location. As the blade leading edge approaches a slot (0 to 45% blade passing in the figure) the effect of the slots on the blade loading is small. However, as the blade leading edge moves over the slot entrance (45 to 65% blade passing) the loading on the *whole blade upstream of mid-chord* reduces progressively. Once the leading edge has passed the slot, the blade loading upstream of mid-chord rises rapidly before falling back to the smooth wall value (65 to 95% blade passing). This cycle then repeats. The lower graph in Figure 7.9 shows the impact of slotted wall 'B'. In this case, the blade loading upstream of mid-chord again reduces as the blade leading edge crosses the slot entrance. The loading then increases (as in the single slot case) but the next slot is then reached and the blade loading falls rapidly again. This causes a continuous, *in-phase*, blade loading oscillation. Both treatments have little effect on the loading downstream of mid-chord.

It is not clear from these results what causes the loading increase after the blade leading edge has passed the slot. To investigate this, the blade loading was evaluated at a large number of chord-wise locations and plotted as a contour map showing the impact of the slots on the blade loading at any point on the blade with the blade in any position. These plots are shown in Figure 7.10. The contour maps show that the blade loading increase occurs as the part of the blade near 20% chord passes the slot. This occurs after the leading edge passes the slot (due to the blade stagger angle).

These results show that during a slot-passing, the blade loading falls as the leading edge passes the slot, then rises as the part of the blade near 20% chord passes the slot, and then falls back toward the smooth wall value until the next slot-passing occurs. In cases where the slots are close together (like slotted wall 'B') the next slot may be reached before this process is complete, causing a continuous oscillation in blade loading. The present slots extend from the leading edge to 25% chord and vary the blade loading up to mid-chord; it is also interesting that the loading variations in this region are in-phase along the blade.

These changes in blade loading should be considered during compressor design because

their magnitude reaches 60% of the inlet dynamic head (see Figure 7.9) and they occur in the forward part of the blade tip. This is the worst part of the blade to excite from a vibration perspective, so fatigue problems could occur (Cumpsty, 1989a). It is tempting to use an integer number of slots per blade when designing slots with CFD (to simplify the calculation), but this would excite all the rotor blades in-phase, worsening the problem. The variations in blade loading and overall pressure rise may also generate unacceptable noise (the Natal compressor is much noisier when casing slots are installed). Lapworth (2006) suggested varying the slot geometry around the annulus to reduce these problems, but the parametric study results in the present work suggest that this could reduce the performance of the treatment.

This section has shown that the time-mean impact of casing slots on the blade loading is similar to the impact of casing grooves: the loading is moved slightly aft. By contrast, the unsteady changes in blade loading caused by casing slots are large and could cause noise and blade vibration. The next section examines the changes to the near-casing flow that cause these variations in loading.

7.4 Near-Casing Flow Effects: Unsteady Aerodynamics

This section investigates the impact of casing slots on the near-casing flow in order to explain the results presented thus far and allow comparison with the casing groove results in Chapter 5. Before studying the unsteady fluid dynamics however, it is necessary to introduce the methods used to present the results.

Slotted wall 'B' will be studied throughout this section. To display the results, each slot-passing is divided into six equi-spaced time instants (t_1 to t_6), as shown in Diagram 7.1 below. To aid comparison, each plot is cropped so the blade location matches the groove results. The slots thus appear to move from right to left.

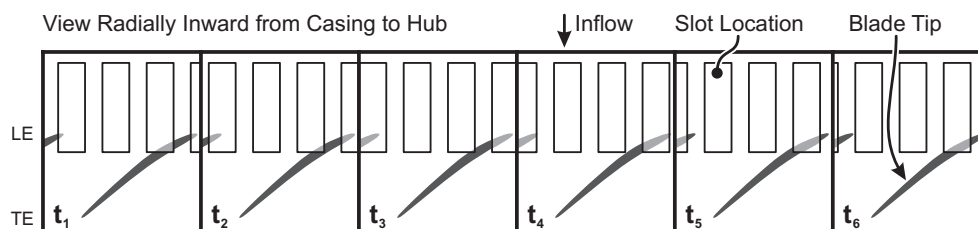


Diagram 7.1: The six time instances (t_1 to t_6) across a slot-passing.

Slotted wall 'B' has three slots per blade row, so by considering the three slots in turn, a given slot can be observed during a whole *blade-passing* using data from just one *slot-passing*. The interaction between the slot and near-casing flow during a *blade-passing* divides into four periods. These are defined below and presented graphically in Figure 7.11.

1. During period 1, the blade leading edge passes the slot entrance. This period occurs for the right-most slot (shaded in red in Figure 7.11) during t_1 , t_2 , t_3 and t_4 .
2. During period 2, the part of the blade near 20% chord passes the slot entrance. This period occurs during t_5 , t_6 and then t_1 again, but considering the next slot to the left (as shown in the figure).
3. During period 3, the tip leakage vortex passes the slot entrance. This period occurs during t_2 , t_3 , t_4 , t_5 , t_6 and t_1 , again skipping one slot to the left between t_6 and t_1 .
4. During period 4, a weak interaction occurs while slot awaits the next blade passing. This period occurs from t_2 to t_6 .

The next section considers the impact of the slots on casing static pressure, to allow comparison with the blade loading results.

7.4.1 The Impact of Slots on Casing Static Pressure

In Chapter 5, the impact of casing grooves on blade tip loading was linked to changes in the casing static pressure. This section applies the same analysis to casing slots. The casing static pressure was extracted from CFD solutions of the smooth wall and slotted wall 'B' near the smooth wall stall point ($\phi=0.48$) for the time-mean flow and the six equi-spaced instants introduced above. The time-mean smooth-wall cut was then subtracted from the unsteady and time-mean slotted wall cuts to create 'difference plots' showing the impact of the slots on the casing static pressure (this differencing process is presented graphically in Figure 5.7). The resulting plots are shown in Figure 7.12, and are representative of changes radially across the tip clearance.

During period one (t_1 to t_4), the blade leading edge moves across the slot entrance. The pressure of the flow near the blade tip and suction surface increases (label '1') indicating that the tip leakage flow (which is normally at a low pressure) is interrupted by the slot. As the leading edge crosses the slot, the pressure of the flow near the blade pressure surface decreases ('2') indicating flow entering the slot. These effects cause the continuous reduction in blade loading as the leading edge passes the slot that was found in Section 7.3.2.

During period two (t_5 to t_1 again), the part of the blade near 20% chord passes the slot entrance. The increased pressure shown by label '1' dissipates and the region of reduced pressure at '2' moves to the suction surface with the slot ('3'). The pressure near the pressure surface then increases as the blade moves past the slot corner ('4'). These effects cause the loading increase reported in Section 7.3.2. Throughout period two, the pressure over the whole slot entrance reduces as it passes the low-pressure tip leakage flow ('5').

During period three (t_2 to t_1), the slot interacts with the tip leakage flow. The red areas at '6' and '7' indicate that the slot interferes with the low pressure core of the tip leakage vortex, while the blue area at '8' indicates that the tip leakage vortex grows rapidly downstream of the slot. This causes the increased loading downstream of the slot (shown in Figure 7.8) as seen in the case of the leading-edge groove 'A' in Chapter 5.4.4 (although the interaction with casing slots is unsteady). During period four (t_2 to t_6) the slot interacts weakly with the near-casing flow until the next blade arrives to restart the interaction.

The effect of these unsteady processes on the time-mean casing static pressure is shown by the upper plot in Figure 7.12. The features at label '9' are those responsible for the loading changes during the first two periods. The low-pressure region upstream of the blade row at '10' is caused by the pressure drop during the second period. The third period, during which the slot interferes directly with the tip leakage flow, causing the tip leakage vortex to grow rapidly downstream of the slot, is shown by the red and blue lines at '11' and '12'. The weak interactions that occur during period four are visible at '13'.

These results provide insights into the blade loading results in Section 7.3.2. The blade loading decreases as the leading edge crosses the slot because the low-pressure tip leakage flow is diverted into the slot. The loading then increases because of the interaction between the slot and the part of the blade near 20% chord. This interaction also causes the small oscillations in overall pressure rise observed in Section 7.3.2. The area of increased static pressure near the pressure surface ('4'), which increases the blade loading, dissipates toward the trailing edge by t_3 and increases the exit pressure. The exit pressure then falls again between t_5 and t_6 . The oscillation in overall pressure rise is therefore a delayed effect of the features that cause the loading increase.

The *time-mean* impact of the slots on the blade loading and casing static pressure is similar to that of a casing groove located near the leading edge. The blade loading is moved aft, interfering with the development of the tip leakage vortex near the leading edge and causing the vortex to grow rapidly downstream of the slots. By contrast, the *unsteady* interactions between the slots and the near-casing flow are stronger than is seen with grooves, and cause larger variations in blade loading. Slots also alter the flow upstream of the rotor, which grooves cannot do.

A time-dependant pressure difference has also been observed between adjacent slots. This pressure difference will apply a force to the lands between the slots and could cause them to crack in an engine environment (Lapworth, 2006). This potential fatigue problem should be considered during design.

The impact of the slots on the casing static pressure has been linked to the blade loading results and compared to the work on grooves. The next section investigates the effect of slots on the velocity of the near-casing flow.

7.4.2 Effect of Slots on Near-Casing Flow Velocity

To study the impact of slots on the velocity of the near-casing flow, data was taken from CFD solutions for the smooth-wall and slotted wall 'B' near the smooth wall stall point (as in the previous section). Constant radius cuts were taken at 5% tc for the time-mean flow and three of the six instances used previously (t_1 , t_3 and t_5), before difference plots of axial, radial and tangential velocity were made. These plots are representative of the impact of slots on the whole near-casing flow, and are shown in Figure 7.13.

As the leading edge moves over the slot entrance, the axial velocity of the tip leakage flow increases at label '1' (indicating interruption of the axially reversed tip clearance flow) and the radial velocity increases near the pressure surface at '2' (indicating flow diverting into the slot). Flow also starts to emerge from the slot slowly over the whole slot area at '3' and more rapidly near the blade suction surface at '4'. The tangential velocity also increases over the downstream area of the slots.

As the part of the blade near 20% chord passes the slot, the flow emerging radially from the whole slot area reduces, but the flow moving in and out of the slot near the pressure and suction surfaces remains vigorous ('5'). As the blade passes the slot corner at t_1 , a complex interaction occurs between the slot and the tip leakage flow ('6' and '7') during the loading increase identified in previous sections. The slot also reduces the tangential velocity of the near-casing flow upstream of the blade row (best seen on the time-mean plot at '12').

After the blade passing, the impact of the slots on radial velocity is small, but the axial and tangential velocity plots still show interactions between the slot, inflow and tip leakage flow. The effect of these interactions is clearest in the time-mean plots. The time-mean axial velocity plot shows that the slots increase the axial velocity of the near-casing flow upstream of the blade row by up to 10% of the mid-span blade speed ('8'). The interaction of the slots with the tip leakage vortex is visible at '9' and '10'. The time-mean tangential velocity plot

shows that the slots increase the tangential velocity of the flow near 20% chord ('11'). The slots have little effect on the flow downstream of mid-chord.

As seen in previous sections, the time-mean impact of the casing slots is similar to a groove located near the leading edge, but the unsteady interactions are stronger. Slots also alter the upstream flow, which grooves cannot do. The literature review in Chapter 2 suggested that stability may be improved by increasing through-flow and reducing cross-flow of the tip clearance flow (or increasing axial velocity and tangential velocity). Like the casing grooves, the slots have this effect on the flow in the tip clearance.

The next section investigates the impact of casing slots on the near-casing flow structure.

7.4.3 Changes to Near Casing Flow Structures Caused by Slots

This section considers the effect of casing slots on the detailed structure of the near-casing flow (presented for the smooth wall case in Figure 5.10). As in the groove tests in Chapter 5, experimental oil-flow visualisation and cuts through the computational model at 5% tc showing the absolute flow field near the smooth wall stall-point are used. The computational data is gathered with slotted wall 'B' installed, at three time instances (t_1 , t_3 and t_5 as previously). The results are plotted in Figure 7.14, where the colour bars match those used for the grooved cases.

The computational results show that slots have a much larger impact on the near-casing flow structures than grooves do (see Figure 5.16). The two-dimensional separation line between the tip leakage and inflow is obliterated, and the three-dimensional separation point is swallowed by each successive slot. The experimental flow visualisation shows that the black line is not present on the land between the slots. At the same axial location as the black line on the smooth wall however, high-speed flow appears to enter the slot (label '1') and there is some scouring on the land ('2'). The time-mean CFD (overlaid on the flow visualisation) shows a saddle point between the slots ('3') because the separation point does not cross the land, agreeing with the disappearance of the black line.

These results show that, like the leading edge groove 'A' in Figure 5.16, the slots obliterate the black line and interrupt the separation line in their vicinity. However, while the separation line and tip leakage vortex re-grow downstream of the casing groove, this does not happen when slots are installed, as the tip leakage vortex remains fragmented. The impact of the casing slots on the tip leakage flow is thus stronger than a groove near the leading-edge, although downstream of mid-chord the impact of both treatments is small.

7.5 Casing Slot Internal Flow

Having studied the complex impact of casing slots on the core and near-casing flows, this section considers the less complex flow-field contained within the slots themselves.

7.5.1 Pressure Oscillations inside Casing Slots

Pressure oscillations were detected inside early casing slot treatments (located entirely over the blade row) by Osborn *et al.* (1971) and Prince *et al.* (1974), but these authors deemed them less important for stability than the flow recirculating through the slots. However, the flow rate through the present slots (located forward of the blade row) is much smaller than in the early designs (Seitz, 1999), so this section investigates the importance of pressure oscillations in the present configuration.

The Pressure Oscillations To measure the pressure oscillations, a high-frequency pressure transducer was installed in the rear of the casing slots at the same axial location as the blade leading edge. The static pressure of the flow at the same location was also extracted from the CFD model of slotted wall 'B'. The results are shown in Figure 7.15. The plot shows clear pressure oscillations occurring within the slots. Oscillations '1', '2' and '3' (labelled in the figure) occur between blade passings. They are clearly visible in the computational and experimental results, which agree very well. Oscillation '4' occurs as the blade passes the slot entrance. It is indistinct in the experimental data and obscured in the CFD results.

One possible source of these oscillations is a quarter wave resonance governed by the equation $a = f\lambda = 4fd$, where d is the slot depth. Re-arranging this equation and evaluating constants for the Natal compressor gives $n(d + e) = 0.0461897$, where n is the number of oscillations per blade passing and e is a correction for the effective resonant slot depth. For four oscillations in one blade passing, $d + e = 11.5\text{mm}$. The slot depth (d) is 11.2mm, which gives a reasonable 0.3mm for the effective length correction. These results suggest that the oscillations are indeed caused by a quarter-wave resonance. Similar analysis of the oscillations in the old slot-based treatment tested by Prince *et al.* suggests that these were also caused by a quarter-wave resonance.

The Importance of the Pressure Oscillations If the pressure oscillations have a large effect on the performance of slot-based treatments, the design of slots in high and low-speed compressors could be quite different due to the different blade passing frequencies. To measure the importance of the pressure oscillations, the blade passing frequency was changed

to alter the number of oscillations per blade passing. The Reynolds Number was always higher than 1×10^5 , so the smooth-wall stall point was not affected by the varying rotational speed (see Section 3). The treatment with the deepest slots from Section 7.1 was used because its resonant frequency is lower than slotted wall A, B or C, which makes the oscillations clearer. The deep slots are similarly effective and have the same dimensions as slotted wall 'A', except that the slot depth (d) is 83% $c_{x,r}$ instead of 52% $c_{x,r}$. The blade passing frequency was set to 1440, 1550, 1650, 1760 and 1860 Hz (full speed). At 1440 Hz, there are three pressure oscillations per blade passing, while at 1860 Hz, there are two. The 1650 Hz case is situated between these two cases and is therefore 'mis-tuned'. The effect of these changes on the performance of the casing treatment is shown in Figure 7.16, with schematics showing the slot pressure oscillations.

The results show that the slot pressure oscillations have little impact on the stall margin, pressure rise, efficiency or design point flow rate improvement generated by the casing slots. The performance of the mis-tuned case (1650 Hz, black markers in the figure) is slightly lower than the other cases, but the differences are small. Comparing these small changes with the parametric study results in Section 7.1 shows that changing the slot geometry has a much larger impact on the performance of casing slots than the pressure oscillations do. This result agrees with the results for changing slot depth in Section 7.1, where there were no increases in performance at more resonant slot depths.

Since the importance of pressure oscillations inside the slots is small, the next section considers the flow patterns inside the slots.

7.5.2 The Flow Field inside Casing Slots

Brignole *et al.* (2008) suggested that the flow in the slot could be split into two parts: direct leakage across the blade tip (or interaction with the blade-to-blade flow field) and recirculation through the slot. To investigate the behaviour of these two flow fields, longitudinal cuts inside the slots at half-width were extracted from the CFD model of slotted wall 'B'. The flow coefficient was set close to the stall point of the treated compressor, at $\phi = 0.44$. The flow on the cuts was visualised with vectors coloured by absolute velocity. Data was extracted for periods one to four (introduced in Section 7.4) and the time-mean solution. The results are shown in Figure 7.17.

The interaction between the slot and the blade-to-blade flow is shown by label '1'. It varies throughout the blade passing. The interaction is vigorous during periods one and two, as flow is forced into the slot and across the blade tip while the blade passes the slot entrance.

The interaction is weak during period three, when the slot entrance is adjacent to the low-pressure tip leakage flow, and period four, when increasing pressure near the slot entrance caused by the next approaching blade simply drives flow into the slot. The interaction of these effects with core flow was presented in Section 7.4.

The recirculation of flow through the slot is shown by label '2' in Figure 7.17. Unlike the interaction with the blades, this flow is similar in all the plots, indicating it is approximately steady. To check this, the velocity of the recirculating flow at point 'P' in Figure 7.17 was investigated by extracting the absolute velocity from the computational model and measuring it using a single-element hotwire (yawed to gain absolute velocity, see Section 3). These results are plotted in Figure 7.18. They show that flow recirculates with an average velocity of around half the mid-span blade speed, with superimposed oscillations caused by the blades passing the slot entrance.

These results show that while the interaction of the slots with the near-casing flow is complex and unsteady, the flow field within the slots themselves principally a much simpler quasi-steady recirculation. The agreement between the computational and experimental results is also reassuring from a validation perspective.

The next section considers the impact of the slots on entropy in order to understand why casing slots reduce the efficiency of the compressor.

7.6 Entropy Generation by Casing Slots

This section considers the impact of casing slots on efficiency by investigating the entropy they generate. The analysis method is similar to that used on casing grooves in Chapter 5, but here axial cuts through the computational domain are used for clarity. Data was extracted from the computational model of the smooth wall and slotted wall 'B' near the design point ($\phi=0.58$). Cuts were taken at two axial locations: 12% chord, to show the formation of the tip leakage vortex and the flow entering the slots, and 50% chord, to show the developed tip leakage vortex. In the slotted wall case, data was extracted at two time instants to show the flow throughout a blade passing: instant t_3 , when the blade leading edge has just crossed the slot, and t_6 , when the leading edge has just crossed the land. The results are shown in Figure 7.19. The colour map is designed to allow comparison with the casing groove results in Figure 5.17.

At 12% chord (left-hand side of the figure), the tip leakage vortex is forming in the smooth wall case. In the slotted case, a complex interaction between the slot and tip leakage flow

occurs, which generates entropy through corner separations and radial mixing. This high-entropy flow is then drawn up into the recirculating flow in the slot (see previous section), where it is mixed out while decelerating, before being injected into the core flow upstream of the blade row. This further increases the entropy of the flow near the casing. Casing slots thus generate much more entropy than grooves.

At 50% chord (right-hand side of the figure), the tip leakage vortex is well developed in the smooth wall case. In the slotted case, the slots have damaged the structure of the vortex, so it appears as an unsteady region of swirling high-loss flow. The high levels of entropy generated by the interaction between the near-casing flow and the slots increase the entropy over the whole near-casing region.

These results show that the main sources of loss due to casing slots are corner separations and radial mixing. Although these sources of loss are similar, the loss generated by the casing slots is much greater than the grooves. The results also show that casing slots damage the structure of the tip leakage vortex and increase the entropy of the near-casing flow over the whole pitch, unlike grooves.

Having investigated the performance of casing slots and their impact on the flow field, the next section investigates the performance of the slots when the tip clearance changes.

7.7 The Effect of Increasing Tip Clearance

As discussed in the tip clearance tests on casing grooves (see Chapter 6.4) the clearance between the rotor blades and casing in a real engine tends to increase with time. In an untreated compressor, increased tip clearance causes reduced stability and efficiency. Tests by Fujita and Takata (1984) on slots located entirely over the blade tips suggested that casing slots reduce the impact of increasing tip clearance on both stall margin and efficiency. The present work extends this study to slots extending forward of the blade leading edges.

Back-to-back tests with a smooth wall and slotted wall 'A' were performed at tip clearances of 0.97, 1.54 and 1.94% of rotor blade span (0.56, 0.89 and 1.12% c_r respectively). The tip clearance was increased by progressively machining away the rotor blade tips. ϕ_{stall} and $\psi_{s,stall}$ were measured, and the stall margin and pressure rise improvements (SMI and PRI) were calculated as previously, along with the maximum efficiency and design point flow improvements (MEI and DPF). The results are shown in Figure 7.20.

As seen in the groove tests, ϕ_{stall} and $\psi_{s,stall}$ increase and decrease respectively as the tip clearance increases. These changes are smaller with the slotted wall installed compared to

the smooth wall, so the stall margin and peak pressure rise improvements generated by the slots (the boxed numbers on the graphs) both increase slightly as the tip clearance increases.

Figure 7.20 also shows that the efficiency of the treated cases decrease more than the smooth wall case as tip clearance increases. The efficiency penalty of increasing tip clearance is therefore larger with casing slots installed than it is in the smooth wall case. The design point flow improvement also decreases as tip clearance increases.

These results show that the stall margin improvement generated by casing slots increases slightly as the tip clearance increases, although the overall stall margin and efficiency of the compressor still reduce with increasing tip clearance when slots are installed.

7.8 Discussion

The experimental parametric study found an optimum slot depth of $60\% c_{x,r}$. Shallower slots generated a lower stall margin improvement and efficiency, while deeper slots generated no further stall margin improvement and reduced efficiency. This suggests that the slots must be sufficiently deep to accommodate the recirculating flow pattern described in Section 7.5, but no deeper. The ratio of slot depth to slot length may be important. In the present work, the total slot length ($l_u + l_d$ in Figure 7.1) was $101\% c_{x,r}$, giving an optimum slot depth to length ratio of 0.6. This value agrees with the geometries proposed by Seitz (1999), who varied up and downstream slot length (l_u and l_d) rather than depth (d). The present work also shows that although quarter-wave pressure resonances do occur within the slots, tuning the slot depth to encourage resonance does not improve performance.

The experiments also found an optimum slot width of $30\% c_{x,r}$. Narrower slots generated a lower stall margin improvement and efficiency, while wider slots generated no further stall margin improvement and reduced efficiency. There is an interesting link between the optimum slot width and the blade tip geometry: after the blade leading edge has passed an optimal width slot, the pressure surface is next to the opposite slot corner, creating a triangular gap (see Diagram 7.2). However, further work on different compressors is required to verify the significance of this observation.

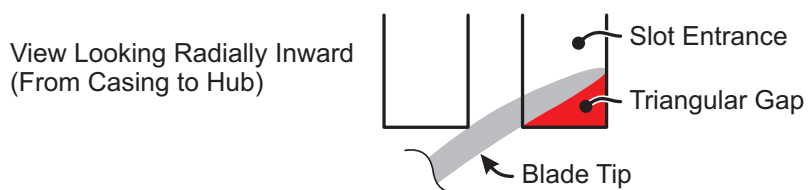


Diagram 7.2: The relationship between blade stagger and optimum slot width.

The width of the land between the slots can be reduced to improve stall margin at the expense of efficiency (or *vice-versa*). Since there is little interaction between neighbouring slots, adding more of them (by reducing the land width) will increase the interaction between the casing treatment and the near-casing flow. In a real engine however, the minimum practical land width is set by the integrity of the land under the differential pressures in neighbouring slots and the integrity of the abradable lining that must be fixed to the land. If maximum stall margin improvement is required, the land width is thus set by mechanical constraints. However, large areas of near-casing blockage were observed when operating at the very low flow rates made possible by effective casing slots (see Section 7.3). In a multi-stage environment, this blockage could de-stabilise downstream blade rows, making the stall margin improvement lower than expected. Treatments with large land widths (greater than 50% $c_{x,r}$) generate useful stall margin improvements with smaller efficiency losses, and thus may be a good design choice.

As the porosity of the tested slot designs increased, the stall margin increased and efficiency decreased approximately linearly. Porosity can thus give a quick check on casing slot designs. However, the performance trends for the slot and land width are different, so attempting to predict performance based on porosity alone may give poor results, especially if the treatment has particularly narrow or wide slots. Since an optimum slot width exists, it is better to use this and then choose an appropriate land width.

The present results can be combined with published data to suggest an optimal slot geometry. Seitz (1999) found that the skew angle (α) should be as large as possible, recommending 60° to maintain a strong land. The recommended length of slot upstream of the leading edge (l_u) was 75% $c_{x,r}$ (with smaller values reducing stability) and the recommended downstream length (l_d) was 25% $c_{x,r}$ (with larger values improving stability but reducing efficiency). It is interesting that the downstream edge of an optimally-placed groove near the blade leading edge is at 22% $c_{x,r}$, suggesting that slots and grooves should both be as far forward as possible while remaining adjacent to the most vigorous tip clearance flow. Work by Lu *et al.* (2006a) supports these results. However, using a high-speed machine with contoured endwalls, Wilke *et al.* (2005) found that the downstream length should be greater (around 50% $c_{x,r}$) to position the downstream edge of the slot behind the shock and increase the pressure driving the flow through the slot. In other work, Lu *et al.* (2006a) found that bending the downstream length of the slot toward the blade stagger angle improved performance. Cumpsty (1989b) also showed that slots are still effective if they are not evenly distributed around the annulus.

All the slot-based treatments tested in the present work reduced efficiency. None of the efficiency improvements observed by Seitz (1999) were recorded; tests using different slot

lengths up and downstream of the leading edge to try and repeat the Seitz results were unsuccessful. Figure 7.19 shows that the entropy created by corner separations and mixing processes dwarf any loss reductions caused by modifying the tip leakage vortex. Casing slots reduce efficiency more than grooves because they generate more entropy (even though the loss mechanisms are similar). Wilke and Kau (2004) use slots with a semi-circular cross-section to guide the recirculating flow (see Section 2), but this will not remove the loss sources above, so large efficiency improvements are unlikely. However, using transonic compressors treated with slots, Brignole *et al.* (2008) and Lin *et al.* (2008) observed greater efficiencies at full speed than at low speed, with similar flow fields inside the slots. Work by Kau *et al.* (2006) suggests that this may be due to the slots reducing losses caused by the tip leakage vortex bursting on the passage shock at high speeds. Hathaway (2002) also improved the efficiency of a high-speed compressor using a recirculating treatment. The efficiency penalty associated with slots may thus be lower in some high-speed compressors than in low-speed machines.

The impact of casing slots on the outflow blockage and time-mean blade loading is similar to a groove located near the leading edge, yet the groove generates one quarter of the stall margin improvement generated by the slots. As found in the groove tests, there is thus no clear link between the outflow blockage, or time-mean blade loading, and the stall margin improvement generated by casing slots or grooves.

Although slots have a small impact on the *time-mean* blade loading, they cause large *unsteady* loading oscillations. These oscillations reach half an inlet dynamic head, affect the blade tip region upstream of mid-chord, and are in-phase along the blade. The blade tip loading falls as the leading edge passes a slot, and then rises as the part of the blade near 20% chord passes the slot. This latter effect also causes a small oscillation in the overall pressure rise. Both of these effects could cause noise and vibration, especially if there are an integer number of slots per blade. This should not be neglected during design.

The impact of the slots on the pressure and velocity of the near-casing flow field is similar to a groove located near the leading edge. Both treatments interfere with the tip leakage vortex, obliterating the so called 'black line' and interrupting the separation line in their vicinity. However, slots interfere with the structure of the tip leakage flow more than grooves, so that the tip leakage vortex becomes an unsteady region of swirling high-loss flow. As the blade leading edge passes the slot entrance, the tip leakage and pressure-surface flows are diverted into the slot, reducing the blade loading. Flow emerges from the slot near the blade suction surface and most of the slot entrance due to recirculation. The part of the blade near 20% chord then passes the slot entrance; the suction-surface pressure falls and the pressure-surface pressure rises, causing the blade loading increase discussed above. Once the blade

has moved away, the slot interacts with the tip leakage flow. These interactions interfere with the formation and early growth of the tip leakage vortex, so it grows more rapidly downstream of the slots, moving the blade loading aft. After the tip leakage flow moves away, there is a weak interaction between the slots and the near-casing flow until the next blade arrives and the process restarts. As suggested in the literature, the slots increase the through-flow and decrease the cross-flow components of the tip clearance flow (as seen in the work on grooves). Downstream of mid-chord, the impact of both treatments is small. Upstream of the rotor blades, the slots increase the inflow velocity.

While the interaction between the slots and near-casing flow is highly unsteady, the flow within the slots themselves is principally a quasi-steady recirculation moving flow from near the blades to upstream of the rotor. This suggests that the slots could be modelled using a steady method (such as that of Ning and Xu, 2008), which would significantly reduce the computational cost of designing them. As discussed in Section 7.1.4, increasing treatment porosity appeared to give linear changes in stall margin and efficiency, suggesting that steady, rather than unsteady, effects dominate. However, since there is an optimum slot width, circumferential length scales (and hence unsteady effects) are important, agreeing with Prince *et al.* (1974) and Seitz (1999). The flow study also showed that the unsteady interaction between the slots and the near-casing flow is stronger than the time-mean interaction. These observations suggest that while steady analysis may be useful in initial design, unsteady analysis is necessary for final design.

Casing slots can generate four times the stall margin improvement of a groove located near the leading edge. The unsteady impact of the slots on the near-casing flow is greater than that of the grooves, but not four times greater. There are, however, three additional factors that could account for the large stall margin improvements generated by the slots. Firstly, the slot recirculation increases as the compressor is throttled (Seitz, 1999), which allows the slots to 'switch on' as stall approaches, progressively increasing the interaction with the near-casing flow (grooves cannot 'switch on' in this way). Secondly, slots can influence the flow upstream of the rotor, which steady blowing tests by Seitz (1999) suggest improves stability (grooves cannot affect the upstream flow). Thirdly, slots destroy spikes once they have formed, so that the first spike to form does not lead to stall (with grooves installed the first spike to form generally causes stall). However, until the fundamentals of stall inception are understood, it will be difficult to evaluate the relative importance of these factors.

7.9 Conclusions

It is concluded that:

1. Experiments show there is an optimum depth for casing slots of $60\% c_{x,r}$. Slots that are shallower than this generate a lower stall margin improvement and efficiency, while deeper slots generate no further stall margin improvement, and reduce efficiency.
2. Quarter-wave pressure resonances occur inside the slots, but experiments have shown that tuning the slot depth to encourage them has little impact on performance.
3. The experiments show there is an optimum slot width of $30\% c_{x,r}$. Slots narrower than this generate a lower stall margin improvement and efficiency, while wider slots generate no further stall margin improvement, and reduce efficiency.
4. The experiments show that reducing the width of the land between slots improves stall margin but reduces efficiency. In real engines, the land width will be limited by mechanical integrity requirements. Small land width designs also enable the compressor to operate at very low flow-rates, which can cause large near-casing blockage. In a multi-stage environment, this may de-stabilise downstream blade rows, making the stall margin improvement lower than expected. Land widths greater than $50\% c_{x,r}$ may, therefore, be a sensible design choice.
5. Increasing the porosity of slotted casing treatments causes approximately linear increases in stall margin improvement and reductions in efficiency. However, because porosity combines the different impacts of slot and land width on performance, it should not be used as a design parameter.
6. The optimum distance between the blade leading edge and the downstream edge of the slots ($25\% c_{x,r}$) is similar to the distance from the leading edge to the downstream edge of an optimally placed forward circumferential groove ($22\% c_{x,r}$). In these locations, both treatments are as far forward as possible, while remaining adjacent to the most vigorous near-casing flow.
7. As seen in the groove results, there is no *clear* link between outflow blockage and stall margin improvement.
8. The time-mean impact of casing slots on the blade tip loading is to move the loading slightly aft. However, the unsteady impact of the slots is greater; the slots cause large, in-phase oscillations in the blade tip loading as the blade passes the slots. The impact of these loading oscillations on noise and vibration should be considered during design.

9. Casing slots remove the black line from a casing flow visualisation and interfere with the formation of the tip leakage vortex (which moves the blade tip loading aft). The unsteady interaction between the slots and near-casing flow is complex, but acts to reduce the cross-flow and increase the through-flow components of the tip clearance flow. Slots also increase the velocity of the upstream flow before it enters the rotor.
10. While the interaction between the casing slots and near-casing flow is highly unsteady, the flow inside the slots is principally a quasi-steady recirculation from near the rotor to the inflow. Steady models of slot-based casing treatments may be useful for initial design, but the present work suggests that unsteady flow effects are also important and should be considered during the design process.
11. As the tip clearance increases, the stall margin improvement generated by casing slots increases slightly. However, the overall stall margin and efficiency of the treated compressor still reduce as the tip clearance increases.
12. The stall inception pattern in the Natal compressor (spike-type) is not affected by the presence of casing slots, even though the slots interfere with the development of the tip leakage vortex.

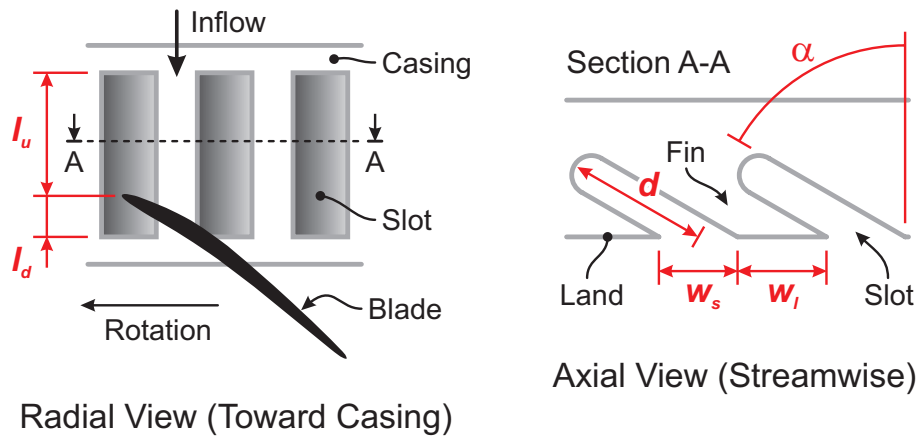


Figure 7.1: A schematic showing the geometry of the circumferentially discrete slot-based casing treatment, with dimensions.

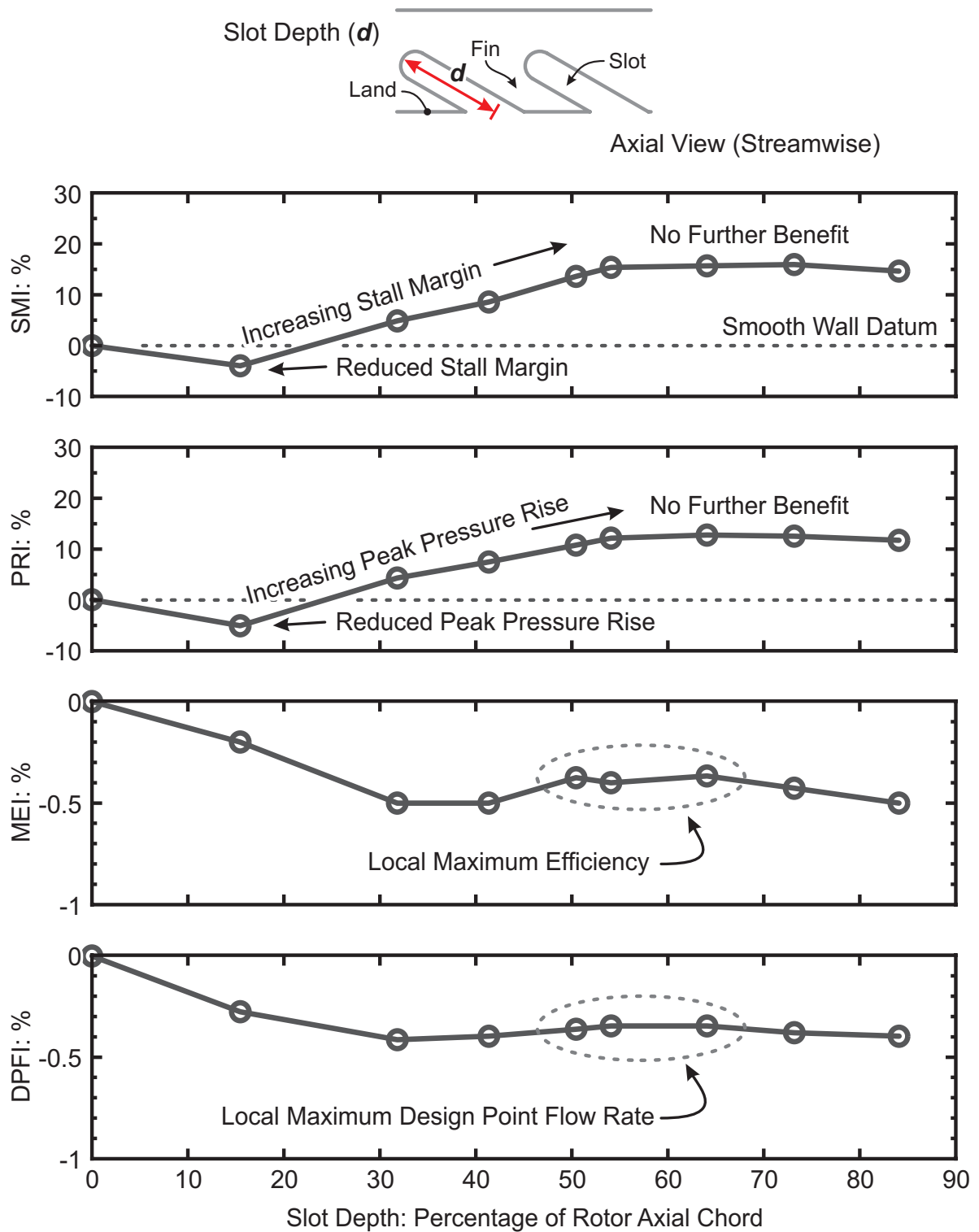


Figure 7.2: The effect of altering the depth of the casing treatment slots on stall margin improvement (SMI), pressure rise improvement (PRI), maximum efficiency improvement (MEI) and design point flow increase (DPFI).

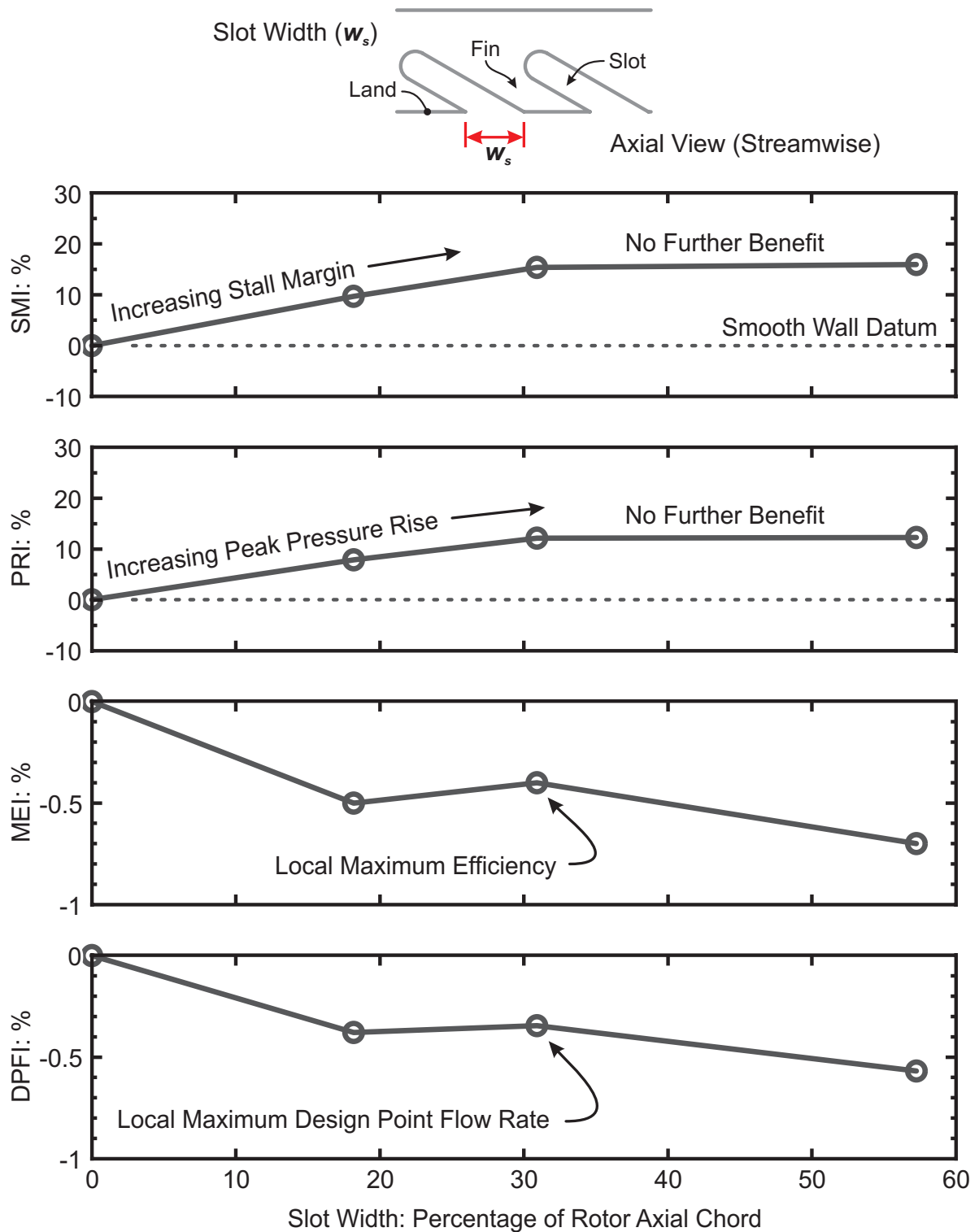


Figure 7.3: The effect of altering the width of the casing treatment slots on stall margin improvement (SMI), pressure rise improvement (PRI), maximum efficiency improvement (MEI) and design point flow increase (DPFI).

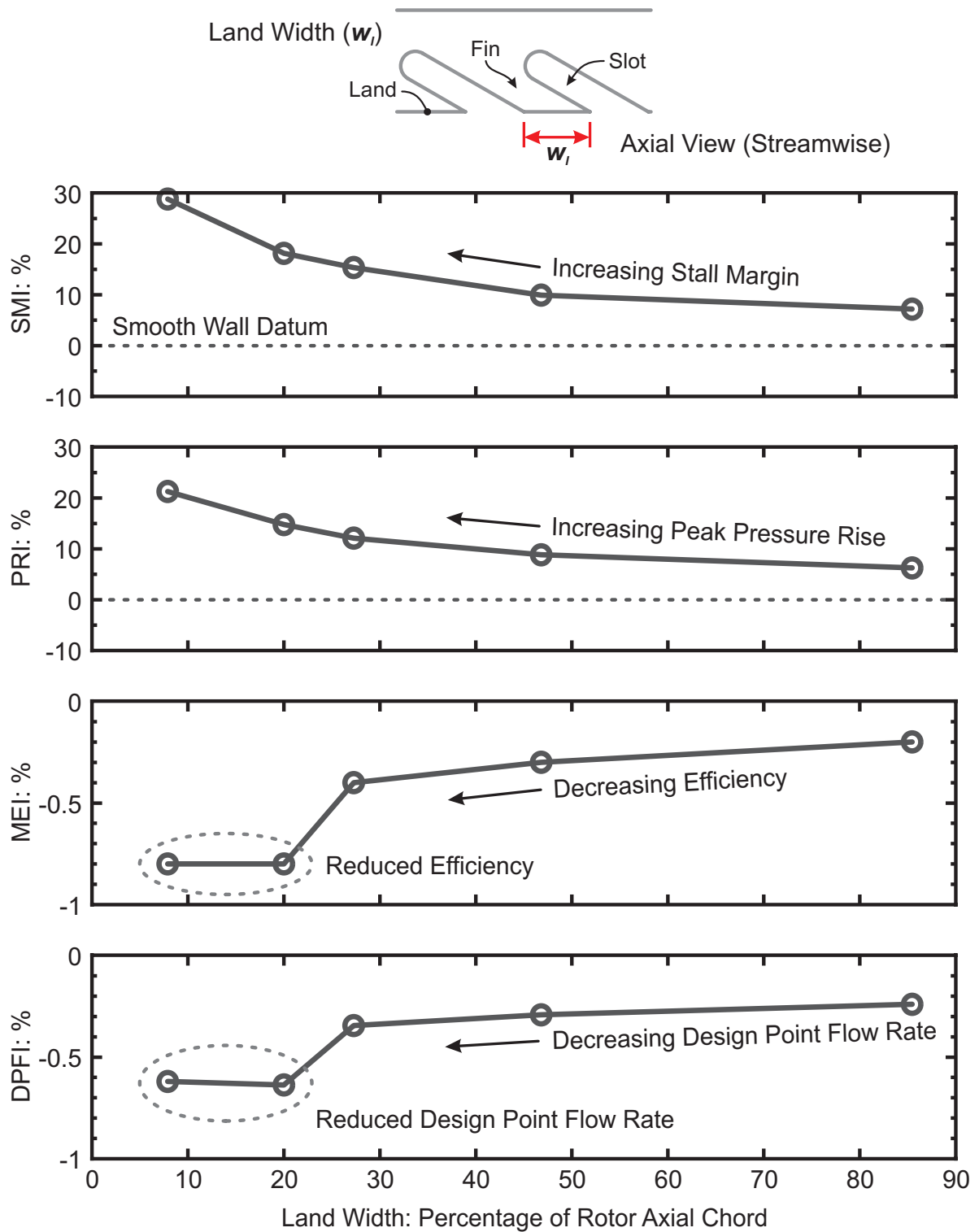


Figure 7.4: The effect of altering the width of the land between casing treatment slots on stall margin improvement (SMI), pressure rise improvement (PRI), maximum efficiency improvement (MEI) and design point flow increase (DPFI).

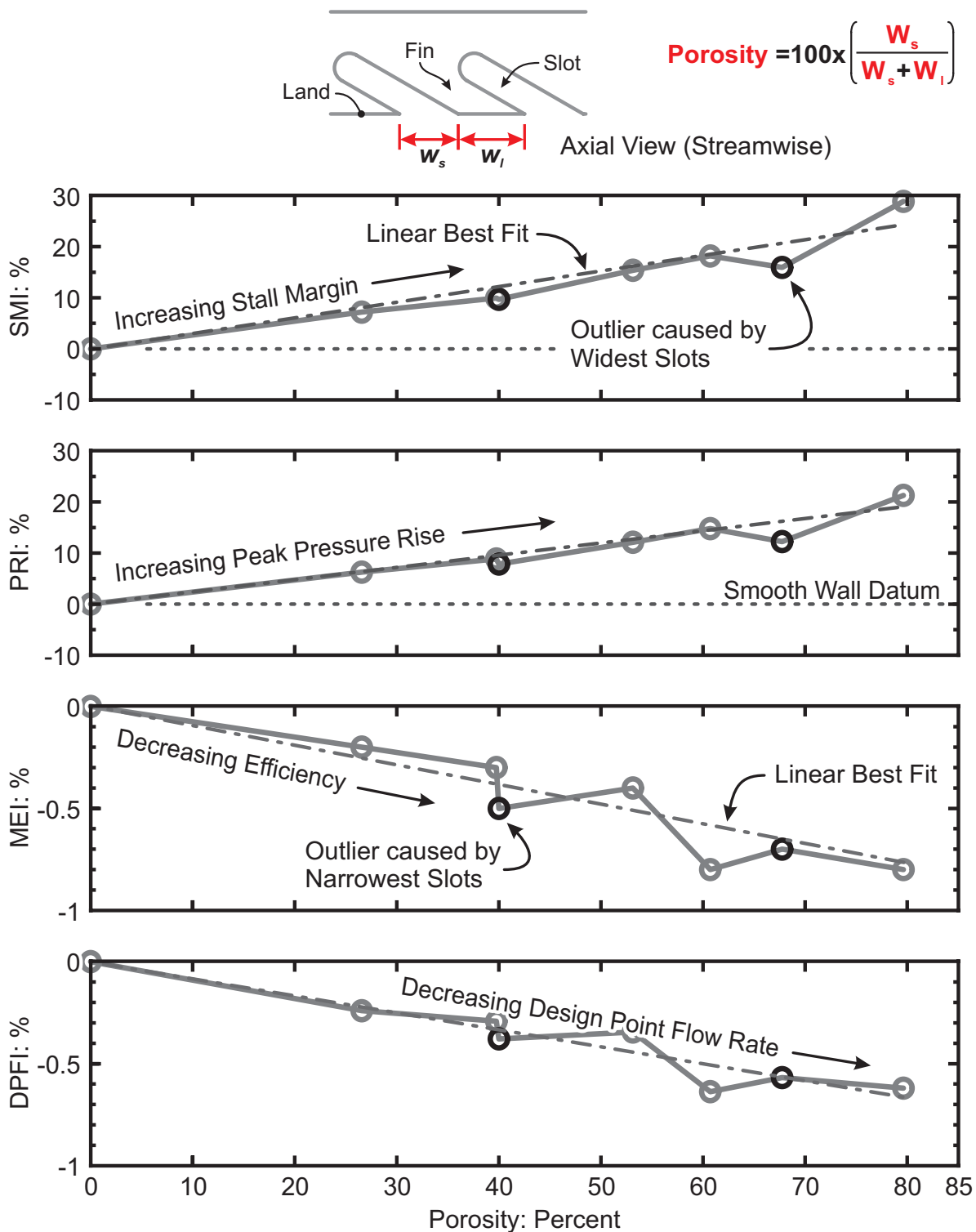


Figure 7.5: The effect of altering casing treatment porosity on stall margin improvement (SMI), pressure rise improvement (PRI), maximum efficiency improvement (MEI) and design point flow increase (DPFI).

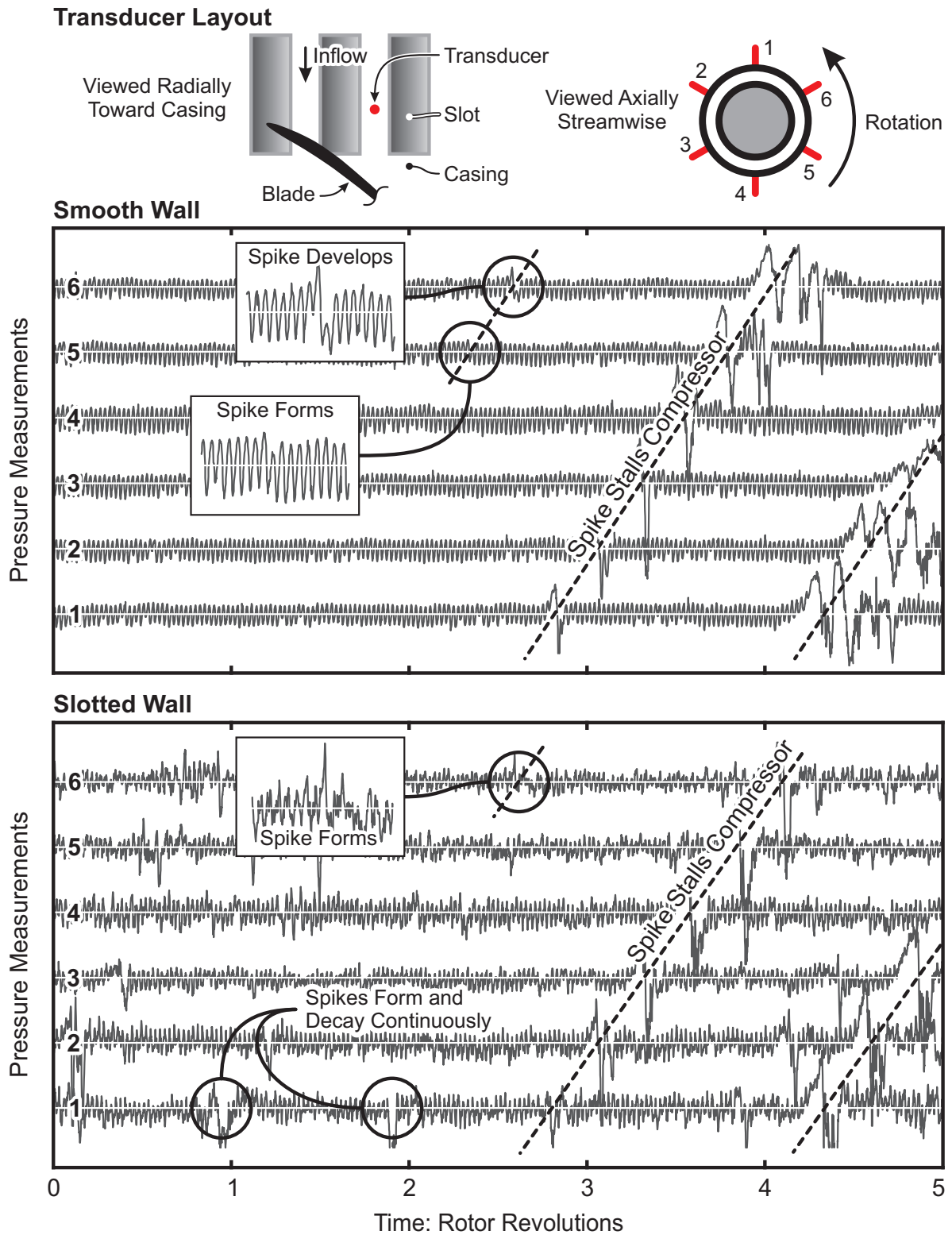


Figure 7.6: The effect of adding casing slots on the stall inception behaviour of the Natal compressor, showing Kulite pressure measurements at six circumferential locations just upstream of the rotor blade tips at stall inception.

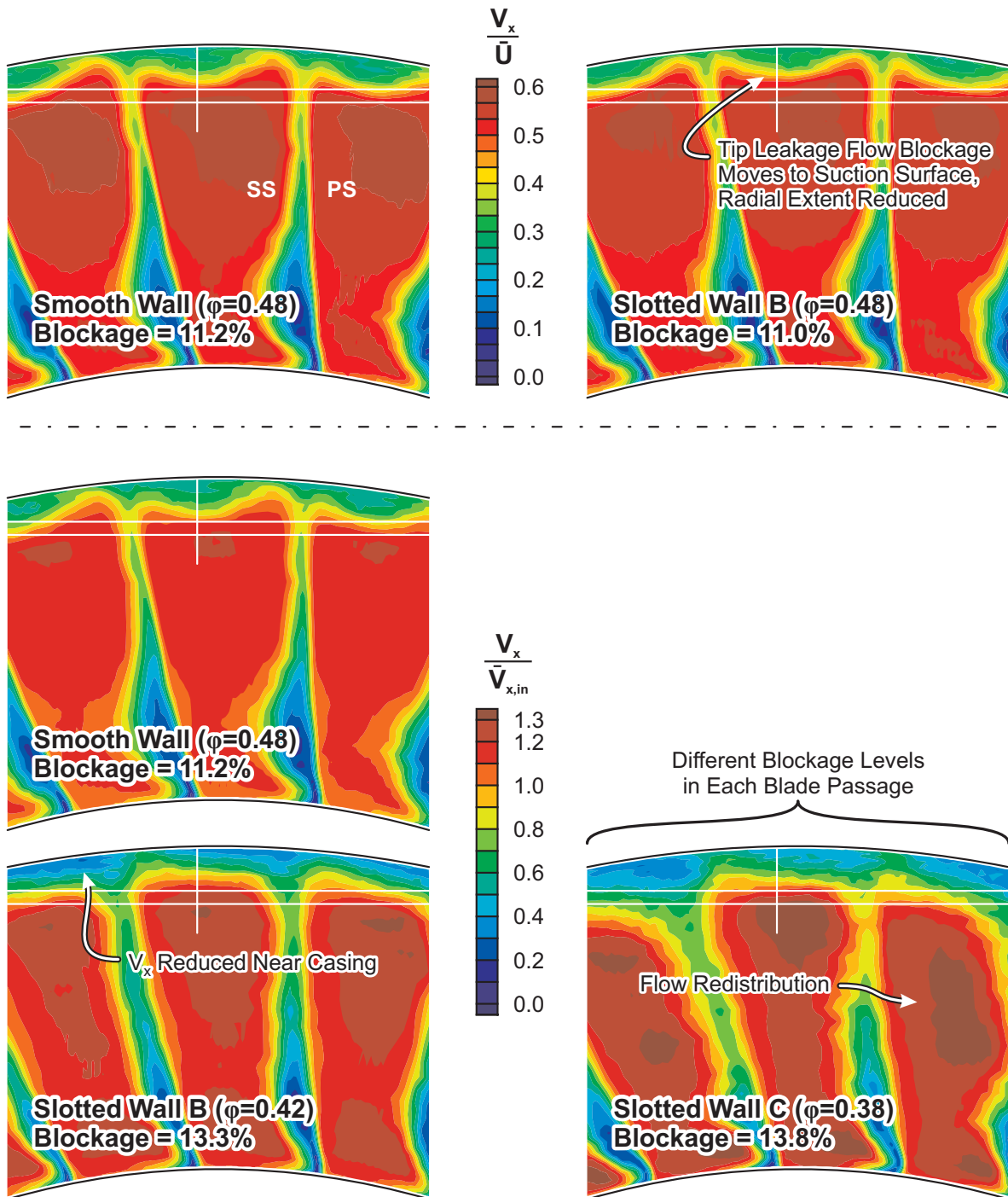


Figure 7.7: The effect of adding slotted casing treatments on the outflow blockage. All plots show contours of axial velocity measured using hotwire traverses immediately downstream of the rotor trailing edge (regions of low axial velocity are represent flow blockage). The upper plot shows the impact of slotted wall B on the smooth wall outflow blockage near the smooth wall stall point. The lower plot shows the outflow blockage near the stall points of the smooth wall and slotted walls B and C. The two plots are normalised by different quantities for reasons explained in Section 7.3.

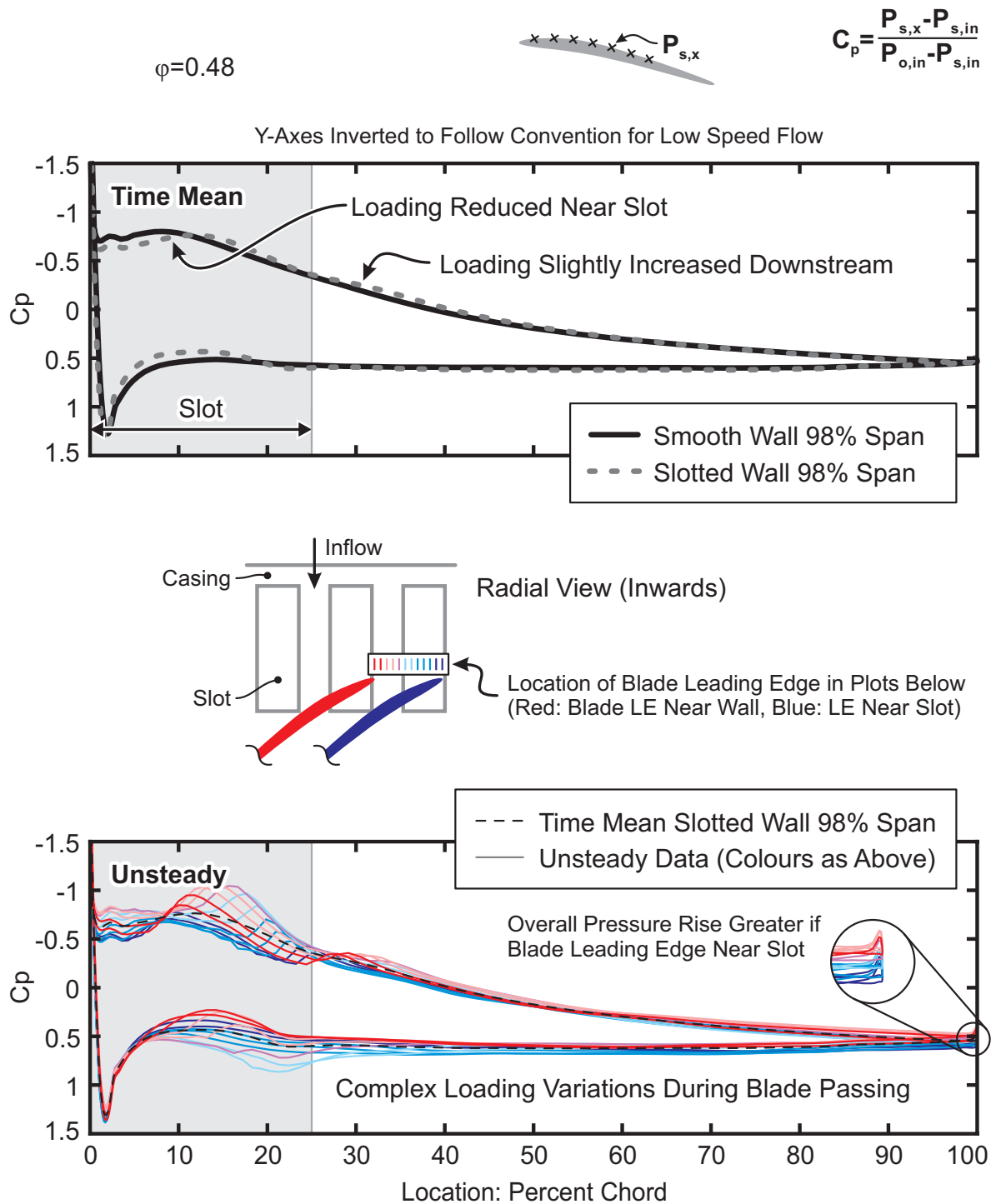


Figure 7.8: The impact of the slotted wall on blade loading. Surface-pressure distributions from CFD solutions of the smooth and slotted walls at 98% span are shown. The upper plot compares the blade loading of the time-mean slotted and smooth wall cases. The lower plot shows the blade loading at 12 equi-spaced time-steps across one slot-passing. The plots are colour-coded as shown in the schematic. The y-axes are inverted to follow convention for low speed flow.

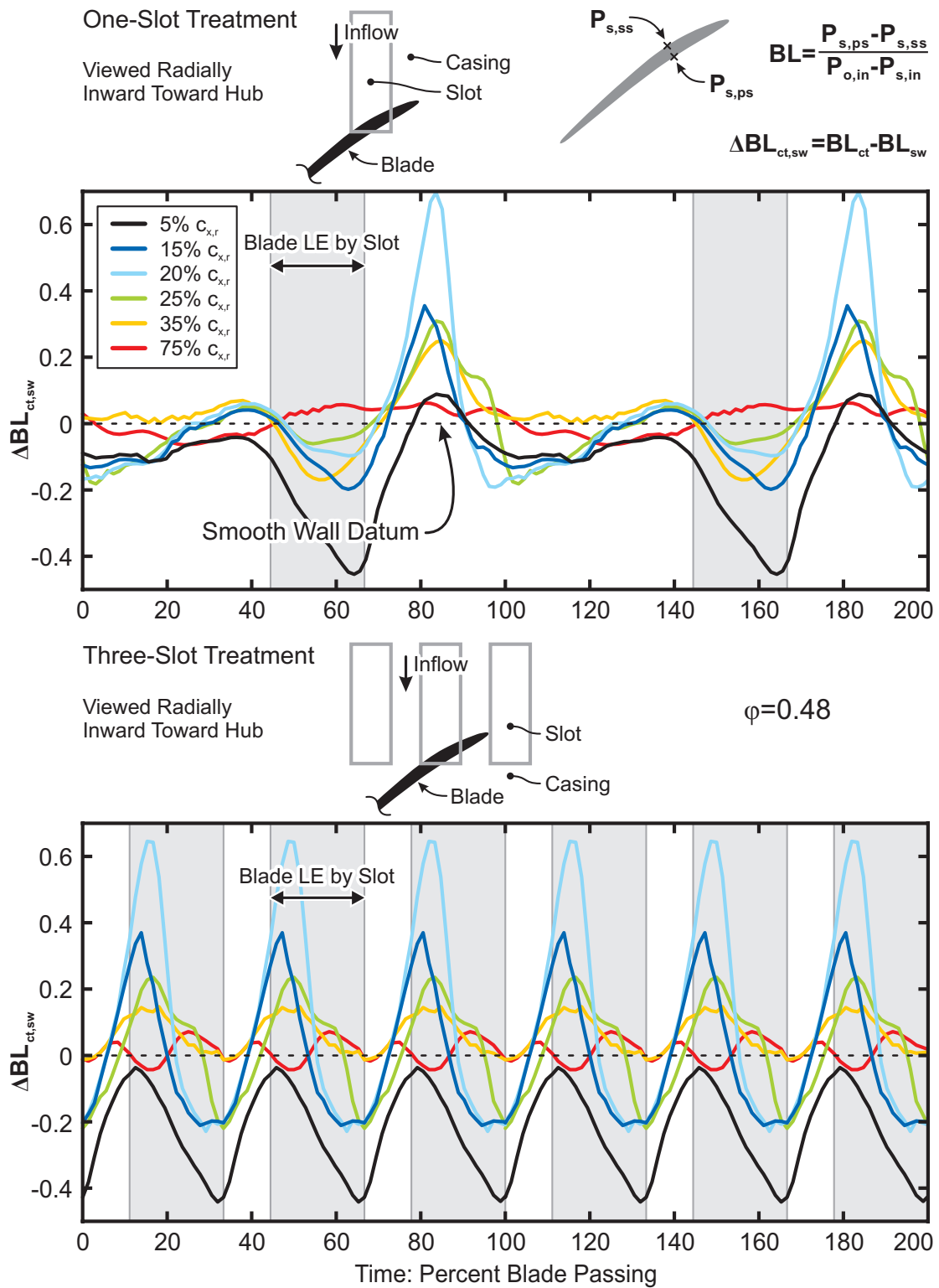


Figure 7.9: The unsteady impact of a slotted wall on the blade loading at 98% span. The graphs show the difference in blade loading between the slotted and smooth wall cases at six different chord-wise locations near the smooth wall stall point ($\phi=0.48$). The upper plots show data for a treatment with one slot per blade pitch, while the lower plots show the data for slotted wall 'B' (three slots per blade pitch).

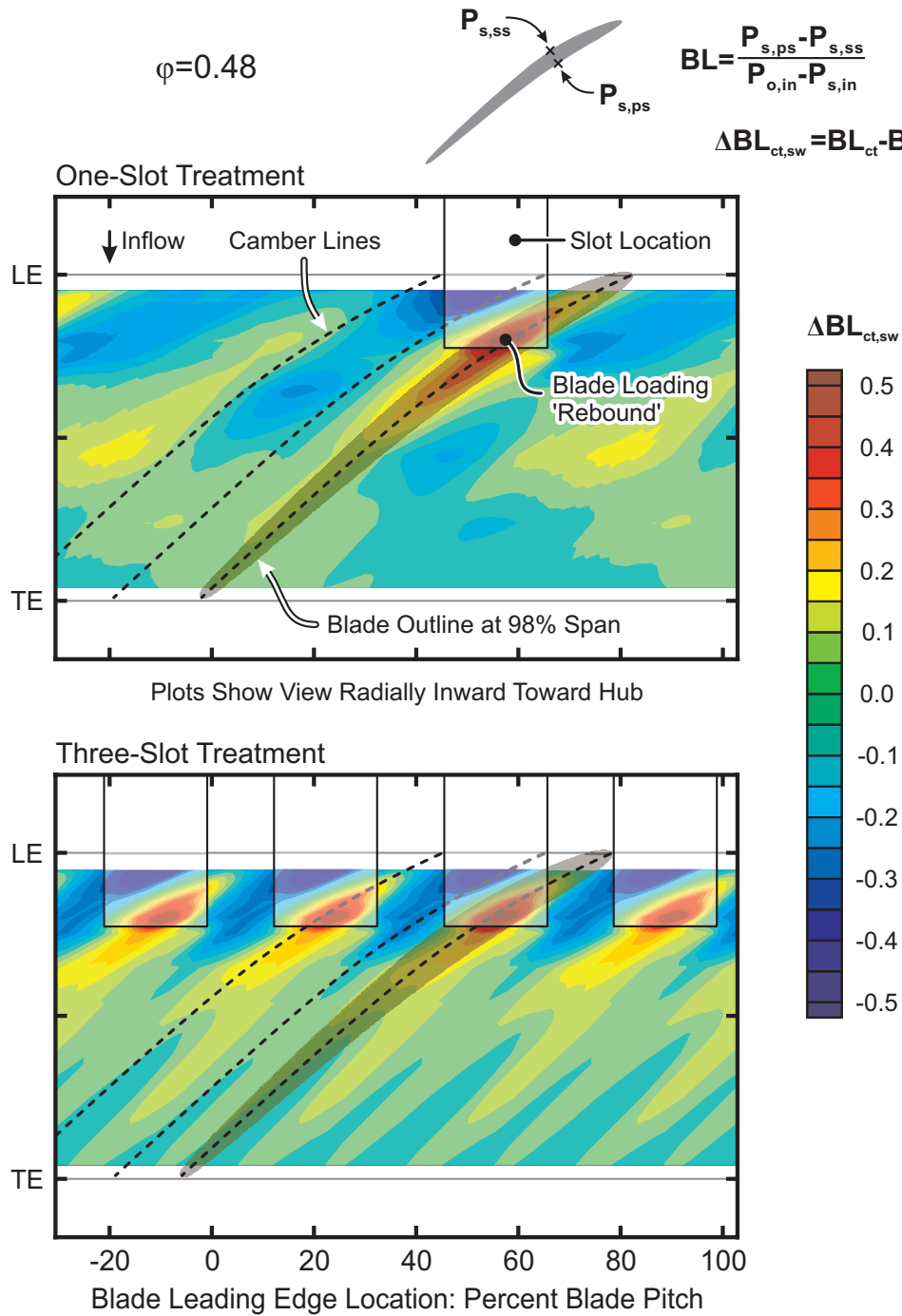


Figure 7.10: The unsteady impact of a slotted wall on the blade loading at 98% span. Contour maps showing changes in blade loading caused by the slots at different times and different chord-wise locations near the smooth wall stall point ($\phi=0.48$). The upper plots show data for a treatment with one slot per blade pitch, while the lower plots show the data for slotted wall 'B' (three slots per blade pitch).

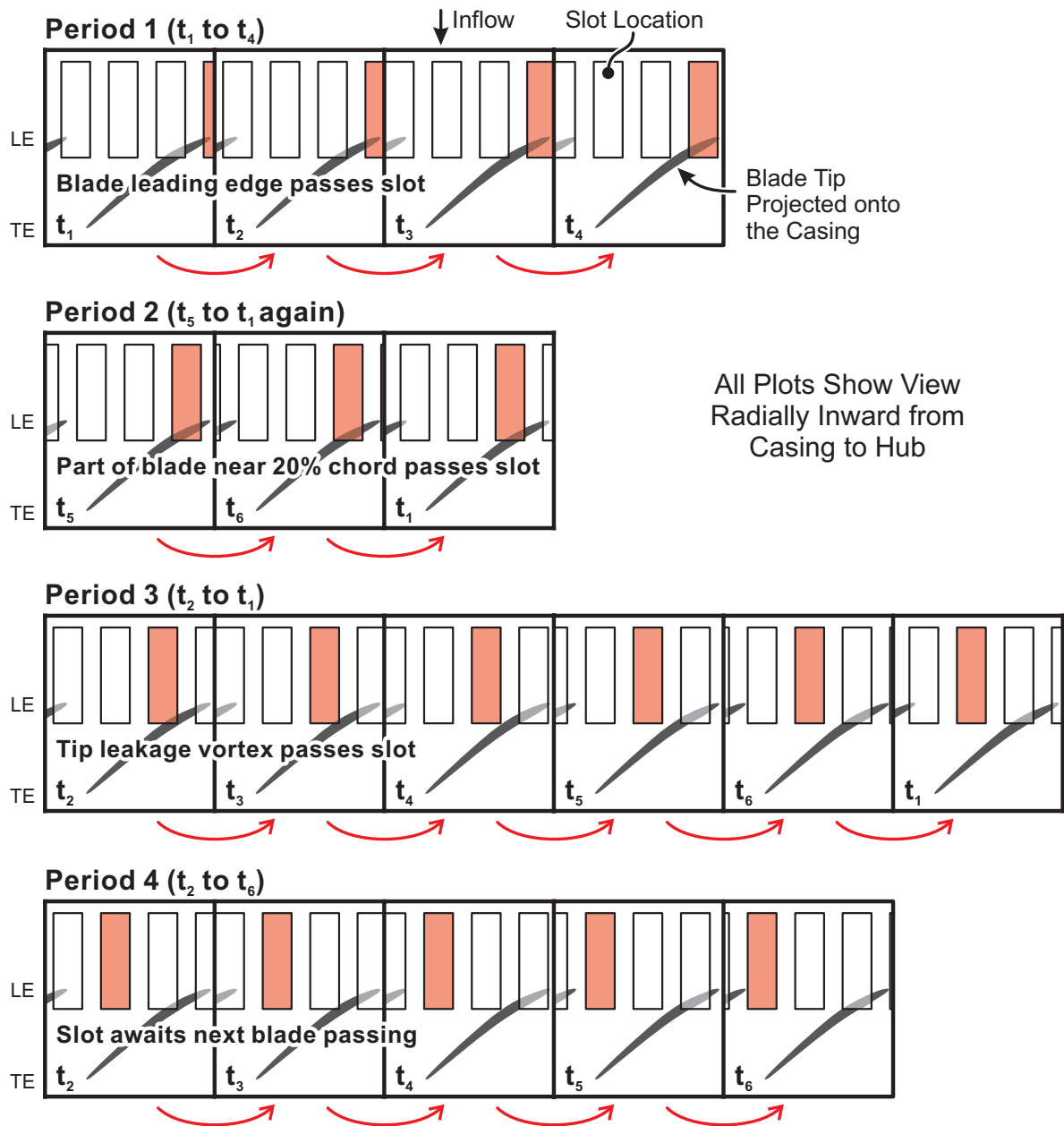


Figure 7.11: The progress of a casing slot through the four periods of a blade passing. The slot of interest is shaded in red. The blade location is fixed, and is the same as it was in the grooved wall plots in Chapters 5 and 6, to aid comparison. Since the blade location is fixed, the slot appears to move from right to left. The end of period one (t_4) corresponds to $x = 0$ in the unsteady blade loading plots (Figure 7.9).

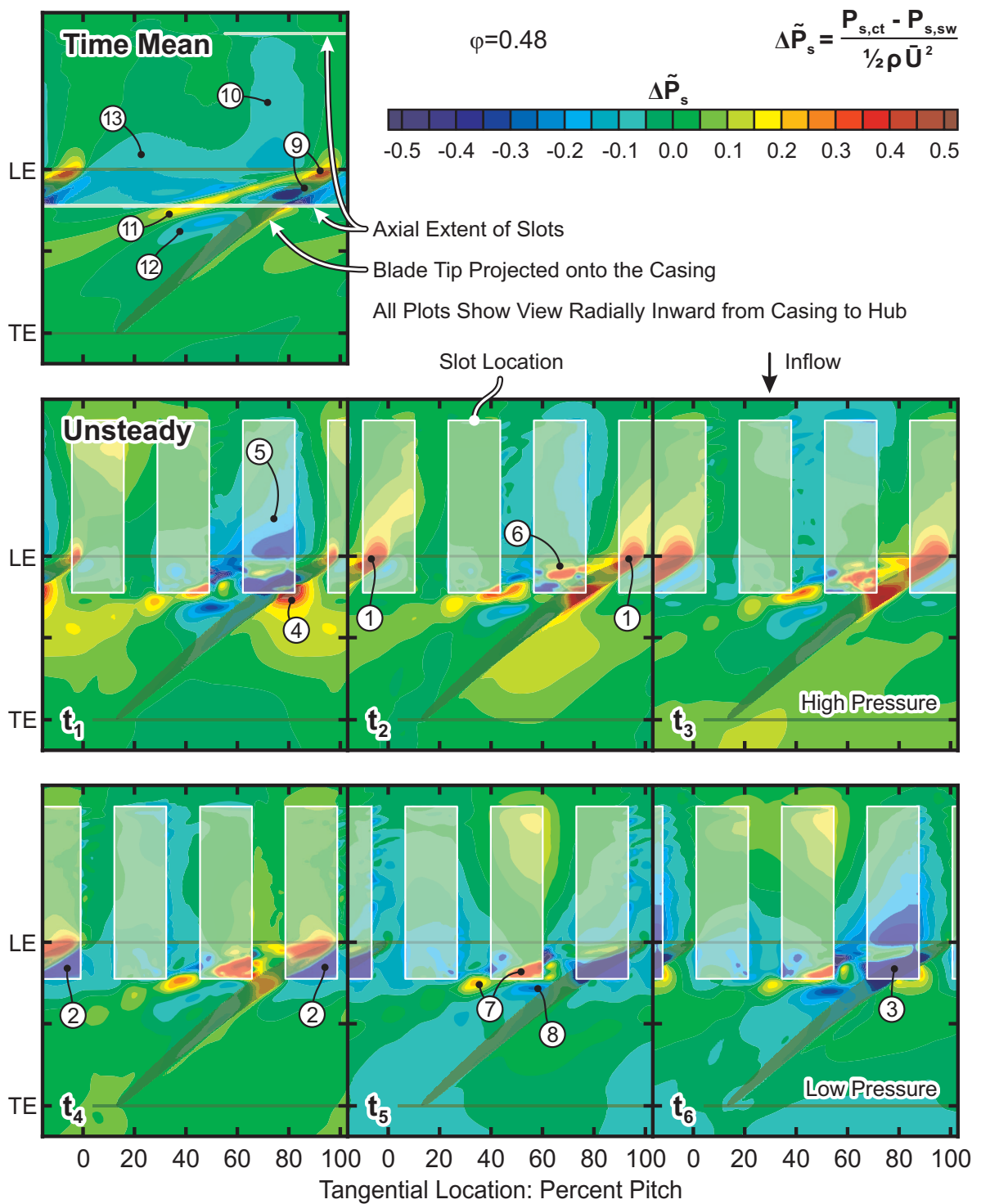


Figure 7.12: The effect of adding slots on the casing static pressure when the compressor is operating near the smooth-wall stall point ($\phi=0.48$). Contours show normalised changes to the casing static pressure ($\Delta \tilde{P}_s$) created by subtracting the smooth-wall case from the equivalent slotted case. The time-mean and six equally spaced instances across a period are shown.

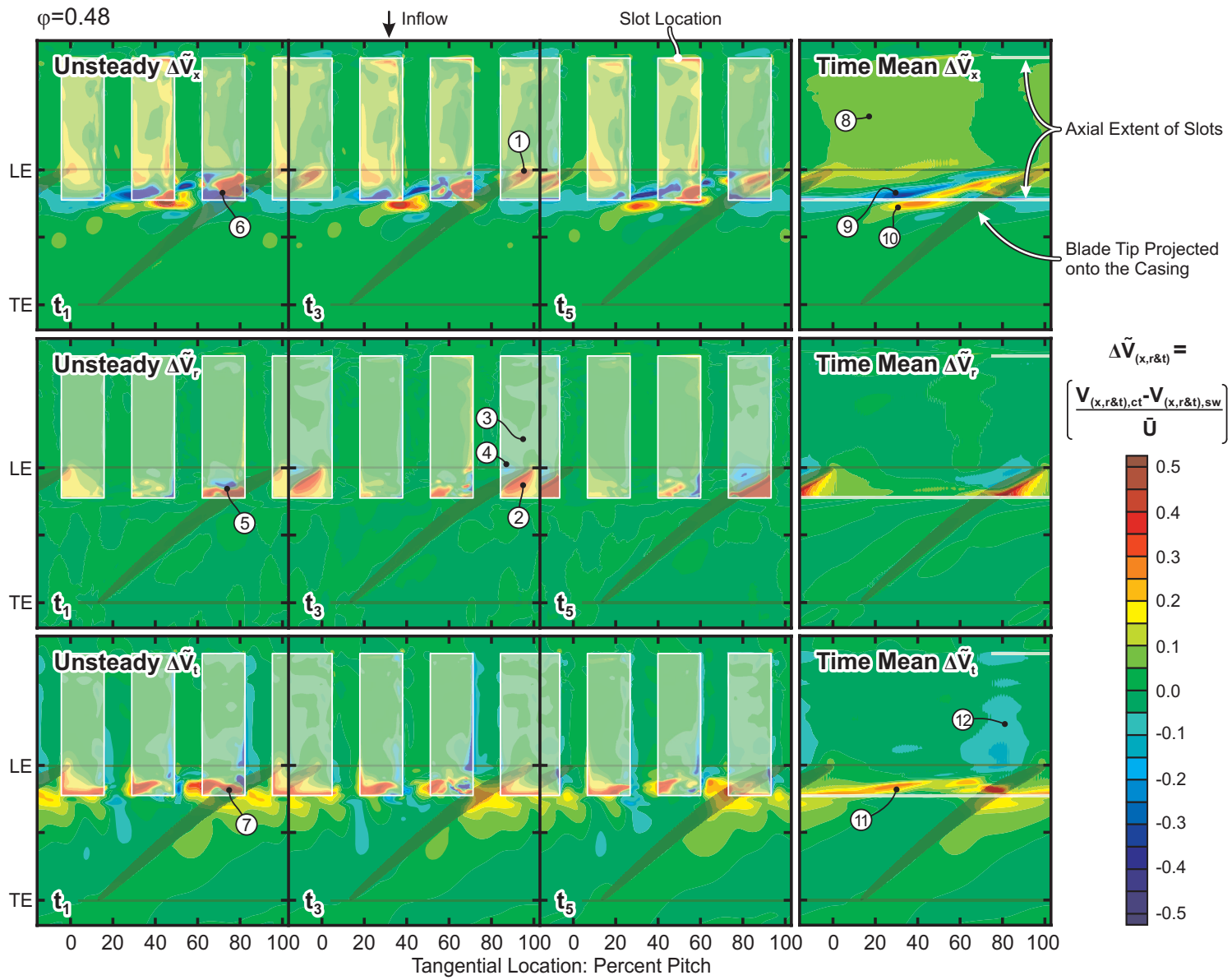
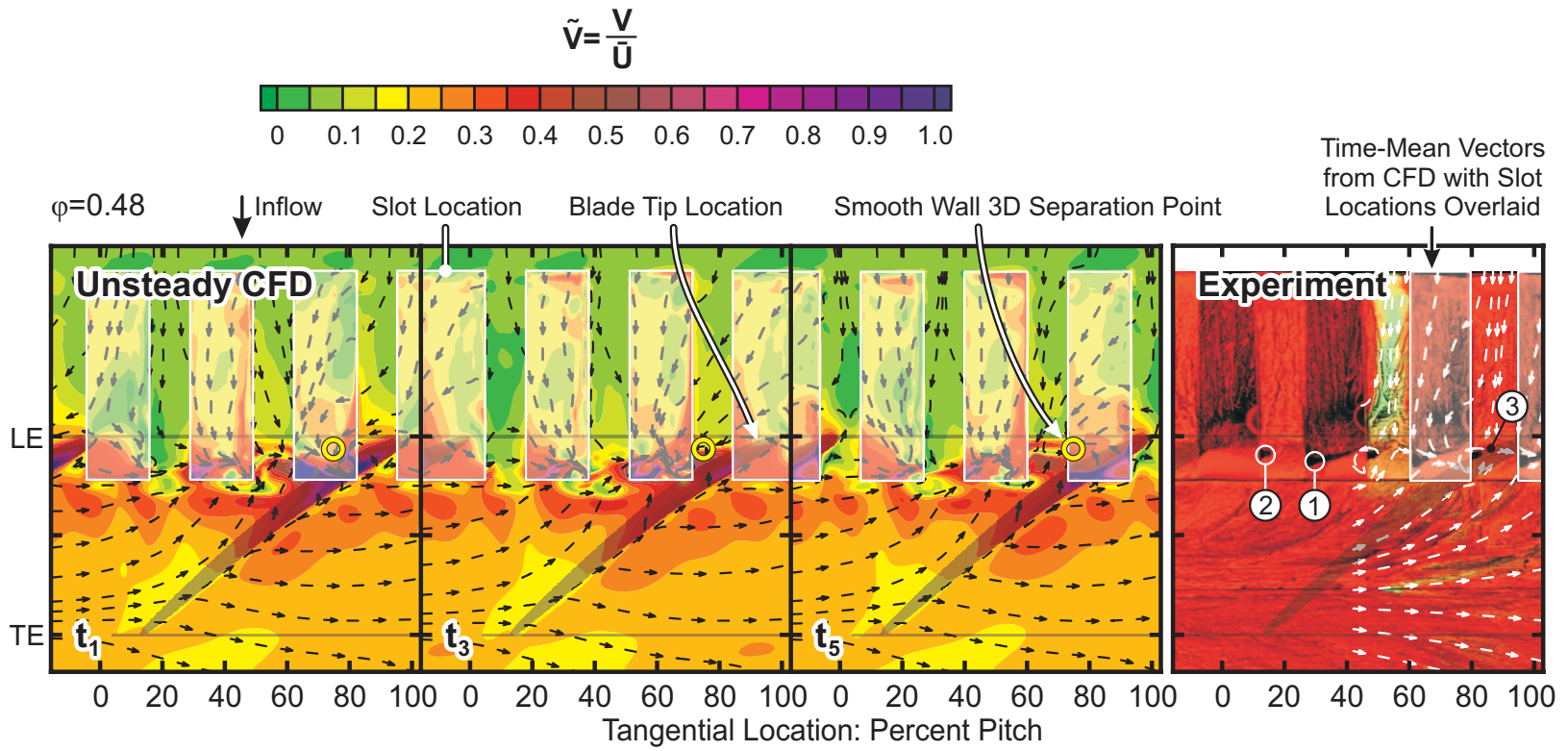


Figure 7.13: The effect of adding slots on the velocity of the near-casing flow when the compressor is operating near the smooth-wall stall point ($\phi=0.48$). Contours show normalised changes to the velocity components ($\Delta\tilde{V}_x$, $\Delta\tilde{V}_r$ and $\Delta\tilde{V}_t$) of the near-casing flow. Constant radius cuts were taken from the slotted wall CFD model at 5% t_c and the equivalent smooth-wall case was subtracted to create the plots. The time-mean and three equally spaced instances across a period are shown. The view is radially inward through the casing.

Figure 7.14: The effect of the slots on the near-casing flow patterns near the smooth-wall stall point. Constant radius cuts from the unsteady CFD model at 5% t_c showing absolute velocity contours with vectors alongside an experimental flow visualisation are shown.



All Plots Show View Radially Inward from Casing to Hub

Probe Location Schematic

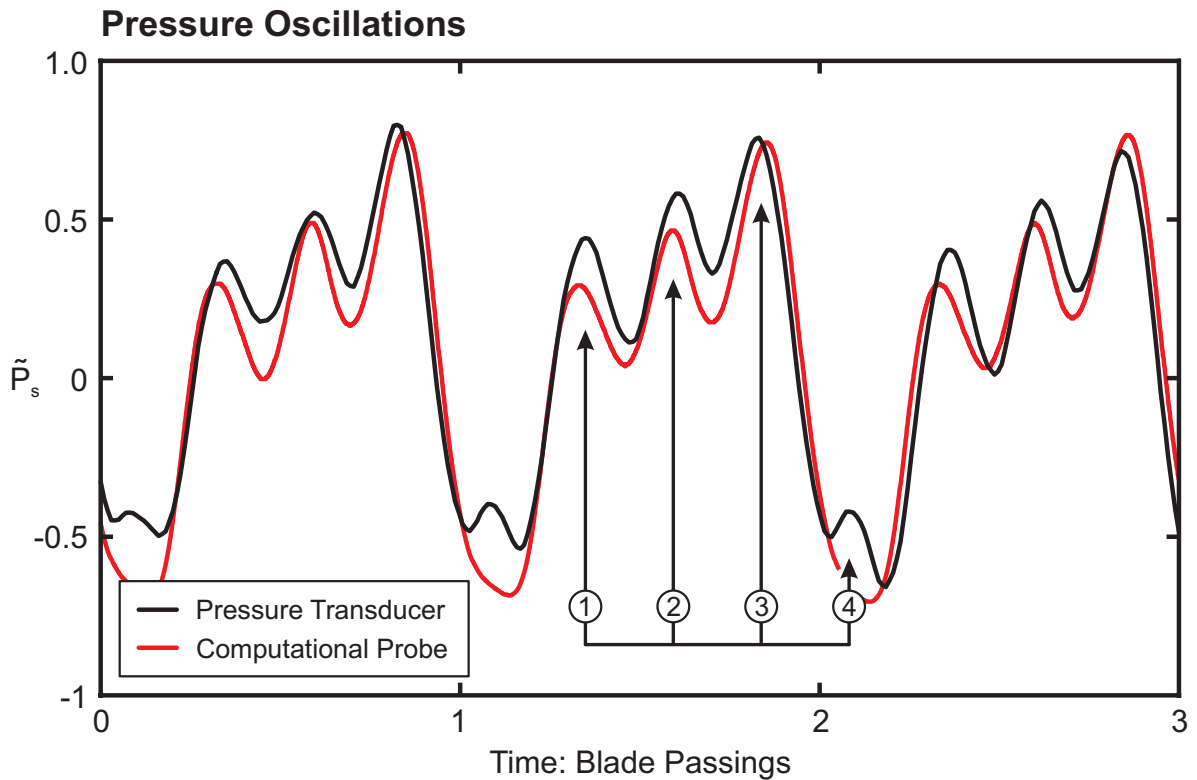
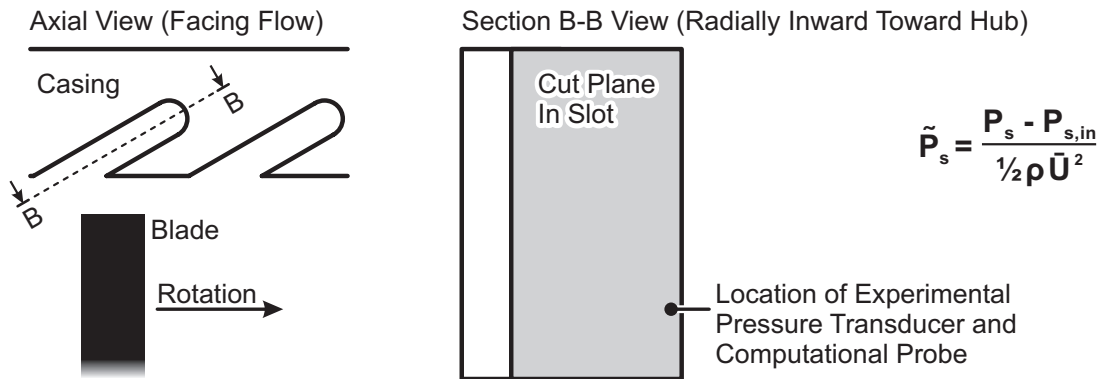
 $\phi=0.44$


Figure 7.15: The pressure oscillations inside the treatment slots shown using high-frequency experimental pressure measurements and data from the computational model. The graph shows how the normalised static pressure inside a casing slot (from slotted wall 'B') changes with time near the casing treatment stall point ($\phi=0.44$).

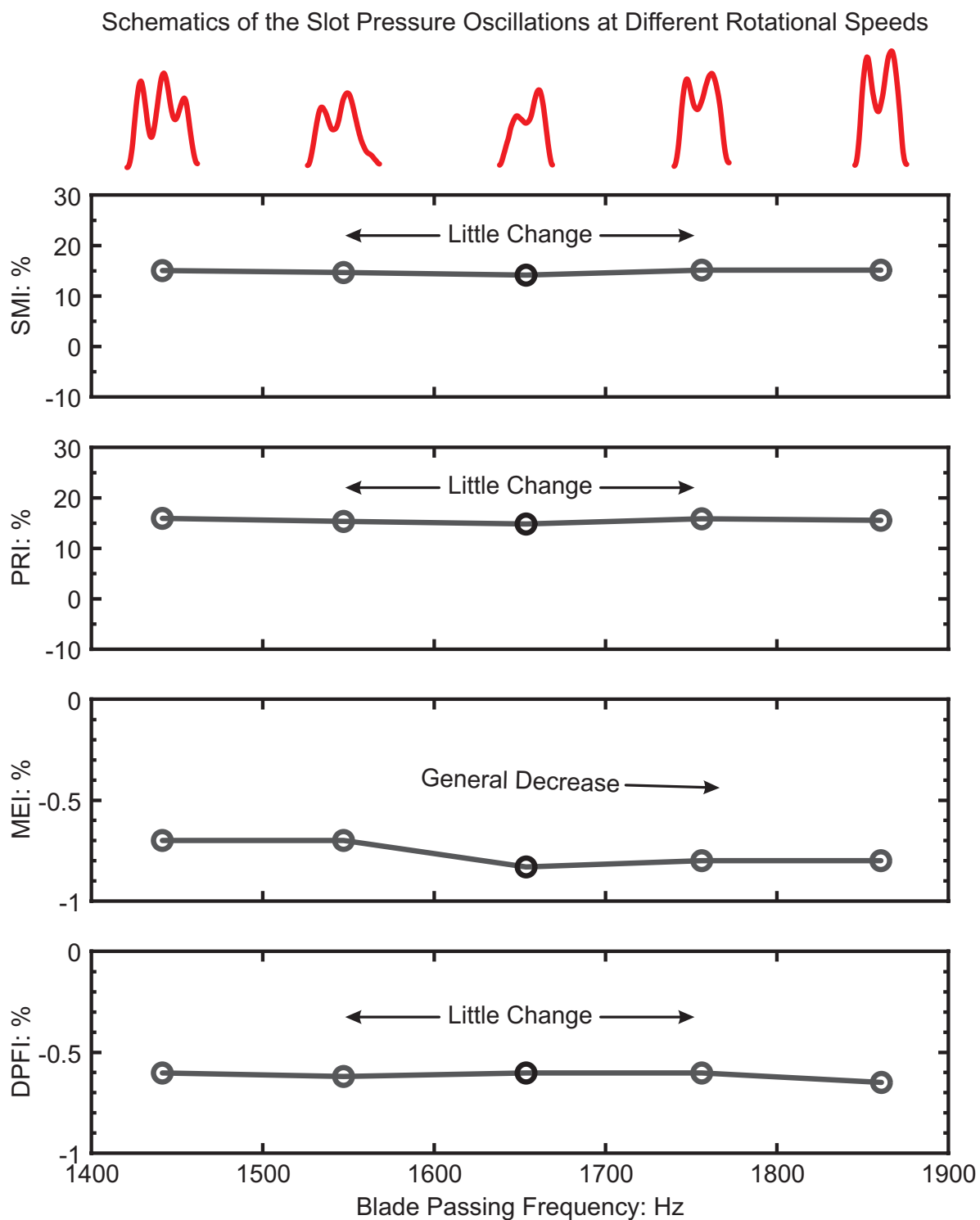
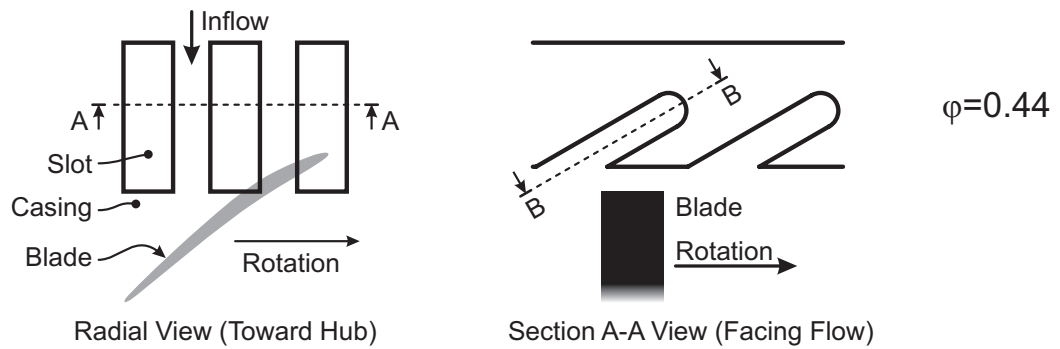


Figure 7.16: The effect of casing treatment slot pressure oscillations on stall margin improvement (SMI), pressure rise improvement (PRI), maximum efficiency improvement (MEI) and design point flow increase (DPFI).



Absolute Velocity Vectors on Section B-B (at the Slot Centre)

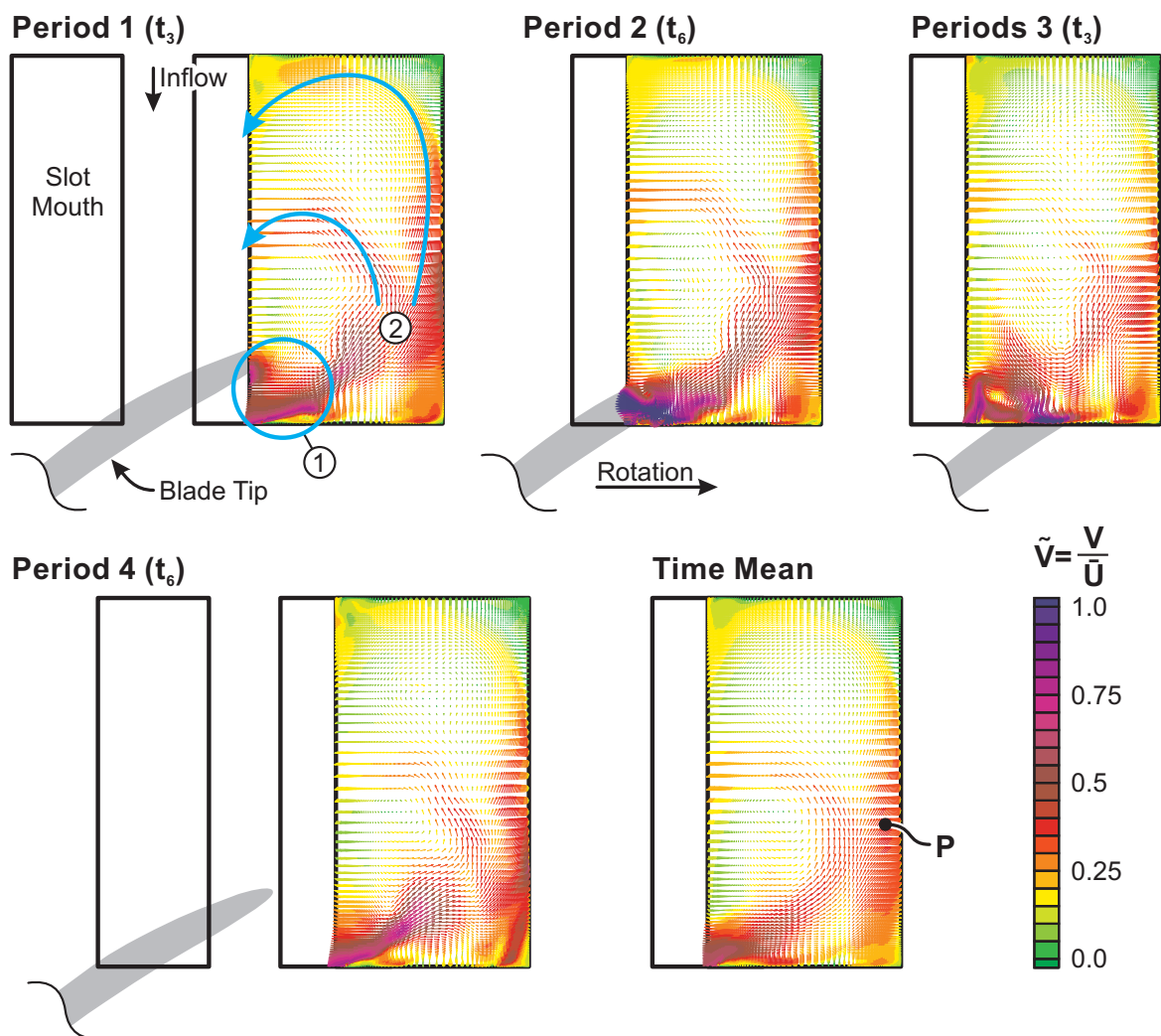


Figure 7.17: The flow field inside the slots near stall ($\phi=0.44$). The plots show normalised absolute velocity vectors on cut-planes in the middle of the slot during the four periods of a blade-passing, as well as the time-mean flow. The vectors are coloured by normalised absolute velocity to aid clarity.

Probe Location Schematic

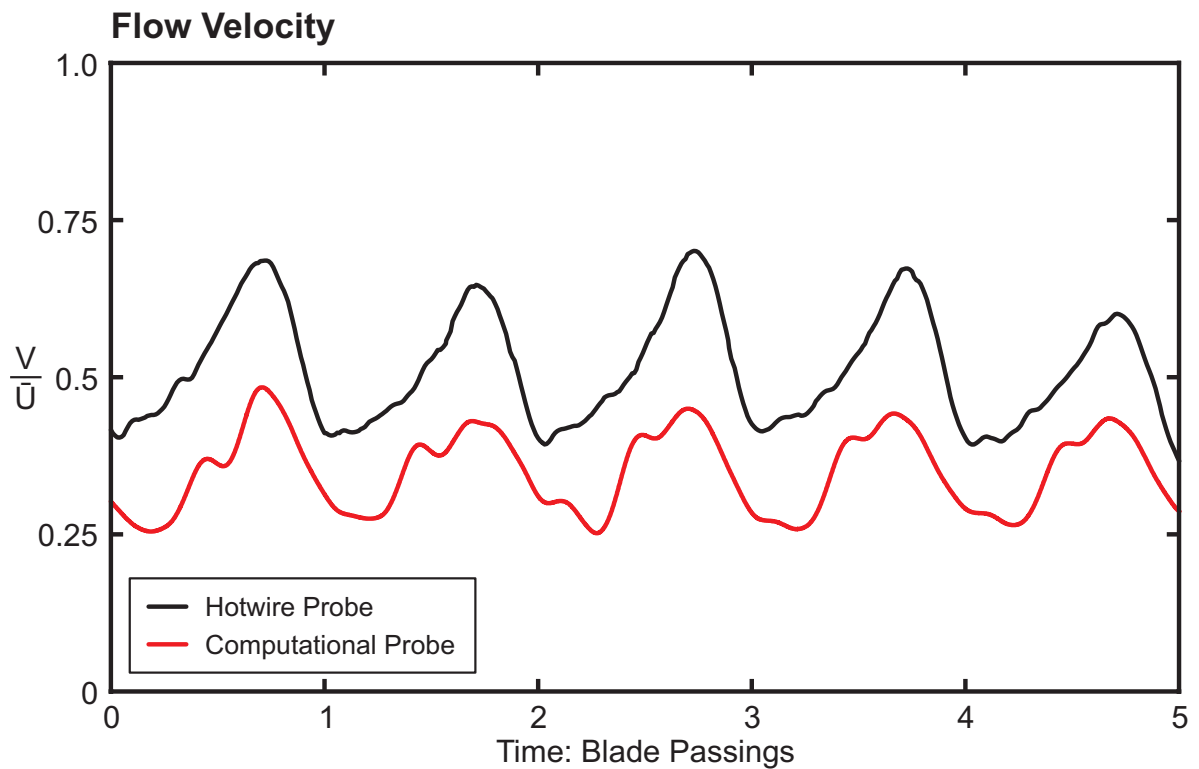
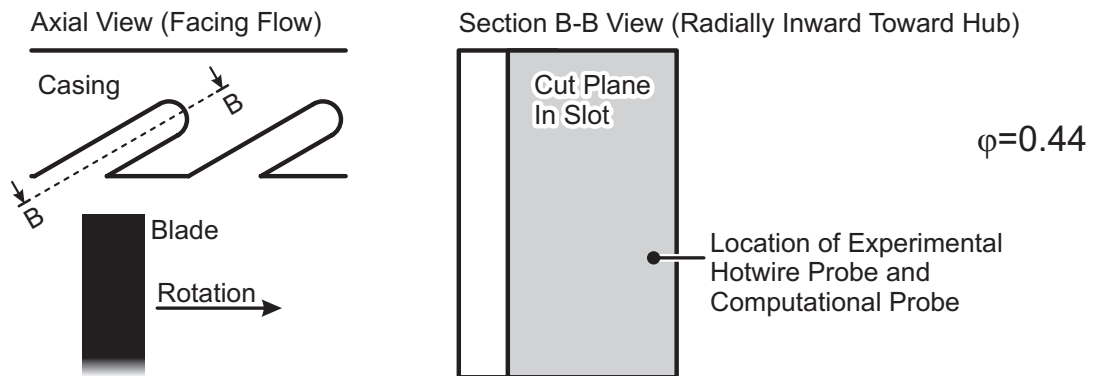
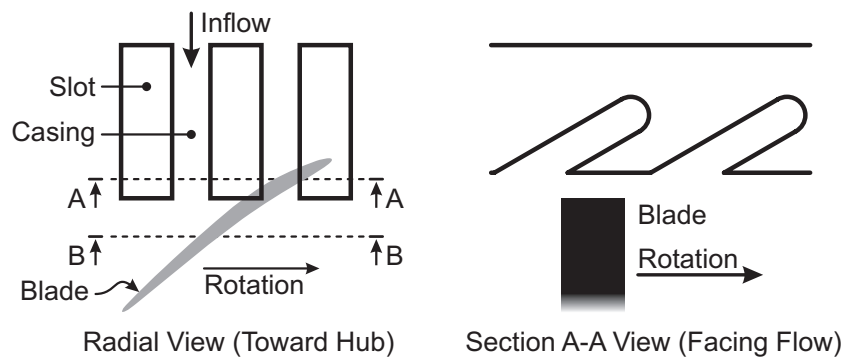


Figure 7.18: The velocity of the flow inside the treatment slots shown using hotwire experiments and data from the computational model. The graph shows how the normalised absolute velocity inside a casing slot (from slotted wall 'B') varies with time near the casing treatment stall point ($\phi=0.44$).

Cut Location Schematic



$$\phi=0.58$$

$$\Delta S:JK^{-1}$$



Views on Cut A-A

Views on Cut B-B

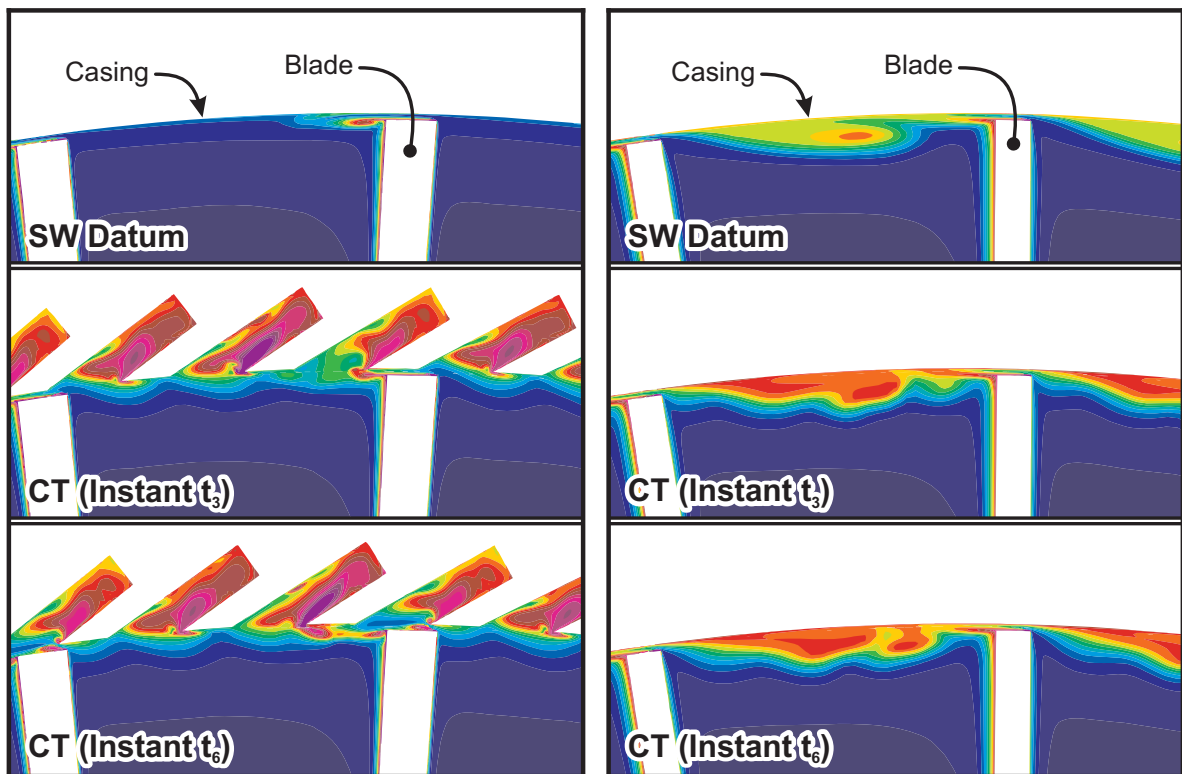
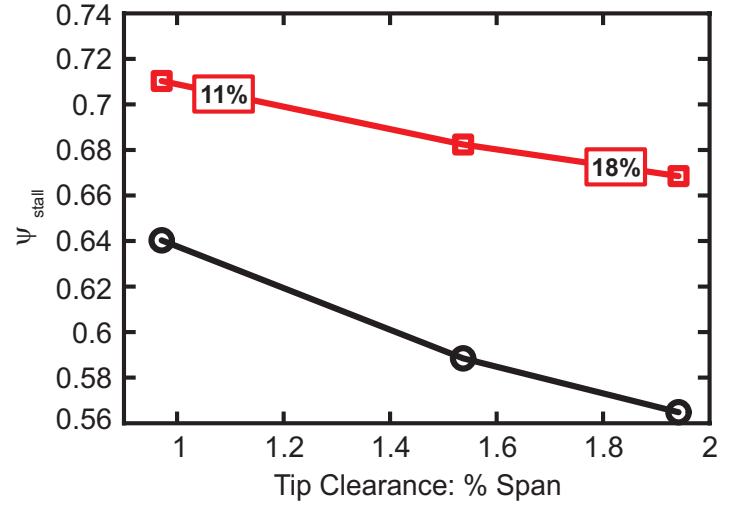
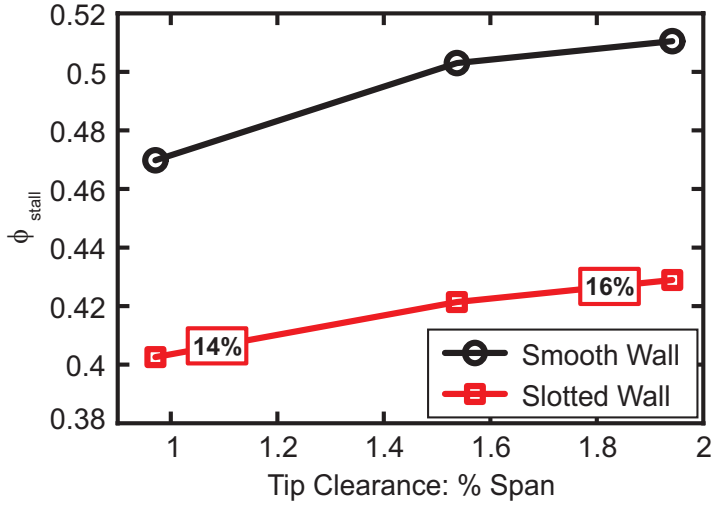


Figure 7.19: The entropy generated with casing slots and a smooth wall at the design point ($\phi=0.58$), shown using axial cuts at two locations. The left-hand side cuts are taken at 12% $c_{x,r}$, half-way between the blade leading edge and the slot trailing edge. The right-hand side cuts are taken at mid-chord. Two time instants are presented to show the unsteady behaviour with the slots installed.

Flow Rate and Pressure Rise at Stall



Maximum Efficiency and Design Point Flow Rate

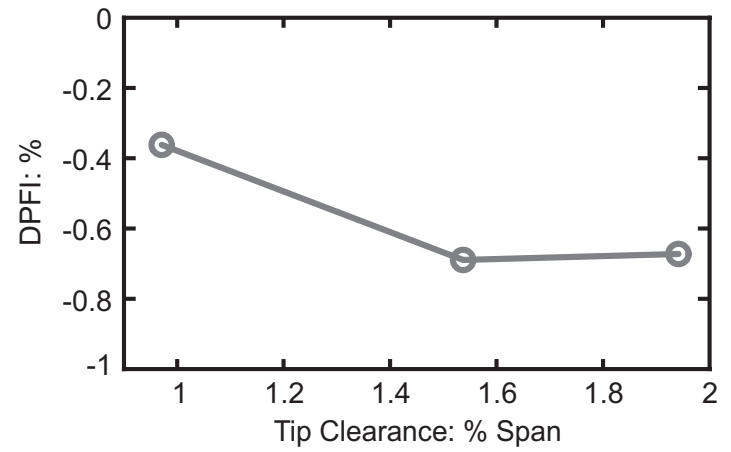
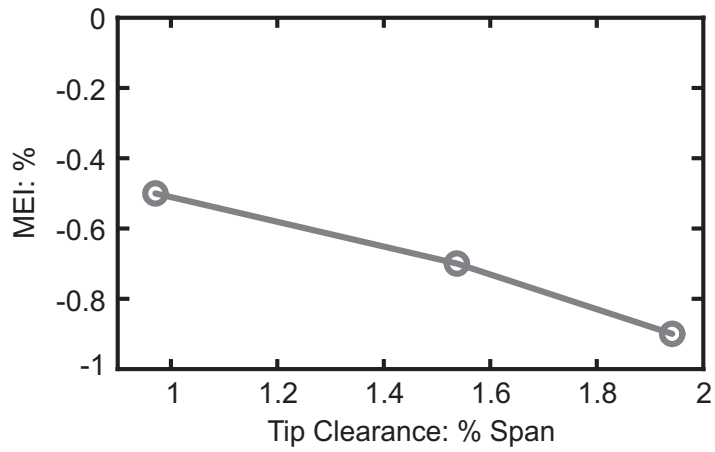


Figure 7.20: The impact of changing tip clearance on compressor performance. The upper plot shows the impact on ϕ_{stall} and $\psi_{s,stall}$ (stall margin improvement, SMI, and pressure rise improvement, PRI, are shown in the boxes). The lower plot shows the impact on maximum efficiency improvement (MEI) and design point flow rate increase (DPFI).

Chapter 8

Casing Grooves, Stall Inception and Solidity

The experimental and computational analysis in previous chapters has all been performed using the Natal compressor. This compressor stalls with a spike-type stall inception whether casing treatment is applied or not, but not all compressors exhibit this behaviour. This chapter presents experiments performed on the Red compressor, which exhibits a variety of stall inception mechanisms.

The work is divided into three parts. In the first part, an experimental parametric study is used to design single and multiple-groove casing treatments. The second part investigates the impact of stall inception mechanisms on the performance of the multiple-groove treatment, before testing the ability of published models to predict the observed behaviour. The third part uses results from both previous sections to evaluate the possibility of reducing blade count and installing casing grooves in order to improve efficiency while retaining adequate stall margin.

8.1 The Impact of Grooved Casings on the Red Compressor

This section presents two experimental parametric studies. The first study investigates the performance of a single circumferential groove at different axial locations, while the second considers the effect of using multiple grooves.

8.1.1 The Axial Location of a Single Casing Groove

In Chapter 5.1, it was found that a single circumferential groove was effective in two axial locations, when the upstream edge of the groove was at 8 and 50% chord, but not in between. This section ascertains whether the trend in stall margin improvement that was found using the Natal compressor also applies to the Red compressor. This provides useful comparative data because the characteristics of the Red compressor are different to the Natal compressor, due to the different rig geometry and the presence of IGVs (see Chapter 3).

A single groove was moved axially from the rotor blade leading edge to the trailing edge in a series of discrete tests (as described in Chapter 3). The groove had the same width and depth (as a percentage of $c_{x,r}$) as the deep rectangular groove used in the Natal compressor tests. At each location, improvements in stall margin (SMI), pressure rise at stall (PRI), maximum efficiency (MEI) and design point flow rate (DPFI) were measured. The results are shown in Figure 8.1, with the Natal compressor results included for reference.

Figure 8.1 shows that the trend in stall margin improvement with axial location generated by the groove has two local maxima in *both* the Red and Natal compressors. The first local maxima at around 10% $c_{x,r}$ are a similar size and shape in both compressors. The groove in the Red compressor generates a peak stall margin improvement of 3%, while in the Natal compressor it generates 4%. The second local maxima near mid-chord are slightly different, with the Red compressor maximum of 6% at 40% $c_{x,r}$ larger and further forward than the Natal compressor maximum of 4% at 50% $c_{x,r}$. The groove in the Red compressor generates a similar trend in pressure rise improvement at stall to that of stall margin improvement, with a maximum of 5% at 40% $c_{x,r}$. This also agrees with the Natal compressor results. The efficiency and design point flow rate reductions decrease as the groove moves aft, with the efficiency improvement increasing from -0.1% near the leading edge to negligible near mid-chord. This behaviour again matches the Natal compressor results.

These results show that the single circumferential groove performs particularly well when located near mid-chord in both compressors, giving the greatest stall margin improvement

with the least efficiency loss. The impact of the groove on compressor performance at different axial locations is remarkably similar in both the Red and Natal compressors.

Having identified the best locations to apply casing grooves in two compressors, the next section investigates whether the treatment can be improved by using more than one groove.

8.1.2 Multiple Casing Grooves

In Chapter 6.3, it was found that combining multiple casing grooves in the Natal compressor improved the stall margin improvement due to casing treatment. This section extends this investigation to the Red compressor. Two multiple-groove treatments were tested. The first treatment had two grooves at 33 and 60% $c_{x,r}$, centred on the maximum in stall margin improvement near mid-chord. The second treatment had an additional groove at 7% $c_{x,r}$ (near the leading edge maximum) making three grooves in total. The treatments were tested as previously, and the results are shown in Figure 8.2.

The results show that the two-groove treatment generates a greater stall margin improvement (8%) than either of its individual component grooves in isolation (5%). The combined stall margin improvement is, however, less than the sum of the isolated component grooves. The stall margin improvement generated by the three-groove treatment is 1.5% *lower* than the two-groove treatment, and is therefore much less than the sum of the isolated component grooves. The trend in pressure rise at stall matches that of stall margin improvement. The efficiency reduction caused by the two-groove treatment is greater than that of either of its component grooves and the three-groove treatment reduces the efficiency even more. These efficiency losses are the *sum* of the reductions for each isolated component groove.

These results show that the stall margin improvement is less than the sum of that generated by each individual groove. The efficiency losses, by contrast, are equal to the sum of each groove. This again agrees with the results of the Natal compressor tests. A single carefully positioned groove is therefore a sensible design choice, if a modest stall margin improvement is all that is required. The decrease in stall margin that occurs when the third groove is added to the two-groove treatment in the Red compressor is, however, counter-intuitive and does not agree with the Natal compressor results. In order to investigate this surprising result, four Red compressor characteristics, recorded during the parametric study, are shown in Figure 8.3.

The shape of the characteristics at peak pressure rise in Figure 8.3 is interesting. In the smooth wall and single groove cases, the pressure rise falls away sharply at stall when the characteristic gradient is negative. By contrast, with two and three grooves installed

the characteristics appear to 'roll over' smoothly to a positive gradient, before the loss of pressure rise occurs.

According to Camp and Day (1998), a change in the characteristic shape just prior to stall can be indicative of a change in the stall inception mechanism. High-frequency pressure transducer measurements of the stall inception pattern were therefore made. The smooth wall and single groove cases stalled with a spike inception, but the two and three-groove cases stalled with a modal inception. The three-groove characteristic rolls over at a higher flow rate than the two-groove characteristic, so modal stall occurs earlier. The small pressure rise improvement generated by the multiple-groove treatments is caused by these characteristics 'rolling over' near stall.

This suggests an interesting link between the stall inception mechanism and the effectiveness of casing grooves. This will be investigated further in the next section.

8.2 Casing Treatment and Stall Inception

In the Natal compressor tests, stall occurred via a spike inception without pre-stall modes, whether or not casing treatment was installed. In the previous section, however, pre-stall modal activity in the Red compressor appeared to limit the stall margin improvement generated by casing grooves. There is little scope to further investigate this apparent link between the effectiveness of casing grooves and stall inception mechanism by changing the casing geometry, so in this section, the blade configuration is altered to change stall inception.

The Red compressor's blade configuration was changed by re-staggering the IGVs and rotor blades in two separate sets of experiments. The three-groove treatment from the previous section is used throughout, because it should generate a large stall margin improvement if its performance is not limited by pre-stall modes (as was found in the previous section). This treatment also covers a greater area of casing than a single groove, which reduces the impact of any changes to the trend in stall margin improvement with axial location that may occur (it was impractical to repeat the single groove tests for each blade configuration).

8.2.1 Altering the IGV Stagger Angle

Experiments were performed with the IGVs set at six different stagger angles. The resulting absolute rotor inflow angles were measured in each case using a three-hole probe area traverse, giving -17.3 , -11.4 , -6.0 , -2.0 , 0.7 and 12.3° relative to the design angle of 13.0° (angles

in the direction of rotor motion are positive, see Figure 8.4). This traverse data was then averaged, and velocity triangles were used to calculate the rotor tip incidence at stall relative to that which would occur *at the same stalling flow coefficient* with all the blades at their design stagger angles. By comparing incidence at a constant flow coefficient in this way, the effect of the changing flow coefficient at stall is not included in the results. Values were calculated at the rotor tip (94% span) because previous authors have identified this region as being important for stall inception (Camp and Day, 1998; Simpson and Longley, 2007), and at the mid-span for reference. The characteristics at each incidence, with and without casing grooves, are shown in Figure 8.5, with sketches showing the different characteristic shapes at stall. The stall inception patterns were also measured using high-frequency pressure transducers. These results are shown in Figure 8.6. The methods used to re-stagger blades, perform area traverses and classify stall are presented in Chapter 3.

The results show that all the smooth wall cases stall when the characteristics (black lines in Figure 8.5) have a negative gradient (the characteristics are still rising at stall, although the gradient decreases as incidence rises). The stability of all the smooth wall cases is therefore limited by a ‘Spike’ stall inception as suggested by Camp and Day (1998) and confirmed by experiment in the upper plot of Figure 8.6.

The treated cases (red lines in Figure 8.6) stall with *three* different stall inception mechanisms. The **lowest incidence** case (-1.9°) stalls when the characteristic is still rising. The stability of this case is therefore limited by ‘Spike’ stall inception as illustrated in the upper plot of Figure 8.6). The **medium incidence** cases (-0.1 to 1.8°) are different. These characteristics roll over *just prior* to stall. The roll over of the characteristic occurs rapidly (within forty to eighty rotor revolutions). The stall inception pattern (middle plot in Figure 8.6) shows that the generation of pre-stall modes *leads directly* to stall, with the stall cell growing rapidly out of the modal activity. The stability of this case is therefore described as being limited by a ‘Destabilising Mode’ stall inception. The appearance of this type of modal activity rapidly destabilises the compressor. The **highest incidence** case (2.8°) is different again. Here the characteristic rolls over some way before stall, drops slightly (at point ‘A’ in Figure 8.5) and further throttling is then required before stall occurs. The stall inception pattern (lower plot in Figure 8.6) shows that modes are present some time before stall inception. When stall finally occurs, a broad inception grows out of the modal activity. The stability of this case is therefore described as being limited by a ‘Stable Mode’ inception mechanism, because stable operation with modes is possible before stall.

The stall inception mechanism therefore changes from spikes to modes with increasing rotor incidence as observed by Dobrzynski *et al.* (2007) and Young (2008). The decreasing gradient of the dotted lines in Figure 8.6 also shows that as the stall inception mechanism changes

from spikes to destabilising and stable modes the propagation speed of the emerging stall cell decreases (shown by the decreasing gradient of the dotted lines in the figure).

The impact of these changes of inception mechanism on the stall margin improvement generated by the casing grooves is summarised in Figure 8.7. The stall inception mechanism is labelled in each case. In the low incidence case ('spike limited'), the casing grooves generate the greatest stall margin improvement. As the incidence increases, the onset of destabilising modes starts to progressively limit the stall margin improvement generated by the grooves. The pre-stall modes therefore act as a 'modal barrier', preventing further stall margin improvement. In the highest incidence case ('stable mode limited'), where the compressor operates with a positive characteristic gradient some way before stall, the stall margin improvement generated by the grooves is again much lower than was measured in the spike limited case (there is a slight improvement over the destabilising mode limited case, but this is an isolated point).

The next section expands this study by re-staggering the rotor blades instead of the IGVs.

8.2.2 Altering the Rotor Stagger Angle

The impact of the rotor blade stagger on the stall inception mechanism and casing treatment performance was investigated using two different compressor builds. Build 'A' is the standard compressor configuration, which was tested with stagger angles of 2.3, 1.3, 0.1, -0.3, -1.2, -2.2 and -4.2° relative to the design stagger angle of 30.7°. Build 'B' was identical to Build A, except that the rotor blades were 20% stiffer. Build B was tested with stagger angles of -0.2, -1.2, -2.2 and -4.2° relative to design. The running tip clearances were the same in both builds. The effect of these stagger angle changes on the rotor tip incidence was calculated using the same method as the IGV results and the stall margin improvement and stall inception mechanism were measured as previously.

The results are presented in Figure 8.8. The upper graph shows the characteristics of Build A at five different rotor stagger angles with the stability limits imposed by each stall inception mechanism (some results are omitted for clarity). The stability limits imposed by each stall inception mechanism are also shown. As previously, all the smooth wall cases stall with spike inception, which occurs when the characteristics have a negative gradient, except for the highest incidence case (4.0°). This case stalls with a stable mode inception, and the characteristic has a positive gradient prior to stall. The grooved cases again show all three types of stall inception pattern. The low incidence cases (-2.4 and -1.4°) show spike inception, the medium incidence cases (-0.2 to 2.1°) show destabilising mode inception and the high incidence cases (2.1 and 4.0°) show stable mode inception.

The stall inception mechanism thus changes from spikes to modes as the rotor incidence increases, as seen in the IGV stagger experiments. The links between the gradient of the characteristics at stall and the stall inception mechanisms observed in the IGV stagger experiments were also observed during these rotor stagger tests.

The change in the stall margin improvement generated by the casing grooves as the rotor tip incidence changes is plotted in the lower plot in Figure 8.8. The results from both the IGV and the rotor blade re-staggering experiments are shown, and the stall inception mechanism of each case is labelled, as previously.

The graph shows good agreement between the IGV and rotor stagger tests. When the rotor tip incidence is less than -1.5° , the casing grooves are spike limited and generate the greatest stall margin improvement (9%) in all cases. When the rotor tip incidence is between -1.5° and 2.0° , the stall margin improvement decreases at a rate of 1.8% per degree of incidence as the destabilising modes progressively limit the performance of the grooves. When the rotor tip incidence is greater than 2.0° , stable modes occur and the stall margin improvement falls to around 2%; about a quarter of what it is in the spike limited cases. This good agreement between the IGV and rotor stagger results further suggests that the rotor blade tip incidence is a key factor in setting the stall inception pattern, because the span-wise variation in rotor incidence is very different when the IGVs, as opposed to the rotor blades, are re-staggered.

The contrast between Builds A and B is also interesting. With Build B, the stall margin improvement generated by the grooves *falls to zero* (the casing grooves stop working completely) at an incidence of 2.0° due to destabilising modes. By contrast, Build A switches from destabilising modes to stable modes at a lower incidence than Build B, so the casing treatment continues to work, but still generates a much smaller stall margin improvement than the spike limited cases. This difference occurs because the Build A characteristics roll over more than those of Build B, encouraging the onset of stable modes¹. This result further underlines the previous finding that pre-stall modes are highly deleterious to casing treatment performance, destabilising modes especially so.

These results show that the stall margin improvement generated by casing grooves can be severely curtailed by changes in the stall inception mechanism. The next step is to ascertain whether these changes in stall inception mechanism can be linked to changes in the rotor outflow blockage, as has been suggested in the literature. First however, the stable mode stall inception is investigated further.

¹Since both builds are identical except for rotor blade stiffness, these changes may be caused by Build A untwisting more than Build B under load, increasing the blade tip incidence, but this could not be quantified.

8.2.3 Modal Pre-Stall Behaviour

The previous sections identified two types of modal stall that both reduce the stall margin improvement generated by casing grooves. Destabilising modes lead directly to stall, while stable modes do not. Stable modes occur when the rotor incidence is high due to poor matching of flow angles. This section examines stable modes in more detail.

In Figures 8.5 and 8.8, the stable mode characteristics both rolled over and dropped down slightly (point 'A') before settling onto a positive gradient. Examination of the static pressure rise across the rotor and stator shows that this drop may be caused by falling pressure rise in one or both components. To study the modal behaviour, data from the six high-frequency pressure transducers was collected at three points on the characteristic; before the drop ('A'), after the drop ('B') and at stall inception ('C').

The results in Figure 8.9 show that in the stable mode case, modes appear near the roll over and drop in the characteristic (between points 'A' and 'B' in Figure 8.9). The compressor then operates stably with these modes as it is throttled down the positive characteristic gradient until stall occurs at 'C'. The stall cell then grows from the modal velocity deficit, as seen with destabilising modes. The results for point 'C' also show that spikes may form while the compressor is operating on this part of the characteristic, but they do not stall the compressor. This is different to the behaviour when the characteristic has a negative gradient, where the first spike to traverse the annulus normally causes stall.

The stable operation with spikes observed before stable modal stall is interesting to compare with published work. März *et al.* (2002) observe 'rotating instabilities' that cause noise and vibration in compressors operating near stall. Inoue *et al.* (2004) observe similar features in a 'mild stall' condition. Both papers propose that these effects are caused by vortical flow features cascading around the rotor blades. The characteristics of the compressors used by März *et al.* and Inoue *et al.* rolled over before stall, so comparison with the present results suggests that the observed features may have been a form of spike that did not cause stall (although further experimental work is needed to verify this). Wisler *et al.* (2002) repeated the März *et al.* (2002) experiments on a multi-stage compressor with a characteristic that exhibited very little roll over near stall, and did not find any rotating instabilities. This agrees with the present work: the Red compressor cannot operate stably with spikes when the characteristic is negative near stall.

Camp and Day (1998) also investigated modal activity on a multi-stage compressor, and made the characteristic roll over using a downstream gauze. In this case, modes only occurred at the peak of the characteristic, so the compressor stalled with a spike inception

while the characteristic gradient was negative. Modes and spikes were also observed at opposite ends of the same compressor. These results suggest that the behaviour of modes in a multi-stage compressor is more complex than it is in a single-stage environment.

8.2.4 Outflow Blockage and Stall Inception

Camp and Day (1998) suggested that modal stall might be associated with flow separation near the hub of the rotor. To ascertain whether the changes in the stall inception mechanism observed in the present work are associated with changes in the rotor blockage, hotwire traverses were performed on two of the smooth wall cases from the blade stagger study. One (Case 'S') stalled with spike inception, while the other (Case 'M') stalled with stable modes. The axial velocity was measured near their respective stall points. The results were normalised by the mean inflow axial velocity, to aid comparison, and are shown in Figure 8.10. Low axial velocity is considered blockage.

The traverses show that the changes in blockage between spike and modal stalling case are subtle. The main differences occur near the casing, where in the modal stalling case the blockage is more severe and located nearer the pressure surface than in the spike stalling case. There is no sign of large separation in the modal case as suggested by Camp and Day (1998), and no indication of the location of stall inception moving away from the casing as suggested by Greitzer *et al.* (1979). It is therefore not yet clear from this data why the casing grooves stop working when the compressor stalls with modes.

The work presented thus far has shown that changes to the stall inception mechanism can reduce casing treatment performance, but the associated changes to the compressor flow field are subtle. The next section considers how changes to the stall inception mechanism of a compressor might be predicted during design.

8.2.5 Casing Grooves Performance Prediction

The performance of casing grooves is dependant on the stall inception mechanism. To be sure that grooves will work in a given compressor design, the stall point *and* inception mechanism of the smooth-wall case must be predicted. If the smooth walled compressor stalls with a spike inception pattern (so that installing grooves is worthwhile), the stall point of the treated compressor must then be predicted, allowing for modes curtailing the stability improvement.

These predictions are hard to make due to the complexity of the stalling process. Predicting the stall point has been considered by many authors (see Chapter 2), but predicting the stall inception mechanism has received less attention. This section investigates two published approaches to predicting the stall inception mechanism and hence the possible effectiveness of casing grooves.

Blade and Wall Loading Analysis

This section considers two related loading-based analyses. The first is an early model by Greitzer *et al.* (1979), and the second is a development of Greitzer's work.

Greitzer *et al.* (1979) suggested that casing treatment only works if stall occurs on the casing wall, and presented a method of determining whether stall will occur on the casing or rotor blades. It compares two aerodynamic loading parameters. The first parameter is the diffusion factor (Lieblein *et al.*, 1953) applied to the rotor blades (DF_r), which predicts two-dimensional (or cascade-type) blade stall. The second parameter is the normalised casing static pressure rise ($C_{p,rc}$), which is effectively a de Haller number for the near-casing flow. Greitzer predicts stall when the value of either parameter exceeds 0.6, and shows that casing treatment only works when $C_{p,rc}$ passes this value (i.e. 'wall stall' occurs). The model was published before spike and modal stall were identified (by Day, 1993b), but it is possible that the wall and blade stall in Greitzer were similar phenomena.

This analysis was applied to the Red compressor using data gathered near-stall ($\phi = 2.5\%$ greater than ϕ_{stall}) from three-hole probe and hotwire traverses (as described in Chapter 3). Red compressor data is processed for the IGV (Build 'A') and rotor (Build 'B') stagger tests, with the smooth wall and three-groove treatment from Section 8.1.2 installed. Natal compressor data (shown for reference) is from the smooth wall and slotted wall 'A' (see Chapter 7). The results are plotted on the axes used by Greitzer *et al.* (1979) in the upper graph of Figure 8.11.

All the cases stall before the critical value of diffusion factor is reached. The smooth walled cases stall when $C_{p,rc}$ is close to 0.6, indicating critical endwall loading at stall. The value of $C_{p,rc}$ is greater (up to 0.63) when the casing grooves operate effectively. The Greitzer model therefore predicts wall stall in all cases, and is unable predict the different stall inception mechanisms shown by the tested cases (spikes, destabilising modes and stable modes).

The second analysis investigates the changes to the spanwise distribution of blade loading caused by the varying incidence. The blade loading ($\frac{\Delta h_0}{U^2}$) was therefore evaluated near the stall point of each tested case at 20, 50 and 80% span (in approximately two-dimensional

flow) using three-hole probe traverse data. The mass-averaged value was also found. The lower graph in Figure 8.11 shows these blade loading results plotted against $C_{p,rc}$ (from the Greitzer analysis). As seen in the Greitzer analysis, there is no clear link between blade loading near stall and the stall inception mechanism. In fact, the blade loadings at stall are quite similar, because the higher incidence cases stall at a higher flow coefficient.

These two loading analyses predict that the rotor casing wall is highly-loaded at stall (effective casing treatments may permit greater wall loading). However, they do not predict the stall inception mechanism.

The presence of the stator, blade aspect ratio and tip clearance can also affect stability (Cumpsty, 1989a). The model of Koch (1981) includes these effects using a mean-radius approach with correlations (see Chapter 2), but this model does not predict the stall inception mechanism and the near-casing flow, which casing treatment affects, is not included. The same applies to the related 'effectivity' analysis discussed by Smith (2002). These models are therefore not appropriate for explaining the results in this work.

The next section investigates the impacts of blade incidence and blockage on setting the stall inception pattern.

Incidence and Near-Casing Blockage Analysis

A more recent model by Simpson and Longley (2007) compares two different parameters to those considered in the previous section. The first parameter is the relative inflow angle near the rotor tip at stall. This is essentially a measure of the rotor tip incidence, which will be used here because the tip incidence has been linked to stall inception by the present work and Camp and Day (1998)². The second parameter is the quotient of the axial velocity downstream of the rotor over the upstream value at 94% span. This 'meridional acceleration coefficient' (C_{ma}) was intended by Simpson to measure flow acceleration caused by separations, but it can also measure the increase of near-casing blockage in the rotor. Using inclined upstream gauzes to change the radial flow distribution, Simpson found that a large C_{ma} and small relative inflow angle (i.e. small rotor incidence) indicated modal stall. This suggests that knowledge of the incidence and near-casing flow at stall would be sufficient to predict the stall inception mechanism.

The present results show that modal stall is more likely when the rotor incidence is large, and thus disagree with Simpson. This (as yet unexplained) contradiction notwithstanding,

²Using the relative inflow angle was tried, but gave poor results because changing the blade stagger angle can alter the stall inception mechanism, but not the relative inflow angle.

the Simpson model was applied to the present results to ascertain whether the incidence and C_{ma} could be used to predict the stall inception mechanism.

To this end, the axial velocity up and downstream of the rotor was measured using three-hole probe and hotwire traverses near the stall point of a number of cases from the re-stagger tests (some cases could not be tested due to a blade failure). Velocity triangles were then used to find the true rotor tip incidence at each case's stall point (rather than the relative incidence used previously). Data was extracted at 94% span, but locations closer to the casing gave similar results.

The data is plotted in Figure 8.12, with cases M and S from the blockage tests labelled for comparison. The cases that stall with a spike inception are generally toward the lower left of the plot, while the destabilising mode cases are toward the upper right. Stable mode cases are generally further toward the extreme upper right. The results are, therefore, approximately distributed according to their stall inception mechanism. However, this model could not be used as a design tool because there is no absolute boundary for discriminating between spikes and modes in different compressors. Calculating the meridional acceleration coefficient also requires subtle changes in near-casing blockage to be predicted accurately, which would be difficult during design. Therefore, the Simpson model allows an interesting comparison between similar cases, but cannot be used to predict the stall inception mechanism of a given compressor.

The results in Figure 8.12 also show that the rotor incidence at stall varies from 2 to 4° for the spike-initiated cases. There is therefore no clear 'critical rotor incidence' at which spike-initiated stall will occur (as suggested by Camp and Day, 1998).

The different behaviour of the Red and Natal compressors is also interesting. When casing treatment is added to the Red compressor (red lines), it moves upward and to the right of the smooth wall case (toward modal stall). By contrast, the Natal compressor (black line) moves *downward* and to the right of the smooth wall case (avoiding moving toward modal stall). This may explain why the Natal compressor always stalls with a spike inception, but further work on more compressors is needed to ascertain the significance of this behaviour.

Having demonstrated the importance of stall inception mechanism in casing groove design, the next part of the chapter considers the role of rotor blade solidity and the possibility of using casing grooves to reduce the blade count of a compressor.

8.3 Casing Treatment and Blade Solidity

If the solidity of a rotor is slightly reduced by removing rotor blades, the efficiency may increase (due to reduced wetted area) but the stall margin may decrease (due to increased loading). Casing grooves can improve stability with a small efficiency penalty, so this section considers the possibility of removing blades to improve efficiency and then using casing grooves to maintain stability. Removing rotor blades is desirable because they are expensive, and removing them reduces the weight and cost of the rotor assembly.

To this end, a rotor with 5% fewer blades was made for the Red compressor (from 58 to 55 blades, solidity from 1.48 to 1.40). The two rotors were then tested with identical blades using the same running tip clearance. The blades in the 55-blade rotor were re-staggered slightly (by 0.25°) so the characteristics of both rotors matched at the design flow rate. The casing treatment used was a single groove at $33\% c_{x,r}$, which in the parametric study (Section 8.1.1) gave a good stall margin improvement with small efficiency loss, and was convenient to test. The characteristics of the smooth wall and treated cases were recorded in back-to-back tests with both rotors. They are shown in Figure 8.13.

The characteristics show that with either rotor installed, the casing groove generates a stall margin improvement of 5% relative to the datum 58 rotor build. At the same time, the efficiency of the treated 55-blade rotor was 0.25% higher than the smooth-walled 58-blade rotor. The treated 55-blade rotor therefore has a greater stall margin and greater efficiency than the datum smooth-walled 58-blade case.

All three cases shown in Figure 8.13 stall with spikes, but the characteristic for the treated 55-blade rotor has a shallower gradient at stall than the treated 58-blade rotor. This indicates that the modal limit is closer with the 55-blade rotor installed. To test this, the two-groove treatment from the parametric study (Section 8.1.2) was applied to the 55-blade rotor. The two-groove treatment generated a stall margin improvement of 8% with the 58-blade rotor, but with the 55-blade rotor it only generates 5.5%. As expected, this is because the characteristic rolls over at a higher flow rate with the 55-blade rotor, causing modes and premature stall. The three-groove treatment was also tested, and generated a lower stall margin improvement than two grooves due to the onset of modes (as previously).

These results show that removing blades and adding casing treatment requires care. It is possible to remove rotor blades to improve efficiency, and then apply casing treatment to improve stability, but if too many blades are removed, the characteristics will roll over, modes will occur at higher flow rates, and the stall margin improvement generated by the casing treatment will be reduced. With care however, efficiency and stability improvements may be possible by considering casing treatment and blade design as a unified system.

8.4 Discussion

This paper has shown that the stall margin improvement generated by casing grooves in different compressors is similar, so long as the compressors continue to stall with a spike inception when the grooves are applied. If this condition is met, the optimum location for a single groove is near mid-chord, where the stall margin improvement is large and the efficiency losses are small. Using more than one groove causes efficiency losses that are the sum of each component groove, while the stall margin improvement is less than the sum of the individual component grooves.

Casing treatment effectiveness can be seriously reduced by the onset of modal stall inception. Two kinds of modal stall have been identified: destabilising and stable modes. Destabilising modes lead directly to stall. They appear as the characteristic rolls over immediately prior to stall. Stable modes do not lead directly to stall. They appear as the characteristic rolls over, but this can occur some time prior to stall. Both types of modal stall inception reduce casing treatment effectiveness, and in some cases, modes can stop casing treatment working altogether.

Predicting the stall inception mechanism is thus important for ensuring that a casing treatment will work properly. The prediction method used by Greitzer *et al.* (1979), which compares the relative loading on the casing wall and the blade, predicted separation on the casing wall in all the present cases. The Greitzer *et al.* method was therefore found to be unsuitable for predicting the type of stall inception mechanism. The model used by Simpson and Longley (2007), which essentially compares the blade tip incidence and the generation of near-casing blockage, provides an interesting framework for comparing cases, but cannot give a definitive prediction of the stall inception mechanism. Therefore, these models cannot be used to predict whether casing treatment performance will be limited by the early onset of modes in a given compressor design.

In the present work, increasing the rotor tip incidence (for a given flow rate) made the stall inception mechanism change from spikes to modes. This change in stall inception was observed whether the incidence on the rotor tips was increased by re-staggering the IGVs or the rotor blades. However, comparison with the literature suggests that multi-stage environments can make this more complex. Using a four-stage compressor with a similar blade design to the machine used in the present work, Camp and Day (1998) found that increasing the incidence on the first-stage rotor blades (using IGVs) caused stall inception to change from modes to spikes. This is the opposite of the present results and is due to multi-stage effects. As the incidence increases in Camp and Day, the characteristics of the *first stage* start rolling over before stall (as seen in the present work), but the characteristics

of the compressor as a whole actually stop rolling over (due to the effect of the three downstream stages). Since the onset of modes is linked to the overall compressor characteristic, spikes, rather than modes, occur as the incidence increases. Changes in stage matching at different speeds can also alter the stall inception mechanism of a multi-stage compressor (Day, 1993b), so casing treatment may not work at all speeds. These comparisons suggest that predicting the stall inception mechanism (and hence casing treatment performance) in multi-stage compressors will be difficult.

Changing the rotor tip clearance and stator stagger angle can also alter the stall inception mechanism (Day, 1993b; Simpson and Longley, 2007), but it was not possible to study these factors in the present work.

This chapter has focussed on core-flow parameters that could be used in design, and has therefore ignored the detail of the near-casing flow field. It has been suggested that spillage of flow associated with the tip leakage vortex forward of the rotor leading edges leads to spike-stall (Hoying *et al.*, 1999; Vo *et al.*, 2008). However, the detailed investigation of the near-casing flow field in the spike-stalling Natal compressor in Chapter 5 found that the leakage vortex was always well downstream of the leading edge plane near stall. Further work by Yoon *et al.* (2006) found that decreasing the rotor incidence (which should cause spike-stall according to the present work) moves the vortex downstream and away from the leading edges, also making forward spillage less likely. Note: Vo *et al.* (2008) also proposed flow moving forward from the rear of the blade tip as a second initiator of spike-stall. However, until the mechanisms of spike and modal stall are better understood, predicting the stall inception mechanism is likely to remain difficult.

If changes to the stall inception mechanism rule out casing treatment, active control can still be used. This can prevent both mode and spike stall (Day, 1993a), but active control has other disadvantages (see Chapter 2).

The solidity tests show that efficiency and stability improvements may be achieved by designing the casing treatment and blading as a cohesive unit, but equally, improper design can lead to the casing treatment not working due to the premature formation of modes. Robust design is therefore difficult while the onset of modes remains difficult to predict. This is an important challenge for the future.

8.5 Conclusions

It is concluded that:

1. The stall margin improvement generated by a single circumferential groove as it is moved aft from the leading edge has been shown to be similar in two different compressors. In both cases, the stall margin is maximised when the groove is either near the leading edge (10% chord) or near 50% chord. The efficiency loss due to the groove reduces to negligible as it is moved aft, so the optimal location is near 50% chord.
2. The efficiency loss caused by multiple grooves is the sum of the losses generated by the component grooves, but the stall margin improvement is less than the sum of the improvement due to the component grooves.
3. Two kinds of modal stall inception have been identified. If the characteristic rolls over immediately prior to stall 'Destabilising Modes' occur and lead directly to stall. If the characteristic becomes horizontal, or rolls over, some way before stall 'Stable Modes' occur and further throttling (with modes present) is required to stall the compressor.
4. The maximum possible stall margin improvement to be gained by adding casing grooves will only be achieved if spike-type stall inception is present before and after the grooves are added. If the addition of the casing grooves leads to the occurrence of modes, the stall margin gain is likely to be curtailed. Little or no stall margin improvement is to be expected if casing grooves are added to a compressor where the smooth wall configuration exhibits modal stall inception.
5. Increasing the incidence on the rotor blades, either by altering the IGV or rotor stagger angle, causes the stall inception mechanism to change from spikes to destabilising modes, and then stable modes. The propagation speed of the stall cell also reduces as the stall inception changes from spikes to stable modes.
6. It has been shown that efficiency and stability can be improved by removing rotor blades to improve efficiency and then applying casing treatment to maintain stability. However, removing blades from a rotor can cause modes to appear prematurely, limiting the stall margin improvement that can be expected of the grooves.
7. The variations in the rotor outflow blockage associated with spike and modal stall inceptions are small and cannot be easily used to predict the stall inception type. A combined blade tip incidence and near-casing blockage analysis similar to that proposed by Simpson and Longley (2007) has been shown to provide a comparison between similar cases in the same compressor, but no reliable design tool for accurately predicting the stall inception mechanism in a given compressor has been identified.

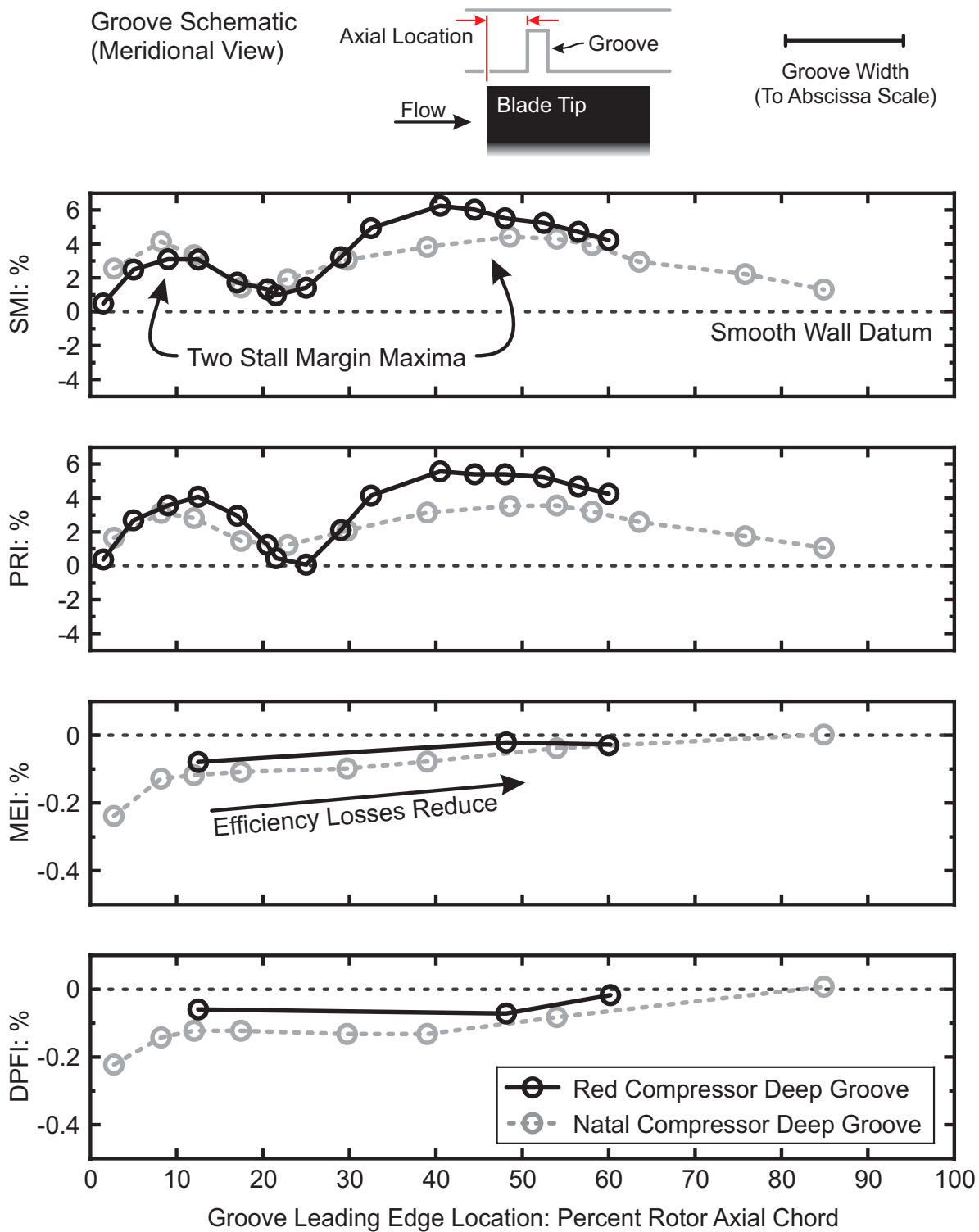


Figure 8.1: The effect of altering the axial location of a single circumferential groove on stall margin improvement (SMI), pressure rise improvement (PRI), maximum efficiency improvement (MEI) and design point flow increase (DPFI) in the Red and Natal Compressors.

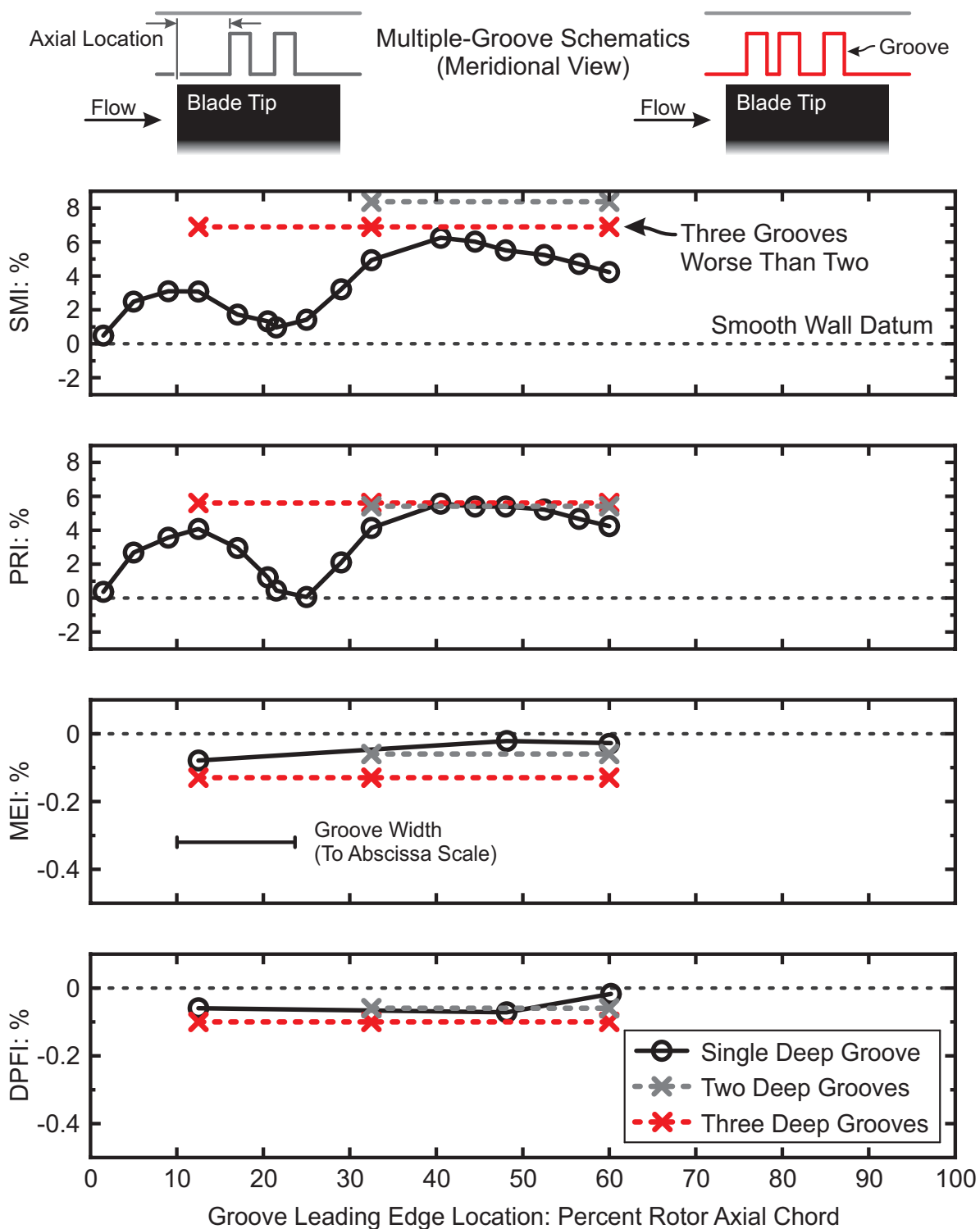


Figure 8.2: The effect of applying casing treatments containing two and three circumferential grooves on stall margin improvement (SMI), pressure rise improvement (PRI), maximum efficiency improvement (MEI) and design point flow increase (DPFI) in the Red Compressor.

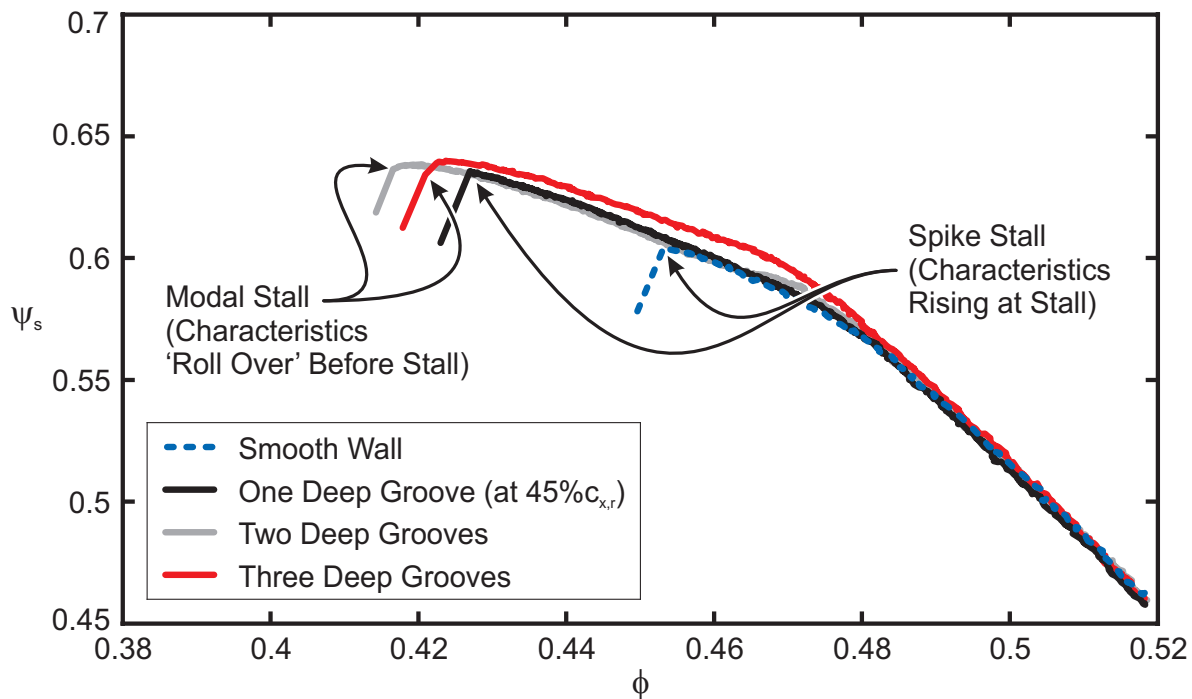
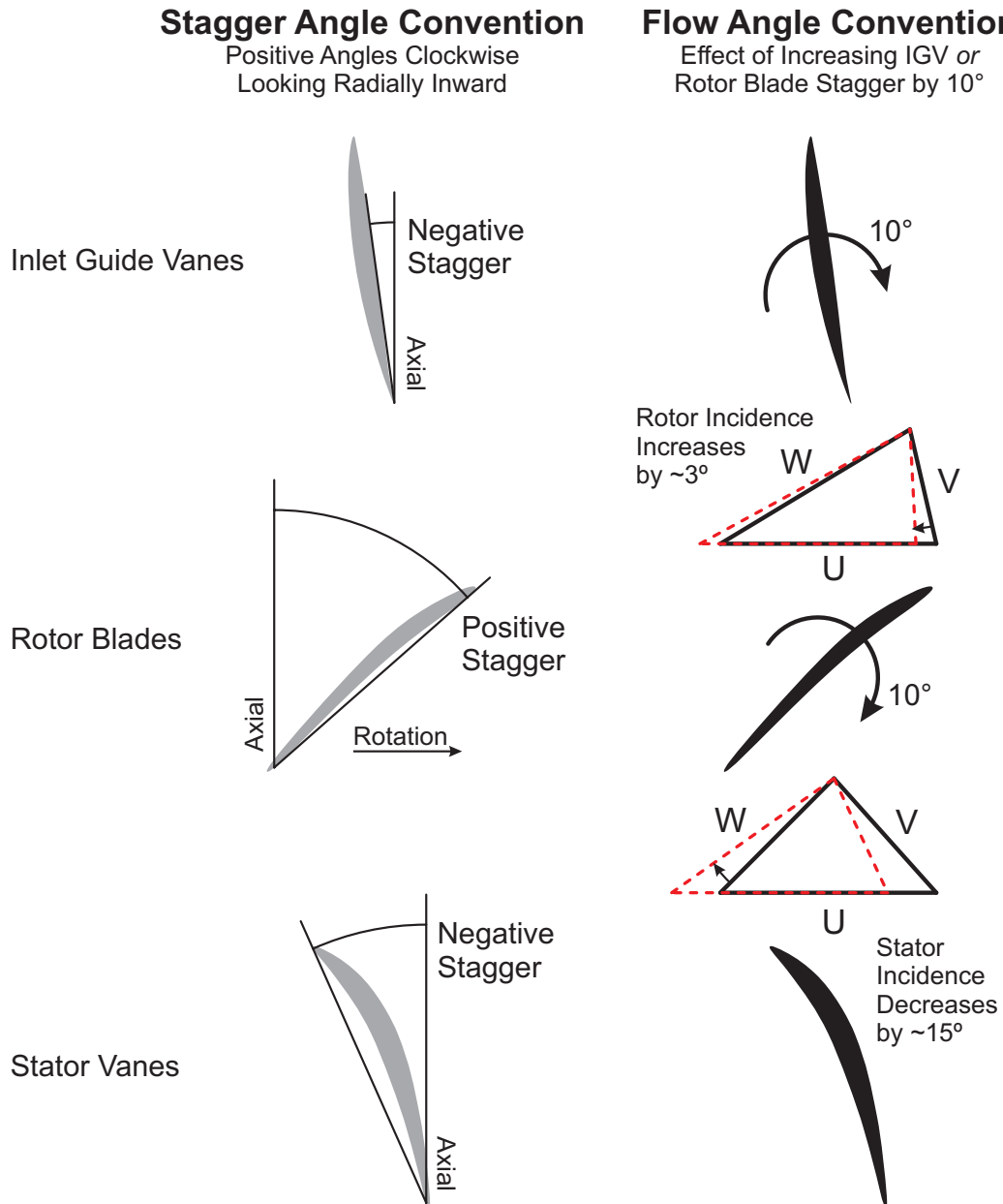


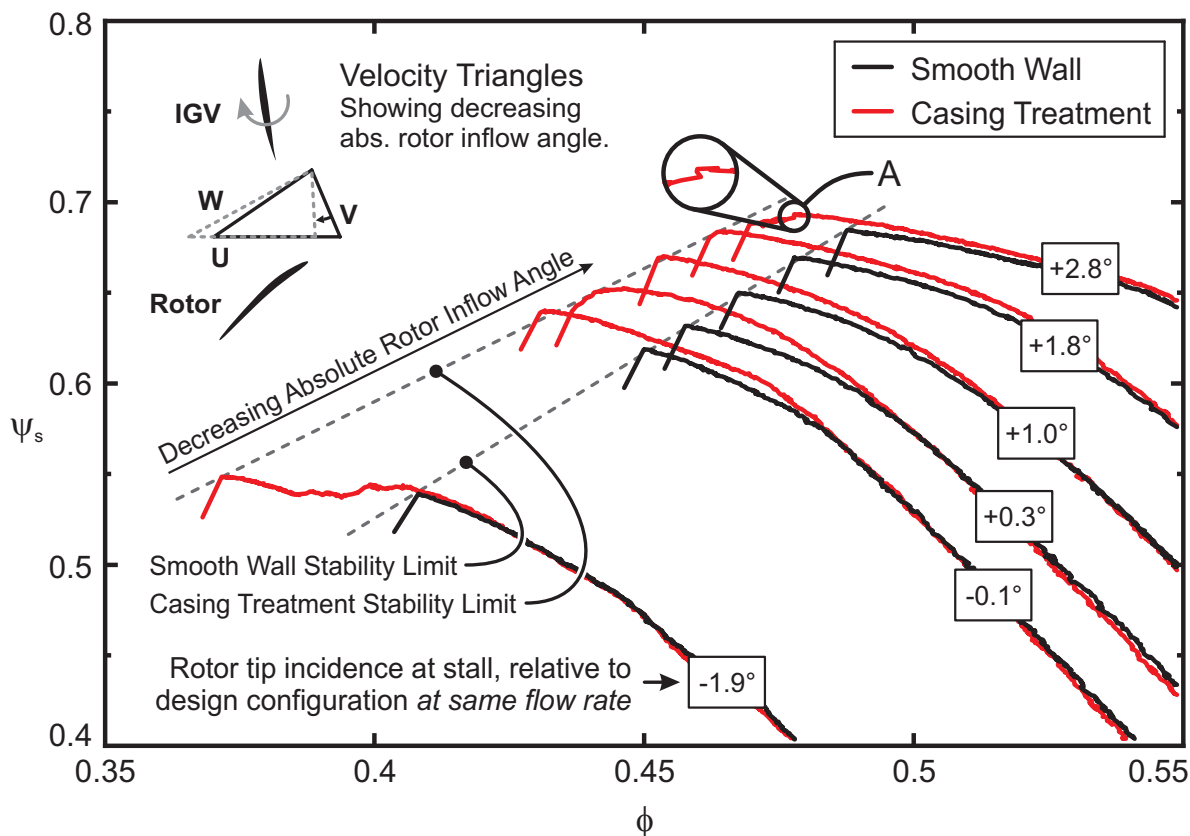
Figure 8.3: Total-to-static characteristics of the Red compressor with a smooth wall and casing treatments containing one, two and three grooves, showing the characteristics 'rolling over' near the stall point when two or more grooves are applied.



Positive Stagger Angle Changes cause Negative Changes in Flow Angle

This Increases Rotor Incidence where the IGV Stagger Angle is Changed or
Decreases Stator Incidence where the Rotor Blade Stagger Angle is Changed.

Figure 8.4: Two sets of schematics illustrating the angle convention used in this thesis. The left hand pane shows the stagger angle convention, while the right hand pane shows the effect that a change in IGV or rotor blade stagger has on the flow angles and incidence on the rotor blades and stator vanes at mid-span and at the design flow coefficient.



The shapes of characteristics prior to stall with each stall inception mechanism

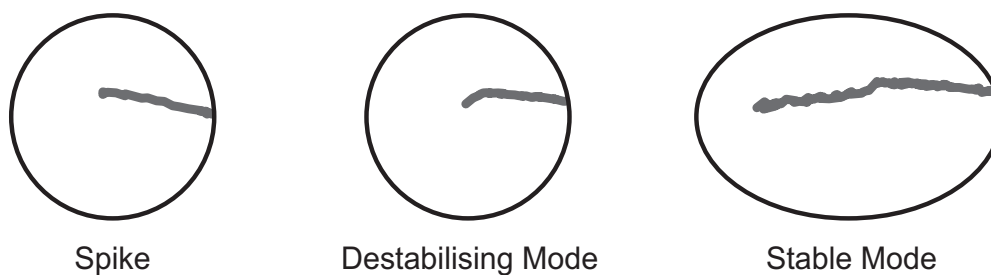


Figure 8.5: The effect of changing the IGV stagger angle on the performance of casing treatment. The upper graph shows Red compressor characteristics with smooth and treated walls installed at different rotor incidences (calculated at 94% span and relative to the incidence that the design configuration rotor would encounter if it were operating near each case's smooth-wall stall point). The lower schematics show the shapes of the characteristics immediately prior to stall that occur with each type of stall inception mechanism.

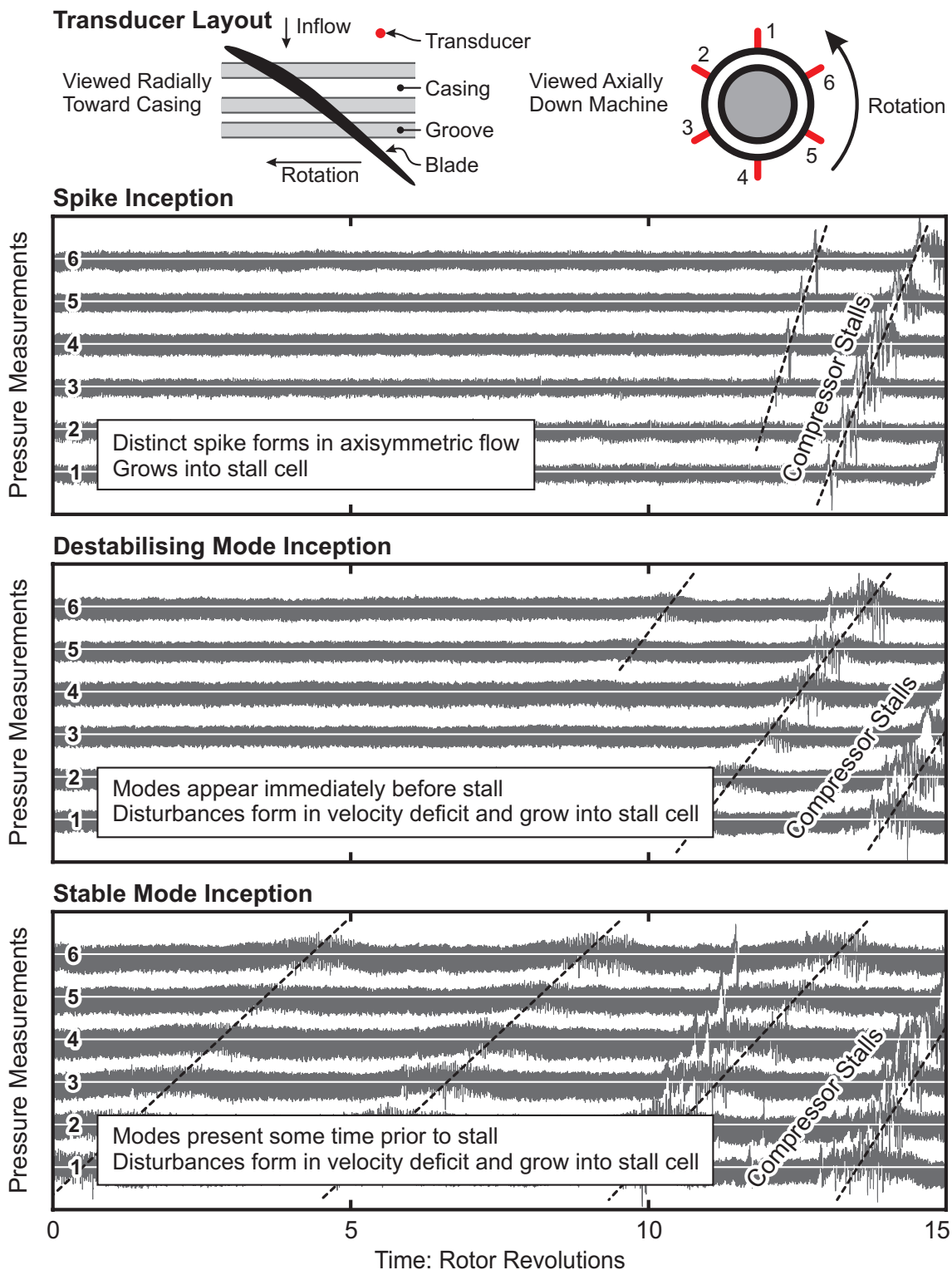


Figure 8.6: The three stall inception mechanisms observed during the IGV stagger tests. The upper plot shows a spike inception, with a single spike emerging in an axisymmetric flow field. The middle plot shows destabilising modes, with the appearance of modes leading directly to stall. The lower plot shows stable modes, with the stall cell growing from modes that have existed for some time prior to stall (a spike also forms, but does not cause stall).

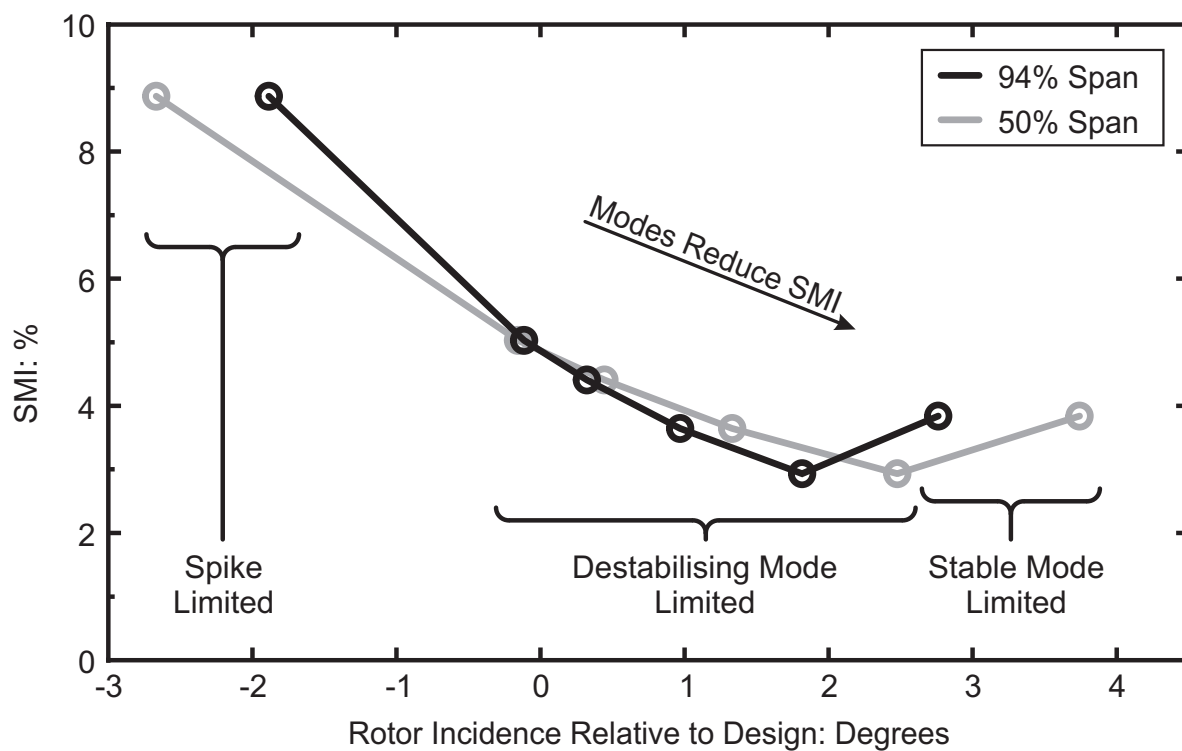


Figure 8.7: The impact of rotor incidence on the stall margin improvement generated by the grooved wall casing treatment in the Red compressor. Incidences have been calculated at 94 and 50% span using the method described in Figure 8.5.

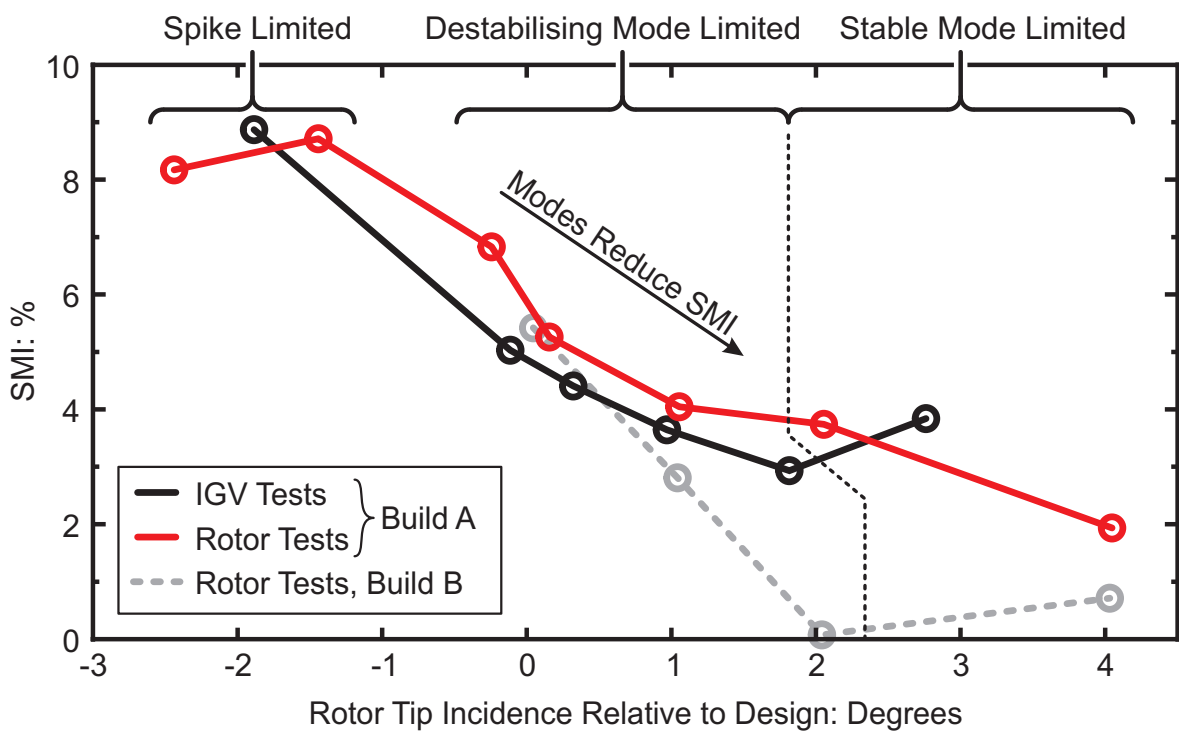
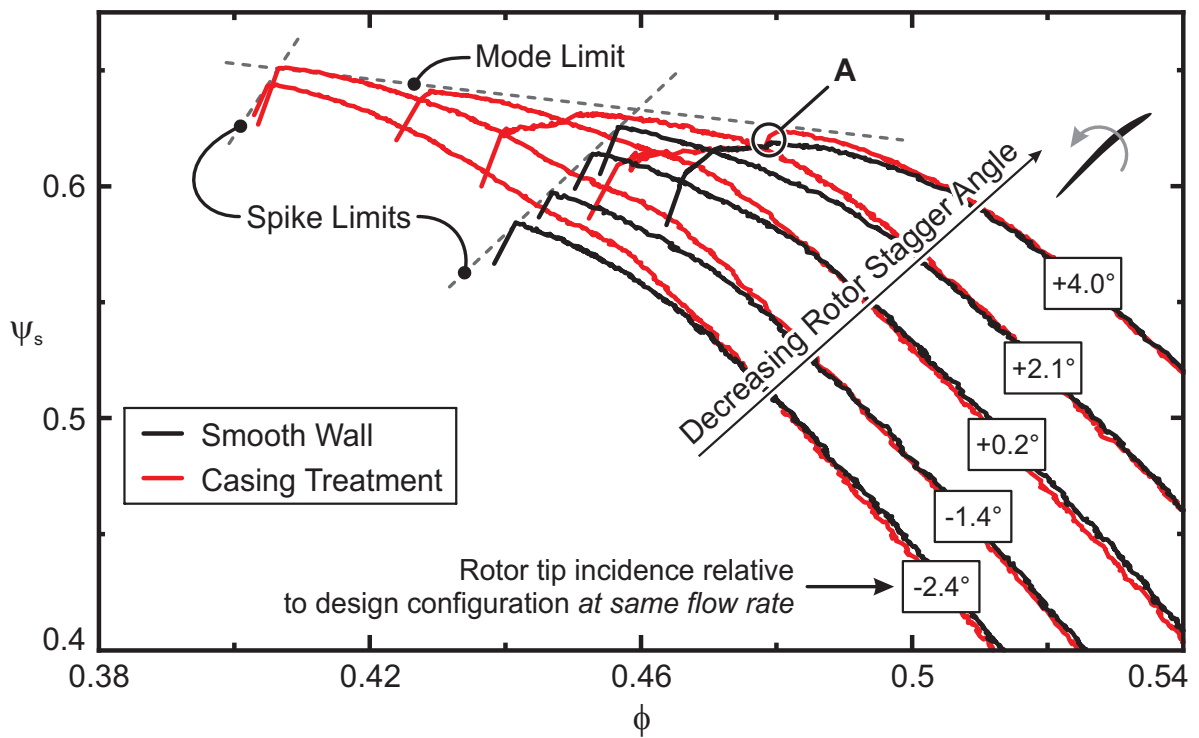


Figure 8.8: The effect of changing the rotor stagger angle on the performance of casing treatment. The upper graph shows Red compressor characteristics with smooth and treated walls installed at different rotor incidences (some cases omitted for clarity). The lower graph shows how the stall margin improvement generated by the treatment varies with rotor incidence.

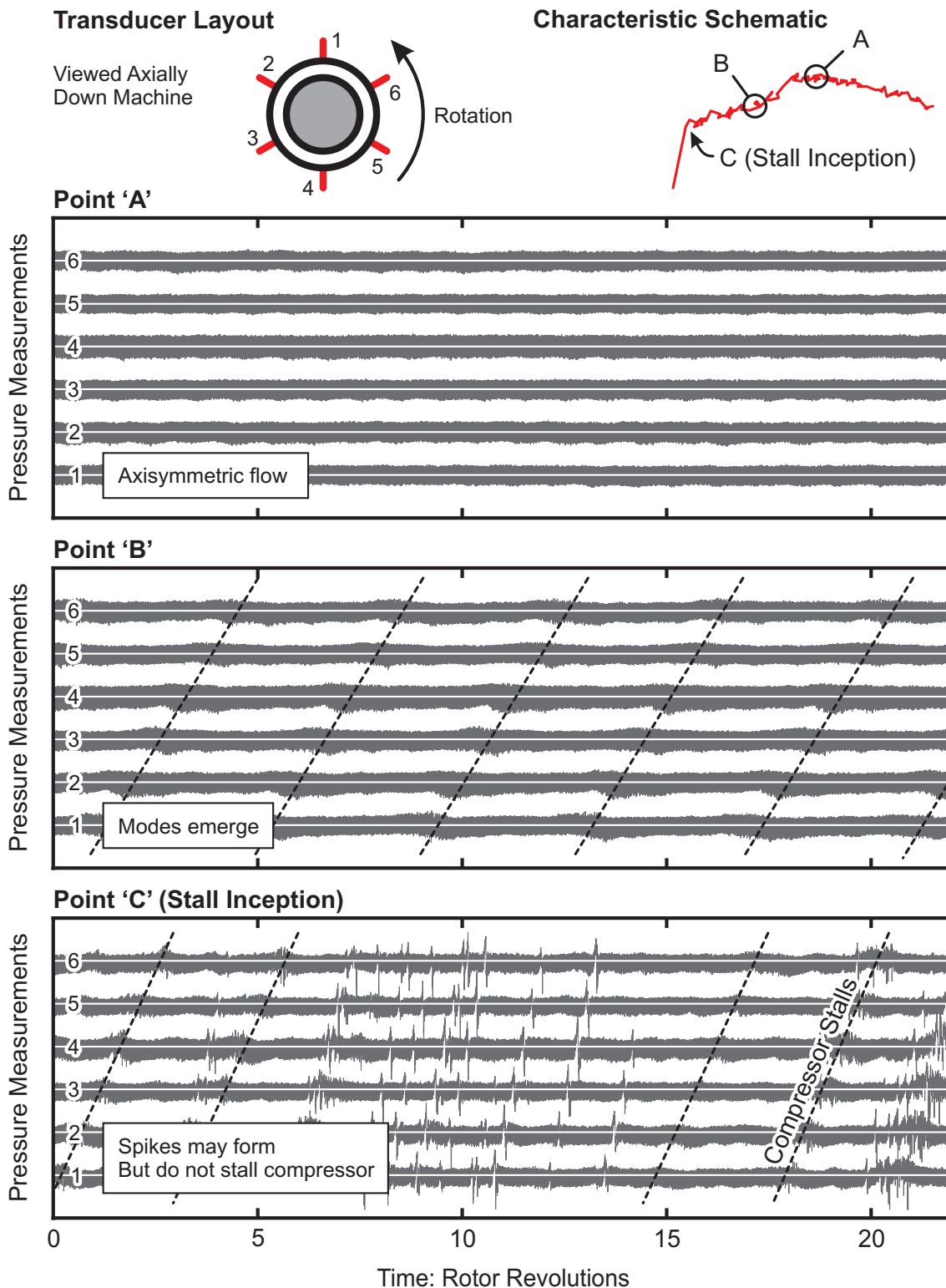


Figure 8.9: Stable mode behaviour in the Red compressor. High-frequency pressure transducer measurements showing modes appearing near the roll over and drop in the characteristic. Spikes may form when the characteristic has a positive gradient, but they do not stall the compressor (when the characteristic has a negative gradient, the first spike to traverse the annulus usually causes stall).

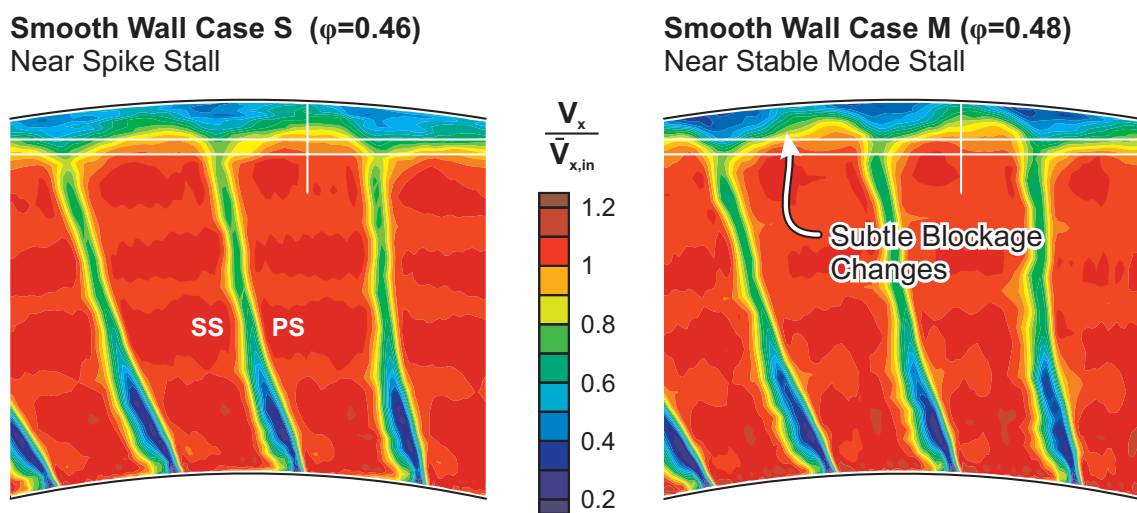


Figure 8.10: The axial velocity of the Red compressor's rotor outflow for spike and modal stalling cases operating near their respective stall points (low axial velocity is considered blockage). The axial velocity was measured using a hotwire traverse downstream of the trailing edge, and the data is normalised by the mean value at the rotor inflow (to aid comparison between the cases).

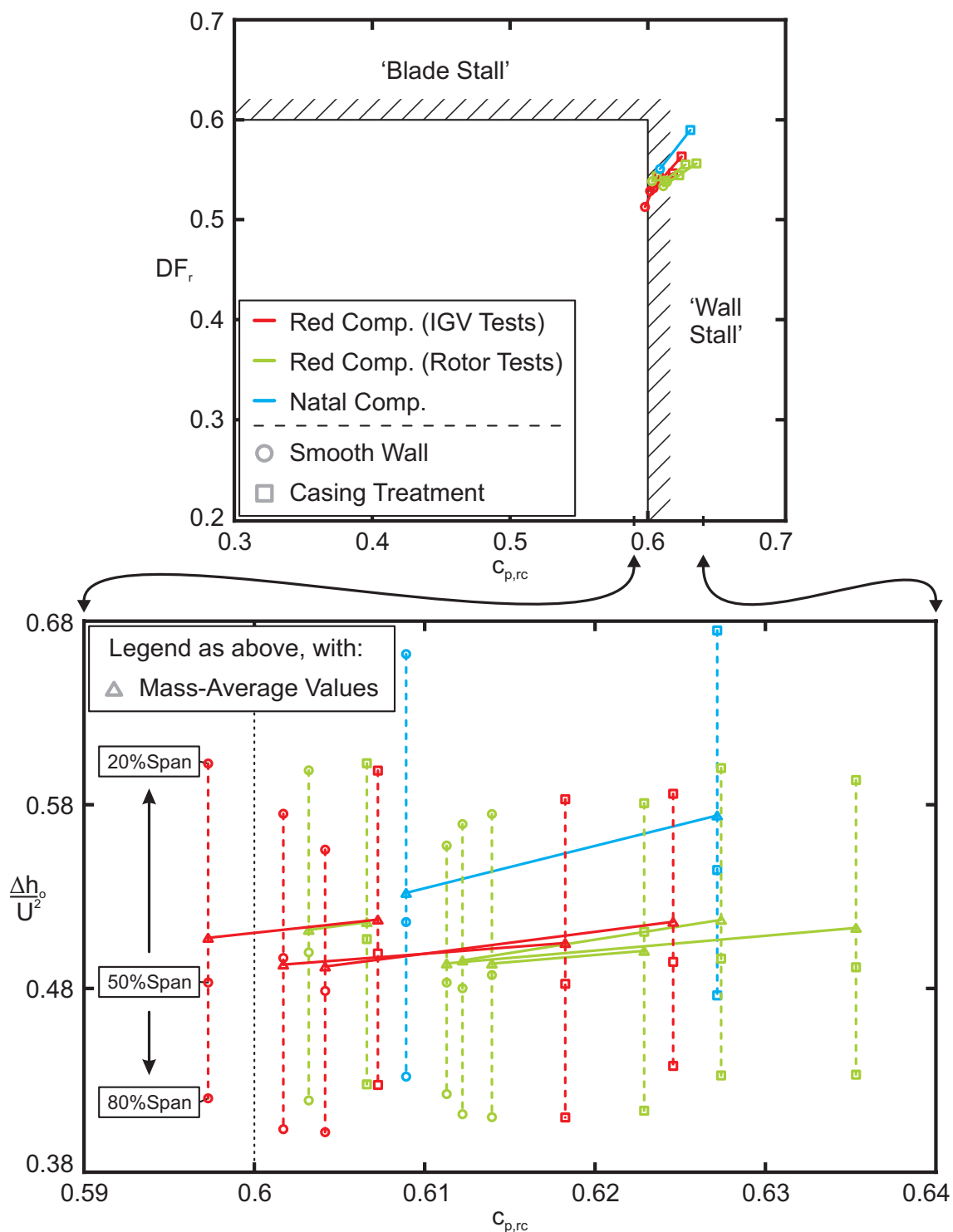


Figure 8.11: Loading analysis. The upper graph applies the analysis of Greitzer *et al.* (1979) to the Natal and Red compressors for smooth and treated wall cases. The lower graph plots loading at 20, 50 and 80% span and the mass-mean value against the same abscissa as the upper plot (but at a larger scale).

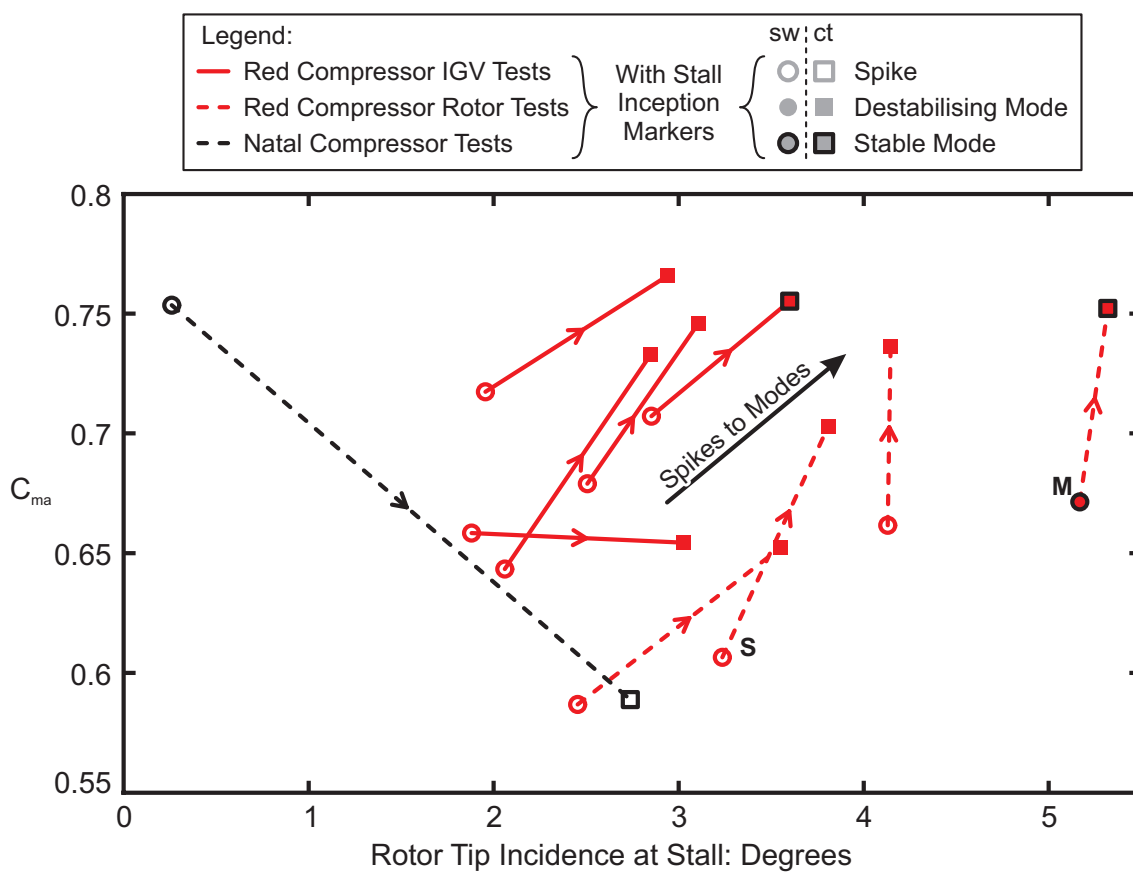


Figure 8.12: An analysis based on the model of Simpson and Longley (2007) applied to the Red and Natal compressors for smooth and treated wall cases.

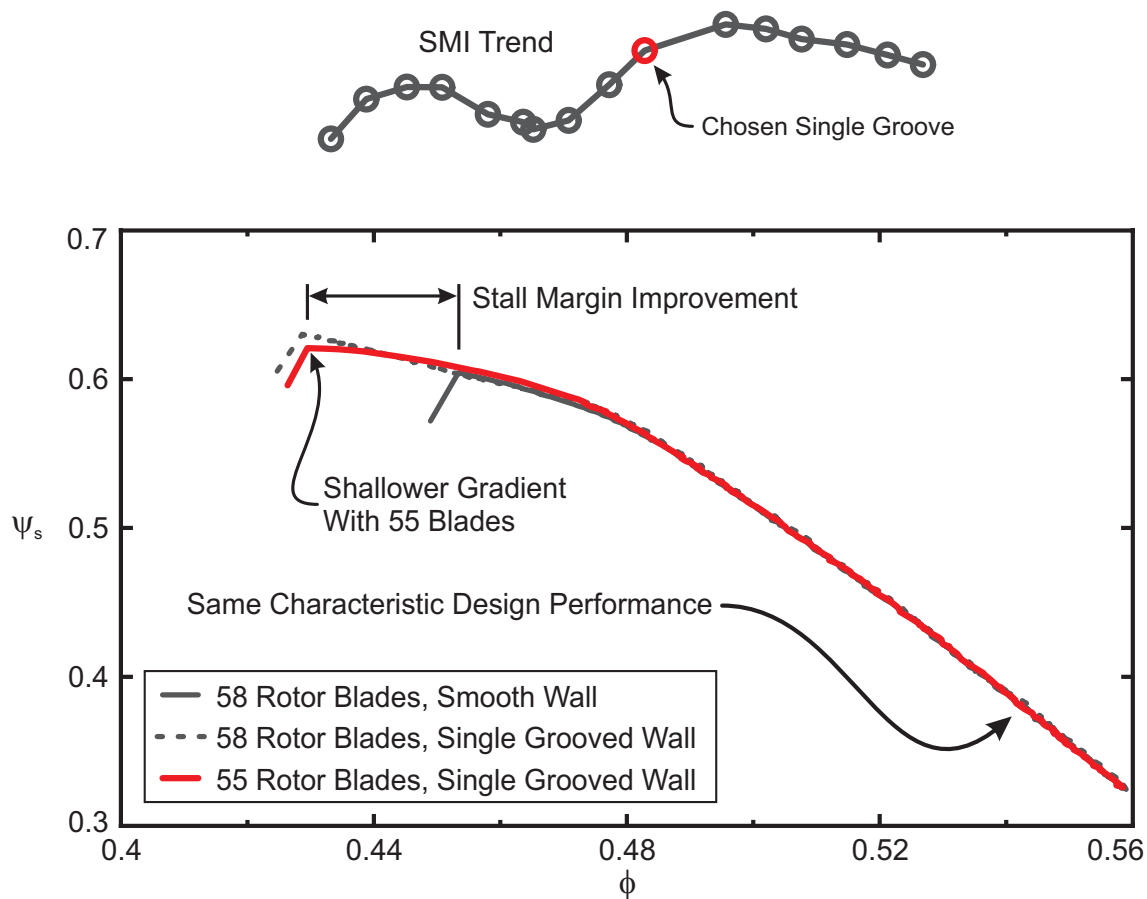


Figure 8.13: Characteristics showing the impact of adding a single-groove casing treatment to the Red compressor with 58 and 55 rotor blades installed. The groove is located at 33% $c_{x,r}$. The groove's position on the SMI trend from Figure 8.1 is shown on the schematic at the top of the figure.

Chapter 9

Conclusion

Despite over sixty years of research, compressor stall is not well understood and remains a hazard for aero-engine compressors. This lack of understanding precludes the development of technologies to precisely target stall inception. However, the present work uses experimental and computational methods to contribute to the long history of empirical development of stall prevention techniques.

This section summarises this contribution, and is divided into four parts. The first and second parts regard the circumferential groove and axial slot treatments respectively. The third part reports the findings that are relevant to both of these casing treatments. The fourth part considers the impact of stall inception mechanism and solidity on the performance of casing treatment. Finally, ideas for further work are discussed.

9.1 Circumferential Grooves

Experimental testing in two different compressors has shown, for the first time, that there are two locations over the rotor tips where a single circumferential groove generates a local maximum stall margin improvement. The first location is near the leading edge (forward edge of groove at 8% chord) and the second is at 50% chord. By contrast, the stall margin improvement is minimised at the blade leading and trailing edges and at 18% chord. These findings explain some long-standing contradictions in the literature, where some authors recommend locating grooves near the leading edge, and others recommend mid-chord.

It has been shown that when the groove is near the first stall margin maximum (8% chord) it interacts strongly with the highly energetic near-casing flow field, changing the tip leakage flow, tip leakage vortex development and blade loading. These complex interactions cause considerable losses due to separations and radial mixing, and this reduces the efficiency of the compressor. When the groove is near the second stall margin maximum (50% chord) it interacts weakly with the near-casing flow field, merely increasing the tangential velocity of the flow adjacent to the groove. This interaction occurs through viscous shear, causes minimal loss, and thus does not reduce the efficiency of the compressor as much as the interaction when the groove is in the forward position. Therefore, this work shows that the optimum location for a single groove is near mid-chord.

Grooves installed near 8% and 50% chord generate similar stall margin improvements, but only the groove at 8% chord changes the early growth and trajectory of the tip leakage vortex. The fact that the stall margin is improved by the groove at 50% chord shows that altering the tip leakage vortex is not a necessary requirement for stall margin improvement. This finding will be interesting for researchers studying stall inception.

It has been shown that it is hard to improve on the performance of a single circumferential groove located near mid-chord by altering the cross-sectional shape of the groove. In the present work, a groove with a square cross-section (which is 14% $c_{x,r}$ wide and deep) worked well in this location. Rounding off the aft groove corner is unlikely to be a good design choice as it offers no performance advantage and is difficult to manufacture.

If further stall margin improvement is required, the designer can include additional grooves near mid-chord or the leading edge (with baffles installed inside them to reduce sensitivity to the stall margin minimum at 18% $c_{x,r}$ if required). However, this is likely to reduce the efficiency of the compressor. If greater mechanical integrity is required, or there are problems with inlet distortion, non-uniform tip clearances or clashes between components, intermittent grooves (a new treatment with small circumferential sections of groove placed to best advantage) are a sensible design choice.

9.2 Axial Slots

It has been shown that there is an optimum depth for casing slots of $60\% c_{x,r}$. Slots that are shallower than this generate a lower stall margin improvement and efficiency, while deeper slots generate no further stall margin improvement, and reduce efficiency.

Quarter-wave pressure resonances inside the slots have been observed using experimental and computational methods, but tuning the slot depth to encourage them has little impact on performance.

It has been shown that there is an optimum slot width of $30\% c_{x,r}$. Slots narrower than this generate a lower stall margin improvement and efficiency, while wider slots generate no further stall margin improvement, and reduce efficiency.

The impact of changing the land width is different: reducing the width of the land between slots improves stall margin but reduces efficiency. In real engines, the land width will be limited by mechanical integrity requirements. Small land widths also enable the compressor to operate at very low flow-rates, which can cause large near-casing blockage. In a multi-stage environment, this may de-stabilise downstream blade rows, making the stall margin improvement lower than expected. Land widths greater than $50\% c_{x,r}$ may, therefore, be a sensible design choice.

Increasing the porosity, or the amount of casing wall that is machined away to create a slotted casing treatment, tends to increase stall margin improvement but reduce the efficiency. However, because it combines the different effects of slot and land width, it is concluded that porosity should not be used as a design parameter.

It has been shown that casing slots cause large, in-phase, oscillations in the blade tip loading as the blade passes the slots. Large oscillating pressure differences between adjacent slots have also been observed. The impact of these oscillations on noise, vibration and fatigue should be considered during design.

Using experimental and computational methods, it has been shown that while the interaction between the casing slots and near-casing flow is highly unsteady, the flow inside the slots is principally a quasi-steady recirculation from near the rotor to the inflow. Steady models of slot-based casing treatments may be useful for initial design, but the present work suggests that unsteady flow effects are also important and should be considered during the design process.

9.3 A Comparison of Casing Grooves and Slots

The present work shows that, for well designed casing treatments that have been applied to well designed rotors, generating large stability improvements causes large efficiency losses. Comparison with the literature suggests that the efficiency will only be improved by casing treatment if it removes a large source of loss in the blade row (such as blockage or a tip leakage vortex breakdown). Careful design is thus required to get the best balance between stability and efficiency in a treated compressor.

Computational work shows that the entropy sources that cause these efficiency reductions are corner separations and radial mixing caused by flow moving in and out of the treatment. The sources of loss are similar for both casing grooves and slots, but the magnitude of loss caused by slots is generally greater than grooves, both at the design point and near stall.

The present work has found no *clear* link between the stall margin improvement generated by casing grooves or slots and the outflow blockage or time-mean blade loading. Such links have been postulated in the literature, but are not supported by the present work.

It is interesting that the optimum distance between the blade leading edge and the downstream edge of the slots ($25\% c_{x,r}$) is similar to the distance from the blade leading edge to the downstream edge of an optimally-placed forward circumferential groove ($22\% c_{x,r}$). In these locations, both treatments are as far forward as possible, while remaining adjacent to the region of most vigorous tip clearance flow.

The near-casing flow in an axial compressor has been accurately modelled. This validated model was used to investigate the cause of a line of scouring that occurs on a casing flow visualisation called the 'black line'. It has been shown that the black line is caused by a three-dimensional separation point that occurs on the separation line between the incoming and tip leakage flows, the position of which is set by a balance of axial momentum. The black line is not caused by a divide between the inflow and axially reversed flow over the blade tip (as suggested in the literature).

The interaction of casing slots and the optimally-placed forward circumferential groove with the near-casing flow is remarkably similar. Both treatments interfere with the formation and growth of the tip leakage vortex (moving the blade tip loading aft) and remove the black line. Both treatments also increase the axial and tangential velocity of the near-casing flow in the vicinity of the blade tip, which increases the component of the tip clearance flow directed along the blade and decreases the component directed across the blade. The literature suggests that both of these effects improve stability. However, casing slots have a larger impact on the tip leakage flow than grooves. Slots also increase the velocity of the

flow upstream of the rotor and have a stronger interaction with the near-casing flow near stall, which grooves do not.

Although steady RANS-based CFD models can be used to accurately model the near-casing flows (and the impact of casing treatment upon these flows), they should not be trusted to accurately predict the stall margin improvement generated by casing grooves. It is better to design casing treatments by considering their interaction with near-casing flow features.

If the tip clearance increases concentrically when casing grooves or slots are installed, both treatments maintain their stall margin improvement. However, the overall stall margin and efficiency of the treated compressor still reduce as the tip clearance increases. The performance of casing grooves may reduce if the casing becomes eccentric.

The stall inception pattern in the Natal compressor (spike-type) is not affected by the presence of casing grooves or slots, even when the casing treatment alters the trajectory of the tip leakage vortex. Both treatments can prevent spike formation, but casing slots can also suppress and slow emerging spikes. It is interesting that the stall inception mechanism remains similar, even though casing treatments alter the tip leakage flow structure.

9.4 Casing Treatment, Stall Inception and Solidity

Two kinds of modal stall inception have been identified. If the characteristic rolls over immediately prior to stall 'Destabilising Modes' occur and lead directly to stall. If the characteristic becomes horizontal, or rolls over, some way before stall 'Stable Modes' occur and further throttling (with modes present) is required to stall the compressor.

For the first time, it has been shown that the maximum possible stall margin improvement to be gained from adding casing grooves will only be achieved if spike-type stall inception is present before and after the grooves are added. If the addition of casing grooves leads to the occurrence of modes, the stall margin gain is likely to be reduced. Little or no stall margin improvement is to be expected if casing grooves are added to a compressor where the smooth-wall configuration exhibits modal stall inception.

While investigating the performance of casing grooves, it was found that increasing the incidence on the rotor blades, either by altering their inflow or stagger angle, causes the stall inception mechanism to change from spikes to destabilising modes, and then stable modes. The propagation speed of the stall cell reduces as the stall inception changes from spikes to stable modes. Reducing the blade count also encourages the onset of modes.

It has been shown that efficiency and stability can be improved by removing rotor blades to improve efficiency and then applying casing treatment to maintain stability. However, removing blades from a rotor can cause modes to occur at higher flow rates, thus limiting the stall margin improvement that can be expected from the grooves.

It has been found that the variations in the rotor outflow blockage associated with spike and modal stall inceptions are small and cannot easily be used to predict the stall inception type. A model which compares the blade tip incidence and generation of near-casing blockage in the blade row (similar to that of Simpson and Longley, 2007) allows an interesting comparison between similar cases, but no reliable design tool for accurately predicting a given compressor's stall inception mechanism, and hence the effectiveness of casing treatment, has been identified.

9.5 Closure

There is no obvious 'best' casing treatment. Each design must be carefully considered alongside the compressor it is intended to be used in. However, for a well designed compressor that is required to be efficient, only needs a small stability improvement, and stalls with a spike inception, a single circumferential groove at mid-chord is a compelling choice.

9.6 Suggestions for Further Work

The performance of casing grooves can be significantly reduced by changes to the stall inception mechanism. Predicting the type of stall inception in a given compressor is therefore important, but there is currently no accurate way of doing this.

It would be interesting to investigate the impact of different radial loading distributions on the stall inception mechanism and the performance of casing grooves. It would also be useful to see whether changes to the stall inception mechanism affect casing slots in the same way as grooves, as it was not possible to investigate this in the present work.

The operation of casing treatment will be very difficult to explain until the physics of stall inception are understood. It is also not clear why the onset of modes reduces the performance of casing treatments.

The present work has shown that basic tests on a single casing groove can be useful in understanding the operation of casing treatment. It would be interesting to extend the present work by measuring the performance of single grooves of different widths at varying axial locations.

It would be useful to measure the performance of a casing groove at different axial locations in a transonic compressor test rig.

It would also be useful to investigate the impact of very effective casing treatments (which allow the compressor to operate at very low flow rates) on downstream stages in a multi-stage environment.

Bibliography

- Adamczyk J J, Celestina M L and Greitzer E M (1993)** The Role of Tip Clearance in High-Speed Fan Stall. *ASME Journal of Turbomachinery*, **115**(1), p. 28. doi:10.1115/1.2929212.
- Azimian A R, Elder R L and McKenzie A B (1990)** Application of Recess Vaned Casing Treatment to Axial Flow Fans. *ASME Journal of Turbomachinery*, **112**(1), p. 145. doi:10.1115/1.2927411.
- Bae J W, Breuer K S and Tan C S (2005)** Active Control of Tip Clearance Flow in Axial Compressors. *ASME Journal of Turbomachinery*, **127**(2), p. 352. doi:10.1115/1.1776584.
- Bailey E E (1972)** Effect of Grooved Casing Treatment on the Flow Range Capability of a Single-Stage Axial-Flow Compressor. Technical Report TM X-2459, NASA.
- Barnett M, Graf M, Raw J A, Sharma O and Sprout W D (2003)** Casing Treatment for a Fluid Compressor. Patent US 2003/0138317 A1 published by the United States Patent and Trademark Office.
- Beheshti B H, Ghorbanian K, Farhanieh B, Teixeira J A and Ivey P C (2006)** A New Design for Tip Injection in Transonic Axial Compressors. *ASME Conference Proceedings*, **2006**(4241X), p. 39. doi:10.1115/GT2006-90007.
- Bennington M A, Cameron J D, Morris S C and Gendrich C P (2007)** Over Rotor Casing Surface Streak Measurements in a High Speed Axial Compressor. *ASME Conference Proceedings*, **2007**(47950), p. 445. doi:10.1115/GT2007-28273.
- Brignole G A, Danner F C T and Kau H P (2008)** Time Resolved Simulation and Experimental Validation of the Flow in Axial Slot Casing Treatments for Transonic Axial Compressors. *ASME Conference Proceedings*, **2008**(43161), p. 363. doi:10.1115/GT2008-50593.
- CAA (2004)** ATA 72 - Engine - HP Compressor - Test/Modification. Technical Report AD:G-2004-0010, Civil Aviation Authority.
- Camp T R and Day I J (1998)** A Study of Spike and Modal Stall Phenomena in a Low-Speed Axial Compressor. *Journal of Turbomachinery*, **120**(3), p. 393. doi:10.1115/1.2841730.

- Camp T R and Shin H W (1995)** Turbulence Intensity and Length Scale Measurements in Multistage Compressors. *Journal of Turbomachinery*, **117**(1), p. 38. doi:10.1115/1.2835642.
- Cargill A M and Freeman C (1991)** High-Speed Compressor Surge With Application to Active Control. *Journal of Turbomachinery*, **113**(2), p. 303. doi:10.1115/1.2929108.
- Chen G T, Greitzer E M, Tan C S and Marble F E (1991)** Similarity Analysis of Compressor Tip Clearance Flow Structure. *ASME Journal of Turbomachinery*, **113**(2), p. 260. doi:10.1115/1.2929098.
- Chima R V (1998)** Calculation of Tip Clearance Effects in a Transonic Compressor Rotor. *ASME Journal of Turbomachinery*, **120**(1), p. 131. doi:10.1115/1.2841374.
- Christensen D, Cantin P, Gutz D, Szucs P N, Wadia A R, Armor J, Dhingra M, Neumeier Y and Prasad J V R (2008)** Development and Demonstration of a Stability Management System for Gas Turbine Engines. *ASME Journal of Turbomachinery*, **130**(3), 031011. doi:10.1115/1.2777176.
- Crook A J, Greitzer E M, Tan C S and Adamczyk J J (1993)** Numerical Simulation of Compressor Endwall and Casing Treatment Flow Phenomena. *ASME Journal of Turbomachinery*, **115**(3), pp. 501. doi:10.1115/1.2929280.
- Cumpsty N A (1989a)** *Compressor Aerodynamics*. ISBN 0-582-01364-X. Longman Scientific.
- Cumpsty N A (1989b)** Part Circumference Casing Treatment and the Effect on Compressor Stall. *ASME Gas Turbine and Aero-engine Congress and Exposition, Canada*.
- Cumpsty N A and Greitzer E M (1982)** A Simple Model for Compressor Stall Cell Propagation. *Transactions of the ASME*, **104**, p. 170.
- Cumpsty N A and Horlock J H (2005)** Averaging Non-Uniform Flow for a Purpose. *ASME Conference Proceedings*, **2005**(47306), p. 1. doi:10.1115/GT2005-68081.
- Day I, Williams J and Freeman C (2008)** Rain Ingestion in Axial Flow Compressors at Part Speed. *ASME Journal of Turbomachinery*, **130**(1), 011024. doi:10.1115/1.2366511.
- Day I J (1993a)** Active Suppression of Rotating Stall and Surge in Axial Compressors. *ASME Journal of Turbomachinery*, **115**(1), p. 40. doi:10.1115/1.2929216.
- Day I J (1993b)** Stall Inception in Axial Flow Compressors. *ASME Journal of Turbomachinery*, **115**(1), p. 1. doi:10.1115/1.2929209.
- Day I J (1994)** Axial Compressor Performance During Surge. *AIAA Journal of Propulsion and Power*, **10**(3), p. 329.

- Day I J, Breuer T, Escuret J, Cherrett M and Wilson A (1999)** Stall Inception and the Prospects for Active Control in Four High-Speed Compressors. *ASME Journal of Turbomachinery*, **121**(1), p. 18. doi:10.1115/1.2841229.
- Day I J and Cumpsty N A (1978)** The Measurement and Interpretation of Flow Within Rotating Stall Cells Within Axial Flow Compressors. *ASME Journal of Mechanical Engineering Science*, **20**, p. 101.
- Day I J and Freeman C (1994)** The Unstable Behavior of Low and High-Speed Compressors. *ASME Journal of Turbomachinery*, **116**(2), p. 194. doi:10.1115/1.2928353.
- Day I J, Greitzer E M and Cumpsty N A (1977)** Prediction of Compressor Performance in Rotating Stall. *ASME Journal of Engineering for Power*, **100**, p. 1.
- Denton J D (1993)** Loss Mechanisms in Turbomachines. *ASME Journal of Turbomachinery*, **115**(4), p. 621. doi:10.1115/1.2929299. The 1993 IGTI Scholar Lecture.
- Deppe A, Saathoff H and Stark U (2004)** Stall Inception Phenomena in Three Single-Stage Low-Speed Axial Compressors. *10th Int. Symp. on Transport Phenomena and Dynamics of Rotating Machinery, Hawaii*.
- Deppe A, Saathoff H and Stark U (2005)** Stall Inception Phenomena in Three Single-Stage Low-Speed Axial Compressors. *6th European Turbomachinery Conference, France*.
- Dickens A (2008)** *Highly Loaded Compressors*. Ph.D. thesis, Cambridge University Engineering Department.
- Dobrzynski B, Saathoff H and Kosyna G (2007)** Influence of the Rotor Tip Stagger Angle on Axial Compressor Stall Inception. *7th European Turbomachinery Conference, Athens*.
- Dobrzynski B, Saathoff H, Kosyna G, Clemen C and Gümmer V (2008)** Active Flow Control in a Single-Stage Axial Compressor Using Tip Injection and Endwall Boundary Layer Removal. *ASME Conference Proceedings*, **2008**(43161), p. 139. doi:10.1115/GT2008-50214.
- Ffowcs Williams J E, Harper M F L and Allwright D J (1993)** Active Stabilization of Compressor Instability and Surge in a Working Engine. *ASME Journal of Turbomachinery*, **115**(1), p. 68. doi:10.1115/1.2929219.
- Freeman C (1985)** The Effect of Tip Clearance Flow on Compressor Stability and Engine Performance. *Von Karman Institute for Fluid Mechanics Lecture Series 1985-05*.
- Freeman C, Wilson A G, Day I J and Swinbanks M A (1998)** Experiments in Active Control of Stall on an Aeroengine Gas Turbine. *ASME Journal of Turbomachinery*, **120**(4), p. 637. doi:10.1115/1.2841773.

- Fujita H and Takata H (1984)** A Study on Configurations of Casing Treatment for Axial Flow Compressors. *The Bulletin of the JSME*, **27**(230), p. 1675.
- Furukawa M, Inoue M, Saiki K and Yamada K (1999)** The Role of Tip Leakage Vortex Breakdown in Compressor Rotor Aerodynamics. *ASME Journal of Turbomachinery*, **121**(3), p. 469. doi:10.1115/1.2841339.
- Gbadebo S A, Cumpsty N A and Hynes T P (2007)** Interaction of Tip Clearance Flow and Three-Dimensional Separations in Axial Compressors. *ASME Journal of Turbomachinery*, **129**(4), p. 679. doi:10.1115/1.2720876.
- Gerolymos G A and Vallet I (1999)** Tip-Clearance and Secondary Flows in a Transonic Compressor Rotor. *ASME Journal of Turbomachinery*, **121**(4), p. 751. doi:10.1115/1.2836729.
- Gourdain N, Burguburu S, Michon G J, Ouayahya N, Leboeuf F and Plot S (2006)** About the Numerical Simulation of Rotating Stall Mechanisms in Axial Compressors. *ASME Conference Proceedings*, **2006**(4241X), p. 1723. doi:10.1115/GT2006-90223.
- Graf M B, Wong T S, Greitzer E M, Marble F E, Tan C S, Shin H W and Wisler D C (1998)** Effects of Nonaxisymmetric Tip Clearance on Axial Compressor Performance and Stability. *ASME Journal of Turbomachinery*, **120**(4), p. 648. doi:10.1115/1.2841774.
- Greitzer E M (1976)** Surge and Rotating Stall in Axial Flow Compressors: Part 2. *ASME Journal of Engineering for Power*, **98**(2), p. 199.
- Greitzer E M and Moore F K (1986)** A Theory of Post-Stall Transients in Axial Compression Systems: Part 2 - Application. *ASME Journal of Engineering for Gas Turbines and Power*, **108**(2), p. 231. doi:10.1115/1.3239893.
- Greitzer E M, Nikkanen J P, Haddad D E, Mazzawy R S and Joslyn H D (1979)** A Fundamental Criterion for the Application of Rotor Casing Treatment. *ASME Journal of Fluids Engineering*, **101**(3), p. 237.
- Hah C, Schulze R, Wagner S and Hennecke D K (1999)** Numerical and Experimental Study for Short Wavelength Stall Inception in a Low-Speed Axial Compressor. *AIAA*.
- Hathaway M D (2002)** Self-Recirculating Casing Treatment Concept for Enhanced Compressor Performance. *ASME Conference Proceedings*, **2002**(3610X), p. 411. doi:10.1115/GT2002-30368.
- Hathaway M D (2007)** Passive Endwall Treatments for Enhancing Stability. Technical Report TM-2007-214409, NASA.
- Hills N (2007)** Achieving High Parallel Performance for an Unstructured Unsteady Turbomachinery CFD Code. *The Aeronautical Journal*, **111**(1117), p. 1.

- Hoeger M, Lahmer M, Dupslaff M and Fritsch G (2000)** A Correlation for Tip Leakage Blockage in Compressor Blade Passages. *ASME Journal of Turbomachinery*, **122**(3), p. 426. doi:10.1115/1.1303707.
- Höss B, Leinhos D and Fottner L (2000)** Stall Inception in the Compressor System of a Turbofan Engine. *ASME Journal of Turbomachinery*, **122**(1), p. 32. doi:10.1115/1.555425.
- Howard M A, Ivey P C, Barton J P and Young K F (1994)** Endwall Effects at Two Tip Clearances in a Multistage Axial Flow Compressor With Controlled Diffusion Blading. *ASME Journal of Turbomachinery*, **116**(4), p. 635. doi:10.1115/1.2929454.
- Hoying D A, Tan C S, Vo H D and Greitzer E M (1999)** Role of Blade Passage Flow Structures in Axial Compressor Rotating Stall Inception. *ASME Journal of Turbomachinery*, **121**(4), p. 735. doi:10.1115/1.2836727. Also published as MIT Gas Turbine Lab report number 224.
- Inoue M, Kuroumaru M, Tanino T and Furukawa M (2000)** Propagation of Multiple Short-Length-Scale Stall Cells in an Axial Compressor Rotor. *ASME Journal of Turbomachinery*, **122**(1), p. 45. doi:10.1115/1.555426.
- Inoue M, Kuroumaru M, Yoshida S, Minami T, Yamada K and Furukawa M (2004)** Effect of Tip Clearance on Stall Evolution Process in a Low-Speed Axial Compressor Stage. *ASME Conference Proceedings*, **2004**(41707), p. 385. doi:10.1115/GT2004-53354.
- Jorgensen F E (2005)** How to Measure Turbulence with Hotwire Anemometers: A Practical Guide. Technical note published via the Dantec Dynamics website.
- Kang S and Hirsch C (1994)** Tip Leakage Flow in Linear Compressor Cascade. *ASME Journal of Turbomachinery*, **116**(4), p. 657. doi:10.1115/1.2929458.
- Kau H P, Brignole G and Wilke I (2006)** Designing a Casing Treatment for a Multistage Compressor. *VKI Lecture Series*.
- Khalid S A, Khalsa A S, Waitz I A, Tan C S, Greitzer E M, Cumpsty N A, Adamczyk J J and Marble F E (1999)** Endwall Blockage in Axial Compressors. *ASME Journal of Turbomachinery*, **121**(3), p. 499. doi:10.1115/1.2841344.
- Khalsa A S (1996)** *Endwall Blockage in Axial Compressors*. Ph.D. thesis, Massachusetts Institute of Technology.
- Koch C C (1970)** Experimental Evaluation of Outer Case Blowing or Bleeding of Single Stage Axial Flow Compressor: Part 6 - Final Report. Technical Report CR-54592, NASA.
- Koch C C (1981)** Stalling Pressure Rise Capability of Axial Flow Compressor Stages. *ASME Journal of Engineering for Power*, **103**(4), p. 645.

- Lapworth B L (2006)** Compressor with Casing Treatment Slots. Patent GB 2 418 956 published by the United Kingdom Intellectual Property Office.
- Lapworth B L (2007)** Advanced Compressor Design Incorporating Real Geometry Features. *ISABE*.
- Lee N K W and Greitzer E M (1990)** Effects of Endwall Suction and Blowing on Compressor Stability Enhancement. *ASME Journal of Turbomachinery*, **112**(1), p. 133. doi:10.1115/1.2927410. Also published as MIT Gas Turbine Lab report number 192.
- Leinhos D C, Scheidler S G, Fottner L, Grauer F, Hermann J, Mettenleiter M and Orthmann A (2002)** Experiments in Active Stall Control of a Twin-Spool Turbofan Engine. *ASME Conference Proceedings*, **2002**(36061), p. 9. doi:10.1115/GT2002-30002.
- Lieblein S, Schwenk F C and Broderick R L (1953)** Diffusion Factor for Estimating Losses and Limiting Blade Loadings in Axial-Flow Compressor Blade Elements. Technical Report RM-E53D01, NASA.
- Lin F, Ning F and Liu H (2008)** Aerodynamics of Compressor Casing Treatment: Part 1 - Experiment and Time-Accurate Numerical Simulation. *ASME Conference Proceedings*, **2008**(43161), p. 731. doi:10.1115/GT2008-51541.
- Lu X, Chu W, Zhu J and Wu Y (2006a)** Experimental and Numerical Investigation of a Subsonic Compressor With Bend Skewed Slot Casing Treatment. *ASME Conference Proceedings*, **2006**, p. 49. doi:10.1115/GT2006-90026.
- Lu X, Chu W, Zhu J and Wu Y (2006b)** Mechanism of the Interaction Between Casing Treatment and Tip Leakage Flow in a Subsonic Axial Compressor. *ASME Conference Proceedings*, **2006**, p. 79. doi:10.1115/GT2006-90077.
- Lu X, Chu W, Zhu J and Zhang Y (2009)** Numerical Investigations of the Coupled Flow Through a Subsonic Compressor Rotor and Axial Skewed Slot. *ASME Journal of Turbomachinery*, **131**(1), p. 011001. doi:10.1115/1.2948959.
- Madden D S and West M A (2005)** Effects of Inlet Distortion on the Stability of an Advanced Military Swept Fan Stage With Casing Treatment. *ASME Conference Proceedings*, **2005**(47306), p. 269. doi:10.1115/GT2005-68693.
- März J, Hah C and Neise W (2002)** An Experimental and Numerical Investigation into the Mechanisms of Rotating Instability. *ASME Journal of Turbomachinery*, **124**(3), p. 367. doi:10.1115/1.1460915.
- McDougall N M, Cumpsty N A and Hynes T P (1990)** Stall Inception in Axial Compressors. *ASME Journal of Turbomachinery*, **112**(1), p. 116. doi:10.1115/1.2927406. Also published as a PhD thesis in Cambridge University.

- Moinier P and Giles M B (1998)** Preconditioned Euler and Navier-Stokes Calculations on Unstructured Grids. *6th ICFD Conference on Numerical Methods for Fluid Dynamics, Oxford, UK*.
- Moore F K and Greitzer E M (1986)** A Theory of Post-Stall Transients in Axial Compression Systems: Part 1 - Development of Equations. *ASME Journal of Engineering for Gas Turbines and Power*, **108**(1), p. 68. doi:10.1115/1.3239887.
- Moore R D, Kovich G and Blade R J (1971)** Effect of Casing Treatment on Overall and Blade-Element Performance of a Compressor Rotor. Technical Report TN D-6538, NASA.
- Müller M W, Schiffer H P and Hah C (2007)** Effect of Circumferential Grooves on the Aerodynamic Performance of an Axial Single-Stage Transonic Compressor. *ASME Conference Proceedings*, **2007**(47950), p. 115. doi:10.1115/GT2007-27365.
- Ning F and Xu L (2008)** Aerodynamics of Compressor Casing Treatment: Part 2 - A Quasi-Steady Model for Casing Treatment Flows. *ASME Conference Proceedings*, **2008**(43161), p. 745. doi:10.1115/GT2008-51542.
- NTSB (1977)** Southern Airways Flight 242 Accident Report. Technical report, NTSB.
- Osborn W M, Lewis G W and Heidelberg L J (1971)** Effect of Several Porous Casing Treatments on Stall Limit and Overall Performance of an Axial Compressor Rotor. Technical Report TN D-6537, NASA.
- Paduano J D, Epstein A H, Valavani L, Longley J P, Greitzer E M and Guenette G R (1993)** Active Control of Rotating Stall in a Low-Speed Axial Compressor. *ASME Journal of Turbomachinery*, **115**(1), p. 48. doi:10.1115/1.2929217.
- Peacock R E (1982)** A Review of Turbomachinery Tip Gap Effects: Part 2 - Rotating Machinery. *International Journal of Heat and Fluid Flow*, **4**(1), p. 3. doi:10.1016/0142-727X(83)90019-X.
- Prince D C, Wisler D C and Hilvers D E (1974)** Study of Casing Treatment Stall Margin Improvement Phenomena. Technical Report CR-134552, NASA.
- Saathoff H, Deppe A and Stark U (2003)** Steady and Unsteady Casingwall Flow Phenomena in a Single-Stage Low-Speed Compressor at Part-Load Conditions. *International Journal of Rotating Machinery*, **9**(5), p. 327. doi:10.1155/S1023621X03000307.
- Scheidler S G and Fottner L (2003)** Active Stabilization of the Compression System in a Twin-Spool Turbofan Engine at Inlet Distortions. *International Symposium for Air Breathing Engines*.

- Scheidler S G and Fottner L (2006)** Experimental Operating Range Extension of a Twin-Spool Turbofan Engine by Active Stability Control Measures. *ASME Journal of Engineering for Gas Turbines and Power*, **128**(1), p. 20. doi:10.1115/1.2031247.
- Schlichting H and Das A (1969)** On the Influence of Turbulence Level on the Aerodynamic Losses of Axial Turbomachines. *The Symposium on Flow Research on Blading, Baden*. L. S. Dzung.
- Seitz P A (1999)** *Casing Treatment for Axial Flow Compressors*. Ph.D. thesis, Cambridge University Engineering Department.
- Shabbir A and Adamczyk J J (2005)** Flow Mechanism for Stall Margin Improvement due to Circumferential Casing Grooves on Axial Compressors. *ASME Journal of Turbomachinery*, **127**(4), p. 708. doi:10.1115/1.2008970.
- Shahpar S and Lapworth L (2003)** PADRAM: Parametric Design and Rapid Meshing System for Turbomachinery Optimisation. *ASME Conference Proceedings*, **2003**(36894), p. 579. doi:10.1115/GT2003-38698.
- Simpson A K (2005)** *An Investigation into Stall Inception in a Single Stage, Low Speed Axial-Flow Compressor*. Ph.D. thesis, Cambridge University Engineering Department.
- Simpson A K and Longley J P (2007)** An Experimental Study of the Inception of Rotating Stall in a Single-Stage Low-Speed Axial Compressor. *ASME Conference Proceedings*, **2007**(47950), p. 87. doi:10.1115/GT2007-27181.
- Sirakov B T and Tan C S (2003)** Effect of Unsteady Stator Wake-Rotor Double-Leakage Tip Clearance Flow Interaction on Time-Average Compressor Performance. *ASME Journal of Turbomachinery*, **125**(3), p. 465. doi:10.1115/1.1574822.
- Smith G D J and Cumpsty N A (1984)** Flow Phenomena in Compressor Casing Treatment. *ASME Journal of Engineering for Gas Turbines and Power*, **106**(3), p. 532. doi:10.1115/1.3239604. Also Cambridge University Engineering Department report Turbo/TR112.
- Smith L H (2002)** Axial Compressor Aerodesign Evolution at General Electric. *ASME Journal of Turbomachinery*, **124**(3), p. 321. doi:10.1115/1.1486219.
- Spalart P R and Allmaras S R (1992)** A One-Equation Turbulence Model for Aerodynamic Flows. *AIAA 30th Aerospace Sciences Meeting*.
- Storer J A and Cumpsty N A (1991)** Tip Leakage Flow in Axial Compressors. *ASME Journal of Turbomachinery*, **113**(2), p. 252. doi:10.1115/1.2929095. Also published as a PhD thesis in Cambridge University.

- Storer J A and Cumpsty N A (1994)** An Approximate Analysis and Prediction Method for Tip Clearance Loss in Axial Compressors. *ASME Journal of Turbomachinery*, **116**(4), p. 648. doi:10.1115/1.2929457.
- Strazisar A J, Bright M M, Thorp S, Culley D E and Suder K L (2004)** Compressor Stall Control Through Endwall Recirculation. *ASME Conference Proceedings*, **2004**(41707), p. 655. doi:10.1115/GT2004-54295.
- Suder K L (1998)** Blockage Development in a Transonic, Axial Compressor Rotor. *ASME Journal of Turbomachinery*, **120**(3), p. 465. doi:10.1115/1.2841741.
- Suder K L and Celestina M L (1996)** Experimental and Computational Investigation of the Tip Clearance Flow in a Transonic Axial Compressor Rotor. *ASME Journal of Turbomachinery*, **118**(2), p. 218. doi:10.1115/1.2836629.
- Suder K L, Hathaway M D, Thorp S A, Strazisar A J and Bright M B (2001)** Compressor Stability Enhancement Using Discrete Tip Injection. *ASME Journal of Turbomachinery*, **123**(1), p. 14. doi:10.1115/1.1330272.
- Takata H and Tsukuda K (1977)** Stall Margin Improvement by Casing Treatment: Its Mechanism and Effectiveness. *ASME Journal of Engineering for Power*, **99**, p. 121.
- Tryfonidis M, Etchevers O, Paduano J D, Epstein A H and Hendricks G J (1995)** Prestall Behavior of Several High-Speed Compressors. *ASME Journal of Turbomachinery*, **117**(1), p. 62. doi:10.1115/1.2835644.
- Vo H D (2001)** *Role of Tip Clearance Flow on Axial Compressor Stability*. Ph.D. thesis, Massachusetts Institute of Technology.
- Vo H D, Tan C S and Greitzer E M (2008)** Criteria for Spike Initiated Rotating Stall. *ASME Journal of Turbomachinery*, **130**(1), p. 011023. doi:10.1115/1.2750674.
- Waterman M J C (1992)** Axial Flow Compressor Surge Margin Improvement. Patent GB 2 245 312 published by the United Kingdom Intellectual Property Office.
- Weigl H J, Paduano J D, Fr chet te L G, Epstein A H, Greitzer E M, Bright M M and Strazisar A J (1998)** Active Stabilization of Rotating Stall and Surge in a Transonic Single-Stage Axial Compressor. *ASME Journal of Turbomachinery*, **120**(4), p. 625. doi:10.1115/1.2841772. 1997 Best Controls and Diagnostics Paper Award. Also published as MIT Gas Turbine Lab report number 226.
- Wilde G L (1953)** Improvements in or Relating to Compressors. Patent GB 701 576 published by the United Kingdom Intellectual Property Office.

- Wilke I and Kau H P (2004)** A Numerical Investigation of the Flow Mechanisms in a High Pressure Compressor Front Stage With Axial Slots. *ASME Journal of Turbomachinery*, **126**(3), p. 339. doi:10.1115/1.1731465.
- Wilke I, Kau H P and Brignole G (2005)** Numerically Aided Design of a High-Efficient Casing Treatment for a Transonic Compressor. *ASME Conference Proceedings*, **2005**(47306), p. 353. doi:10.1115/GT2005-68993.
- Wilson A G and Freeman C (1994)** Stall Inception and Development in an Axial Flow Aeroengine. *ASME Journal of Turbomachinery*, **116**(2), p. 216. doi:10.1115/1.2928356.
- Wisler D C, Beacher B F and Shin H (2002)** Effects of Loading and Clearance Variation on Tip Vortex and Endwall Blockage. *9th International Symposium on Transport Phenomena and Dynamics of Rotating Machinery*.
- Yoon Y S, Song S J and Shin H W (2006)** Influence of Flow Coefficient, Stagger Angle, and Tip Clearance on Tip Vortex in Axial Compressors. *ASME Journal of Fluids Engineering*, **128**(6), p. 1274. doi:10.1115/1.2354522.
- Young A (2008)** *Blade Tip Shape and Compressor Stall*. MEng Report, Cambridge University Engineering Department.